MODELING TIME-DEPENDENT DEFORMATION BEHAVIOR OF JOINTED ROCK MASS

by

Mingzheng Wang

A thesis submitted in partial fulfillment of the requirements for
the degree of Doctor of Philosophy (PhD) in Natural Resources Engineering

The Faculty of Graduate Studies
Laurentian University
Sudbury, Ontario, Canada

THESIS DEFENCE COMMITTEE/COMITÉ DE SOUTENANCE DE THÈSE
Laurentian Université/Université Laurentienne
Faculty of Graduate Studies/Faculté des études supérieures

Title of Thesis Titre de la thèse	MODELING TIME-DEPENDENT DEFORMATION BEHAVIOR OF JOINTED ROCK MASS
Name of Candidate Nom du candidat	Wang, Mingzheng
Degree Diplôme	Doctor of Philosophy
Department/Program Département/Programme	Natural Resources Engineering
Date of Defence Date de la soutenance	July 4th 2022

APPROVED/APPROUVÉ

Thesis Examiners/Examinateurs de thèse:

Dr. Ming Cai
(Supervisor/Directeur de thèse)

Dr. Krishna Challagulla
(Committee member/Membre du comité)

Dr. Eugene Ben-Awah
(Committee member/Membre du comité)

Dr. Marie-Helene Fillion
(Committee member/Membre du comité)

Dr. Navid Bahrani
(External Examiner/Examinateur externe)

Dr. Richard Smith
(Internal Examiner/Examinateur interne)

Approved for the Faculty of Graduate Studies
Approuvé pour le Bureau des études supérieures

Tammy Eger, PhD
Vice-President, Research (Office of Graduate Studies)
Vice-rectrice à la recherche (Bureau des études supérieures)
Laurentian University / Université Laurentienne

ACCESSIBILITY CLAUSE AND PERMISSION TO USE

I, **Mingzheng Wang**, hereby grant to Laurentian University and/or its agents the non-exclusive license to archive and make accessible my thesis, dissertation, or project report in whole or in part in all forms of media, now or for the duration of my copyright ownership. I retain all other ownership rights to the copyright of the thesis, dissertation or project report. I also reserve the right to use in future works (such as articles or books) all or part of this thesis, dissertation, or project report. I further agree that permission for copying of this thesis in any manner, in whole or in part, for scholarly purposes may be granted by the professor or professors who supervised my thesis work or, in their absence, by the Head of the Department in which my thesis work was done. It is understood that any copying or publication or use of this thesis or parts thereof for financial gain shall not be allowed without my written permission. It is also understood that this copy is being made available in this form by the authority of the copyright owner solely for the purpose of private study and research and may not be copied or reproduced except as permitted by the copyright laws without written authority from the copyright owner.

Abstract

Long-term stability analysis and stand-up time prediction of underground excavations are important in engineering design and construction. In this thesis, a numerical study of the time-dependent deformation behavior of jointed rock mass is presented.

Firstly, creep deformation behavior of intact rock is studied numerically using the grain-based modeling (GBM) approach based on the Distinct Element Method (DEM). A grain-based time-to-failure (GBM-TtoF) creep model for intact brittle rocks is proposed to simulate creep deformations in the first two creep stages and time-dependent failure at the tertiary creep stage. Parameters of the TtoF model are calibrated using experimental data of Lac du Bonnet (LdB) granite. Simulations of the time-dependent deformation of rock pillars using the GBM-TtoF model are conducted. The influence of pillar shape (width to height ratio) and loading ratio (stress / strength) on the time-dependent spalling on pillar walls is investigated.

Secondly, creep deformation of rock joints is simulated by using the grain-based joint models that are established using the GBM-TtoF model. The influences of joint roughness and loading conditions (normal and shear stresses) on the long-term shear strength and creep sliding velocity of joints are investigated. A new creep model is proposed, which can be used to control the creep deformation behavior of flat joints in the DEM. The model is validated using experimental data of joints.

Thirdly, a creep model for jointed rock masses, which can consider time-dependent deformations of both rock and joints, is proposed. Creep deformations of jointed rock masses are simulated using a few jointed rock mass models, i.e., a rock mass model with a single joint, a jointed pillar model and a high rock slope model. The creep deformation characteristics of the jointed rock mass models are analyzed.

Finally, time-dependent deformation behaviors of tunnels excavated in jointed rock masses are simulated using the creep model for jointed rock masses. The weakening of face-effect due to creep deformation of the rock mass is modeled using the internal pressure reduction method and the convergence-confinement method. The stand-up time of unsupported tunnels is simulated considering the influence of rock mass quality and the unsupported roof span. The simulated result is validated using Bieniawski's stand-up time chart.

The models developed in this thesis provide novel numerical approaches to simulating creep deformations of rock, joints and jointed rock masses, and are important for improving the understanding of the time-dependent deformation behavior of jointed rock masses.

Keywords

Time-dependent deformation behavior, creep deformation, grain-based model, distinct element method, time-to-failure, Lac du Bonnet granite, rock pillar, spalling, creep model of joint, GBM-UDEC, jointed rock mass, tunnels, convergence-confinement method, stand-up time.

Acknowledgments

This research was financially supported by NSERC (Natural Science and Engineering Research Council of Canada, RGPIN-2016-04052, ALLRP 560390-20), the China Scholarship Council (Grant No. CSC201806370225), and MIRARCO of Laurentian University.

I would like to thank my supervisor Prof. Ming Cai. Even though the pandemic brought many unexpected challenges to my research plan, he could always solve my problems in time and help me to reach each milestone on schedule. His patient guidance and valuable suggestions really helped me and influenced me deeply. I believe that the doctoral study under his supervision must be one of the most valuable experience in my academic career.

I would like to acknowledge my current committee members, Dr. Eugene Ben-Awuah, Dr. Krishna Challagulla and Dr. Marie-Helene Fillion, and former committee members, Dr. Mounir Naili and Dr. Shailendra Sharan. Through their courses and valuable discussions, I learned many useful skills about numerical modeling methods and research methods.

I would also like to thank colleagues and staffs at MIRARCO, thank Mrs. Qin Liang, Dr. Subash Bastola, Dr. Xin Wang, Dr. Guang Liu and Dr. Jianlin Xie for valuable help and useful discussions.

Thank you all for your kindly support!

Finally, the most importantly, I would like to thank my dear wife, Mrs. Guangjie Shi. Four years ago, I am so grateful that you chose to come here and study at Laurentian with me. I

still remember the night that I picked you up at Sudbury airport. In the moment, we started an absolutely new life which just belongs to you and me. In the past four years, you made every day of my life full of love and joy. Recently, you just gave birth to our daughter. She is so lovely. Smiles on her face always remind me countless loving moments with you in my memory. It had always been my greatest honor, to be your classmate in 2008, to be your boyfriend in 2011, to be your husband in 2018, to be the father of our baby in 2021, and to love you all in the rest of my life.

Mingzheng Wang

Valentine's Day 2022

In Greater Sudbury

Table of Contents

List of Tables

List of Figures

List of abbreviations and symbols

Abbreviation	Description
3DEC	Three-dimensional distinct element code
DEM	Distinct element method
FEM	Finite element method
FDM	Finite difference method
GBM	Grain-based model
GBM−TtoF	Grain-based time-to-failure model
GRC	Ground reaction curve
GSI	Geological strength index
LdB granite	Lac du Bonnet granite
LDP	Longitudinal displacement profile
PFC	Particle flow code
TtoF	Time-to-failure
UDEC	Universal distinct element code

Greek symbols

Symbols	Description	Unit
α	Inclination angle of joint	°
β	Model parameter of TtoF model	Dimensionless
γ	Model parameter of TtoF model	Dimensionless
$\Delta t_{\max}^{cr}$	Maximum creep timestep	s
$\Delta t_{\min}^{cr}$	Minimum creep timestep	s
ε	Strain	Dimensionless
$\dot{\varepsilon}$	Creep strain rate	h^{-1}
ξ	Long-term shear strength ratio of joint	Dimensionless
ξ_0	Basic long-term shear strength ratio of joint	Dimensionless
ξ	Pillar strength ratio	Dimensionless
ξ_N	Normalized pillar strength ratio	Dimensionless

$\xi_{W/H=1}$	Strength ratio ξ of a pillar with W/H =1.0	Dimensionless
η_m	Viscosity coefficient of Maxwell component	GPa^{-1}
η_k	Viscosity coefficient of Kelvin component	GPa^{-1}
ν	Poisson's ratio of rock	Dimensionless
ρ	Density of rock	g/cm^3
ρ'	Density of grains	g/cm^3
σ	Stress	MPa
σ_0	In-situ field stress (hydrostatic condition)	MPa
σ_1	First principal stress	MPa
σ_1^f	Value of σ_1 on the ultimate strength circle (when σ_3 keeps constant)	MPa
σ_2	Second principal stress	MPa
σ_3	Third principal stress	MPa
σ_3^f	Value of σ_3 on the ultimate strength circle (when σ_1 keeps constant)	MPa
σ_{ci}	Crack initiation stress	MPa
σ_{cd}	Crack damage stress	MPa
σ_E	Radius of central-ultimate strength circle as shown in the Mohr's diagram	MPa
σ_H	Horizontal stress applied on two sides of model	MPa
σ_h	Horizontal stress applied to the out-of-plane surfaces	MPa
σ_L	Long-term compressive strength	MPa
σ_{MAX}	Maximum principal stress	MPa
σ_n	Normal stress	MPa
σ_r	Radial stress	MPa
σ_S	Short-term compressive strength	MPa
σ_t	Tensile strength of rock	MPa

σ_t'	Tensile strength of mineral grains	MPa
σ_t^{ct}	Tensile strength of grains contact	MPa
σ_t^{j}	Tensile strength of joint	MPa
σ_t^{j-c}	Tensile strength of contact elements on joint surface	MPa
σ_V	Vertical stress	MPa
σ_Y	Yield strength of plastic component	MPa
σ_θ	Hoop stress	MPa
τ	Shear stress	MPa
τ_L	Long-term shear strength of joint	MPa
τ_S	Short-term shear strength of joint	MPa
τ/τ_S	Shear loading ratio	MPa
ϕ	Friction angle of rock	°
ϕ^{cd}	Friction angle of σ_{cd} envelope defined by the Mohr–Coulomb strength criterion	°
ϕ'	Friction angle of mineral grains	°
ϕ^{ct}	Friction angle of grains contact	°
ϕ_b^{j}	Basic friction angle of joint	°
ϕ_{mob}	Mobilized joint friction angle	°
ϕ^{j-c}	Friction angle of contact elements on joint surface	°
φ'	Dilation of grains	°

Alphapet

Symbols	**Description**	**Unit**
a	Model constant of the TtoF model	Dimensionless
b	Model constant of the TtoF model	Dimensionless
c	Cohesion of rock	MPa
c′	Cohesion of mineral grains	MPa

c_0'	Initial value of cohesion of grains	MPa
c^{ct}	Cohesion of grains contact	MPa
c_0^{ct}	Initial value of cohesion of contact	MPa
c_Y^{ct}	Ultimate cohesion value of contact on the yield boundary	MPa
c_Y'	Ultimate value of grains cohesion on the yield boundary	MPa
c^{cd}	Cohesion of σ_{cd} envelope defined by the Mohr–Coulomb strength criterion	MPa
c^{j}	Cohesion of joint	MPa
c^{j-c}	Cohesion of contact elements on joint surface	MPa
C_j	Model parameter in creep-slipping model of joint	Dimensionless
D	Tunnel diameter	m
D_{ct}	Damage index of contact	Dimensionless
d_z	Shear displacement for zero dilation	m
D_z	Damage index of contact element or zone	Dimensionless
$D_{z-ct}^{(1)}$	Damage indexes of zones near the contact located in blocks 1	Dimensionless
$D_{z-ct}^{(2)}$	Damage indexes of zones near the contact located in blocks 2	Dimensionless
E	Young's modulus of rock	GPa
$fobl$	Lower unbalanced force limit for timestep adjusting	N
$fobu$	Upper unbalanced force limit for timestep adjusting	N
G	Shear modules	GPa
G_k	Shear modules of Kelvin component	GPa
G_m	Shear modules of Maxwell component	GPa
i^{ct}	Dilation of contact	°
i^{j-c}	Dilation angle of contact elements on joint surface	°

J_n	Joint set number	Dimensionless
J_r	Joint roughness number	Dimensionless
J_a	Joint alteration number	Dimensionless
J_w	Joint water reduction factor	Dimensionless
JCS	Joint wall compressive strength	MPa
JCS_0	Joint wall compressive strength of lab-scale joint	MPa
JCS_n	Joint wall compressive strength of in-situ scale joint	MPa
Jks^{ct}	Shear stiffness of grains contact	Pa/m
Jkn^{ct}	Normal stiffness of grains contact	Pa/m
Jks^{j-c}	Shear stiffness of contact elements on joint surface	Pa/m
Jkn^{j-c}	Normal stiffness of contact elements on joint surface	Pa/m
Jkn^{j}	Normal stiffness of joint	Pa/m
Jks^{j}	Shear stiffness of joint	Pa/m
JRC	Joint roughness coefficient	Dimensionless
JRC_0	Roughness coefficient of lab-scale joint	Dimensionless
JRC_{mob}	Mobilized joint roughness	Dimensionless
JRC_{c-mob}	Mobilized joint roughness due to creep damage	Dimensionless
JRC_n	Roughness coefficient of in-situ scale joint	Dimensionless
k	Field stress ratio, ratio of horizontal stress to vertical stress	Dimensionless
K'_v	Bulk modulus of grains	GPa
L_0	Length of lab-scale joint	m
L_n	Length of in-situ scale joint	m
l_v	Average edge length of grain	m
m	Hoek-Brown parameter (rock mass material constant)	Dimensionless

n_1	Number of zones near the contact located in blocks 1	Dimensionless
n_2	Number of zones near the contact located in blocks 2	Dimensionless
n_v	Iteration parameter of Voronoi cell	Dimensionless
P_0	Initial pressure on tunnel walls (unexcavated status)	MPa
P_i	Hypothetical internal pressure applied on tunnel walls	MPa
q	Model constant of the time-to failure model	Dimensionless
q'	Model constant in micro-ttof equation	Dimensionless
R	Tunnel radius	m
R^*	Normalized plastic zone radius (maximum plastic zone radius/tunnel radius)	m
RMR	Rock mass rating	Dimensionless
RQD	Rock quality designation	Dimensionless
r_{sc}	Central driving-stress ratio	Dimensionless
r_{sl}	Left driving-stress ratio	Dimensionless
r_{sr}	Right driving-stress ratio	Dimensionless
r_v	Round length of Voronoi cell	m
s	Hoek-Brown parameter (rock mass material constant)	Dimensionless
SRF	Stress reduction factor	Dimensionless
t_0	The time that the short-term compressive strength is measured	s
t_0'	Lifetime of a zone under the ultimate stress state (micro-parameters of zone)	s
T_F	Time-to-failure of rock	s
T_F'	Lifetime of a zone (micro-parameters of zone)	s
u^*	Normalized wall displacement (displacement/maximum displacement)	m
UCS	Uniaxial compressive strength	MPa
W/H	Width to height ratio	Dimensionless

X^*	Normalized distance (distance to the tunnel face/tunnel diameter)	Dimensionless

Preface

Results of this thesis (Chapters 2 to 7 and Appendix A) have been published as journal and conference papers. Publications related to this thesis are listed below.

Chapter 3 and Appendix A

Wang, M., & Cai, M. (2020). A grain-based time-to-failure creep model for brittle rocks. *Computers and Geotechnics*, 119, 103344.

Chapter 4

Wang, M., & Cai, M. (2021). Numerical modeling of time-dependent spalling of rock pillars. *International Journal of Rock Mechanics and Mining Sciences*, 141, 104725.

Wang, M., & Cai, M. (2021). Simulation of time-dependent deformation of brittle rock pillars using a grain-based time-to-failure model. In *55th US Rock Mechanics/Geomechanics Symposium*. American Rock Mechanics Association.

Chapter 5

Wang, M., & Cai, M. (2021). A simplified model for time-dependent deformation of rock joints. *Rock Mechanics and Rock Engineering*, 54(4), 1779-1797.

Wang, M., & Cai, M. (2020). Modeling time-dependent deformation of rock joint. In *54th US Rock Mechanics/Geomechanics Symposium*. American Rock Mechanics Association.

Chapter 6

Wang, M., & Cai, M. (2022). Modeling of Time-Dependent Deformation of Jointed Rock Mass. *Rock Mechanics and Rock Engineering*, 55 (4), 2049–2070. https://doi.org/10.1007/s00603-021-02750-2

Chapter 7

Wang, M., & Cai, M. (2022). Numerical modeling of stand-up time of tunnels considering time-dependent deformation of jointed rock masses. *Rock Mechanics and Rock Engineering*, 55 (7), 4305–4328. https://doi.org/10.1007/s00603-022-02871-2

Chapter 1 Introduction

1.1 Background and motivation

The time-dependent response of jointed rock mass, which usually results from creep deformations of rock and joints, is an important issue for geotechnical structures with a long service life-time, such as nuclear waste repositories (Habib and Berest, 1993, Chen et al., 2007, Lau et al., 2000), permanent pillars in underground mines (Li et al., 2019, Esterhuizen et al., 2011a) and high rock slopes (Hermanns et al., 2013, Mercer, 2007, Zhang et al., 2014, Feng et al., 2003). Accidents, fatality and damage to excavations and equipment usually occur due to the time-dependent deformation of rock mass, and one example is shown in Figure 1-1.

Figure 1-1. Severe damage caused by time-dependent deformation in a haulage in quartzite of 120 MPa UCS at a depth of 2600 m (Ortlepp, 2001).

If the long-term strength of a rock mass is well understood, the long-term stability of the rock mass can be evaluated effectively (Brady and Brown, 1993). If the time-dependent deformation of a rock mass is estimated accurately, ground support design can be conducted effectively, and the deformation of excavations can be well controlled (Hoek et al., 2000).

The current understanding of time-dependent deformation behaviors of rock mass is insufficient. For example, the stand-up time is the time that an unsupported tunnel would remain stable after excavation before it collapses. Bieniawski (1973) found that the stand-up time of unsupported tunnels is significantly influenced by the rock mass quality (represented by RMR) and the unsupported roof span. A stand-up time chart was developed, as shown in Figure 1-2, which is widely used to evaluate the stability of unsupported excavations. However, owing to the complexity of jointed rock masses which presents a large variation of mechanical properties and the difficulty to measure the rock mass structures completely, the empirical relation between the stand-up time and RMR shown in Figure 1-2 contains many uncertainties. Moreover, some important factors that influence time-dependent responses of rock mass, such as in-situ stress (Sharifzadeh et al., 2013), excavation method (Malan, 1999, Paraskevopoulou and Diederichs, 2018, Wu et al., 2018) and cross-section profile (Manh et al., 2015, Kabwe et al., 2020b, Pan and Dong, 1991), have not been considered. As a result, it is difficult for engineers to use the stand-up time estimation method shown in Figure 1-2 in practice to address the issue of balancing between long-term reliability and cost-efficiency in mining and civil tunneling designs.

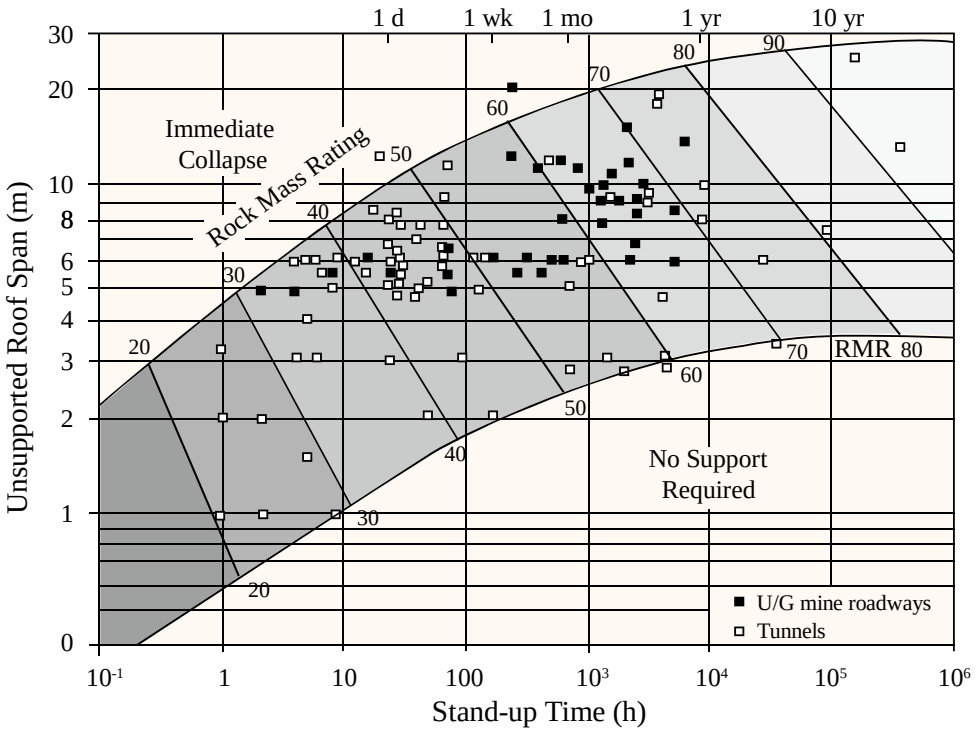

Figure 1-2. Relation between the unsupported roof span, rock mass rating (which is plotted using different shades) and stand-up time of tunnels (Bieniawski, 1973).

In general, the lack of understanding about the time-dependent deformation behavior of rock mass is attributed to three main challenges (Jing and Hudson, 2002, Kaiser and Kim, 2008, Aydan et al., 2013, Brady and Brown, 1993).

First, the complexity of the rock mass. When rock discontinuities (structural breaks in rock masses which have low tensile strength) are considered, the mechanical response of a jointed rock mass is nonlinear plastic, which is hard to capture and model.

Second, a lack of field data. To obtain usable field data of time-dependent response of a rock mass, such as the time-to-failure and the associated deformations, it usually requires long-term observations, resulting in very limited field data about time-dependent features of jointed rock masses.

Third, a lack of effective analysis methods. Most analytical methods and numerical simulations of time-dependent deformation behavior of jointed rock mass are carried out based on the assumption of homogenous materials. As a result, the damage resulting from time-dependent deformation of discontinuities cannot be analyzed.

In summary, improving the understanding of time-dependent deformation behavior of jointed rock mass is not only an urgent issue, but also a challenging task.

1.2 Research questions

In a jointed rock mass system, the relative contributions from intact rock and joints determine the overall deformation behavior of the rock mass. As shown in Figure 1-3, in the rock mass with an interlocked joint, the behavior of the intact rock dominates the deformation process. For the rock mass with no joint interlocking, the joint deformation will be dominant. Therefore, to investigate the time-dependent deformation of rock mass, the characteristics of intact rock and joints need to be well understood. Hence, this study starts with several research questions that are listed below.

a. How do we describe the time-dependent deformation behavior of rocks properly? How do we understand the long-term strength of intact rocks?
b. If the time-dependent deformation of discontinuities is considered, how can it influence the time-dependent response of a jointed rock mass?
c. How do we develop an effective analysis approach for the creep deformation of rock mass that can consider time-dependent deformations of both rock and joints?

d. How the time-dependent deformations of jointed rock mass influence the stand-up time of tunnels? How can we predict the stand-up time of a tunnel accurately?

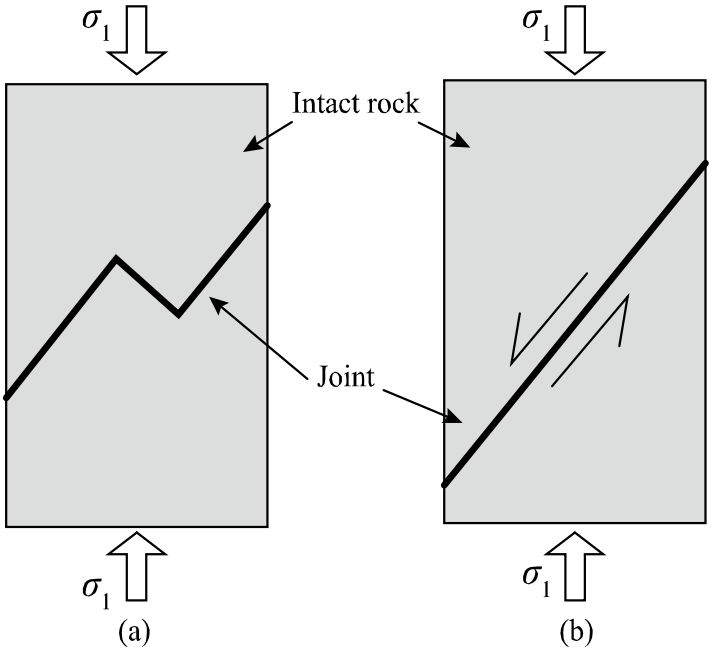

Figure 1-3. Deformation behaviors of two types of jointed rock mass: (a) an interlocked jointed rock mass; (b) a non-interlocked jointed rock mass with a persistent joint.

1.3 Research objectives

The study presented in this thesis aims at improving the understanding of time-dependent deformation behavior of jointed rock mass by developing effective modeling approaches that can be used to assess time-dependent responses of intact rock, rock joints and jointed rock mass. The specific objectives are to:

(a) Model time-dependent deformation behaviors of intact rock, including the creep deformation pattern, the long-term strength and the phenomenon of time-dependent rock failure.

(b) Measure how time-dependent deformation of rock influences the failure mode and the long-term stability of geotechnical structures, such as rock pillars in underground mines.

(c) Model time-dependent deformation behavior of rock joints.

(d) Develop a new model to describe creep deformations of rock joints in response to different normal and shear loadings.

(e) Develop a new model for simulating time-dependent deformation of jointed rock mass, which can consider creep deformations of both rock and joints.

(f) Model the mechanism that governs the stand-up time of tunnels.

(g) Simulate time-dependent deformations of tunnels using the proposed creep model for jointed rock masses.

1.4 Scope of the thesis

This thesis focuses on studying time-dependent deformation behaviors of jointed rock masses. As mentioned in Section 1.2, both intact rock and joints affect the overall deformation of a rock mass. Hence, time-dependent deformation behaviors of intact rock and joints are investigated. The research contents and approaches for four research topics are summarized in Figure 1-4.

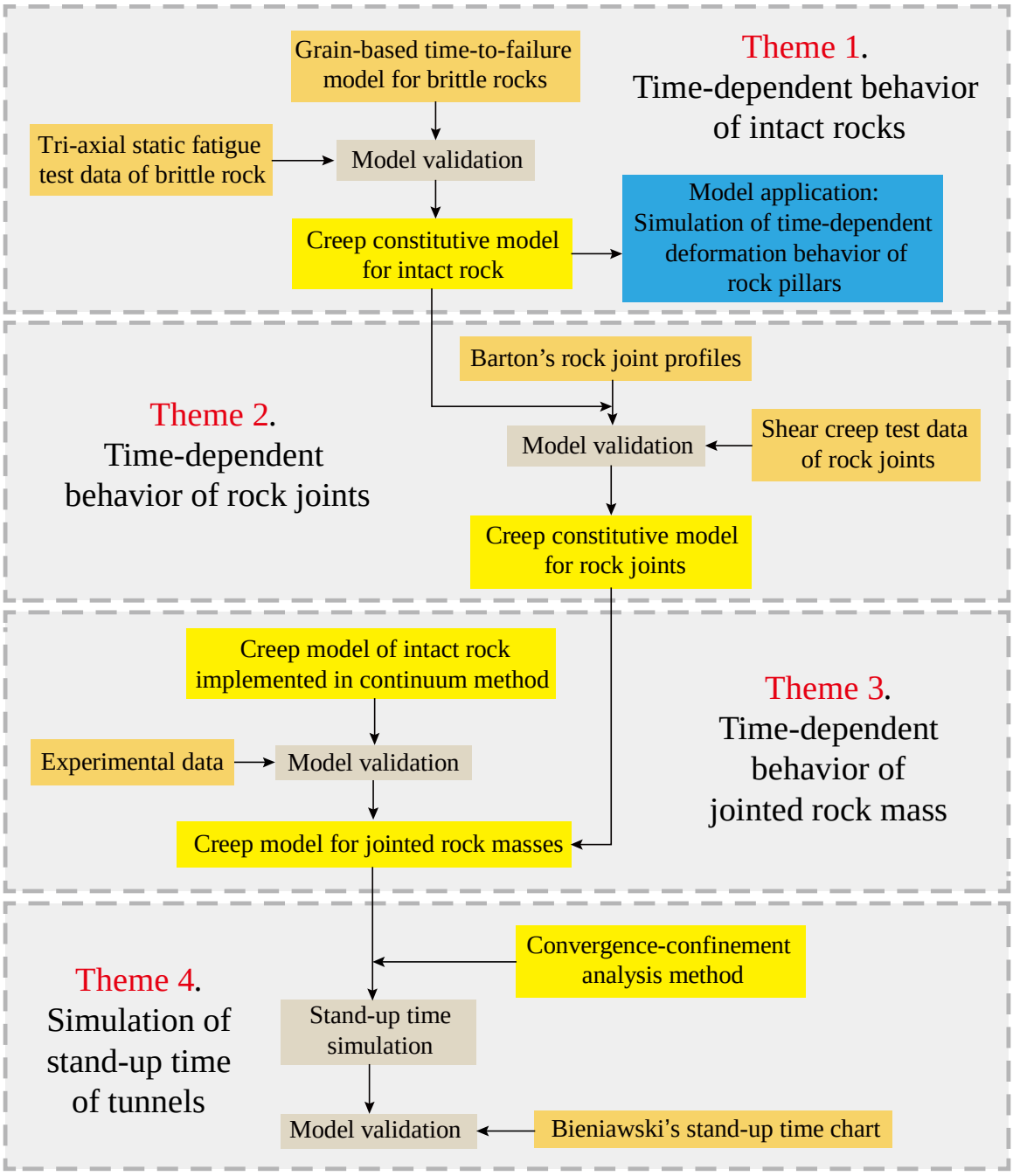

Figure 1-4. Research contents of the thesis.

The research approaches of each topic are presented below.

1.4.1 Theme 1. Simulation of time-to-failure of intact rock

In this study, a new empirical time-dependent rock strength model to simulate time-to-failure of rock will be proposed. Failure will occur in a rock whenever the local stresses exceed the local strength. The local strength of the rock is governed by the stress-time-dependent behavior captured in laboratory tests. This is the underlying governing principle in the model development.

The grain-based modeling approach is adopted. The rock is represented by an assembly of Voronoi cells and the geometry of each cell is different. Zones in a Voronoi cell will fail after a time period when subject to loading, and the time is governed by a proposed empirical relation. After the cell fails, its strength reaches the residual strength and this will cause stress redistribution. The cells in the vicinity of the failed cell will have their stress increased and depending on their strength profile, failure of these cells may be accelerated. As time passes, the coalescence of the failed zones will lead to macroscopic failure of the entire rock and the time-to-failure can thus be predicted.

A new empirical model will be developed, which considers the confinement effect. The model will be implemented into a numerical tool called UDEC (Universal Distinct Element Code), as proposed by Itasca (2015). After the successful model implementation, the proposed model will be validated using laboratory test data. This is to ensure that the model is an accurate representation of the real system. Through the calibration of the model, an iterative process of comparing the model to actual system behavior and using the discrepancies between the two, and the insights gained, the model will be further improved.

This process is repeated until the model is able to predict the time-to-failure of rock samples under different loading conditions.

Time-dependent strength and deformations of rock pillars will be simulated using the proposed creep model of intact brittle rock, with the focus on studying time-dependent spalling (rock splitting damage occurs at the surface of a rock) of pillar walls. Pillar models with different W/H ratios will be built and creep simulations will be conducted to study the influence of loading ratio (the ratio of applied stress to pillar strength) and pillar shape on the long-term stability of rock pillars.

1.4.2 Theme 2. Simulation of time-dependent deformation of rock joints

In the proposed approach, joint roughness will be modeled directly in the model. In an unfilled rough joint, shearing of asperities (unevenness of a joint surface) may explain the time-dependent deformation of joint, as revealed from laboratory test results. The time-dependent element in this deformation process can be the time-dependent failure of the intact rocks at asperities by stress due to stress concentrations induced by the joint geometry. Hence, if the joint asperities are modeled properly, the empirical law that is applicable to rocks in Theme 1 can be used for rocks that contain joints. A joint will slip as the asperities yield progressively and the shear stresses will be redistributed. Zones with weaker strength or higher stress will fail initially. Failed zones will take lower stresses. Hence, stress redistribution occurs in the rock, which may bring additional rock zones and joint segments to failure. Final failure occurs when the rock mass collapses. The effect of joints on the time-dependent deformation of jointed rock masses can thus be modeled without using

time-dependent joint models which are difficult to obtain currently. The time is tracked and the time-dependent deformation behavior of joints can be simulated.

The distinct element method (DEM) will be used to model rock joints. Several laboratory-scale joint models with different roughness will be built using the grain-based model developed in Theme 1. Mechanical parameters of contacts are calibrated using shear experiment data. The properties of the contacts will be adjusted repeatedly according to the theoretical strength of the macro-joints. This step is to ensure that the performance of joint models is reliable compared with the real system.

Creep simulations will be conducted to investigate the time-dependent deformation behavior of rock joints. With joints of different roughness loaded under different normal stresses and shear loading ratios, the time-dependent deformation will be investigated. Thus, major factors that influence the long-term stabilities of rock joints can be determined.

The simulated results will be validated using experimental data of shear creep test of rock joints to ensure that the simulation approach for rock joints is reliable.

1.4.3 Theme 3. Developing a creep constitutive model for a jointed rock mass

It is not practical to use the grain-based creep model to model the response of large-scale structures built in jointed rock masses. To that end, a new modeling method will be developed to simulate the time-dependent deformation behavior of jointed rock masses, where the rock is modeled using the continuum method, and the joints are modeled using

simplified flat joints[1]. In this manner, the computation efficiency can be improved significantly.

To capture the time-dependent deformation of rock, the empirical time-to-failure model, which is developed in Theme 1, will be implemented in a tool based on DEM. The model parameters will be calibrated using experimental data. As to the time-dependent behavior of joints, a creep constitutive model for simplified flat joints will be developed based on the simulation results from Theme 2. The developed model for simplified flat joints can be used to model the long-term shear strength and creep sliding velocity of joints under creep deformation conditions, which can improve the computation efficiently significantly.

Model validation will be conducted using several models, such as jointed rock block models, jointed rock pillar models and jointed rock slope models. The time-dependent deformations due to rock and joints will be analyzed. Performance of the model will be assessed and compared with laboratory and field observations.

1.4.4 Theme 4. Simulation of stand-up time of tunnels excavated in jointed rock masses

Stand-up time of a tunnel excavated in jointed rock masses depends on the interaction of intact rocks with the joint system and the excavation under a given in-situ stress state. Using the approach described in Theme 3, a tunnel model after excavation can be run over time

[1] In this study, the 'flat joint' refers to a joint segment that cuts blocks in UDEC, which is different from the concept of the flat-joint model in PFC.

to initiate failure due to time-dependent failure of rock zones and/or joint segments. Stress will concentrate near the excavation boundary and at locations of joints with interlocking. Failed zones can propagate over time and the stand-up time can be determined when a major roof or wall collapse occurs.

Two-dimensional (2D) modeling will be conducted. In 2D simulation of the tunnel advancing face, the approaches of fictitious internal pressure, Young's modulus reduction, or load-split can be used. When the face advancement stopped, tunnel models will be run over time to check whether failure will be initiated or not due to time-dependent failure of rock zones and/or joint segments. Failed zones can propagate over time and the stand-up time can be determined when major roof or wall collapse occurs. The simulated stand-up time will be compared with data collected by Bieniawski (1993).

1.5 Thesis structure

This thesis presents research into modeling of time-dependent deformation behaviors of jointed rock masses. The thesis consists of eight chapters.

Chapter 1 presents the background, research questions, objectives and scope of the thesis.

Chapter 2 presents a literature review on several research topics that are related to time-dependent deformation behaviors of jointed rock masses. Laboratory creep test results, empirical methods, analytical and numerical approaches of simulating creep deformation behaviors of rock and joints are reviewed. Methods of estimating the long-term strength of rock pillars are discussed and numerical studies on time-dependent deformation behavior of rock pillars are reviewed. Numerical studies of time-dependent deformation behavior of

rock mass using the continuum method are reviewed and challenges of using DEM for studying this issue are discussed. In addition, a literature review on research methods and recent findings on time-dependent deformations of tunnels and stand-up time of tunnels are presented.

Chapter 3 presents the development of a grain-based time-to-failure (GBM-TtoF) creep model for intact rocks. The grain-based modeling approach and strength degradation methods of mineral grains and grain contacts are introduced. Parameter calibration and model verification using experimental data of Lac du Bonnet (LdB) granite are presented.

Chapter 4 presents a numerical study of time-dependent deformation behaviors of rock pillars using the GBM-TtoF creep model for intact rocks developed in Chapter 3. Pillars with different W/H ratios are established. The influence of pillar wall profile on the strength and the deformation characteristics of pillars are investigated. Long-term strength and spalling failure on pillar walls are simulated.

Chapter 5 presents the simulation results of time-dependent deformation of laboratory-scale rock joints, using the GBM-TtoF creep model developed in Chapter 3. Joint models with different roughness are established. The long-term shear strength and the creep sliding velocity of grain-based joint models under different normal and shear loadings are simulated. A creep sliding model for describing the creep deformation of rock joints is proposed, which can be used to model the time-dependent deformation of flat joint structures in distinct element software. The proposed model is verified using experimental data from the literature.

Chapter 6 presents the development of the creep model of jointed rock mass. A time-to-failure creep model for intact rock and the creep-slipping model for joint proposed in Chapter 5 are combined for simulating time-dependent deformations of jointed rock mass using UDEC (Itasca, 2015). Model implementation and parameter calibration are introduced. Model performance is evaluated using a rock mass model with a single joint and a jointed pillar model. A case study of the Oppstadhornet high rock slope in Norway is presented. The creep deformation behavior of the Oppstadhornet slope is simulated and evaluated using field monitored data from 2003 to 2011.

Chapter 7 presents a numerical study of time-dependent deformation behavior of tunnels. The creep model for jointed rock mass, which is developed in Chapter 6, is adopted to build tunnel models in jointed rock masses. The convergence-confinement analysis method is adopted. The internal pressure reduction method is used to mimic the weakening of face-effect due to creep deformation of rock mass. Stand-up times of tunnels with different unsupported roof-spans and rock mass qualities are simulated and compared with Bieniawski's field data.

Chapter 8 presents a thesis summary and main conclusions, original contributions and recommendations for future research.

Chapter 2 Literature review

2.1 Introduction

This Chapter presents a literature review of five research topics that are investigated in this study. The research topics reviewed are listed below.

- Time-dependent deformation behavior of intact rock. Current experimental results, analytical methods and numerical approaches are reviewed.
- Time-dependent deformation behavior of rock pillars. Deformation characteristics of rock pillars, empirical and numerical methods that are used to estimate the field strength of rock pillars are reviewed. Field observations of time-dependent deformation of rock pillars and current analysis methods are discussed.
- Time-dependent deformation behavior of rock joints. Deformation characteristics of rock joints under shear creep loading conditions are reviewed. Methods that are used to analyze shear creep deformations of rock joints are reviewed.
- Time-dependent deformation behavior of jointed rock masses. Rheological models and strength degradation methods that are used in the continuum modeling approach for simulating time-dependent deformation of rock mass are reviewed. Capability of using DEM on simulating time-dependent deformation of rock mass is discussed.
- Time-dependent deformation behavior of tunnels. The convergence-confinement method, which is a well-known two-dimensional method for analyzing the pressure-deformation relation of tunnels, is introduced. Analytical and numerical approaches for studying time-dependent deformation and stand-up time of tunnels are reviewed.

2.2 Time-dependent deformation behavior of intact rocks

2.2.1 Definition and background

Through analyzing the complete stress–strain curve of intact rock, it is found that micro-damage occurs at a very early stage. That is because a rock is made up of many mineral particles with complex microstructures and defects, as shown in Figure 2-1. Rock is not a perfectly elastic material but a mixture of several types of mineral grains with viscous properties, which means rocks exhibit time-dependent deformation behaviors. According to the experimental results of rocks, there are several types of time-dependent phenomenon observed, which are strain-rate dependence, creep, stress relaxation, elastic hysteresis and fatigue. The descriptions of these phenomena are given as follows (Brady and Brown, 1993, Aydan et al., 2013).

Strain-rate dependence: The form of stress–strain curve of the rock is a function of the load-strain rate.

Creep: The strain of the rock increases while the applied load is constant.

Stress relaxation: There is a decrease in stress within the rock when the applied strain is constant.

Elastic hysteresis: There is a delay in the elastic strain of the rock in the loading or unloading process.

Fatigue: There is an increase in strain after cyclical variation in stress.

Rock masses bear loads in rock structures. Rock creep will result in a gradual increase of displacement which can influence the stability of the structures. Hence, among the five time-dependent phenomena of rocks mentioned above, the creep phenomenon received the most attention by scholars. A review of this issue is presented in this section.

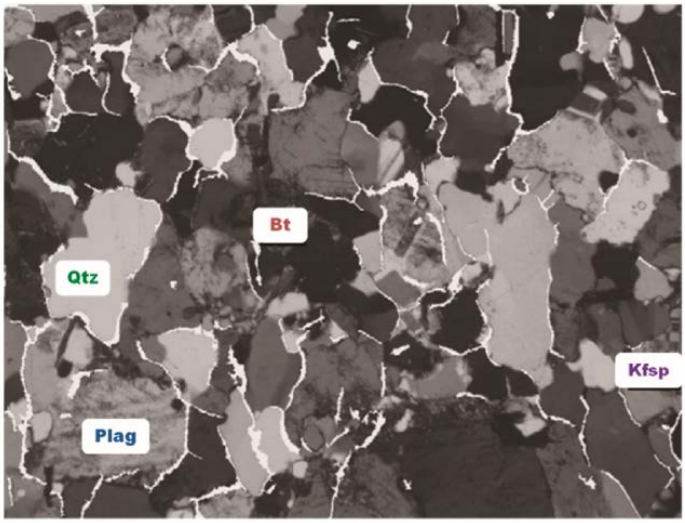

Figure 2-1. Microphotograph of granite. Minerals are denoted by Qtz (Quartz), Plag (plagioclase), Kfsp (potassium feldspar), and Bt (biotite). Image size is 2.78 × 2.10 mm^2 (Lim et al., 2012).

2.2.2 Experimental studies of the creep behavior of rocks

Many scholars conducted creep experiments on different types of rocks, including soft rock (Yang and Jiang, 2010, Haifei et al., 2015, Heap et al., 2009), hard rock (Lajtai, 1991, Schmidtke and Lajtai, 1985, Malan, 1999, Scholz, 1968, Zhao et al., 2018b) and artificial geomaterials, such as concrete (Li and Yao, 2001, Pane and Hansen, 2002) and mineral composites (Lavasani et al., 2015). There are only a few experiments focused on the tensile creep tests (Aydan et al., 2013, Chan et al., 1997). Most experiments are uniaxial (Lajtai, 1991, Schmidtke and Lajtai, 1985, Malan, 1999, Cruden, 1971, Gao et al., 2018, Gao et al., 2015, Zhang et al., 2016c, Zhao et al., 2018a) or tri-axial compression creep tests (Yang

and Jiang, 2010, Nopola and Roberts, 2016, Zhao et al., 2018b, Sharifzadeh et al., 2013, Han et al., 2007, Huang et al., 2010).

According to the experimental results of rock under compression creep test conditions, the rock undergoes three creep stages, which are the primary, secondary and tertiary creep stages. As shown in Figure 2-2, the rock undergoes an immediate strain and a transition-to-stable deformation process in the primary-creep stage. Then, the rock goes through a stable-creep deformation in the secondary stage, where the strain rate is constant. Finally, the deformation is accelerated due to the failure of the rock in the tertiary stage. It should be noted that, when the applied stress is low, whether the rock will inevitably arrive at the tertiary stage is still a debatable issue. Some scholars assume that all rocks will fail, only if the rocks are loaded for an long enough time, regardless of how small the applied load is (Potyondy, 2007). Another common understanding is that there is a creep damage threshold for rock. If the applied stress is higher than the threshold, the rock will undergo the primary and secondary deformation stages, and then yield in the tertiary stage. If the applied stress is lower than the threshold, the rock will just undergo the primary and secondary deformation stages, and stay stable forever. The threshold is approximately equal to the crack damage stress σ_{cd} (Damjanac and Fairhurst, 2010), which is also referred as the long-term strength σ_L of rock. In this study, the crack damage stress as the threshold is adopted.

2.2.3 Rheological models and numerical approaches

To describe the creep deformation of rock under compression, many rheological models, such as the Maxwell model, Kalvin model and Burgers model are proposed. Some of the

rheological models are listed in Table 2-1. It is noted that those models cannot model the transition from the secondary creep stage to the tertiary creep stage properly. Even though the yield phenomenon can be modeled using the plastic component in the Bingham model and the Owen-Hinton model, the strength of the plastic component is stress-dependent, not time-dependent.

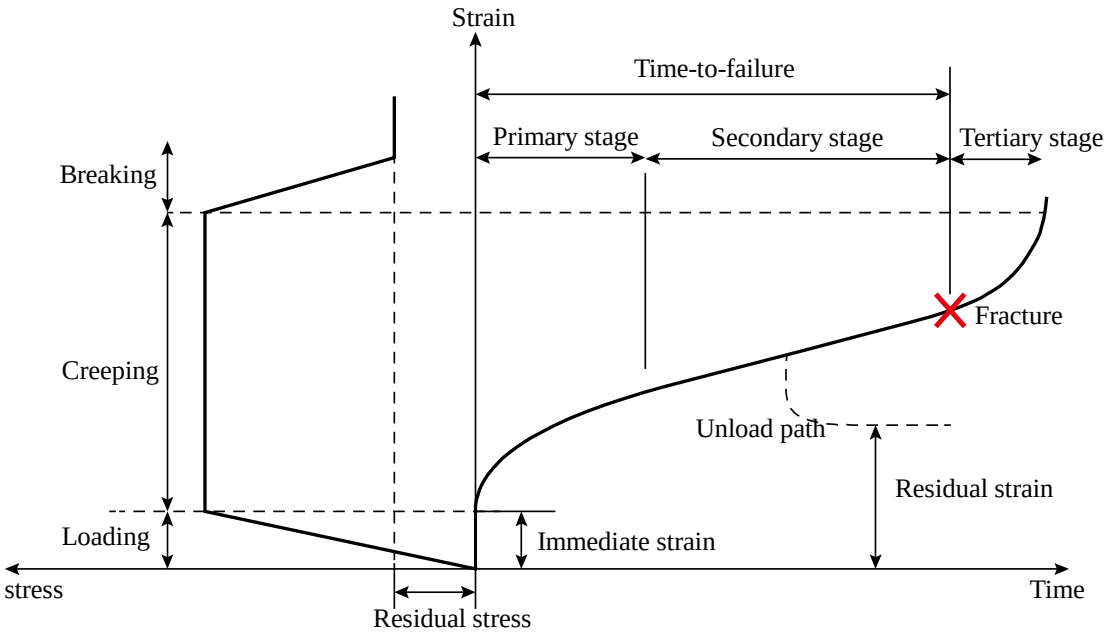

Figure 2-2. Three creep deformation stages of rocks, after Jaeger et al. (2009).

The time when a rock transforms from the secondary to the tertiary creep stages is referred as the time-to-failure of the rock. The relation between the applied stress and the time-to-failure of rock has been investigated experimentally using brittle rocks (Schmidtke and Lajtai, 1985, Aydan and Nawrocki, 1998). For example, Schmidtke and Lajtai (1985) carried out a series of uniaxial compression creep tests on Lac du Bonnet (LdB) granite. All the specimens are loaded higher than σ_{cd} of the rock. According to the experimental

results, the relation between the time-to-failure (T_F) and the loading ratio (σ/UCS) can be written as (Schmidtke and Lajtai, 1985)

$$\ln\left(\frac{\sigma}{UCS}\right) = A\exp\left(B\ln\left(T_F\right)\right) + C, \tag{2.1}$$

where σ is the applied stress, UCS is the uniaxial compressive strength, t is the time-to-failure of rocks, A, B and C are material constants.

To model the time-to-failure phenomenon, some strength degradation models have been proposed and used in numerical simulations (Costin, 1983, Nemat-Nasser and Obata, 1988, Charles, 1958, Kachanov, 1980). Some micro-constitutive models perform well in simulating time-dependent strength of brittle rocks (Xu et al., 2018, Xu et al., 2014, Chen and Konietzky, 2014, Potyondy, 2007). For example, Potyondy (2007) built a bonded-particle model, in which the strength of the contacts was defined by time-dependent parameters. The simulated relation between the time-to-failure (T_F) and the driving-stress ratio, which is defined as $\left(\sigma_1-\sigma_3\right)/\left(\sigma_S-\sigma_3\right)$, where $\sigma_3=\sigma_2$ is the confinement, σ_S is the peak strength, fitted well with the uniaxial compression creep experimental data of Schmidtke and Lajtai (1985), as shown in Figure 2-3.

Despite the progress made, the micro-constitutive models are still in the early-development stage. For example, it has been found that the strength degradation of rock is not totally dependent on the degradation of the contacts of mineral grains. The deformation and breakage of mineral grains also have a large influence on the deformation properties of the rock (Wang and Cai, 2019).

In recent years, many triaxial compression creep experiments have been carried out (Yang and Jiang, 2010, Nopola and Roberts, 2016, Zhao et al., 2018b, Sharifzadeh et al., 2013, Han et al., 2007, Huang et al., 2010). One question to ask is will the degradation method proposed by Potyondy (2007) also perform well in triaxial loading conditions? To improve the understanding in the creep mechanism of intact rock and to find a reliable micro-constitutive creep model for brittle rocks, further research is needed.

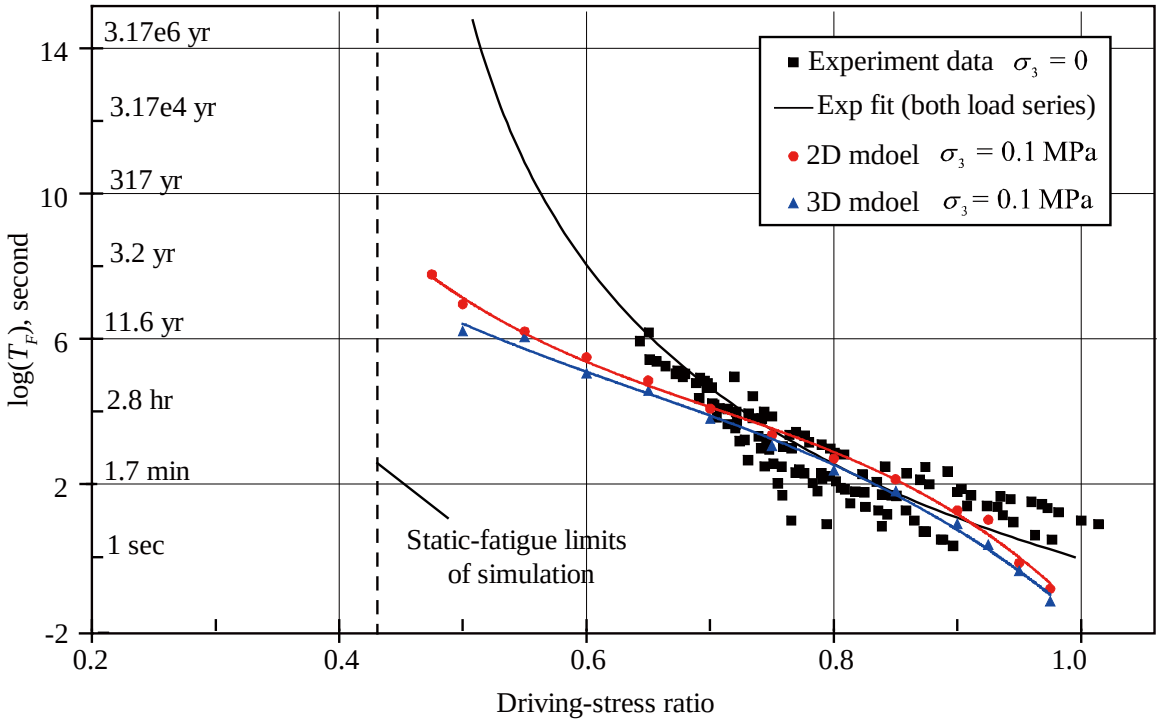

Figure 2-3. Simulated time-to-failure of LdB granite using the bonded-particle model (Potyondy, 2007).

Table 2-1. Rheological models to describe creep behaviors of geomaterials (Glamheden and Hoekmark, 2010, Aydan et al., 2013, Kaiser and Morgenstern, 1981, Misra, 1973)

Model	Geometrical Illustration	Creep Deformation Equation
Basic component		
Hookean component		$\varepsilon = \frac{\sigma}{G}$
Plastic component	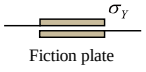	$\begin{cases} \varepsilon = 0, & \sigma < \sigma_Y \\ \varepsilon \to \infty, & \sigma \geq \sigma_Y \end{cases}$
Newton component	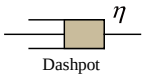	$\varepsilon = \frac{\sigma}{\eta} t$
Rheological model		
St. Venant model	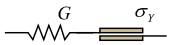	$\begin{cases} \varepsilon = \frac{\sigma}{G}, & \sigma < \sigma_Y \\ \varepsilon \to \infty, & \sigma \geq \sigma_Y \end{cases}$
Kelvin model	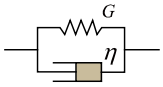	$\varepsilon = \frac{\sigma}{G}\left(1 - e^{-\frac{G}{\eta}t}\right)$
Generalized Kelvin model	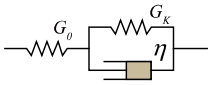	$\varepsilon = \frac{\sigma}{G_0} + \frac{\sigma}{G_K}\left(1 - e^{-\frac{G_K}{\eta}t}\right)$
Maxwell model	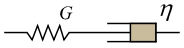	$\varepsilon = \frac{\sigma}{\eta} t + \frac{\sigma}{G}$
Burgers model	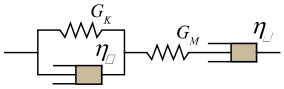	$\varepsilon = \frac{\sigma}{G_M} + \frac{\sigma}{\eta_M} t + \frac{\sigma}{G_K}\left(1 - e^{-\frac{G_K}{\eta_K}t}\right)$
Poyting-Thomson model	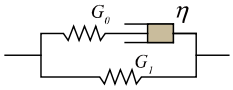	$\varepsilon = \frac{\sigma}{G_1}\left(1 - \frac{G_0}{G_0 + G_1} e^{\frac{-G_0 G_1}{(G_0 + G_1)\eta}t}\right)$
Bingham model	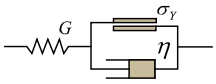	$\begin{cases} \varepsilon = \frac{\sigma}{G}, & \sigma < \sigma_Y \\ \varepsilon = \frac{\sigma - \sigma_Y}{\eta} t + \frac{\sigma}{G}, & \sigma \geq \sigma_Y \end{cases}$
Nishihara model	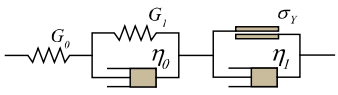	$\begin{cases} \varepsilon = \frac{\sigma}{G_0} + \frac{\sigma}{G_1}\left(1 - e^{-\frac{G_1}{\eta_0}t}\right), & \sigma < \sigma_Y \\ \varepsilon = \frac{\sigma}{G_0} + \frac{\sigma}{G_1}\left(1 - e^{-\frac{G_1}{\eta_0}t}\right) + \frac{\sigma - \sigma_Y}{\eta_1} t, & \sigma \geq \sigma_Y \end{cases}$
Owen-Hinton model	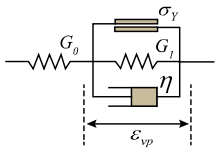	$\begin{cases} \varepsilon = \frac{\sigma}{G_0}, & \sigma < \sigma_Y + G_1 \varepsilon_{vp} \\ \varepsilon = \frac{\sigma}{G_0} + \frac{\sigma - \sigma_Y}{G_1}\left(1 - e^{-\frac{G_1}{\eta}t}\right), & \sigma \geq \sigma_Y + G_1 \varepsilon_{vp} \end{cases}$

2.3 Time-dependent deformation behavior of rock pillars

2.3.1 In-situ strength of rock pillars

Rock pillars are commonly used in underground mines to maintain stability of excavations. The estimation of the strength of rock pillars is important for mining engineering, but it is a challenging task because many factors such as geometry of pillars, in-situ stress, variation of rock types and rock mass quality influence pillar strength. A summary of empirical in-situ rock pillar strengths is shown in Figure 2-4. It is seen that for pillars with a width to height ratio (W/H) in the range of 1 to 2, their strengths are about 30% to 60% of the uniaxial compressive strength (UCS) of the intact rock tested in laboratory.

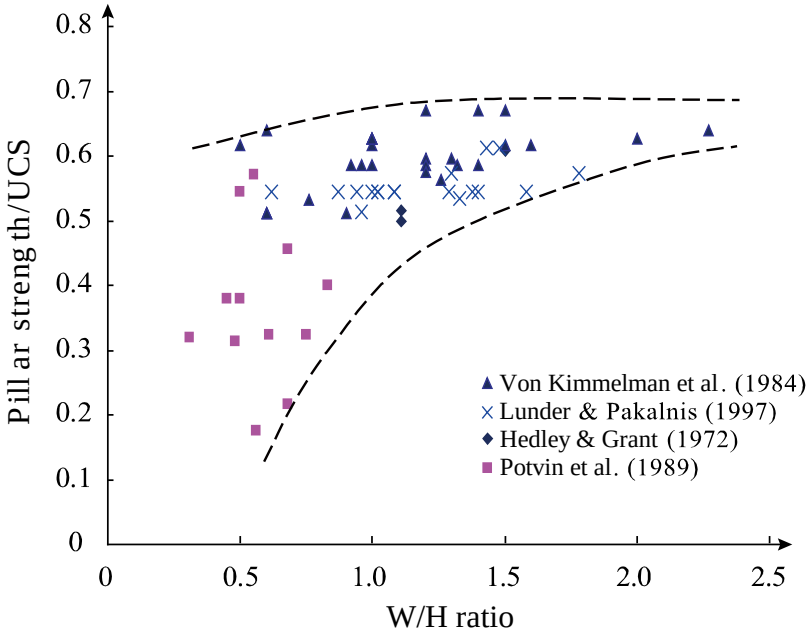

Figure 2-4. Database of in-situ rock pillar strength (Von Kimmelmann et al., 1984, Lunder and Pakalnis, 1997, Hedley and Grant, 1972, Potvin, 2017), after Esterhuizen (2006).

When a rock pillar is loaded with increasing vertical stress, it will go through five deformation stages as shown in Figure 2-5 (Roberts et al., 1998). With gradual spalling on

the walls, an hour-glass-shaped pillar will result, followed by final failure of the structure. For rock pillars without discontinuities, spalling failure on the walls is the typical failure mode observed in the field.

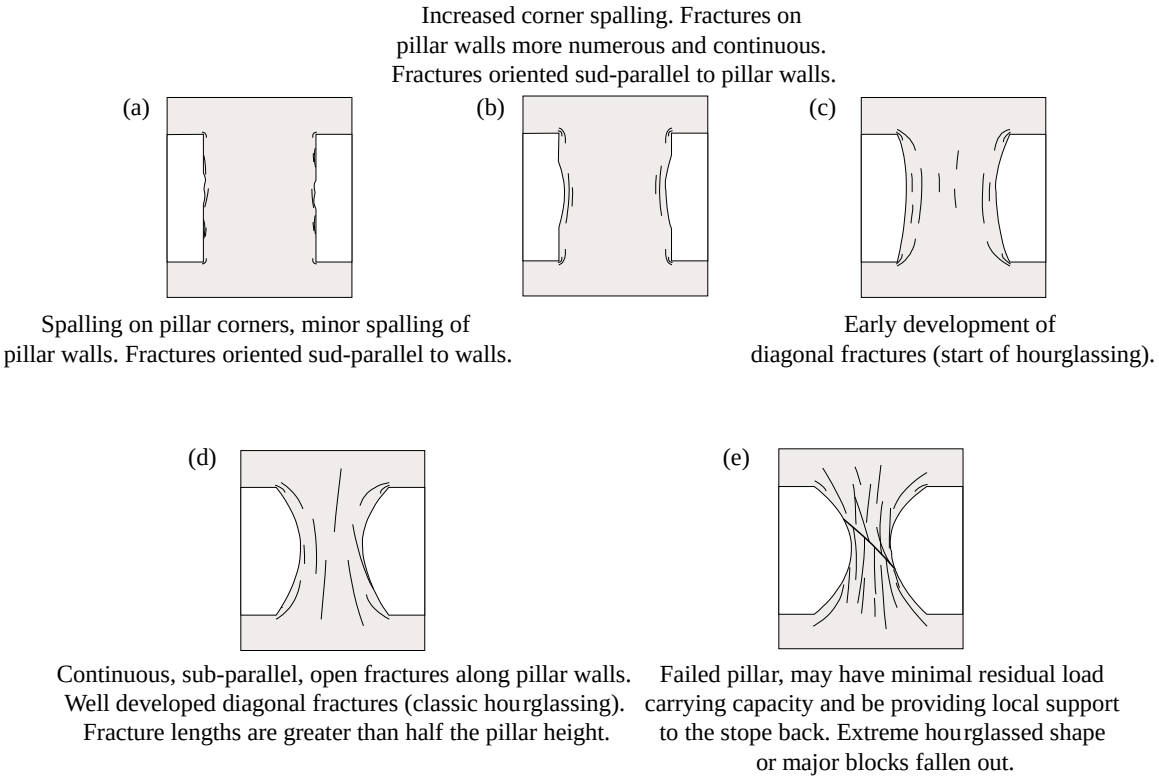

Figure 2-5. Pillar condition rating system, after Roberts et al. (1998).

Some scholars have provided empirical formulas of pillar strength based on different assessment methods (Von Kimmelmann et al., 1984, Sjoberg, 1992, Lunder and Pakalnis, 1997, Krauland and Soder, 1987, Hedley and Grant, 1972, Potvin, 2017, Martin and Maybee, 2000, Esterhuizen, 2006, Kaiser et al., 2011). The results are summarized in Figure 2-6, which are expressed as the relation between the normalized strength and the W/H ratio. Unfortunately, due to the complex nature of the problem, it is hard to judge which pillar strength equation is the most appropriate one.

2.3.2Numerical studies of pillar strength curve

Some scholars tried to find a reliable simulation method to predict the in-situ strength of a rock pillar (Martin and Maybee, 2000, Esterhuizen, 2006, Kaiser et al., 2011, Sinha and Walton, 2018). The continuum methods such as the finite element method (FEM) and the finite difference method (FDM) are commonly used. Factors such as in-situ stress, realistic pillar geometry and rock mass quality can be considered, but the accuracy of a simulation result is largely governed by the input parameters of the rock mass and the applied failure criterion (Renani and Martin, 2018). For example, three simulated pillar strength curves using the modified yield criteria (Figure 2-7) are shown in Figure 2-6. Martin and Maybee (2000) found the in-situ strength of pillars are lower than the simulation results using existing strength criteria such as the generalized Hoek–Brown failure criterion (Hoek et al., 2002) in FEM. They found that using the brittle Hoek–Brown parameters ($m = 0$, $s = 0.11$) resulted in a better strength curve compared with the existing empirical equations, especially for pillars with W/H ratios between 0.5 and 2.0. Meanwhile, it was proven that rock strength and failure pattern are influenced by confinement (Cai, 2010, Kaiser et al., 2011), which means that rocks in the pillar core may obey a different failure criterion compared with rocks near the surface of a pillar. As a result, some modified confinement-dependent strength criteria were proposed. For example, considering the effect of confinement enhancement to the strength of rock in the pillar core, the S-shape strength criterion (Kaiser et al., 2011) was proposed, which is presented as the blue curve in Figure 2-7 with the corresponding simulated pillar strength curve shown in Figure 2-6. Esterhuizen (2006) used a failure criterion with spalling cut-off to consider brittle spalling

failure of rock near pillar walls (green curve in Figure 2-7) and a flat pillar strength curve was obtained (green curve in Figure 2-6), which agreed well with the results by Lunder and Pakalnis (1997). It is seen from the above discussion that using different yield criteria in continuum models leads to different pillar-strength curves. Due to limited field data of failed squat pillars, the in-situ pillar strength of wide pillars with W/H ratios larger than 2.0 is uncertain.

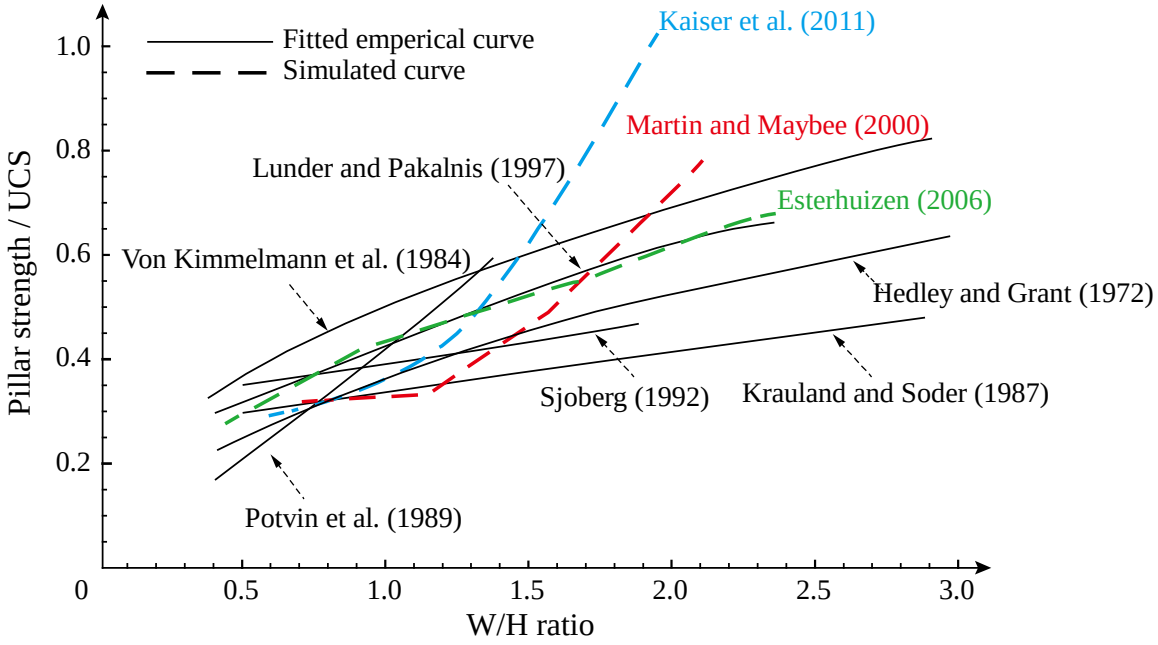

Figure 2-6. Empirical and simulated pillar strength curves (Von Kimmelmann et al., 1984, Sjoberg, 1992, Lunder and Pakalnis, 1997, Krauland and Soder, 1987, Hedley and Grant, 1972, Potvin, 2017, Martin and Maybee, 2000, Esterhuizen, 2006, Kaiser et al., 2011).

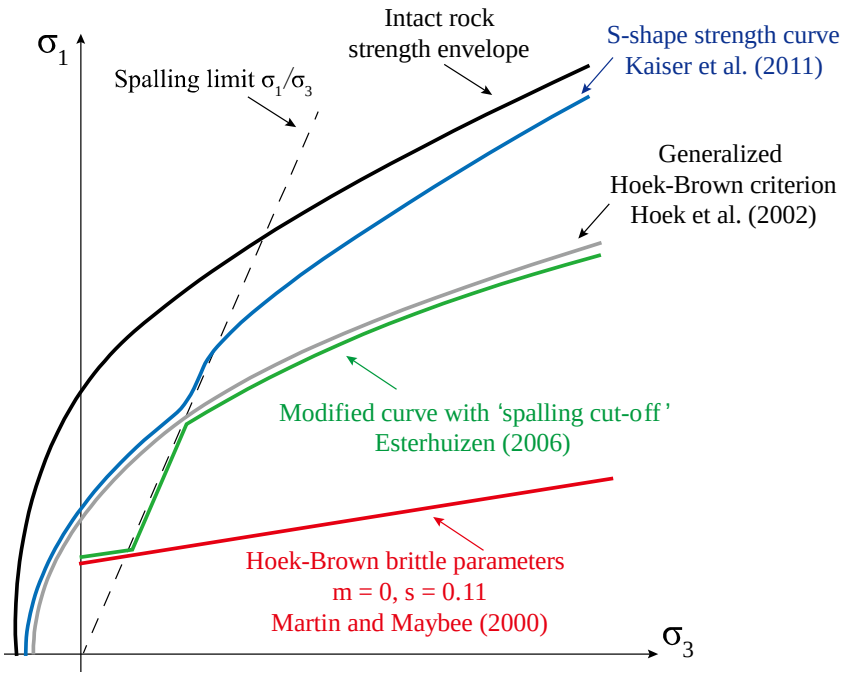

Figure 2-7. Different strength criteria used in pillar strength simulation (Martin and Maybee, 2000, Esterhuizen, 2006, Kaiser et al., 2011, Hoek et al., 2002).

2.3.3 Time-dependent spalling of rock pillars

For most pillars in the field, their failures are in fact time-dependent. Field observations indicate that most temporary pillars have a short service life-time. Even when they are loaded under their short-term strengths, they will eventually fail as spalling failure grows gradually over time (Salmi et al., 2017, Wang et al., 2012, Smith and Rosenbaum, 1993, McClain, 1966). It is also observed that time-dependent spalling can occur for pillars that are stable for many years (Esterhuizen et al., 2011b, Esterhuizen et al., 2011a), and one example is shown in Figure 2-8, showing some stable pillars in a limestone mine at a depth of 275 m below surface. The pillar walls were straight right after the excavation. As time passed, the pillar walls spalled and reached the shape shown in the figure. Time-dependent deformation of the rock mass plays an important role in controlling the stability of geotechnical structures with a long service life-time, such as permanent pillars in

underground mines (Wang et al., 2012, Lunder and Pakalnis, 1997, Salmi et al., 2017, Sjoberg, 1992, Esterhuizen et al., 2011b) and pillars between twin-tunnels (Li et al., 2013, Chen et al., 2009, Ng et al., 2004). The strength and deformation of these structures are time-dependent.

Figure 2-8. Concave pillar geometry formed as a result of time-dependent spalling damage (Esterhuizen et al., 2011b).

A few time-dependent constitutive models (Liu and Cai, 2020, Potyondy, 2007, Li and Konietzky, 2015, Li et al., 2019) have been proposed recently, which consider the viscosity of rock and can be used to improve the understanding of long-term strength and time-dependent spalling of rock pillars. However, none of the numerical models mentioned above consider time-dependent failure of pillars, because none of the models consider the time-to failure phenomenon of rock. Hence, a time-dependent failure model should be used to study strength degradation and time-dependent failure mechanism of rock pillars.

2.4 Time-dependent deformation behavior of rock joints

Many important issues in rock mechanics and rock engineering are related to the presence of fractures in rocks (Kemeny, 2003). This is especially true for brittle rocks because joints usually have a weaker strength and can experience larger displacements (Boon, 2013, Wasantha et al., 2015, Barton, 1995, Bhasin and Høeg, 1998). Many field observations show that the mechanical behavior of rock joints in brittle rock mass should be considered time-dependent. This is important for geotechnical structures that are built in jointed rock masses, their stability is often governed by the time-dependent deformation of joints (Liu et al., 2004, Glamheden and Hoekmark, 2010). Thus, time-dependent strength and deformation of rock joints is an important issue that needs to be addressed in rock engineering design.

2.4.1 Experimental studies of the time-dependent behavior of joints

Lajtai (1989, 1991) found that the peak shear strength of a smooth joint of LdB granite, which is referred to the short-term shear strength τ_S, is time-dependent. Under constant normal and shear loadings, the friction angle increased about 4 degrees after a delayed time of 2 to 3 days. The stress–displacement relation returned to the pre-delayed position after the additional frictional resistance was overcome. This time-strengthening phenomenon may result from the gradual increase of the contact area of the joint surface due to the creep deformation of micro-asperities (Malan, 1998). However, as Lajtai and Gadi (1989) mentioned, such a time-strengthening phenomenon is hard to predict because it is loading-rate dependent. Thus, this additional frictional strength increase is not considered in this study. In addition, according to field observations and experimental results, rock joints can

also present a stress relaxation behavior (Fahimifar and Soroush, 2005, Yang et al., 2017, Wang et al., 2019) and creep behavior (Yang et al., 2013, Zhang et al., 2012). The creep deformation of rock joints can result in large displacement over time, which can have a large influence on the structural stability of rock mass. Hence, the creep behavior of rock joints is focused in this study.

The long-term shear strength of rock joints, which is noted as τ_L, has been studied by many scholars in the laboratory using different types of naturally occurring rock joints (Zhang et al., 2012, 2015, Yang et al., 2007, He et al., 2019, Shen and Zhang, 2010, Malan, 1998) and artificial joints made using concrete (Zhang et al., 2016b, Wang et al., 2017b, Zhang et al., 2019). The existence of the long-term shear strength has been demonstrated through these studies. According to the experimental data of Bowden and Curran (1984), when the shear stress of a joint is lower than a threshold, the creep deformation will stop after sometime (Figure 2-9(a)). If the shear stress is higher than the threshold, the creep deformation will continue, as shown in Figure 2-9(b). Such a threshold is defined as the long-term shear strength τ_L of the joint. In this case, τ_L is around $0.7\,\tau_S$. Wang et al. (2017a) used Goodman's creep model of intact rock (Goodman, 1989) shown in Figure 2-9(c) to describe the concept of long-term shear strength of rock joints. When the applied shear stress is below the long-term shear strength, the time-dependent deformation will stop after reaching the creep terminal locus. On the other hand, when the shear stress is higher than the long-term shear strength, the creep deformation will keep growing till failure.

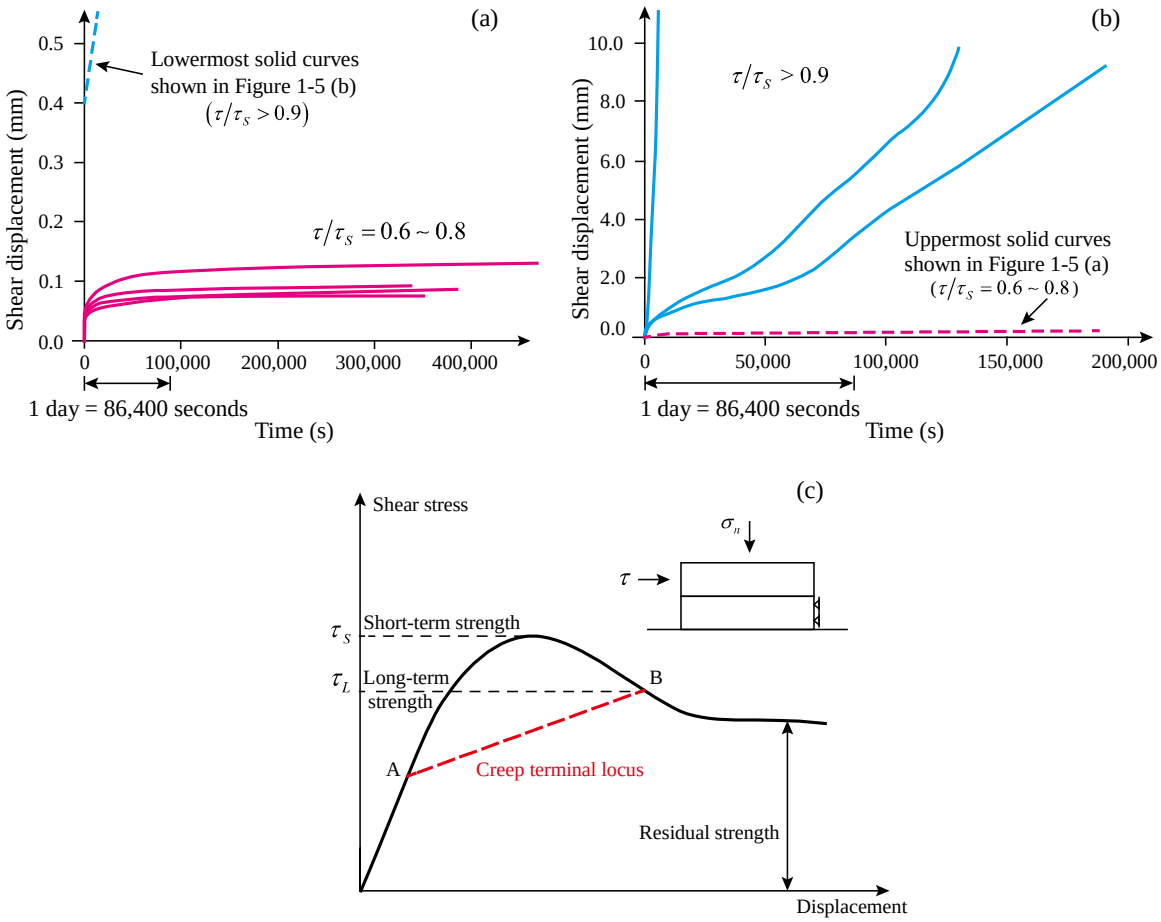

Figure 2-9. The concept of long-term shear strength of rock joints: (a)-(b) Creep deformation of rock joints under different loading ratios (Bowden and Curran, 1984); (c) time-dependent strength of rock joint, after Glamheden and Hoekmark (2010) and Wang et al. (2017a).

As Lajtai and Gadi (1989) stated, it is hard to obtain representative samples for a creep test when using natural joints because the mechanical properties of joints tend to be more variable than intact rock. In addition, conducting a shear-creep test of a joint is time consuming. As a result, compared with the investigations of intact rocks, there is less study focused on the creep behavior of rock joints.

2.4.2 Mathematical model and numerical studies

The Burgers model, which can describe the initial and secondary creep deformation stages shown in Figure 2-2, is widely used to fit creep-strain curves of rock and joint obtained from creep experiments (Yang et al., 2013, Zhang et al., 2012, 2016b, Xu and Yang, 2005, Yang et al., 2007). Normal stress, roughness and shear stress can influence the four model parameters of the Burgers model; however, it is unclear how the model parameters are influenced by normal stress, roughness and shear stress for joints, which is one of the subjects of this research.

There are a few studies that focus on numerical simulation of time-dependent deformation behaviors of rock joint (Xu et al., 2013, Chen et al., 2004, Xue and Mishra, 2019). When modeling time-dependent deformation behavior of jointed rock mass using DEM software such as UDEC (Itasca, 2015), time-dependent displacements of joints should be considered. However, there is no creep constitutive model for rock joints in UDEC, which limits its applications. On the other hand, it has been found that micro-scale models can simulate time-dependent deformation behaviors of intact rock well using the strength degradation method (Potyondy, 2007, Zhang and Wong, 2013, Liu and Cai, 2020). Damage initiation and crack propagation under the creep loading condition can be captured at the grain scale. When a rock joint model is built using a micro-scale model, the mechanical behavior of the rock of the joint walls can be considered time-dependent. As a result, time-dependent deformation behaviors of rock joint can be simulated by simulating time-dependent deformations of intact rock. In this way, the damage of joint wall asperities under creep

loading conditions can be investigated at the grain scale level. It provides a novel approach to investigate the time-dependent deformation behavior of rock joints.

2.5 Time-dependent deformation behavior of rock mass

2.5.1 Background

The mechanical response of rock mass is complex. Due to the presence of discontinuities, the deformation behavior of a rock mass is non-linear and plastic (Brady and Brown, 1993, Bieniawski, 1993, Barton et al., 1985). The failure mode of a rock mass is influenced by stress and joint density, which is shown in Figure 2-10. For massive rock mass and highly jointed rock mass, it is reasonable to simplify the rock mass as a continuum and isotropic material. That is currently what most scholars do when investigating time-dependent deformation behaviors of a rock mass using continuum simulation methods (Jing and Hudson, 2002).

2.5.2 Rheological models and material softening approaches

Rheological models, such as the Burgers model, are commonly used to describe the creep deformation of rock mass using continuum analysis methods (Korzeniowski, 1991, Hu et al., 2018, Kabwe et al., 2020b, Nomikos et al., 2011). For example, tunnel wall deformation after excavation is time-dependent. Sharifzadeh et al. (2013) and Song et al. (2020) analyzed the long-term stability of tunnels considering time-dependent deformations of rock mass using the Burgers model. Sulem et al. (1987) and Kabwe et al. (2020b) simulated the variation of stress and displacement around tunnels after excavation, considering time-

dependent deformation of rock mass. Based on the simulation results, the time to install rock support is determined.

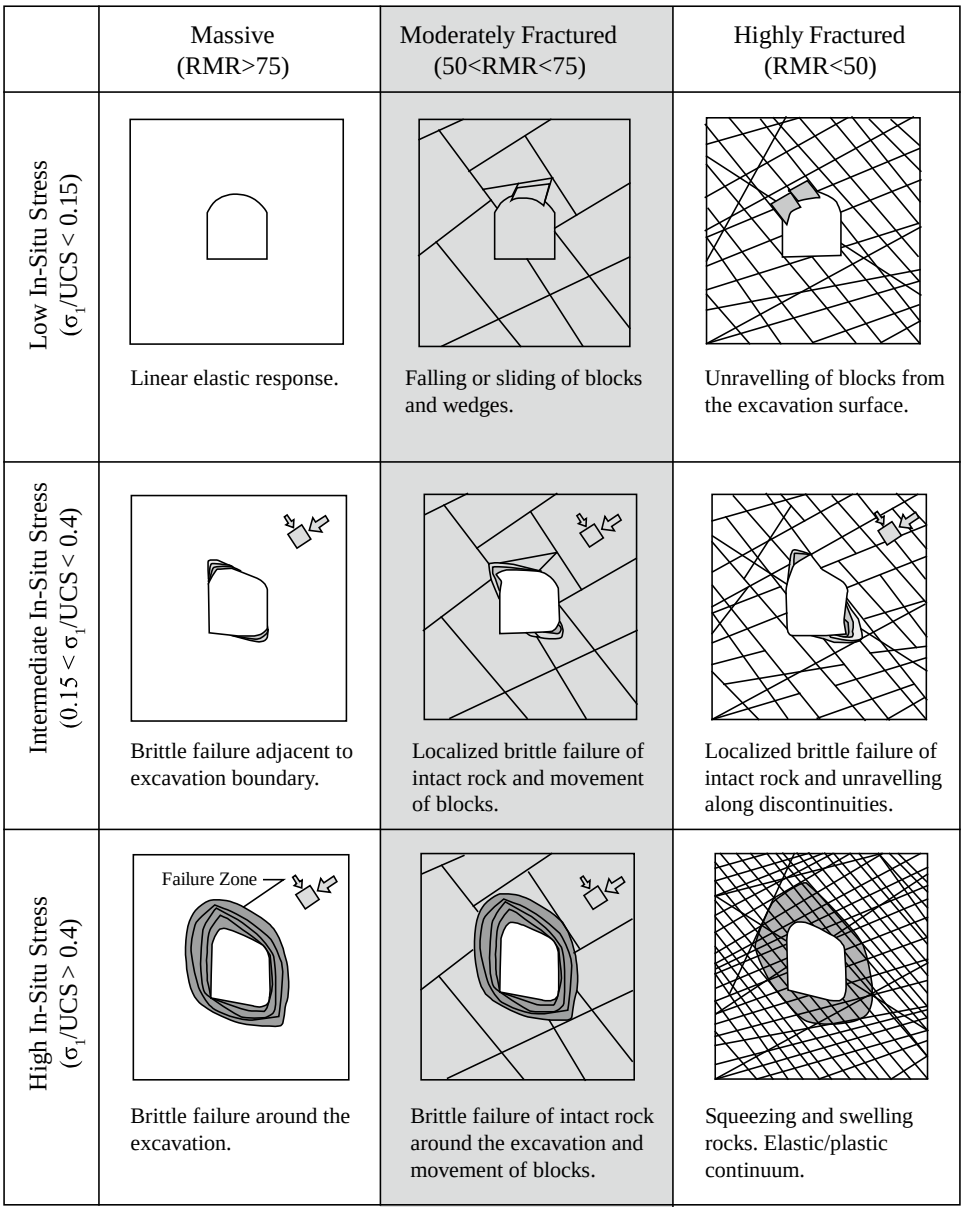

Figure 2-10. Influence of rock mass quality and stress on failure mode of tunnels (Martin et al., 1999).

Material softening approaches are used to model the time-dependent deformation of rock mass. When considering the time-dependent strength of rock mass, some empirical strength

degradation equations are adopted to control the model parameters, such as Young's modulus, Poisson's ratio and cohesion. For example, time-dependent failures of rock pillars (Sainoki and Mitri, 2017), backfilled stope (Qi and Fourie, 2019), rock slopes (Riva et al., 2018) are simulated using empirical strength degradation equations. Moreover, some new constitutive models (Li and Konietzky, 2015, Xu et al., 2013), which are based on the crack evolution theory (Charles, 1958) and damage theory (Kachanov, 1980), are proposed to consider the accumulated damage due to stress erosion under creep loading conditions. These models have been used to simulate crack propagations in rock pillars, tunnels (Li and Konietzky, 2015) and rock slopes (Xu et al., 2013). However, those analysis methods are based on the isotropic material assumption in the continuum-modeling framework. In many rock engineering practices, the mechanical response of tunnels in moderately jointed rock masses, as highlighted in Figure 2-10, needs to be analyzed. For example, large creep displacements resulted from the time-dependent deformation of discontinuities can hardly be handled using continuum numerical modeling methods.

2.5.3 Numerical studies using discontinuum methods

Discontinuum analysis methods, such as the Key block theory (Shi and Goodman, 1989) and the DEM, are usually used to analyze structurally-controlled failure of moderately fractured rock mass as highlighted in Figure 2-10. The Key block theory can analyze structural instability of jointed rock masses influenced by gravity. However, more factors, such as in-situ stress and time-dependent rock deformation cannot be considered. In DEM, the deformations of both rock and joints contribute to the mechanical response of a rock mass model. An example is demonstrated in Figure 2-11. The mechanical responses of

intact rock and joints that are built using block zones and contact elements respectively, and are governed by different constitutive models. Currently, there are some creep constitutive models, such as the Burgers model, power-law model and WIPP model (Itasca, 2015), which can be used to describe the creep deformation of blocks. However, there is no creep constitutive model available to describe the time-dependent response of contact elements. As mentioned above, the pre-existing discontinuities in a rock mass can present continuous and large creep displacement over time. It can influence the long-term stability of the rock mass. If the time-dependent deformation of joints can be considered, a more effective analysis method for time-dependent response of jointed rock mass can be developed.

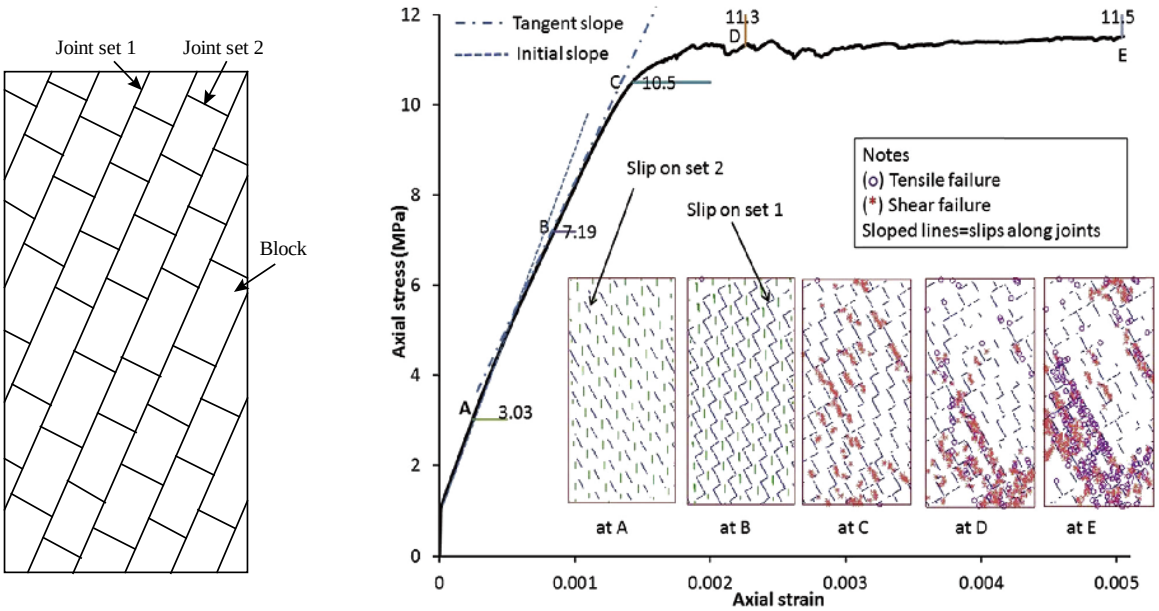

(a) (b)

Figure 2-11. Deformations of rock and joints in a jointed rock mass model (Alshkane et al., 2017): (a) a well-interlocked jointed rock mass; (b) slips of joints and deformations of blocks captured in the rock mass model.

2.6 Time-dependent deformation behavior of tunnels

2.6.1 Convergence-confinement method

Analysis of tunneling-induced stresses and deformations is a complex problem because it must consider many factors such as tunnel shape, excavation method, field stress, rock mass strength, three-dimensional effects and others (Shen and Barton, 1997, Read et al., 1998, Martin et al., 1999, Bieniawski, 1990, Unlu and Gercek, 2003, Cai et al., 2004b, Cai et al., 2007, Carranza-Torres, 2009, Alejano et al., 2010, Fahimifar et al., 2010, Cai, 2011). For simplicity, the two-dimensional method is often used in tunnel excavation response analyses. The convergence-confinement method, which is a quantitative approach proposed by Panet and Guellec (1974), is widely used to analyze deformations of tunnel walls and provide guidelines for rock-support design (Aftes, 1976, Brown et al., 1983, Carranza-Torres and Fairhurst, 2000, Panet and Sulem, 2022).

For a circular tunnel excavated in an isotropic material with hydrostatic stress fields, as shown in Figure 2-12, the stress status in a cross-section sufficiently away from the tunnel face (e.g., section B-B) satisfies the plane-strain condition. When rock supports are installed behind the tunnel face, they do not carry the full support load from the rock mass, and the pressure they bear is lower than the initial pressure P_0. This is due to the support effect from the tunnel face, which bears some of the loads of the rock mass. A hypothetical internal pressure P_i is used to represent the support from the face-effect. As the tunnel face advances, the face-effect P_i on the cross-section under consideration decreases, and the radial displacement on the walls increases. The three-dimensional face advancing process can thus be modeled by adjusting P_i on the interior boundary of a two-dimensional model

based on the convergence-confinement method, which is used in this study for simulating stand-up time of un-supported tunnels.

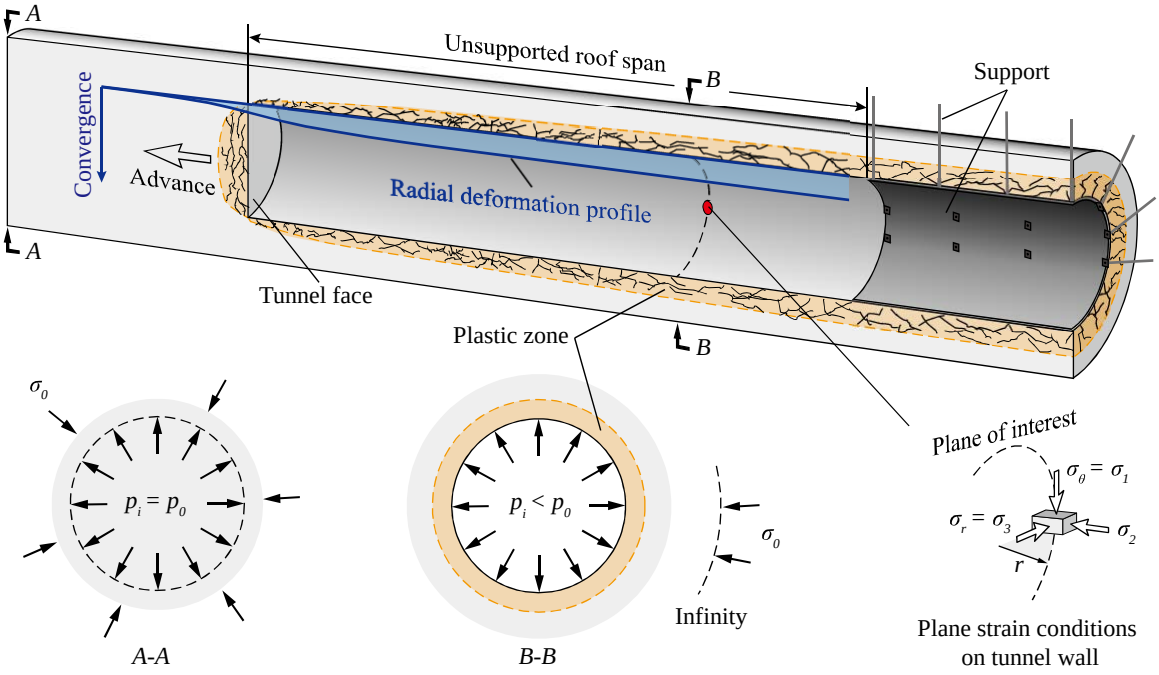

Figure 2-12. Profiles of stress and radial displacement variations along the tunnel axis of a circular tunnel (after Carranza-Torres and Fairhurst (2000)).

2.6.2 Time-dependent deformation of tunnels

The mechanical responses of either civil tunnels with a long service life or underground mine drifts with a short service life are time-dependent, i.e., the stability of an unsupported tunnel is a function of time (Lauffer, 1958, Bieniawski, 1989, Barton, 1978). The time-dependent deformation of tunnels is dependent not only on tunnel-face advancement, but also on rheological deformation of the rock mass. An example is presented in Figure 2-13. Time-dependent deformation in the Lyon-Turin Base Tunnel was investigated numerically by Barla et al. (2012). If the deformation of the rock mass is modeled as time-dependent (a three stages creep model used for this case), the simulated deformation on the wall is closer

to field measured data. Using the elastic-perfectly plastic constitutive model alone, the deformations on tunnel walls during tunnel face advancement cannot be properly simulated.

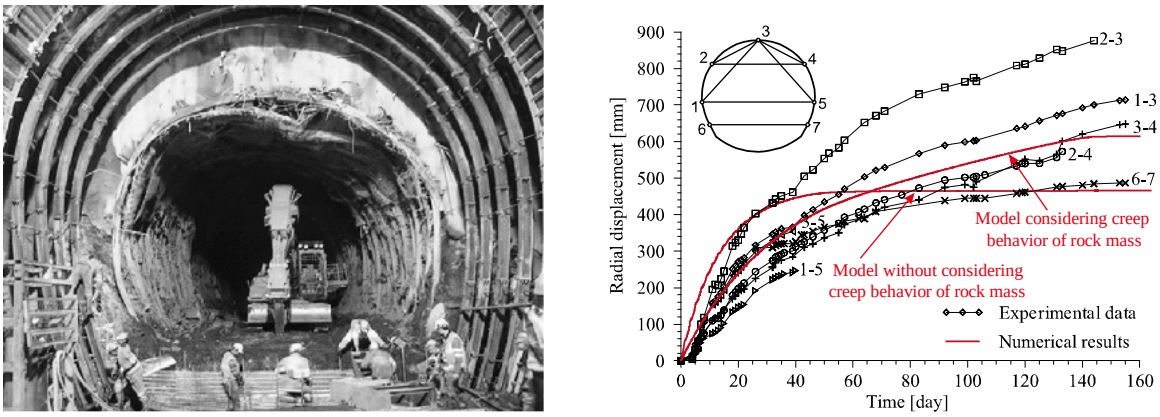

(a) (b)

Figure 2-13. Time-dependent deformations observed at the Lyon-Turin Base Tunnel (Barla et al., 2012): (a) a reduced cross-section captured in the Saint Martin La Porte access adit; (b) simulated tunnel wall convergences considering the creep behavior of the rock mass.

By considering the rheological properties of rock mass, some analytical solutions of radial wall deformations of circular tunnels have been proposed (Sulem et al., 1987, Kabwe et al., 2020b, Pan and Dong, 1991). Time-dependent deformations of rock mass along a tunnel have been simulated using two-dimensional (Sharifzadeh et al., 2013, Malan, 1998, Xu et al., 2019, Barla et al., 2012, Zhang et al., 2016a) and three-dimensional (Manh et al., 2015, Kabwe et al., 2020a, Sainoki et al., 2017, Guan et al., 2008) numerical models. These studies use continuum materials, which are suitable for intact rock and highly jointed rock masses. However, for tunnels excavated in moderately jointed rock masses where the rock masses are anisotropic and discontinuous, large displacements of rock joints cannot be analyzed. As a result, time-dependent deformations of jointed rock masses cannot be evaluated.

2.6.3 Stand-up time of tunnels

The time-to-collapse of tunnels is an important issue. Lauffer (1958) related tunnel stability to time and tunnel span. Using field data collected, Bieniawski (1989) developed a chart of stand-up time of tunnels based on the RMR system, see Figure 1-2. Empirical equations were developed based on field data (Ramamurthy, 2007, Estébanez and Lage, 2018). By considering the creep deformation of rock mass, an analytical solution of stand-up time of circular tunnels has been obtained (Nguyen and Nguyen, 2015). Despite the efforts by many researchers, current understanding of the stand-up time of tunnels excavated in jointed rock mass is still limited due to a lack of an effective analysis method for this situation.

2.7 Summary

A brief summary of the conclusions from the literature review of the research topics is presented below.

It is still necessary to improve the understanding of creep deformation behaviors of intact rock because existing creep models inadequately capture the time-to-failure phenomenon of rock under triaxial loading conditions. The grain-based modeling approach provides a useful tool to investigate the creep mechanism of brittle rocks.

Empirical approaches inadequately evaluate the strength of square pillars with W/H ratio greater than 2.0. According to field observations, deformations of rock pillars are time-dependent. However, the time-dependent failure mechanism of rock pillars is unclear due to a lack of understanding of the spalling failure on pillar walls. By using an effective creep

model of rock that can properly describe the time-to-failure phenomenon of rocks, it is possible to simulate the time-dependent spalling of pillars, and then the time-dependent failure mechanism of pillars could be analyzed.

Current understanding on the time-dependent deformation behavior of rock joints is insufficient due to limited availability of shear creep test data of joints. There is hardly any numerical study focusing on this issue. In DEM, there is no constitutive model that can be used to model the time-dependent deformation of flat joints.

Current analytical methods and numerical studies on the time-dependent deformation behavior of jointed rock mass are based on the homogeneous material assumption, which is suitable for intact rock and highly jointed rock masses. When analyzing moderately jointed rock masses using a DEM tool, the time-dependent response of a rock mass cannot be properly modeled because the time-dependent deformation of rock joints cannot be considered.

Time-dependent deformation of rock mass can result in a radial displacement on tunnel walls, which should be properly considered in the rock-support designs. However, time-dependent behavior of tunnels excavated in moderately jointed rock mass can hardly be modeled because a lack of approaches to consider the deformations of joints. In addition, the understanding of the stand-up time of tunnels needs to be enhanced.

As a consequence of this literature review, the research topics presented in Chapter 1 were identified and the research results are presented in the following chapters.

Chapter 3 A time-to-failure creep model for brittle rocks

This chapter presents a new grain-based time-to-failure (GBM-TtoF) creep model that can be used to simulate time-dependent deformation and fracturing of brittle rock using the grain-based model (GBM). Firstly, a time-dependent deformation model is introduced to present the creep deformations in the first two creep stages. Secondly, strength degradation models of grains and contacts are developed to model the third-creep deformation stage. Parameters of the TtoF creep model are calibrated using test data of Lac du Bonnet (LdB) granite. Finally, uniaxial and triaxial compression experiment simulations are conducted and the creep failure mechanism of brittle rock is discussed.

The main research findings presented in this chapter have been published in a paper entitled "A grain-based time-to-failure creep model for brittle rocks" (Wang and Cai, 2020).

3.1 Modeling of time-dependent deformation of rock

3.1.1 Grain-based model implementation in UDEC

Crystalline rock can be regarded as a heterogeneous material consisting of mineral particles of various types and sizes. The mechanical properties of rock depend on both the mechanical properties and the shape and spatial distribution of these mineral grains. The geometry of mineral grains is very complex and it is unrealistic to model it accurately. The Voronoi polygonal structure is often used to simplify the micro-structure of mineral particles of crystalline rocks (Gao and Stead, 2014, Lan et al., 2010).

In UDEC (Itasca, 2015), Voronoi diagrams can be generated according to the average edge length l_v of grain and the iteration parameter n_v, which are used to control the dimension and heterogeneity of Voronoi cells, respectively. More than one type of minerals can be modeled using different Voronoi tessellations. There are four types of mineral particles in the LdB granite. However, to simplify the model parameter calibration process, only one mineral is considered in the simulation. The mean size of grain can be estimated from photographs of the rock surface. As shown in Figure 3-1, the average mineral grain diameter can be estimated based on the RGB (Red, Green, Blue) value or gray parameter on each sampling point. For the LdB granite, the mean size of mineral particles is about 2.5 mm (Lau et al., 2000, Wang and Cai, 2019).

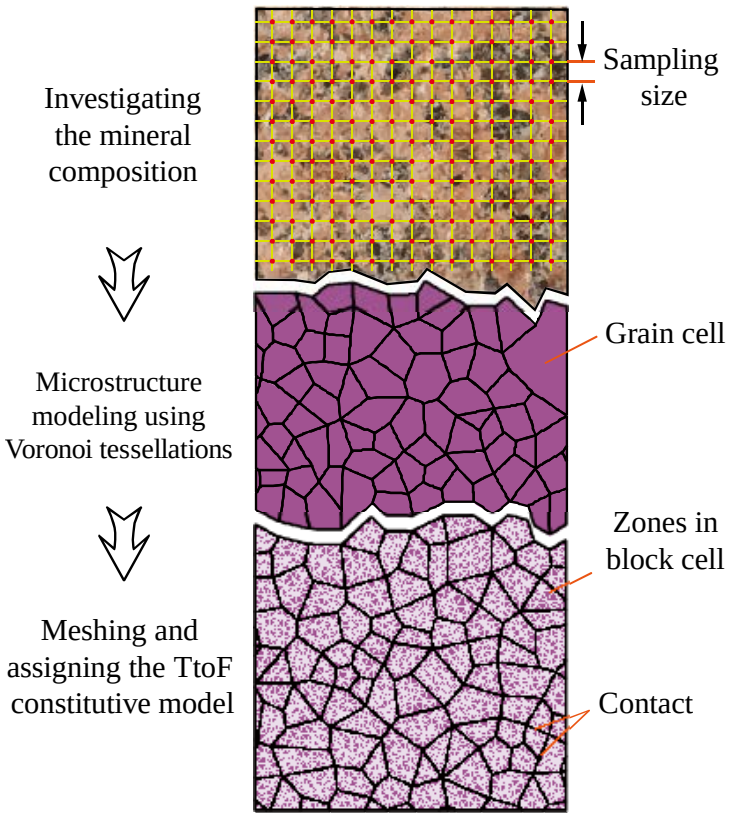

Figure 3-1. Grain-based model using Voronoi tessellations.

In the GBM, the grains are modeled as a homogeneous material and each grain is meshed into many finite-difference zones, which obey the Mohr–Coulomb strength criterion. Deformation properties and time-dependent strength degradation rules are assigned to each zone.

3.1.2 Constitutive model of time-dependent deformation

The intact brittle rock without pre-existing cracks consists of interlocked mineral grains. In the primary and secondary creep stages, the deformation of rock is assumed to be governed by the rheological properties of grains. According to the literature (Aydan et al., 2013, Nomikos et al., 2011, Chin and Rogers, 1987), the Burgers model performs well in describing the rheological behavior of geo-materials, which exhibits an initial strain in the primary creep stage and a stable strain in the secondary creep stage. As shown in Figure 3-2, the Burgers model contains components from the Maxwell and Kelvin models, which are sequentially connected. The time-dependent strain ε under constant compressive loading (Aydan et al., 2013) can be expressed by

$$\varepsilon(t)=\frac{\sigma}{G_m}+\frac{\sigma}{\eta_m}t+\frac{\sigma}{G_k}\left(1-e^{-\frac{G_k}{\eta_k}t}\right), \tag{3.1}$$

where σ is stress, t is time, G_m is the shear modulus of Maxwell component, η_m is the viscosity coefficient of Maxwell component, G_k and η_k are the shear modulus and viscosity coefficient of the Kelvin component, respectively.

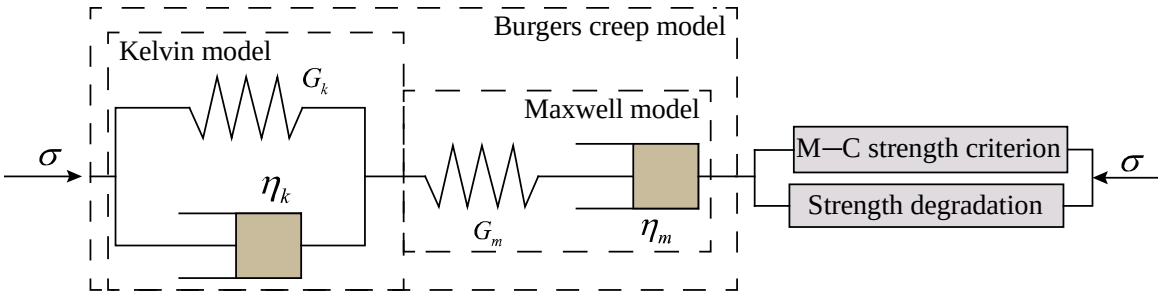

Figure 3-2. Time-to-failure constitutive creep model.

The variations G_m, G_k and η_k control the deformation in the primary creep stage; G_m has a negative relation to the range of initial strain; G_k has a negative relation to the range of strain in the primary creep stage, and η_k has a negative relation to the variation speed of strain in the primary creep stage. The strain rate in the secondary creep stage is negatively correlated with η_m.

According to the results of the uniaxial compression test of Malan (1998), the strain rate in the secondary creep stage is positively correlated with σ_1/σ_c, where σ_c is uniaxial compressive strength. The higher the stress is and the lower the stiffness is, the larger the strain rate will be. Some triaxial compression test results (Zhao et al., 2018b) also confirm that these four parameters (G_m, η_m, G_k, and η_k) are not only material parameters but also a function of stress. The deformation of grains in the secondary creep stage is a focus of this study. Thus, based on the experiment data from Malan (1998), η_m is modified as

$$\eta_m = \frac{\gamma}{\sigma^{\beta}}, \tag{3.2}$$

where γ and β are model parameters.

3.1.3 A strength erosion model for lifetime prediction

Owning to the rheological properties, most brittle rocks under a constant load will creep and finally fail if the load is beyond a threshold (Kaiser and Morgenstern, 1981). The long-term strength is usually considered in many geotechnical engineering structure designs with a long service life. It has been found that there is a relation between the long-term strength and the creep failure phenomenon (Damjanac and Fairhurst, 2010). According to the experiment data of some researchers (Paraskevopoulou et al., 2017, Chen et al., 2017, Lau et al., 2000), brittle rock specimens will not fail under a stress lower than the crack initiation stress σ_{ci}. If a specimen is under a sustained loading higher than σ_{cd}, it will eventually collapse. However, when the loading stress is between σ_{ci} and σ_{cd}, whether the specimen will fail or not becomes somewhat uncertain. The creep damage threshold exists, but it is different among different rock types; it even varies for the same rock type (Damjanac and Fairhurst, 2010). Considering that there is no consensus on creep damage threshold that impels a rock to the tertiary creep stage, for simplicity it is assumed that the crack damage stress σ_{cd} is equal to the creep damage threshold.

When a rock is under a constant load higher than the creep damage threshold, the time-to-failure is closely related to the static stress. The mechanism of stress erosion creep failure and the relation between the time-to-failure and stress is still under intense investigation. Most commonly used creep models are empirical, which are based on experiment data. Aydan (2013) proposed to predict the lifetime of specimen t under uniaxial compression loading σ using

$$\frac{\sigma}{\sigma_S} = 1.0 - b \ln\left(\frac{t}{t_0}\right), \tag{3.3}$$

where t_0 is the time based on which the short-term compressive strength σ_S is measured, and b is a material constant.

Eq. (3.3) is a lifetime prediction model for rock under uniaxial compression, which can be used for structures with no confinement such as unsupported pillars (Aydan et al., 2005). Figure 3-3 presents the relation between the time-to-failure and the driving-stress ratio under uniaxial loading conditions, where driving-stress ratio = $(\sigma_1 - \sigma_3)/(\sigma_S - \sigma_3)$, σ_S is the strength under confinement $\sigma_2 = \sigma_3$. There is a strong positive correlation between $\log(T_F)$ and the driving-stress ratio.

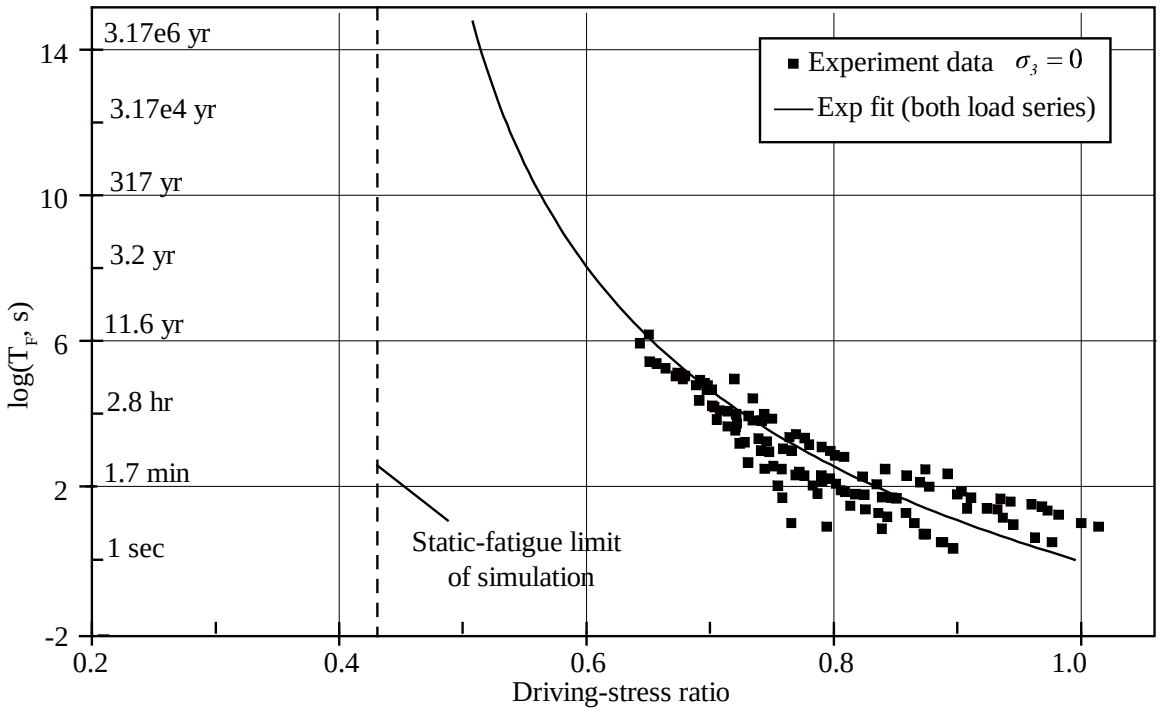

Figure 3-3. The relation between driving-stress ratio and lifetime of rock (Potyondy, 2007).

Experiment data show that confinement has a large influence on the lifetime of brittle rocks (Lau et al., 2000, Potyondy, 2007). The driving-stress ratio, which measures the influence of the differential stress under triaxial compressive loading condition, can be taken as a measurement to determine the strength degradation rate of contacts in the GBM (Liu and Cai, 2018).

However, this type of driving-stress ratio is only suitable for evaluating the tolerance of differential stress under constant confinement. As can be seen in Figure 3-4(a), in the Mohr's diagram, the driving-stress ratio is the ratio of the radii of the loading stress circle R_1 to the ultimate strength circle R_2. In fact, there are at least three ultimate strength circles in the Mohr's diagram. When σ_3 is kept constant, the right-ultimate strength circle can be drawn when σ_1 reaches the maximum value of σ_1^f, as shown in Figure 3-4(a). This driving-stress ratio is referred as r_{sr}. Assuming that σ_1 is kept constant, the left-ultimate strength circle can be drawn when σ_3 reaches the minimum value of σ_3^f, as shown in Figure 3-4(b). This driving-stress ratio is referred as r_{sl}. If the average stress $\left(\sigma_1+\sigma_3\right)/2$ is kept constant, the central-ultimate strength circle can be obtained as illustrated in Figure 3-4(c). This driving-stress ratio is referred as r_{sc}. These three driving-stress ratios select different reference points to compare the given stress status to evaluate the tolerance of differential stress, as illustrated in Figure 3-4(d). The variables r_{sr} or r_{sl} evaluate the impact of σ_1 or σ_3 on the differential stress tolerance when σ_3 or σ_1 is kept constant, respectively. When σ_1 and σ_3 are changing simultaneously, r_{sc} is more suitable to

describe the differential stress tolerance than r_{sr} and r_{sl}, and a simple verification is given in the Appendix A. Thus, the driving-stress ratio of r_{sc} is used in this study.

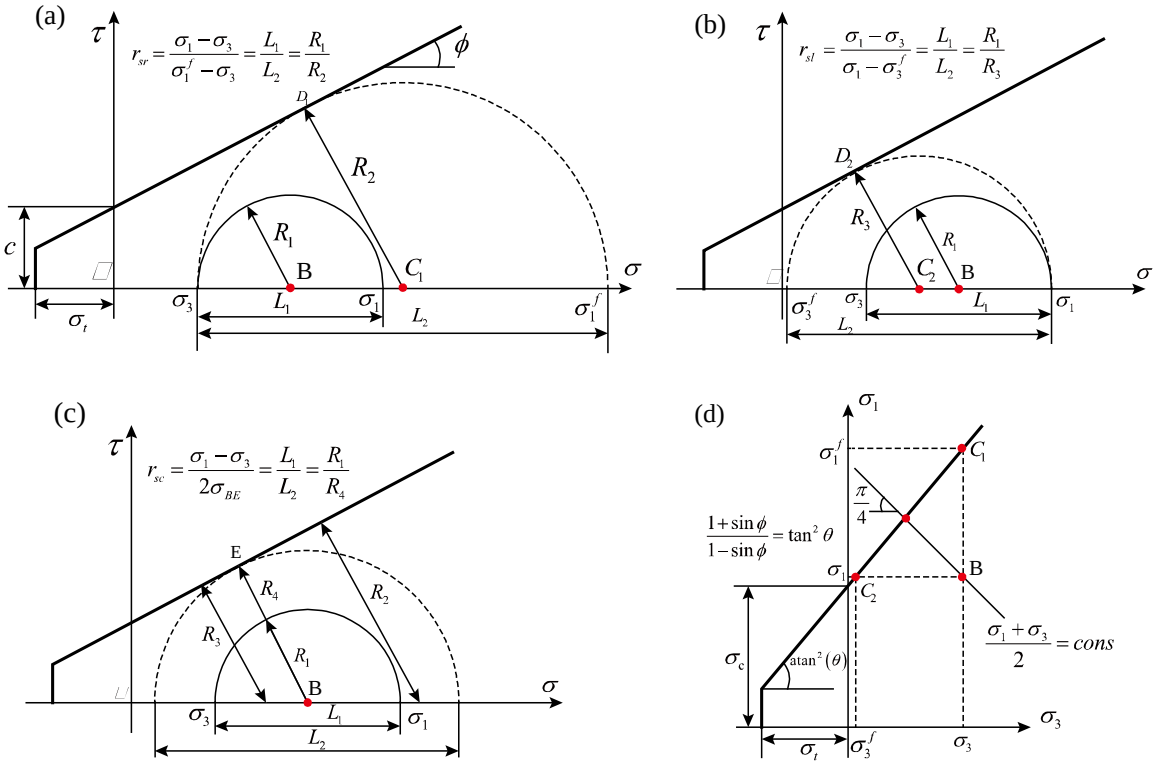

Figure 3-4. Three types of driving-stress ratio in Mohr's diagram: (a) Right-driving-stress ratio; (b) left-driving-stress ratio; (c) center-driving-stress ratio; (d) comparison of three driving-stress ratios.

Many triaxial creep experiments were conducted to investigate the influence of lateral stress on time-dependent strengths of rock. The static fatigue test data of Lajtai (1985, 1986, 1991) and Lau (2000) are used in this study. Even though the rocks used in these two studies are both LdB granite, when comparing the time to failure of unconfined experiments from these two datasets, it is obvious that the strengths of specimens reported in Lau (2000) are much higher than that reported in Lajtai (1985, 1986, 1991). In Lau's tests, the lifetimes are 60 and 12,000 s under 220 and 200 MPa uniaxial loading, respectively. In Lajtai's tests, the short-term uniaxial compressive strength is about 225

MPa; the lifetimes are about 3 to 5 and 20 to 30 s under 220 and 200 MPa loadings respectively. Hence, a nonlinear scaling of the lifetime of Lau's test data is conducted. If the log(t) is divided by 2.5, the lifetimes are about 5 and 20 s under 220 and 200 MPa uniaxial loadings, respectively.

After fitting the test data mentioned above, a relation between r_{sc} and lifetime of the rock is obtained as

$$r_{sc}{}^{a} = 1 - q \ln\left(\frac{T_F}{t_0}\right), \tag{3.4}$$

where T_F is the lifetime of the specimen, t_0 is the time for determining the short-term strength ($t_0 = 1$ s in this study), a and q are model parameters. r_{sc} can be calculated from

$$r_{sc} = \frac{\sigma_1 - \sigma_3}{2\sigma_E}, \tag{3.5}$$

where σ_E is the radius of the central-ultimate strength circle as shown in the Mohr's diagram in Figure 3-4 (c), which can be calculated using

$$\sigma_E = \left[c \cot\phi + \frac{1}{2}(\sigma_1 + \sigma_3) \right] \sin\phi, \tag{3.6}$$

where c is cohesion and ϕ is friction angle.

Fitting Eq. (3.4) using the static fatigue dataset of LdB granite mentioned above, it can be obtained that $a = 2$, $q = 0.01245$, and the fitted curve is shown in Figure 3-5. The macro-relation between time-to-failure and the driving stress ratio of LdB granite is

$$r_{sc}^{\ 2} = 1 - 0.0124 \ln\left(\frac{T_F}{t_0}\right). \tag{3.7}$$

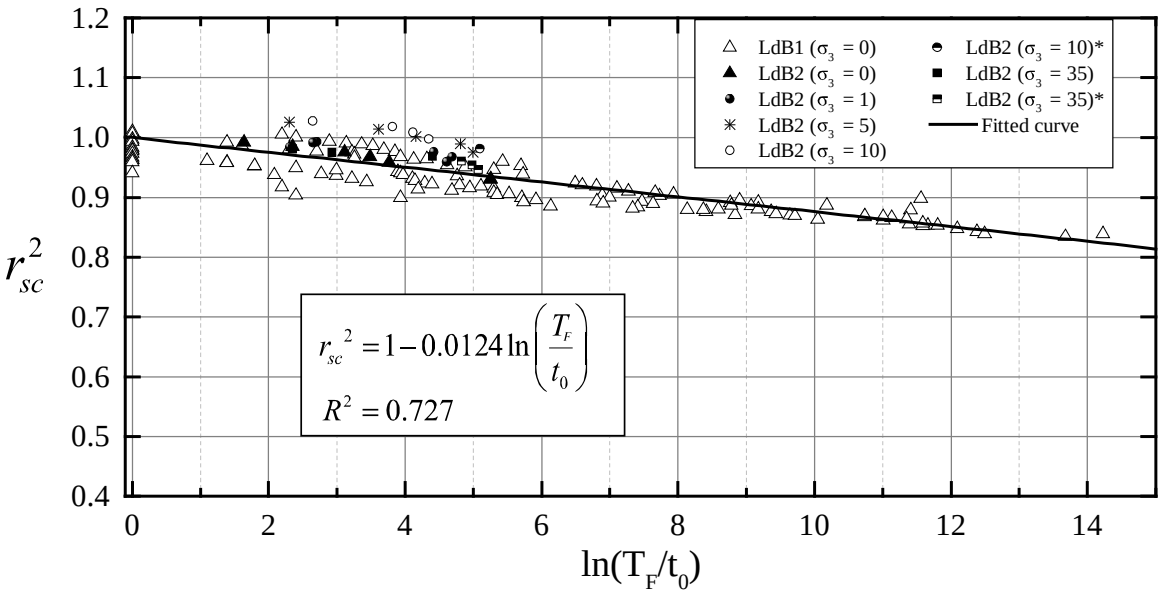

Figure 3-5. Static fatigue test data of Lac du Bonnet granite. (* specimen did not fail)

To mimic the macro-relation mentioned above, the lifetime of the rock in each grain in the grain-based model is calibrated to obey the micro-TtoF relation presented in Eq. (3.8).

$$r_{sc}^{\ a} = 1 - q' \ln\left(\frac{T_F'}{t_0'}\right), \tag{3.8}$$

where T_F', t_0' and q' are micro-parameters of zone. T_F' is the lifetime of a zone, t_0' is the lifetime under the ultimate stress state, and q' is a model constant.

Eq. (3.8), is still a static equation that can only be used in static fatigue situation. However, stress variation induced by excavation or seismic vibration usually happen in many rock engineering structures (Zhang and Pan, 2019, Ahmadi and Eskandari, 2013, Wang et al., 2018b, Wang et al., 2018a). On the micro-scale, even though the specimen is subjected to a constant loading, the stress state of each grain is usually altered due to the stress redistribution resulted from the slippage of contacts or the yielding of adjacent grains. Thus, a static form of Eq. (3.8) is not sufficient. To address this issue, a damage index D_z is defined to track the degree of damage of each zone under changing stress. In each time step increment Δt, the degree of damage can be expressed as a function of $\Delta t/T_F'$. Considering that the lifetime of each zone is a function of time, the damage index D_z at time t can be expressed as

$$D_z(t) = 1 - \int_0^t \left[t_0' \exp\left(\frac{1}{q'} \left(1 - \left(r_{sc}(t) \right)^a \right) \right) \right]^{-1} dt, \tag{3.9}$$

where $D_z = 1$ and 0 represent intact and damaged states, respectively.

For simplicity, only cohesion of grains c' is considered to be degrading with time, whereas the friction angle of grains ϕ' is kept unchanged. As shown in Figure 3-6, the strength envelope of a zone is moving downwards if the stress circle exceeds the creep damage threshold. The position of the strength envelope is defined by D_z. The movement speed of the strength envelope is determined by the rate of variation of D_z, which is determined by the driving stress ratio r_{sc} of the zone. Thus, the degradation of cohesion c' in each time step Δt is defined as

$$c'(t)=\begin{cases}(c_0'-c_Y')D_z(t) & D_z(t)>0\\ c_Y' & D_z(t)=0\end{cases}, \tag{3.10}$$

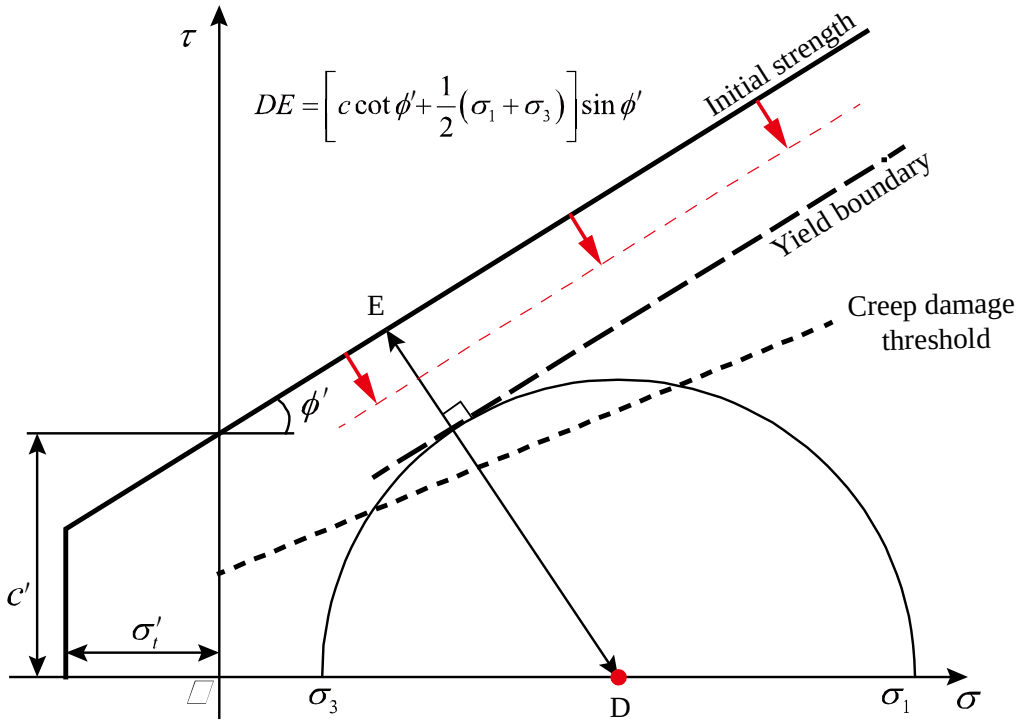

Figure 3-6. Strength reduction method for the TtoF model.

where c_0' is the initial cohesion, c_Y' is the cohesion on the yield boundary, which can be calculated from

$$c_Y'=\frac{(\sigma_1-\sigma_3)(1-\sin\phi_Y')}{2\cos\phi_Y'}. \tag{3.11}$$

Using the backwards difference method, $D_z(t+\Delta t)$ can be calculated using

$$D_z(t+\Delta t)=D_z(t)+\Delta t\dot{D}_z(t+\Delta t). \tag{3.12}$$

The variance ratio of the damage index $\dot{D}_z$ can be determined according to Eq. (3.9), which is

$$\dot{D}_z\left(t+\Delta t\right)=\begin{cases}-\left[t_0'\exp\left(\frac{1}{q'}\left(1-\left(r_{sc}\left(t+\Delta t\right)\right)^a\right)\right)\right]^{-1} & \sigma_1>\sigma_{cd}\\ 0 & \sigma_1\le\sigma_{cd}\end{cases}, \tag{3.13}$$

where the crack damage stress σ_{cd} obtained from the macro-scale experiment data is used as the creep damage threshold.

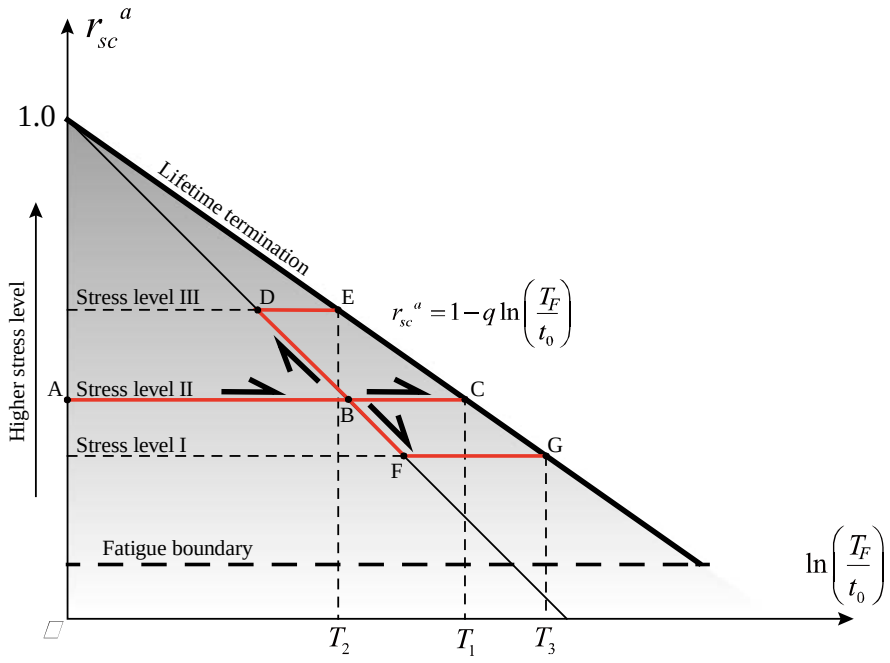

Figure 3-7. Lifetime determination of zone under unstable stress conditions.

As illustrated in Figure 3-7, the lifetime determination diagram can be used to explain the influence of stress variation on the lifetime of a zone. The abscissa $\ln\left(T_F'/t_0'\right)$ represents the lifespan of a zone. The vertical axis r_{sc}^{a} represents the loading status of the zone. There are three loading paths presented in the figure. Loading path ABC represents the stable

loading condition under the stress level II, where the lifetime is T_1. For the loading path of ABDE, the stress is constant till point B; then there is a reloading to bring the stress to level III and the lifetime is reduced to T_2. For the loading path of ABFG, the stress is reduced to stress level I, and the lifetime is extended to T_3.

In the numerical simulation, the lifetime and the damage index of each zone are traced in each time step. When the stress status changes due to the failure of a zone or the slip of grain contacts, the influence of stress redistribution on the strength degradation speed can also be considered using this degradation method.

3.1.4 A degradation model for contacts between blocks

Based on the assumption presented in Section 3.1.2, the creep deformation of a specimen in the primary and secondary creep stages is mostly due to the straining of grains. Therefore, there is no need to have a separate constitutive model to control the creep deformation of contacts. As for the strength reduction of grain contacts, a relation between the strength reduction of grain and the strength reduction of contact is established based on the static fatigue failure of macro-cracks.

In the GBM, when a rock specimen is loaded beyond the crack damage stress, yielding of grain contacts plays an important role in the macro-crack propagation and the failure of the specimen (Potyondy, 2007, Wang and Cai, 2019). However, the mechanism of the yielding of a macro-crack under static fatigue is still unclear. Fortunately, there is a basic physical mechanism available for the yielding of macro-crack under shear loading. For an unfilled rough joint with interlocked surfaces, the shear strength of the joint is determined by the

roughness of the surface profile (Barton, 1973). Considering such a failure mechanism, it is assumed that the strength degradation of macro-cracks may also result from the reduction of the roughness along macro-crack surfaces during static fatigue creep deformation.

In the grain-scale GBM, there is a need to present the macro-crack generation process which is resulted from the slippage and opening of grain contacts. It is assumed that there is a relationship between the damage accumulation of minerals along the contact and the creep fatigue of contacts. Thus, the strength degradation of zones along the micro-cracks' surface is adopted, which consists of zones near the contact, to describe the degradation of the roughness of micro-cracks in the static fatigue process. In this manner, the roughness reduction is resulted from the stress concentration occurring on the edges of grains, and the breaking process of the asperities along the surface can be presented in detail.

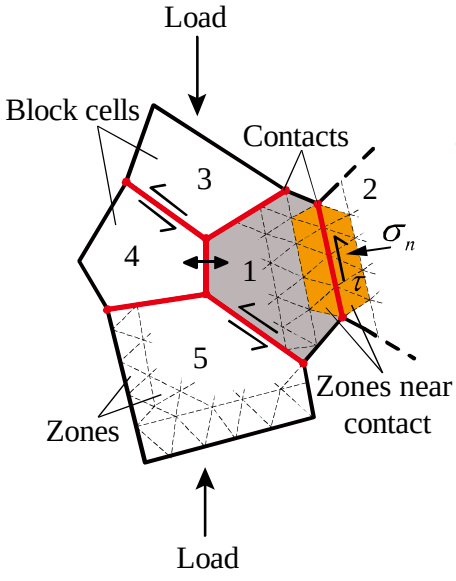

Figure 3-8. Strength degradation mechanism for contact.

As shown in Figure 3-8, for the interface of blocks 1 and 2, the orange triangle zones are defined as the zones near the contact. It is assumed that the friction angle ϕ^{ct} and the tensile

strength σ_t^{ct} of the contact are kept unchanged. The cohesion c^{ct} of contact is degraded based on the damage accumulation among the zones near the contact. The degradation of c^{ct} is governed by

$$c^{ct}\left(t\right)=\begin{cases}\left(c_0^{ct}-c_Y^{ct}\right)D_{ct}\left(t\right) & D_{ct}\left(t\right)>0\\ c_Y^{ct} & D_{ct}\left(t\right)=0\end{cases}, \tag{3.14}$$

where c_0^{ct} is the initial cohesion of the contact, c_Y^{ct} is the cohesion on the yield boundary, which can be calculated from

$$c_Y^{ct}=\tau-\sigma_n\tan\phi^{ct}, \tag{3.15}$$

and $D_{ct}\left(t\right)\in\left(0,1\right)$ is the damage index of contact, which is determined by the mean value of the damage index of all the zones near the contact from

$$D_{ct}\left(t\right)=\frac{\sum_{n_1}D_{z-ct}^{(1)}\left(t\right)+\sum_{n_2}D_{z-ct}^{(2)}\left(t\right)}{n_1+n_2}, \tag{3.16}$$

where $D_{z-ct}^{(1)}\left(t\right)$ and $D_{z-ct}^{(2)}\left(t\right)$ are the damage indexes of zones near the contact located in blocks 1 and 2, respectively. The variables n_1 and n_2 are the numbers of zones near the contact located in blocks 1 and 2, respectively.

In this way, the strength of contact is degraded with the damage accumulation of mineral grains along the contacts due to stress concentration. The benefit of this contact degradation method is that there is no need to create another model to control the degradation speed of

grain contact, which will bring many difficulties to micro-parameter calibration, especially when there are more than one type of mineral grains in the GBM.

3.2 Parameter calibration

In the GBM, the mechanical properties of mineral grains are different from the macro-properties of rock. The micro-parameters of grains and grain contacts need to be calibrated using experimental data.

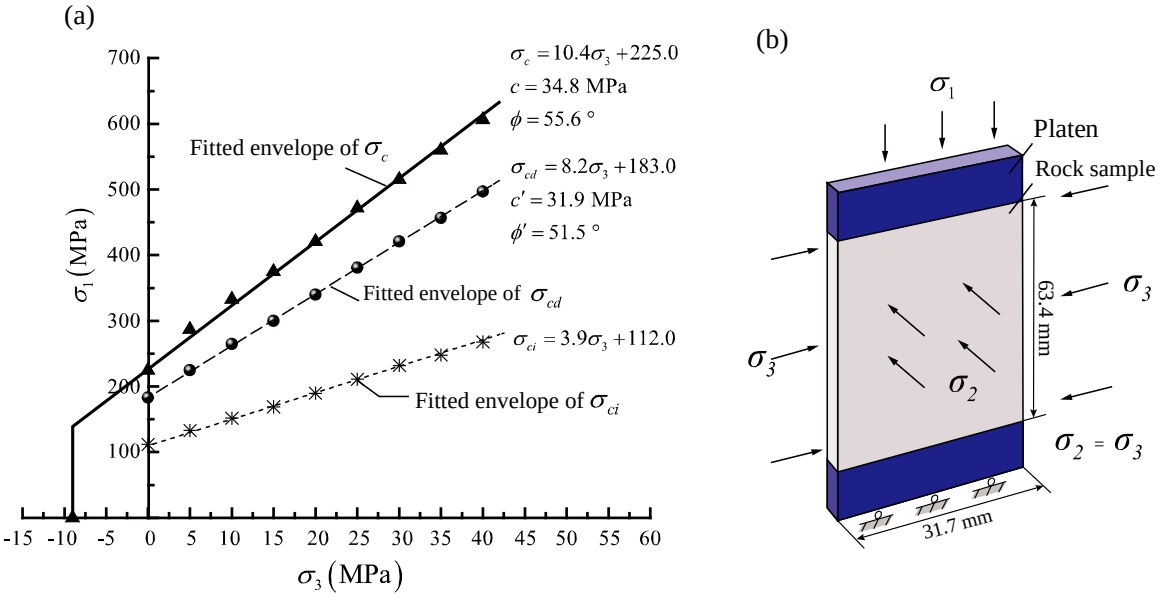

Figure 3-9. Calibrated Mohr-Coulomb strength envelope: (a) Static strength calibration results of LdB granite; (b) triaxial test simulation using plane strain loading.

Plane strain analysis is conducted using UDEC and the loading condition and the boundary condition are presented in Figure 3-9b. First, the short-term static deformation and strength properties of LdB granite are calibrated. Following the calibration procedure by Wang and Cai (2019), the GBM parameters are calibrated using the laboratory test data (Martin and Chandler, 1994, Martin, 1993) and the results are presented in Table 3-1.

Table 3-1. Macro-mechanical properties of calibrated LdB granite

Properties	Experiment	Simulation
Young's modulus, E (GPa)	69 ± 5.8	69
Poisson's ratio, v	0.26 ± 0.04	0.26
Uniaxial compressive strength, σ_S (MPa)	200 ± 25	225
Crack initial strength, σ_{ci} (MPa)	0.3 to $0.5\sigma_S$	$0.5\sigma_S$
Crack damage strength, σ_{cd} (MPa)	0.7 to $0.85\sigma_S$	$0.8\sigma_S$
Cohesion, c (MPa)	34.8	34.8
Friction angle, ϕ (°)	55.6	55.6
Tensile strength, σ_t (MPa)	9.3 ± 1.3	9.0

As mentioned above, the crack damage stress σ_{cd} is assumed as the creep fatigue threshold. The σ_{cd} envelope can be obtained using the triaxial compression test data as shown in Figure 3-9a where the calibrated envelopes of σ_c, σ_{cd} and σ_{ci} are presented. Eq. (3.17) defines the σ_{cd} envelope, which is the creep fatigue threshold in Eq. (3.13).

$$\sigma_{cd} = \frac{1+\sin\phi^{cd}}{1-\sin\phi^{cd}}\sigma_3 + \frac{2c^{cd}\cos\phi^{cd}}{1-\sin\phi^{cd}}, \tag{3.17}$$

where c^{cd} and ϕ^{cd} are cohesion and friction angle of the crack damage stress envelope defined by the Mohr–Coulomb strength criterion.

After the calibration of the short-term deformation and strength properties, time-dependent deformation properties of the GBM are calibrated next. As for the time-dependent strength of LdB granite, the macro-model is presented in Eq. (3.7) based on the experimental data of Schmidtke and Lajtai (1985) and Lau et al. (2000). The micro-parameters (i.e., q' and

t_0' in Eq. (3.8)) that control the strength degradation need to be calibrated to fit the macro-model in Eq. (3.7). The lifetime calibration process is summarized as follows.

(a) Initial value determination. The variable G_m controls the modulus of elasticity in the initial deformation stage, while γ and β control the viscosity coefficient of the Maxwell component, which determines the strain rate in the secondary creep stage; t_0' controls the short-term strength of the specimen and q' controls the degradation speed of material strength. In general, several trials need to be conducted and then G_m, γ, β, t_0' and q' are assigned appropriate initial values, which can reduce the iteration steps of the calibration.

(b) Deformation parameter determination. Adjusting G_m, γ, β, G_k and η_m so that the deformation properties are consistent with the experimental data.

(c) Short-term strength calibration. Adjusting t_0' in the micro-model to ensure that the lifetime of the specimen is $T_F = t_0$ when applying the uniaxial loading $\sigma_1 = \sigma_S$.

(d) Strength degradation speed calibration. Selecting a lower-stress status $\sigma_S > \sigma_1 > \sigma_{cd}$ to calculate the lifetime of the specimen T_p using Eq. (3.7). Adjusting k' in the micro-model to ensure that the time-to-failure of the specimen is $T_F = T_p$.

(e) Iteration. Repeating steps (c) and (d) until the requirements in Steps (c) and (d) are met at the same time.

All the calibrated micro-parameters of the TtoF model are presented in Table 3-2.

Table 3-2. Parameters of the GBM-TtoF model

Parameters		Value
Mineral grain properties		
K_v'	Bulk modulus (GPa)	46.5
c'	Cohesion (MPa)	66
ρ'	Density (g/cm^3)	2.6
φ'	Dilation	0°
ϕ'	Friction	68°
G_K'	Shear modulus for Kelvin component (GPa)	5.5
η_K'	Viscosity coefficient for Kelvin component (GPa^{-1})	85
G_m'	Shear modulus for Maxwell component (GPa)	28
γ	Material constant for Maxwell component	1.55e37
β	Material constant for Maxwell component	3.0
σ_t'	Tensile strength (MPa)	46
q'	Material constant for time-to failure model	8.6e-3
t_0'	The time to obtain the short-term strength (Sec)	2.0e-11
Contact properties		
Jks^{ct}	Shear stiffness (Pa/m)	1.56e14
Jkn^{ct}	Normal stiffness (Pa/m)	3.8e14
ϕ^{ct}	Friction	56.3°
c^{ct}	Cohesion (MPa)	51
i^{ct}	Dilation	6°
d_z	Shear displacement for zero dilation (m)	4.0e-3
c_r^{ct}	Residual cohesion after yielding (MPa)	0.0
ϕ_r^{ct}	Residual friction after yielding	5°
σ_t^{ct}	Tensile strength (MPa)	39.0
Creep timestep setting		
$fobl$	Lower limit for timestep adjusting (N)	1.5e4
$fobu$	Upper limit for timestep adjusting (N)	2.2e4
$\Delta t_{\max}^{cr}$	Maximum creep timestep (s)	0.15
$\Delta t_{\min}^{cr}$	Minimum creep timestep (s)	1e-5
Voronoi diagram parameters		
l_v	Length of edge (m)	2.5e-3
n_v	Iteration parameter	90
r_v	Round length (m)	5e-5

3.3 Model verification

After the static response and time-dependent behavior calibration, uniaxial and triaxial compression test simulations are conducted to verify the TtoF creep model.

First, uniaxial compression tests are performed. The lifetimes of the specimens at 7 stress levels, which are set higher than the crack damage stress, are simulated. The loading condition and the simulated lifetimes of the specimens are presented in Table 3-3.

Table 3-3. Parameters of uniaxial loading experiments

σ_1 (MPa)	r_{sc}	T_F (s)	$\ln(T_F/t_0)$	$\dot{\varepsilon}$ (s^{-1})
225	1.00	1.9	0.64	3.55e-5
220	1.00	2.3	0.83	3.52e-5
215	0.99	5.9	1.77	1.16e-5
210	0.99	5.0	1.61	2.00e-5
205	0.99	6.2	1.82	1.56e-5
200	0.98	11.0	2.40	9.93e-6
195	0.98	94.0	4.54	9.66e-7
190	0.97	148.0	5.00	1.03e-6
185	0.97	250.0	5.52	5.60e-7

The simulated lifetimes of all specimens under different uniaxial loading conditions are compared with the macro-model in Figure 3-10. The calibrated TtoF model agrees well with the macro-model in terms of the time-to-failure prediction. The axial strains of these 7 specimens in the creep process are presented in Figure 3-11 and Figure 3-12. The end of the primary-creep stage and the start of the tertiary creep stage are marked in the figure. It can be observed that with the increase of loading stress, the lifetime of specimen is

decreased (see Figure 3-11) while the strain rate is increased exponentially (see Figure 3-12).

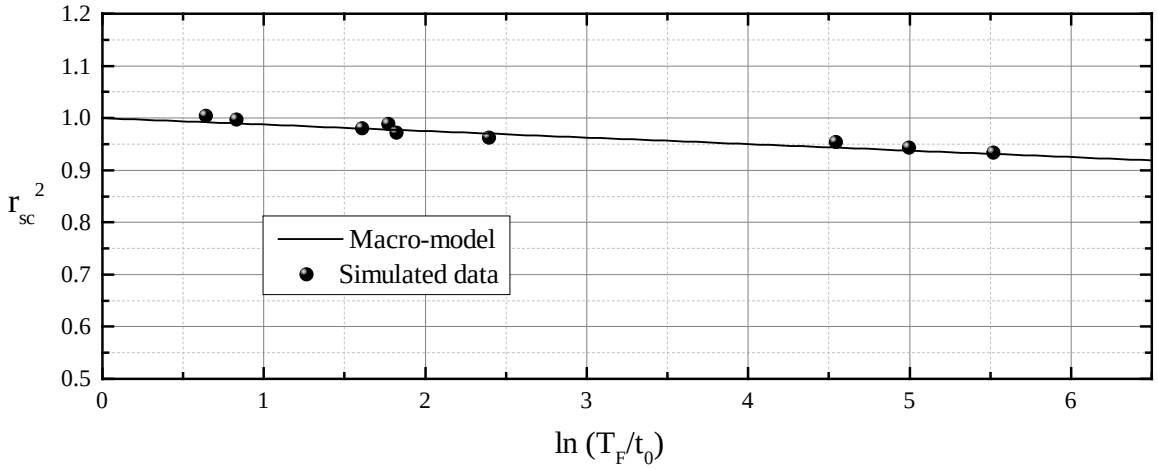

Figure 3-10. Verification using uniaxial compression test results.

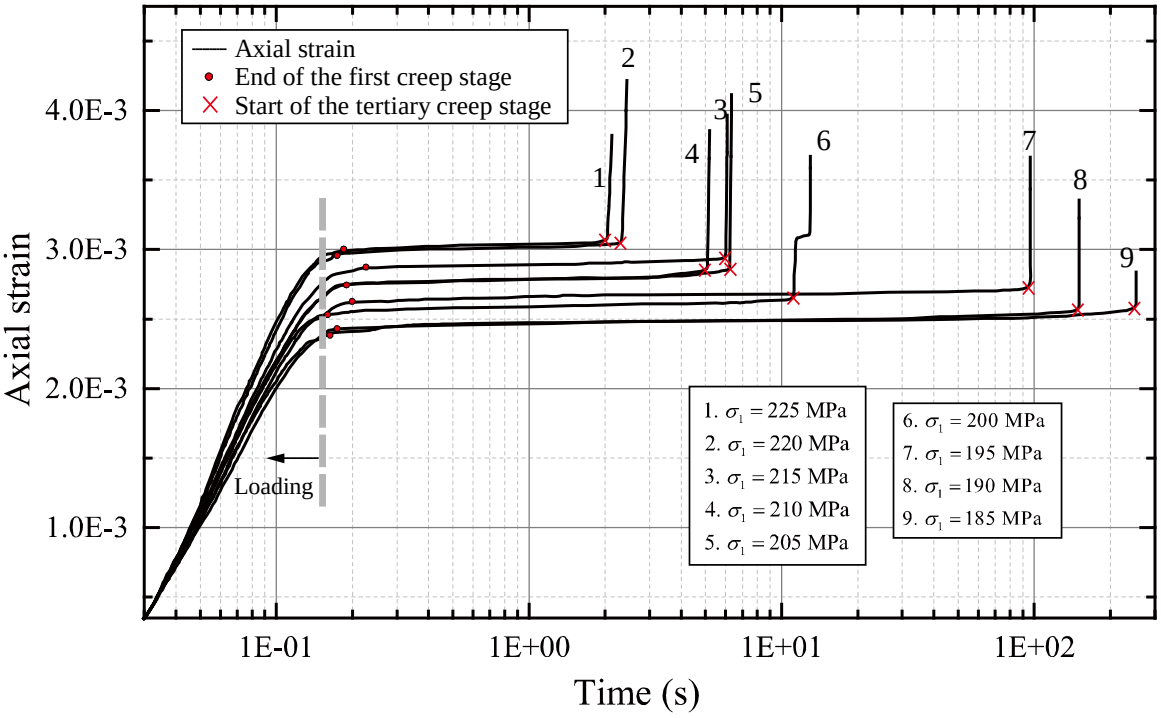

Figure 3-11. Axial strain curves of uniaxial compression tests.

Next, a series of triaxial compression experiment simulations are conducted to verify the TtoF model. In these, σ_1 is fixed to 225, 275, 325 and 375 MPa. For each compression level, 3 to 4 confinement levels are set to observe the time-dependent deformation behaviors under triaxial compression. The loading condition and the simulation results are presented in Table 3-4.

Table 3-4. Parameters of triaxial compression test

σ_1 (MPa)	σ_3 (MPa)	$\sigma_1 - \sigma_3$ (MPa)	r_{sc}	T_F (s)	$\ln(T_F/t_0)$	$\dot{\varepsilon}$ (s^{-1})
225	0	225.0	1.00	1.9	0.64	3.55e-5
225	2.5	222.5	0.98	7.0	1.95	1.44e-5
225	5	220.0	0.96	200.0	5.30	4.77e-7
275	5	270.0	1.00	2.0	0.69	1.90e-5
275	7.5	267.5	0.98	4.0	1.39	1.24e-5
275	10	265.0	0.97	450.0	6.11	3.45e-7
325	10	315.0	1.00	1.1	0.05	1.03e-4
325	12.5	312.5	0.98	2.2	0.79	1.34e-5
325	15	310.0	0.97	125.5	4.83	2.03e-6
325	17.5	307.5	0.96	330.5	5.80	4.23e-7
375	15	360.0	1.00	1.8	0.59	6.65e-5
375	17.5	357.5	0.99	2.0	0.69	5.63e-5
375	20	355.0	0.97	2.5	0.92	6.24e-5
375	22.5	352.5	0.96	54.0	3.99	8.58e-7

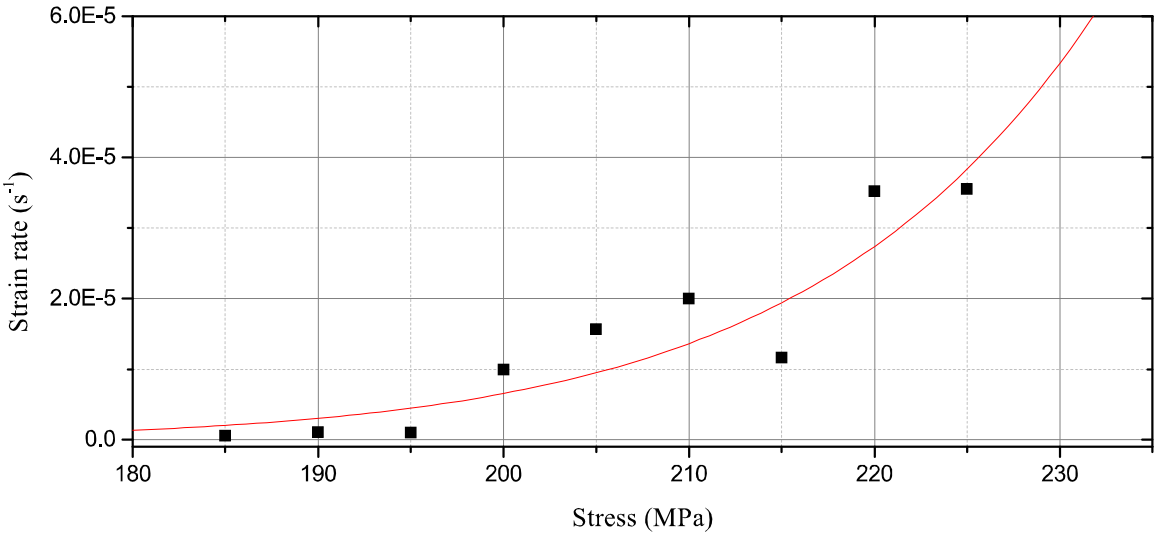

Figure 3-12. Strain rate–stress relation in uniaxial tests.

As shown in Figure 3-13, the simulated results under triaxial loading also agree well with that from the macro-model. The curves of axial strain during the creep process are presented in Figure 3-14. The start and the end of secondary creep stage are marked in the figure. As shown in Figure 3-14, with the increase of confinement, the lifetime of the specimens is increased and the strain rate decreased.

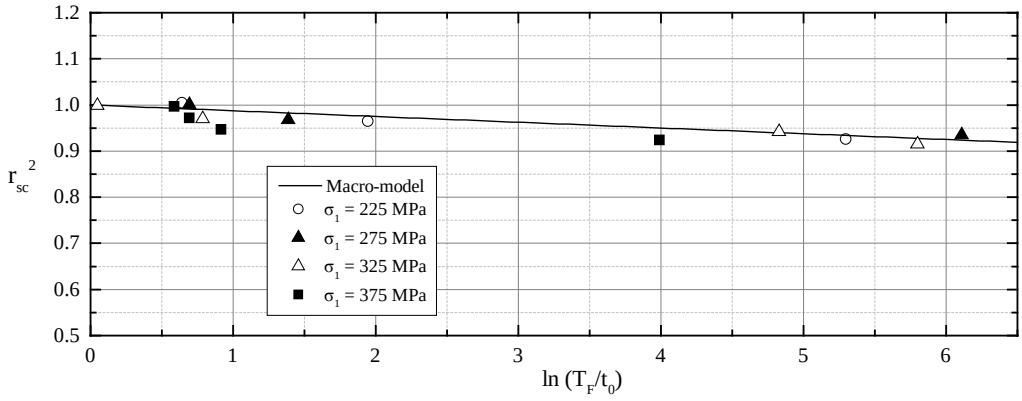

Figure 3-13. Verification using triaxial compression test results.

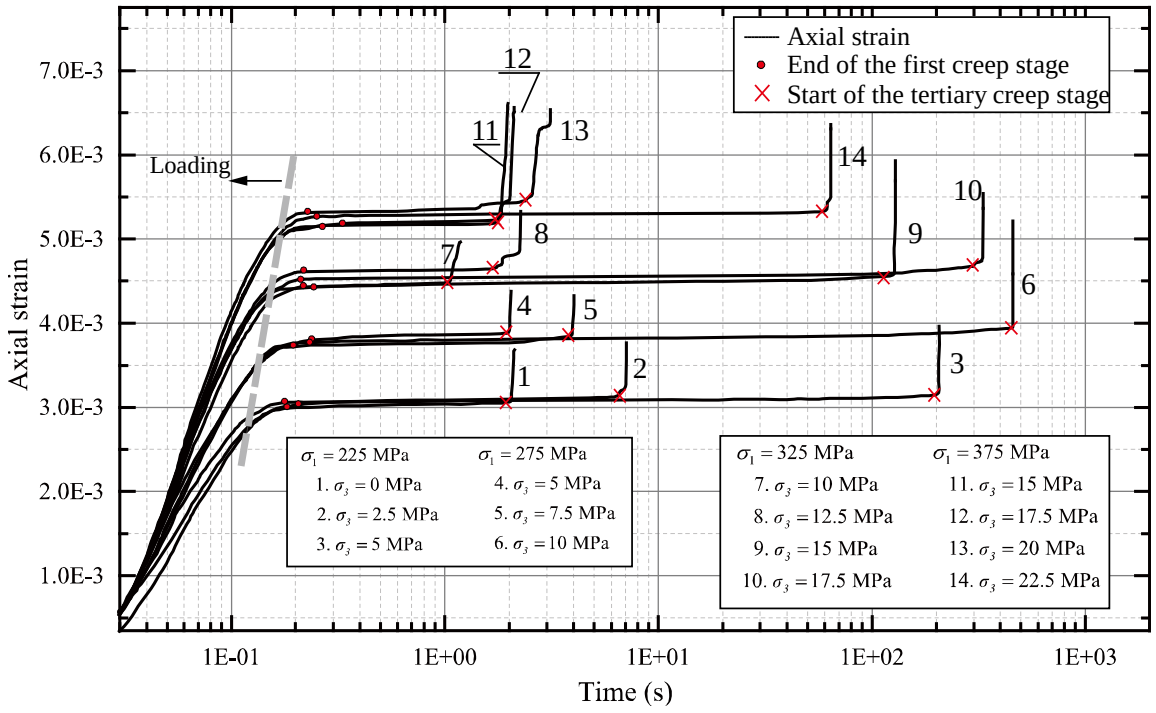

Figure 3-14. Axial strain curves of triaxial compression tests.

3.4 Discussion

The creep failure process is illustrated in Figure 3-15 for $\sigma_1 = 190$ MPa without confinement ($\sigma_2 = \sigma_3 = 0$ MPa). At 0.4 s, initial damage appears after the primary creep stage. Then the rock specimen undergoes a stable creep process for about 150 s. Even though the strain rate is constant, the damage accumulation speed, or the number of newly yielded zones differs. As shown in Figure 3-15 (f), in the first part of the stable creep stage, the yield zones occur sparsely, whereas in the second part the number of yield zones increases steadily. During this process, due to the stress redistribution near the yielded grains and contacts, the accumulated damage propagates along the opened joints as shown in Figure 3-15 (d) & (j). Finally, the emergence of macro-fractures triggers the tertiary creep stage, leading to the failure of the specimen.

The influence of confinement on the creep behavior is also investigated. The creep processes of two specimens, for $\sigma_1 = 275$ MPa and under confinements 5 and 10 MPa, are compared in Figure 3-16. As shown in Figure 3-16 (a) to (c) for the case of $\sigma_3 = 5$ MPa, there are notable stress concentrations at the initial damage stage at 0.2 s. Due to the yielding of these zones and the damage accumulation over time, macro-fractures occur quickly, and then the specimen fails at 2.0 s. For $\sigma_3 = 10$ MPa, there is no obvious stress concentration after the primary creep stage. Even at 50 s, the stress concentration is still not notable compared with the case of $\sigma_3 = 5$ MPa at 0.2 s. Hence, a higher confinement decreases the strength degradation speed and lengthen the secondary creep stage. The lifetime is about 450 s for $\sigma_3 = 10$ MPa.

In this study, it is assumed that the crack damage stress σ_{cd} is the long-term strength of a rock. When the applied stress is higher than the σ_{cd}, the rock undergoes three creep deformation stages, as shown in Figure 3-15 and Figure 3-16. When the applied stress is below the σ_{cd}, creep deformation occurs but the specimen remains stable. A simulation case is presented in Figure 3-17. The applied loading stress is $\sigma_1 = 145$ MPa, which is between σ_{ci} (113 MPa) and σ_{cd} (180 MPa). An initial strain is captured in the primary-creep stage, and local failures occur in the specimen due to the stress concentrations at those locations. However, neither violent damage nor macro-crack propagation is captured, and the specimen remains stable.

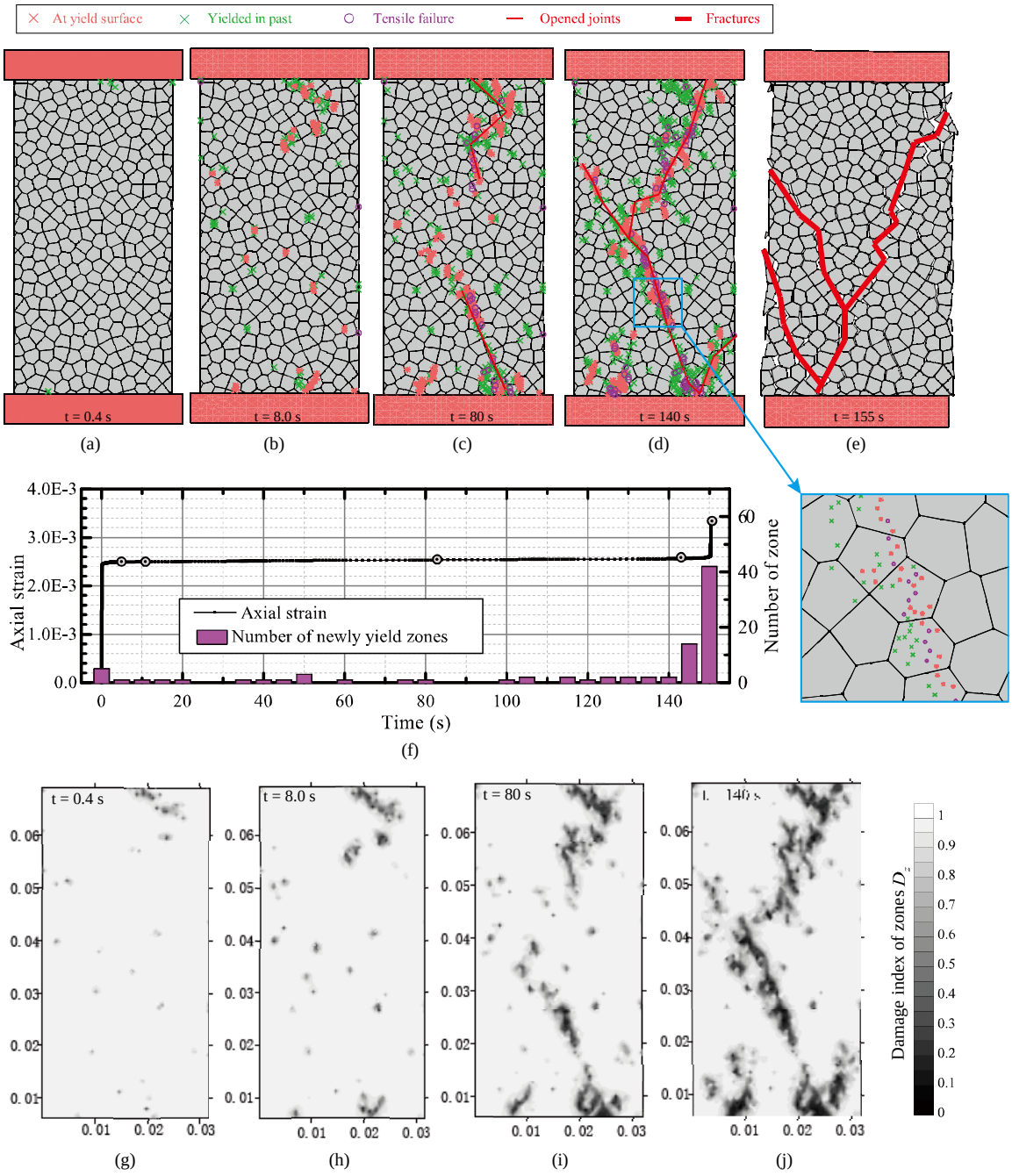

Figure 3-15. Creep process of a rock specimen under uniaxial loading of $\sigma_1 = 190$ MPa: (a) to (e) show distributions of yield zones at different deformation stages; (f) variation of axial strain and newly yield zones over the whole lifetime of the specimen; (g) to (j) contours of damage index at the damage cumulative stage.

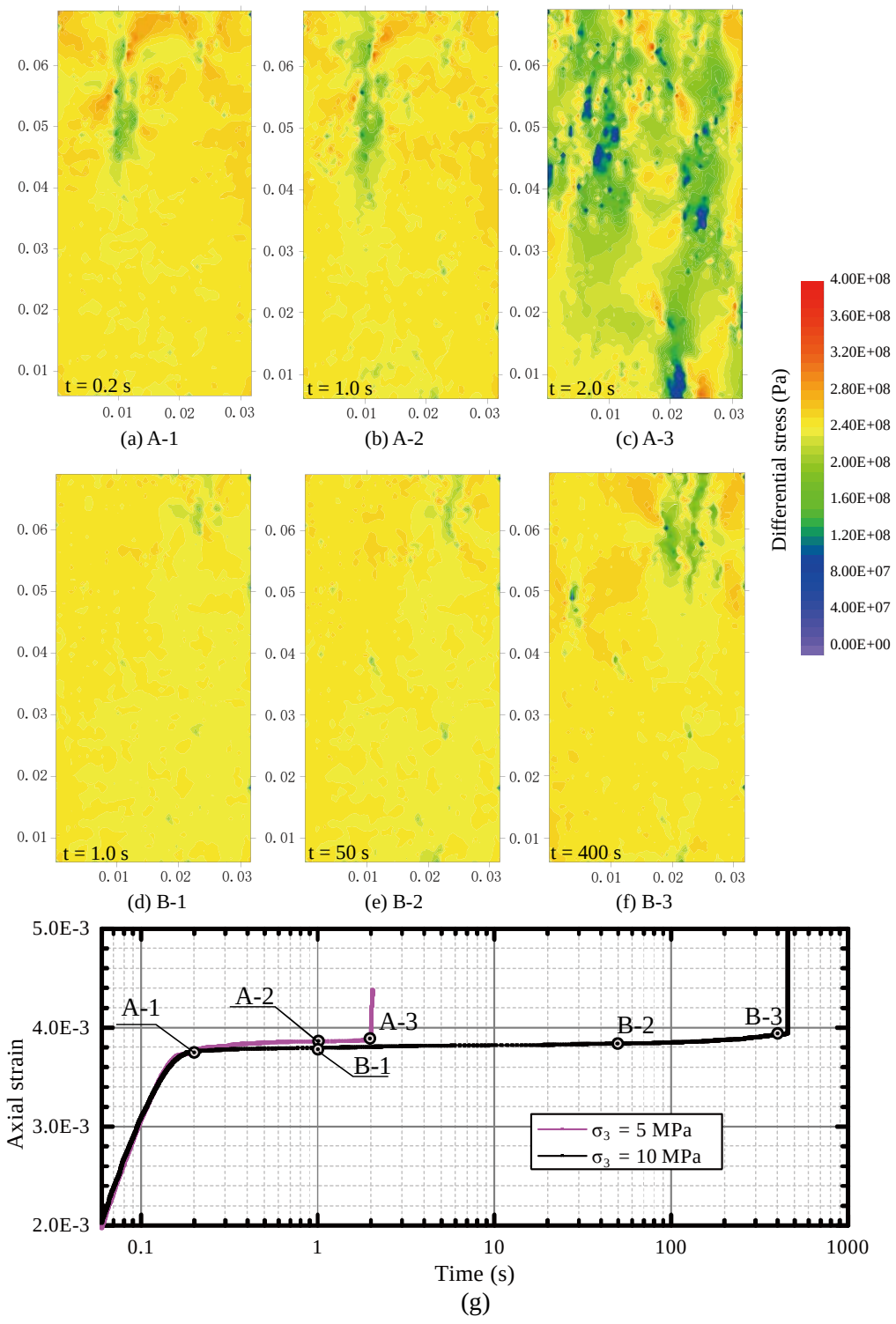

Figure 3-16. Variation of differential stress $\sigma_1 - \sigma_3$ in the creep process: (a) to (c) differential stress distribution under 5 MPa confinement; (d) to (f) differential stress distribution under 10 MPa confinement; (g) the axial strains for two specimens in their creep failure lifetimes.

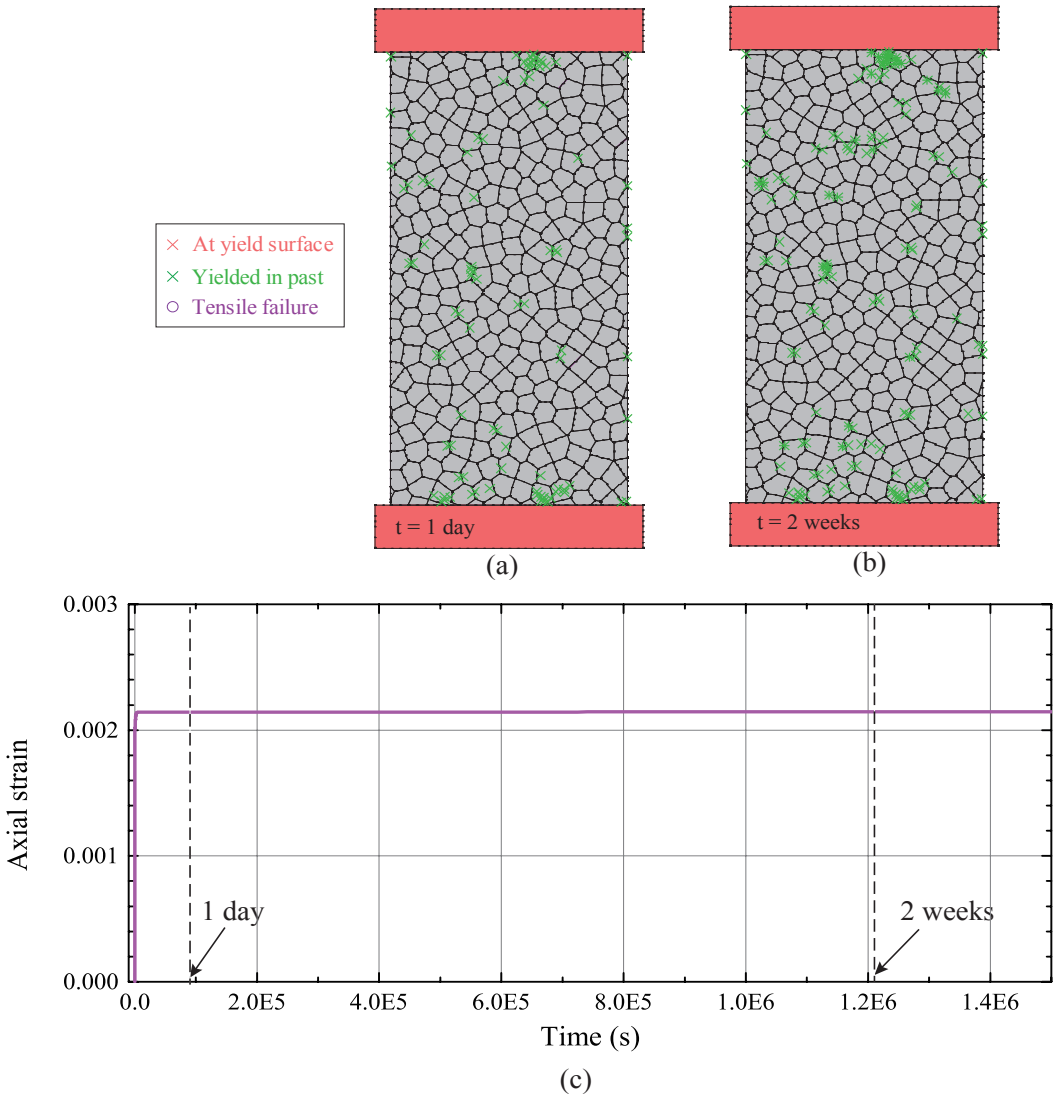

Figure 3-17. Creep process of a rock specimen under uniaxial loading ($\sigma_1 = 145$ MPa) below the long-term strength ($\sigma_{cd} = 180$ MPa): (a) and (b) show the distributions of yielding zones at different times and (c) presents the axial strain–time curve of the specimen.

In this study, some simplifications are adopted in the strength degradation approach of the GBM-TtoF model. According to experimental data, when a rock fails and reaches the residual state, the reduction of cohesion is more significant than the friction angle (Cai et al., 2007). In addition, it will make the calibration process quite complicated if too many

strength degradation parameters are included in the model. Therefore, for simplicity, it is assumed that the cohesion of the mineral grains and grain contacts degrade with time, while the friction angle and tensile strength keep constant until the grains or contacts yield.

Using the grain-based model, micro-crack initiation and propagation due to the opening and sliding of grains boundaries are captured. With the interaction between the deformation of mineral grains and grain contacts, the creep failure of a rock specimen is simulated. It provides a novel grain-scale perspective to investigate the creep deformation mechanism of brittle rocks. It shows distinct advantages of the grain-based model compared with continuum methods. The simulated results in terms of the time-to-failure of brittle rock fitted well with that from the lifetime prediction equation obtained from experiment data. Therefore, the GBM-TtoF model can be used as a powerful tool to investigate the time-dependent deformation behavior of rock mass. However, there are still some issues for the two-dimensional UDEC-GBM model, such as the restriction in the out-of-plane strain in the plane-strain analysis (Gao, 2013, Christianson et al., 2006), the uniqueness of model parameter calibration and numerical instabilities result from the stochastic meshing (Mayer and Stead, 2017). For simplicity, there is only one type of mineral grains in this study. In the future, three-dimensional GBM modeling and accurate meshing techniques will be adopted to model natural grain shapes and textures of crystalline rock.

3.5 Summary and conclusion

This chapter proposes a new creep model based on the grain-based modeling method. The implementation process of the grain-based time-to-failure (GBM-TtoF) model is described

and a series of uniaxial and triaxial compression tests of LdB granite are conducted to verify the model. The micro-mechanism of creep failure is simulated.

The TtoF creep model using the grain-based modeling method can capture the time-dependent deformation behavior of brittle rocks, including the deformation in the first two creep stages and the crack coalescence in the tertiary creep stage.

The failure of a rock is resulted from the damage accumulation in the stable creep stage. It is the sudden generation of new yield zones and the stress redistribution near the failure zones that trigger the expansion of yield zones and the transition from the stable-creep to the tertiary-creep stage.

Confinement affects the lifetime of a rock specimen significantly. Higher confinements can reduce stress concentration and consequently prolong the lifetime of a rock.

In the subsequent chapter, an application of the GBM-TtoF model is presented by simulating time-dependent deformations of rock pillars. Pillars will be modeled using the GBM-TtoF model. The spalling phenomenon on pillar walls and the time-dependent failure mechanism of rock pillars will be analyzed.

Chapter 4 Numerical modeling of time-dependent spalling of rock pillars

In this chapter, time-dependent strength and deformation of rock pillars are simulated using the GBM-TtoF model implemented in UDEC, with a focus on studying time-dependent spalling of pillars. Laboratory-scale pillar models with different W/H ratios are built using the GBM-TtoF model and creep simulations are conducted to study the influence of loading ratio (the ratio of the applied stress to the strength of pillar) and pillar shape on the time-dependent deformation of rock pillars. Time-dependent failure of pillars and the spalling mechanism of pillars with different W/H ratios are discussed.

Main research findings presented in this chapter have been published in a paper entitled "Numerical modeling of time-dependent spalling of rock pillars" (Wang and Cai, 2021a).

4.1 Numerical model implementation

Based on existing understanding of time-dependent deformation behavior of brittle rocks, the concepts of time-dependent strength and deformation of intact hard-rock pillars can be illustrated in Figure 4-1. The theoretical peak strength of a rock pillar, where the time-dependent deformation of rocks is not considered, is referred to as the short-term strength of the pillar. The in-situ strength of a pillar can be understood as the long-term strength σ_L of the pillar, where the time effect is considered. For a rock pillar loaded to a certain stress level which is below its long-term strength but exceeds the spalling initiation stress, time-dependent spalling will occur on the walls of the pillar but this does not influence the long-

term stability of the pillar. If it is loaded above the long-term strength, the pillar will eventually fail. In this chapter, long-term strength of pillars will be studied by numerical simulation.

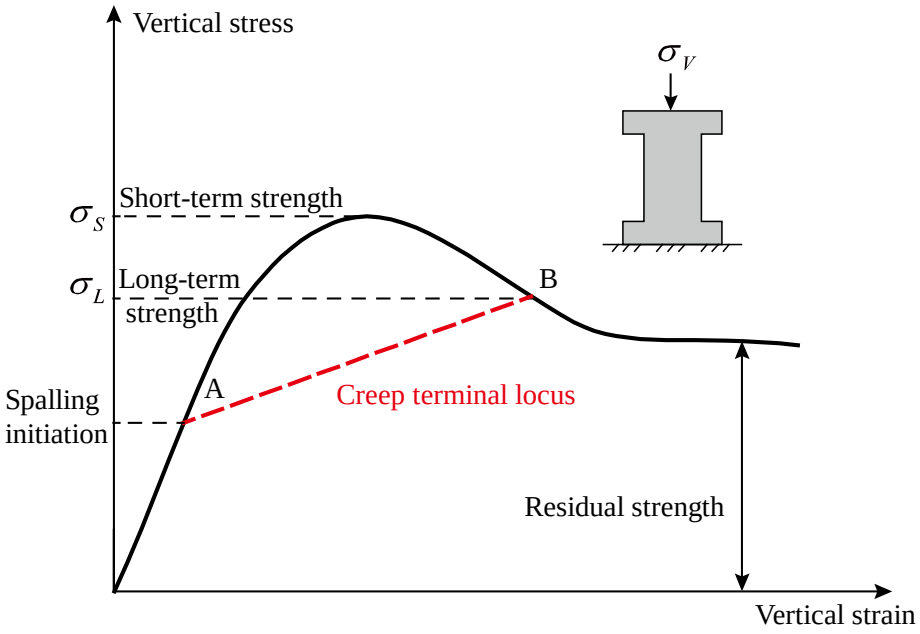

Figure 4-1. Assumption about time-dependent deformation of a rock pillar.

4.1.1 Grain-based model implementation

The GBM-TtoF model proposed in Chapter 3 is used to build the pillar models, and one model is shown in Figure 4-2. The shapes and sizes of the grains are shown in Figure 4-2(c). The heights of the pillar models are all fixed to 0.1 m, and the widths are changed to build models with different W/H ratios. In this chapter, the calibrated mechanical parameters of GBM-TtoF model in Chapter 3 (Table 3-2) are directly used, where the uniaxial and triaxial compression creep test data of LdB granite are used for model calibration.

Because the GBM-TtoF pillar model is a micro-scale creep model, which has an average length of Voronoi cells of 0.0025 m (see Figure 4-2(a) and (c)), it is not possible to build

pillar models with sizes comparable to the ones in the field. Thus, small size models are built to mimic laboratory-scale experiments of rock pillars, which has been proven useful for investigating time-dependent deformation of rocks with a pillar structure (Obert, 1965, King, 1973, Sun et al., 2020).

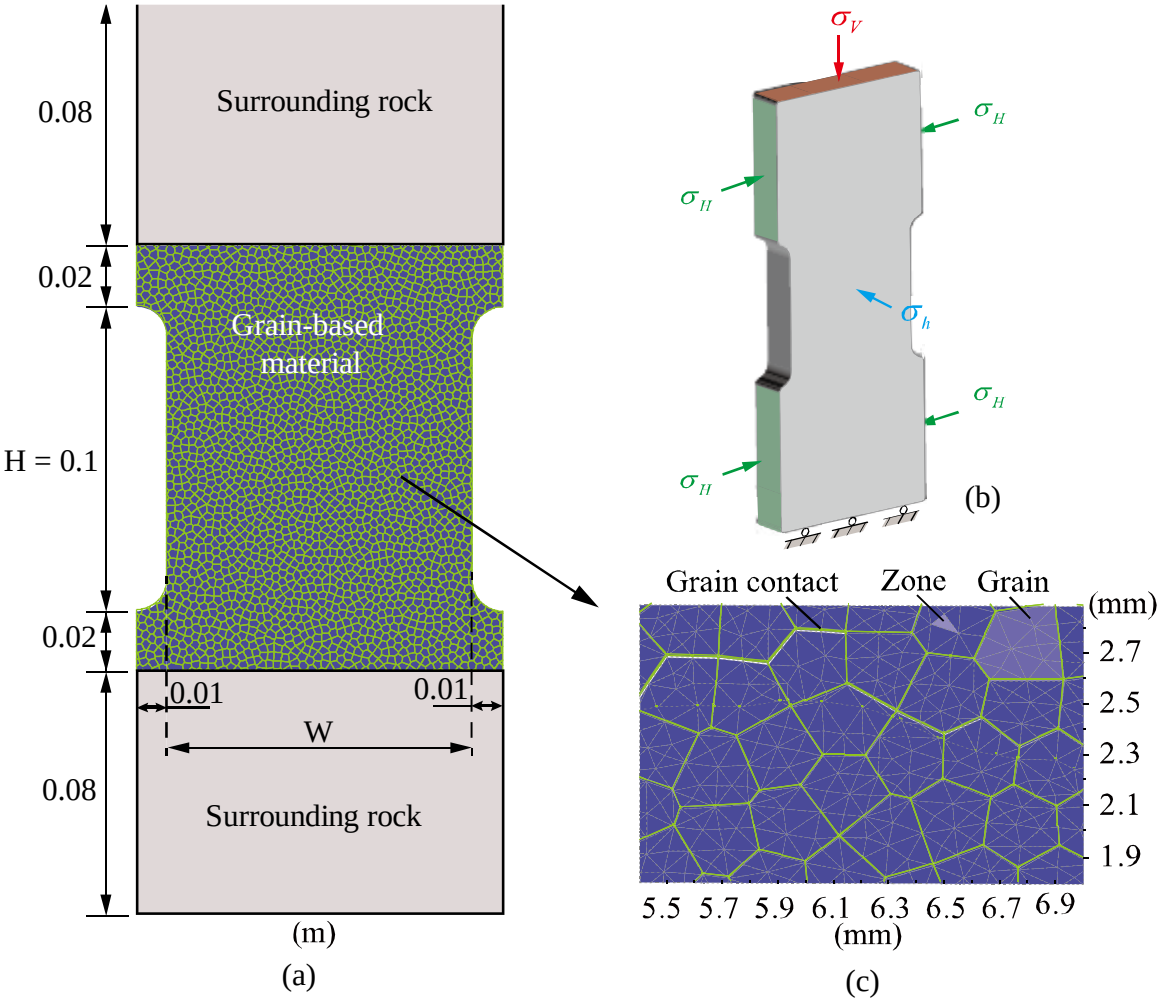

Figure 4-2. Grain-based pillar model: (a) dimension of the model; (b) loading condition of the pillar model; (c) enlarged view of the grain-based material.

To reduce computation time, the surrounding rock zones above and below the pillar are meshed using two zoned-blocks without grains and the calibrated macro-parameters of LdB granite shown in Table 4-1 are applied to the zones. This ensures that the pillars and

the surrounding rocks have similar deformation properties such as Young's modulus and Poisson's ratio. The strength of the contacts between the pillar and the surrounding rocks is assigned a high value to ensure that there is no failure on the contacts. To reduce the influence of using a non-grained material for the surrounding rocks on the modeling results, the non-grained surrounding materials are not connected with the pillar directly. There are two 0.02 m layers of grain-scale material on the roof and the floor of the pillar that act as buffer zones (Figure 4-2 (a)).

Table 4-1. Rock properties and loading conditions

Calibrated macro-parameters of GBM-TtoF model	
Young's modulus (GPa)	69
Poisson's ratio	0.26
UCS (MPa)	225
Cohesion (MPa)	34.8
Friction angle (°)	55.6
Tensile strength (MPa)	9.0
Assumed in-situ stresses	
σ_H (MPa)	20
σ_h (MPa)	10

The loading condition and the in-situ stresses are presented in Figure 4-2 and Table 4-1. The vertical stress is applied on the top surface of the model. The horizontal stresses are kept constant, with σ_H applied to the rocks in the roof and on the floor, and σ_h applied to the out-of-plane surfaces. This loading condition can be used to simulate an isolated pillar located between twin-tunnels (Li et al., 2013, Chen et al., 2009, Ng et al., 2004, Sainoki and Mitri, 2017).

It should be mentioned that the GBM-TtoF model is used to simulate time-dependent failure of intact rock without macro-joints, and the sizes of the GBM-TtoF pillar models are small. While the stress and strain values obtained from the simulation are comparable to the field conditions, the displacement values would be different (Chin and Rogers, 1987). As a result, this study is aimed at improving the understanding of time-dependent spalling of brittle rock within a pillar structure and only qualitative conclusions will be drawn.

4.1.2 Influence of pillar wall profile on pillar strength and deformation

In the grain-based pillar model implementation, smooth and irregular boundary profiles of pillar walls are considered. It has been shown that the boundary profile of an excavation has a large influence on the simulation results such as the depth of spalling notch on the tunnel walls (Cai and Kaiser, 2014). When simplified smooth pillar walls are considered, cracks initiate from the corners of the pillar, then extend to the pillar core (Figure 4-3), which is different from field observations (Roberts et al., 1998, Salmi et al., 2017, Wang et al., 2012, Smith and Rosenbaum, 1993, McClain, 1966). The simulation results by Li et al. (2019) and Li et al. (2013) show that the pillars failed in shear, but in reality it is the gradual spalling on the pillar walls that leads to pillar failures. In this section, the influence of boundary profile on time-dependent deformation of the pillar model is investigated using the GBM-TtoF model.

As shown in Figure 4-4(a), Cai and Kaiser (2014) used semi-circles to build the irregular boundary of the wall of the Mine-by tunnel that honors reality. As a result, higher stress concentration on the tunnel wall can be correctly simulated due to the locally smaller curvature of the surface. In this study, two pillar models with different boundary profiles

are built. The pillar model with a smooth boundary profile is shown in Figure 4-4(b). Another model with a rough boundary profile is illustrated in Figure 4-4(c). Using the "delete range" command of FISH script in UDEC (Itasca, 2015), the rough wall surface can be generated owning to the irregular geometry of the Voronoi tessellation.

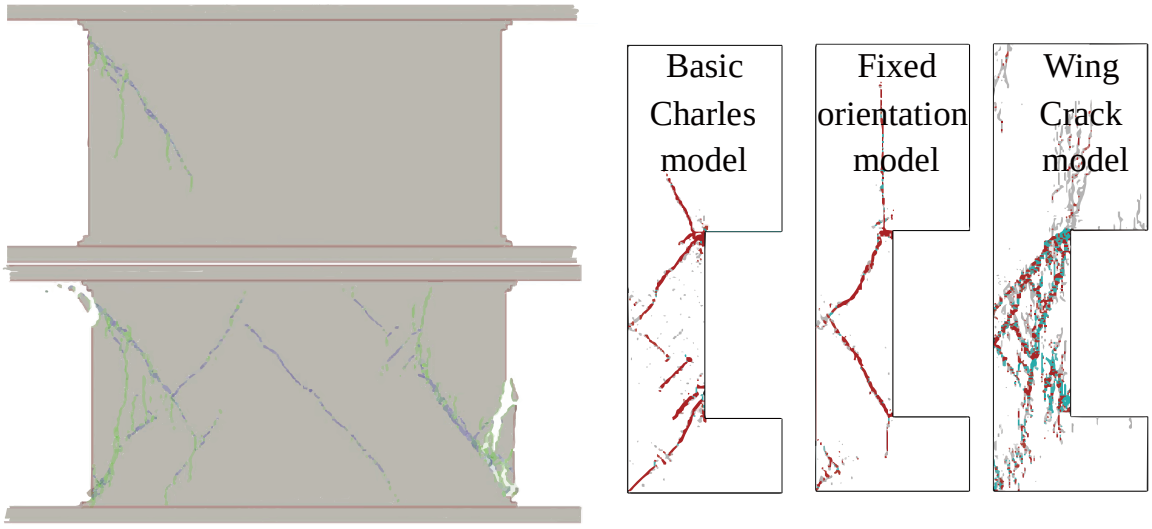

Figure 4-3. Failure pattern of pillar models using the simplified smooth boundary profile: (a) simulation of Creighton granite pillar using the FDEM method (Li et al., 2019); (b) simulation using three time-dependent crack growth models in FLAC (Li et al., 2013)

Considering that pillar models are built with different W/H ratios and boundary profiles, the naming of the pillar models follows a format of X-yZ in this study, where X (= R or S) indicates the type of boundary, with R for rough and S for smooth boundaries. y is the value of W/H ratio. If there are more than one pillar model with the same W/H and boundary type, an additional letter (A or B or C) is used at the Z position. For example, S-2.0 represents a smooth boundary pillar model with W/H = 2.0. R-1.0A and R-1.0B represent two rough boundary pillar models with W/H = 1.0.

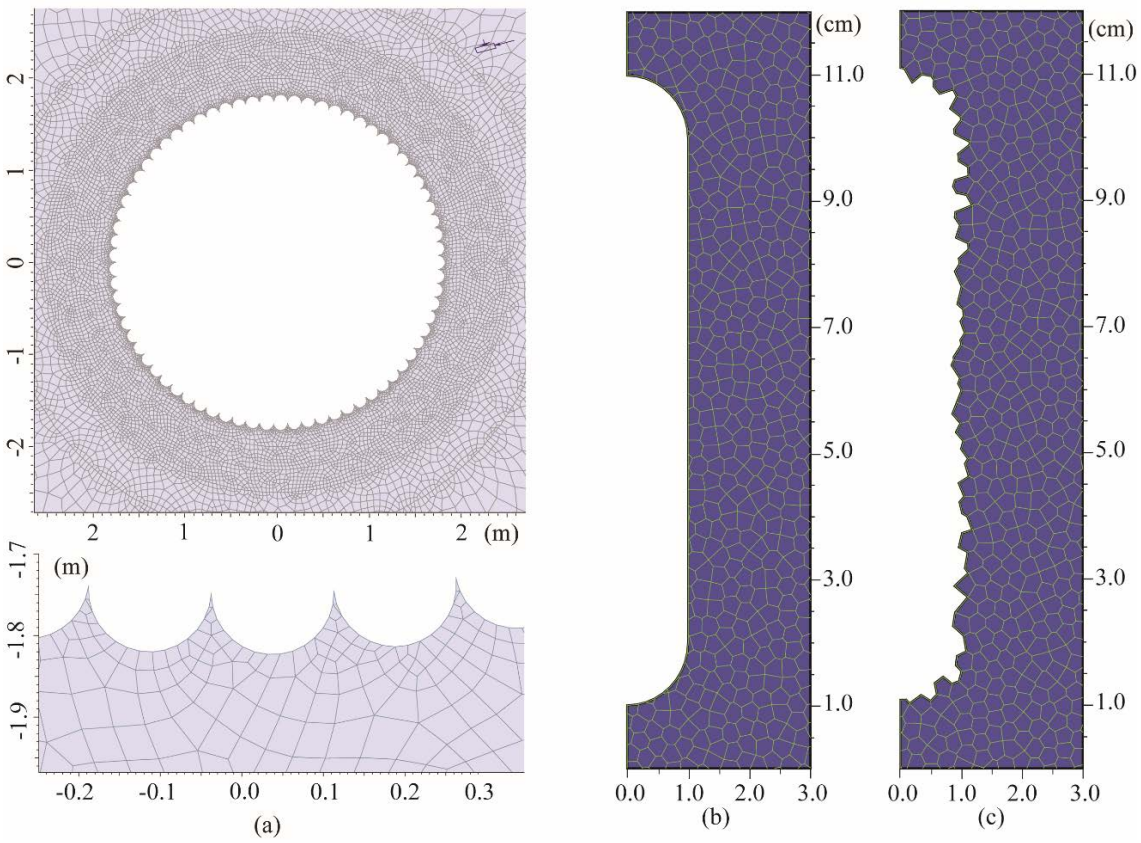

Figure 4-4. Implementation of boundary geometry in numerical models: (a) rough wall geometry used to simulate the Mine-by tunnel boundary (Cai and Kaiser, 2014); (b) smooth pillar boundary profile; (c) rough pillar boundary profile.

To check the influence of the randomness of Voronoi tessellation geometry on pillar strength and deformation, three pillar models with W/H = 1.0 are built separately using smooth and rough boundaries. First, the short-term strengths σ_s of these models are simulated with the creep option turned off. The simulated results are presented in Table 4-2, and the stress–strain curves are shown in Figure 4-5. It is seen that the average short-term strength of the pillar with a smooth boundary (S-1.0A) is slightly lower than that of the pillar with a rough boundary (R-1.0A), and the Young's modulus is slightly higher than that of the rough boundary pillar model at the end of the elastic deformation stage. The

difference of the short-term strengths for the models with smooth and rough boundary profiles is small.

Table 4-2. Short-term strength of pillar models with different boundary profiles

Pillar model	Short-term strength (MPa)
Rough boundary models (W/H = 1.0)	
R-1.0A	333
R-1.0B	333
R-1.0C	321
Average	329
Smooth boundary models (W/H = 1.0)	
S-1.0A	319
S-1.0B	322
S-1.0C	327
Average	323

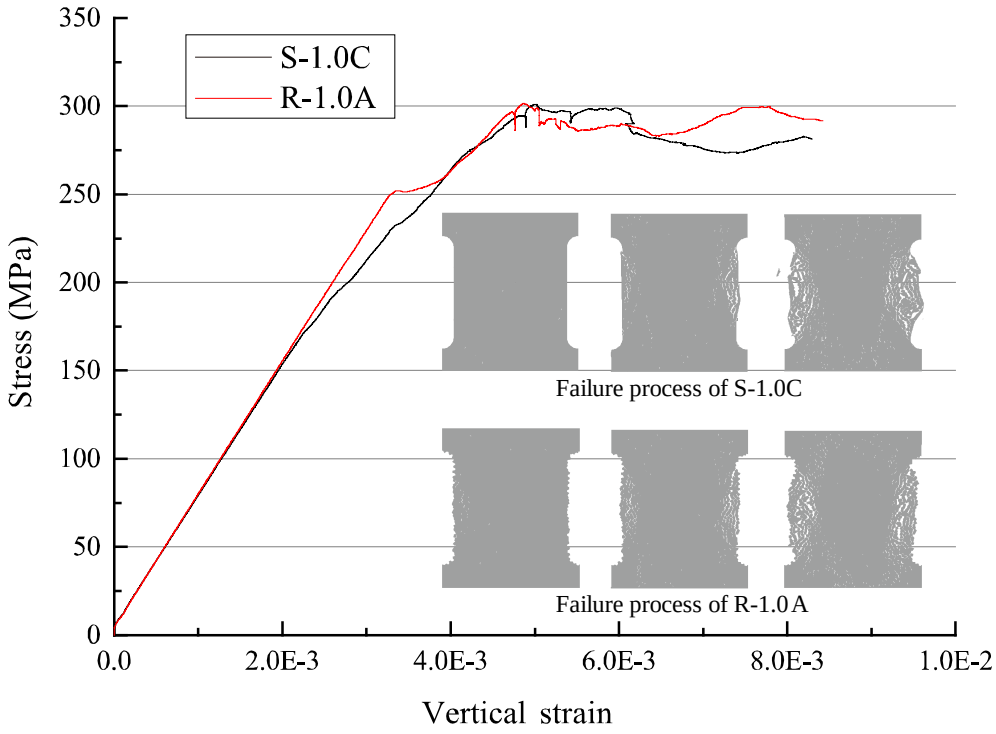

Figure 4-5. Short-term strength tests of two pillars with different boundary profiles (W/H = 1 for both models and R and S stand for rough and smooth pillar walls, respectively).

Next, creep simulations are conducted for the two pillar models (R-1.0A and S-1.0A). For the creep loading, the pillar models are loaded with constant horizontal and vertical stresses. The vertical strain of the pillar is monitored. It is observed that when a pillar model is loaded at a stress level exceeding a threshold stress, spalling damage grows continuously until the pillar fails. When it is loaded below the threshold, the spalling on the wall will stop after some time, and the pillar is stable. This phenomenon can be observed through the creep strain curves and crack evolution patterns shown in Figure 4-6 and Figure 4-7. Taking the model R-1.0A for example, when the applied stress is 130 MPa, the creep strain increases continuously, as shown in Figure 4-6 (a). Macro-cracks propagate gradually, which can be seen in Figure 4-7 (a) to (d). As a result, the pillar cannot stay stable. Cracks have developed extensively in the pillar at t = 4.2e5 s (4.9 days). If the applied stress is lower, for example at 125 MPa, the creep strain stops after some time, as shown in Figure 4-6 (a). Because most zones are loaded below their creep damage threshold, which is set as σ_{cd} (crack damage stress) of the rock in the TtoF model , there is no continuous time-dependent damage occurring in the model (Figure 4-7 (e) to (h)). Despite some small cracks generated due to local stress concentrations, the depth of spalling is stable even at t = 1.0e7 s (3.8 months). Therefore, it can be determined that the long-term strength σ_L of the rough boundary model is between 125 and 130 MPa. In this study, the trial-and-error method is adopted to find σ_L . Because the creep simulation time is very long, the stress interval was set to 5 MPa. Therefore, the long-term strength of the rough boundary model with W/H = 1.0 is determined as 127.5 MPa.

According to the method presented above, it is estimated that the long-term strength σ_L of the pillar model S-1.0A is 162.5 MPa. Even though these two models have the same W/H ratio and similar short-term strengths, the smooth boundary can increase the long-term strength of the pillar by 27.5%.

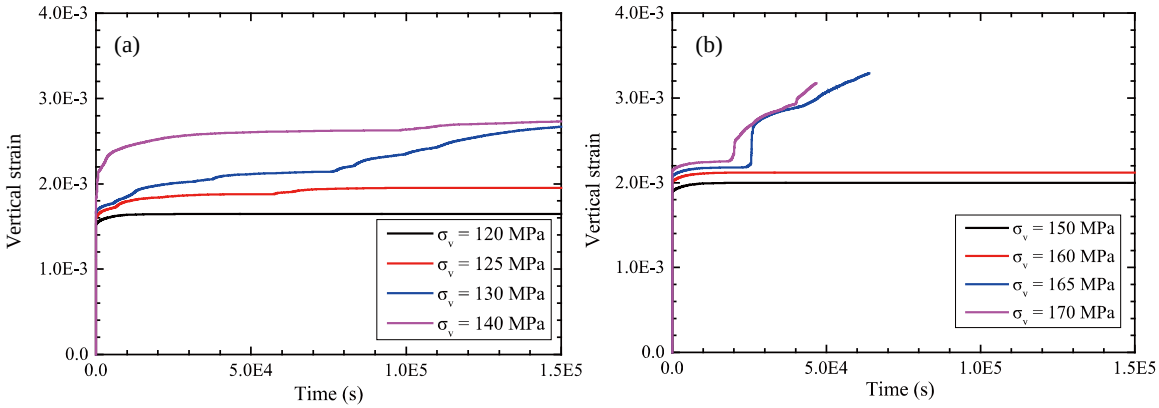

Figure 4-6. Creep strain curves of pillars with different boundary profiles: (a) rough boundary model; (b) smooth boundary model.

The crack initiation and propagation patterns of the two models are also different. Figure 4-8 presents the cracking patterns of the two models at different times in the creep tests. For the smooth boundary model, the applied vertical stress is 165.0 MPa, which is higher than the long-term strength of 162.5 MPa. Cracks initiate from the corner and then extend into the pillar core. As time passes, the cracks extend outward from the damage area of the pillar to the pillar ends. This crack evolution pattern is similar to the simulation results shown in Figure 4-3, where smooth boundary walls are used. For the rough boundary model, the applied vertical stress is 130.0 MPa, which is higher than the long-term strength of 127.5 MPa. Cracks initiate from the pillar surface due to higher stress concentrations on the rough pillar walls. Then many cracks sub-parallel to the walls are generated and

extended into the pillar core. This crack evolution pattern is similar to the spalling phenomenon observed in the field (Roberts et al., 1998).

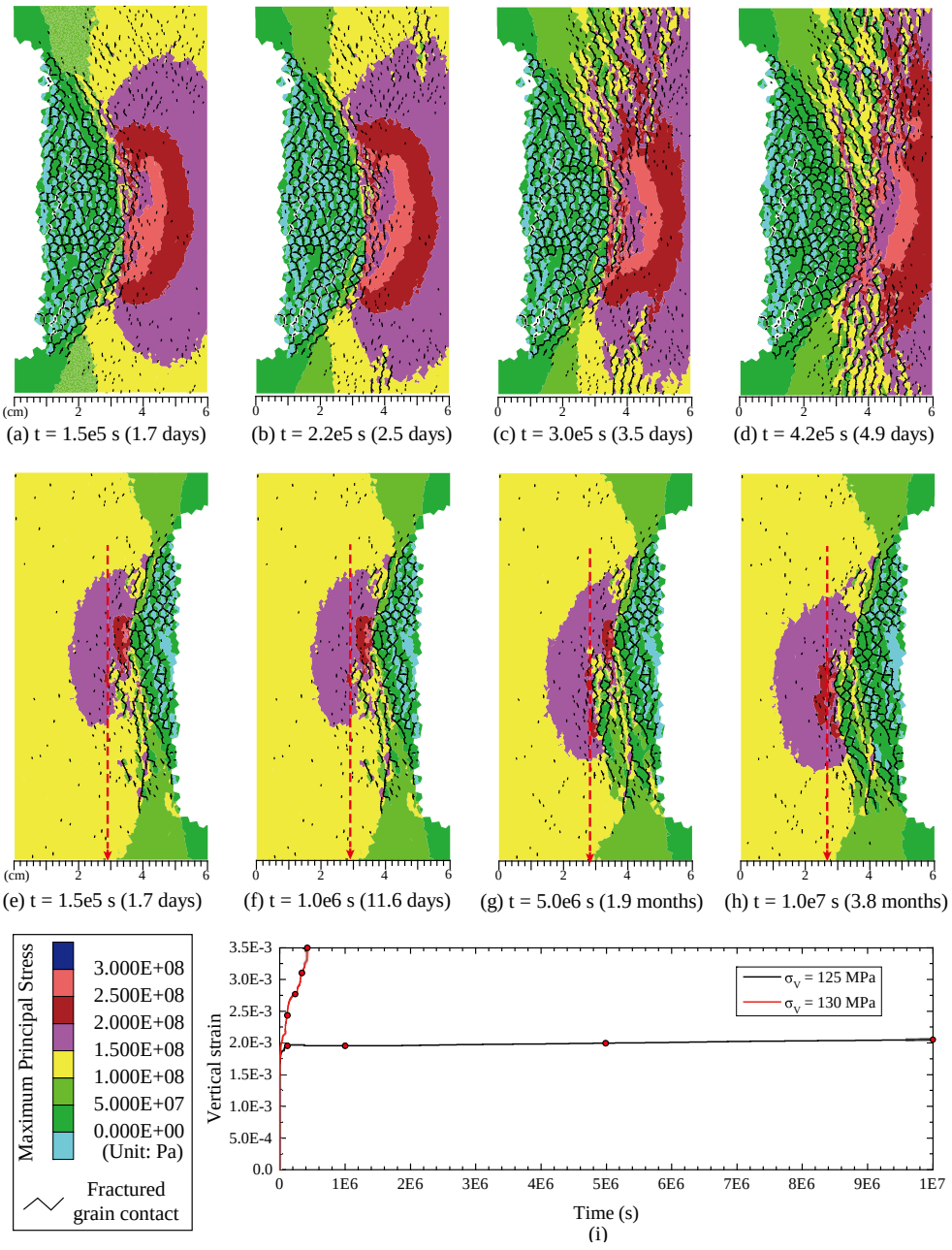

Figure 4-7. Crack and strain evolutions for pillar models loaded below and above the long-term strength: (a) - (d) crack evolution on the left wall of model R-1.0A, σ_V = 130 MPa; (e) - (h) crack evolution on the right wall of model R-1.0A, σ_V = 125 MPa; (i) creep strain curves.

It is seen from the above modeling results that the smooth boundary can increase the long-term strength of a pillar. In other words, if we want to increase the long-term strength of a pillar, we should create smooth pillar walls, although in reality this is not always possible. On the other hand, gradual spalling damage can be simulated when rough pillar walls are considered, and this agrees well with field observations. Therefore, models with rough pillar walls will be used to study the influence of the W/H ratio on time-dependent spalling and deformation of rock pillars in the next section.

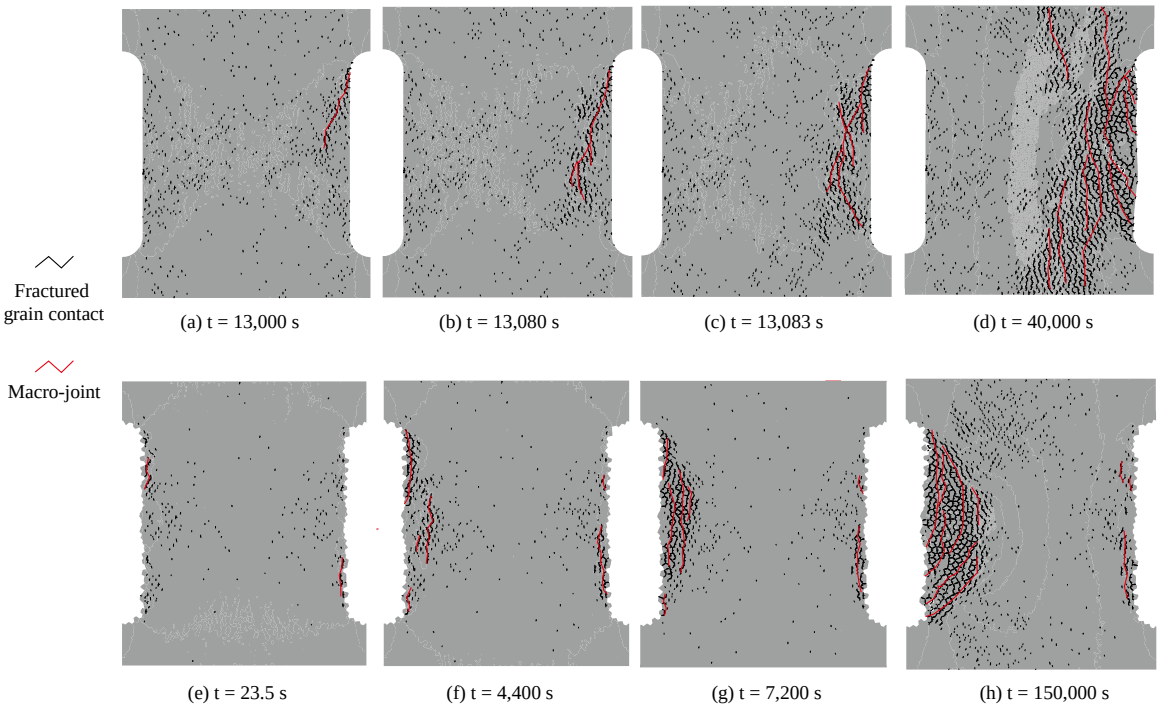

Figure 4-8. Crack initiation and propagation patterns of two pillar models with different boundary profiles: (a) - (d) smooth boundary model, σ_V = 165 MPa; (e) - (h) rough boundary model, σ_V = 130 MPa.

4.2 Simulation of time-dependent spalling and deformation of rock pillars

4.2.1 Long-term strength

In this section, rough boundary pillar models with W/H ratios of 0.5, 1.0, 1.5 and 2.0 are built to investigate the long-term strength and the spalling features of pillars with different shapes. First, the short-term strength test simulations are conducted without the creep option activated. The stress–strain curves of the pillar models with different W/H ratios are presented in Figure 4-9. It is seen that the short-term strength generally increases with increasing W/H ratio.

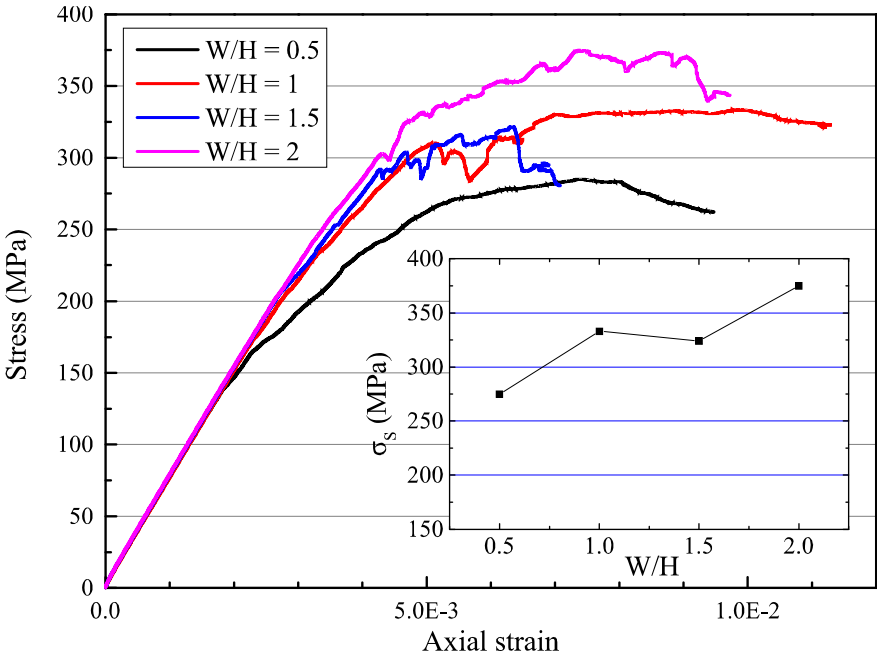

Figure 4-9. Short-term strength test simulations of rough boundary pillar models with different W/H ratios.

Next, creep experiments are conducted for the pillar models. In creep simulation, the horizontal and vertical stresses are kept constant and the axial strain is tracked. The creep strain curves of the four pillar models are presented in Figure 4-10. According to the long-

term strength determination method mentioned in Section 4.2.2, when the applied vertical stress exceeds the long-term strength, unstable creep deformation will occur. Based on this, the long-term strength of a pillar can be determined. According to the simulation results, the long-term strengths are 112.5, 127.5, 142.5, and 147.5 MPa for pillars with W/H ratios of 0.5, 1.0, 1.5, and 2.0, respectively. The simulated short-term and long-term strengths of four pillar models are summarized in Table 4-3.

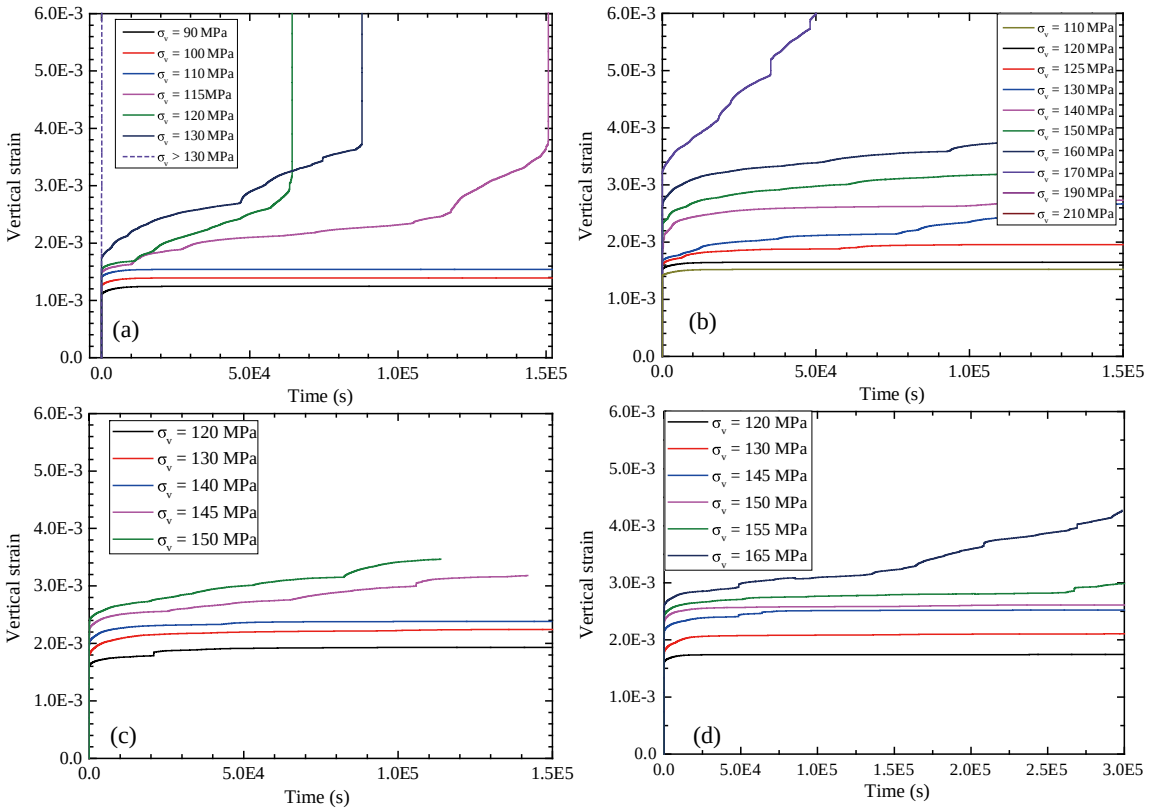

Figure 4-10. Creep strain curves of pillars with different W/H ratios: (a) W/H = 0.5; (b) W/H = 1.0; (c) W/H = 1.5; (d) W/H = 2.0.

The simulated long-term strengths of the pillar models with different W/H ratios are plotted in Figure 4-11. The long-term strengths are normalized by UCS, which is 225 MPa for LdB granite. In general, the simulated long-term strength of a rock pillar is about 50% to 60%

of the UCS of the rock. Similar to the trend of the short-term strength (Figure 4-9), the long-term strength also increases with the increase of the W/H ratio.

Table 4-3. Short-term and long-term strengths of pillar models with different W/H ratios

Pillar model	W/H	Short-term strength (MPa)	Long-term strength (MPa)
R-0.5	0.5	275	112.5
R-1.0A	1.0	333	127.5
R-1.5	1.5	324	142.5
R-2.0	2.0	375	147.5

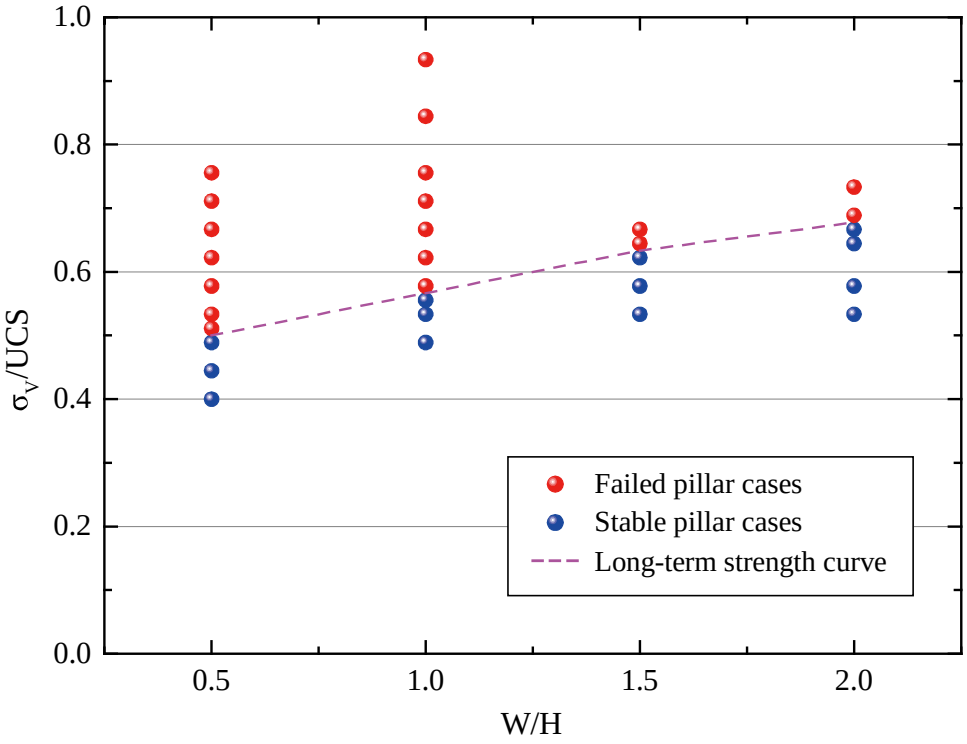

Figure 4-11. Simulated results of long-term strengths of pillars with different W/H ratios.

A pillar strength ratio ξ, defined in Eq. (4.1), can be used to investigate the in-situ strength of rock pillars.

$$\xi = \frac{Pillar\ strength}{UCS}, \tag{4.1}$$

Considering that the size and shape of the GBM pillar models are different from the field cases, a normalized pillar strength ratio ξ_N is defined in Eq. (4.2).

$$\xi_N = \frac{\xi}{\xi_{W/H=1}}, \tag{4.2}$$

where the $\xi_{W/H=1}$ is the strength ratio ξ of a pillar with W/H =1.0.

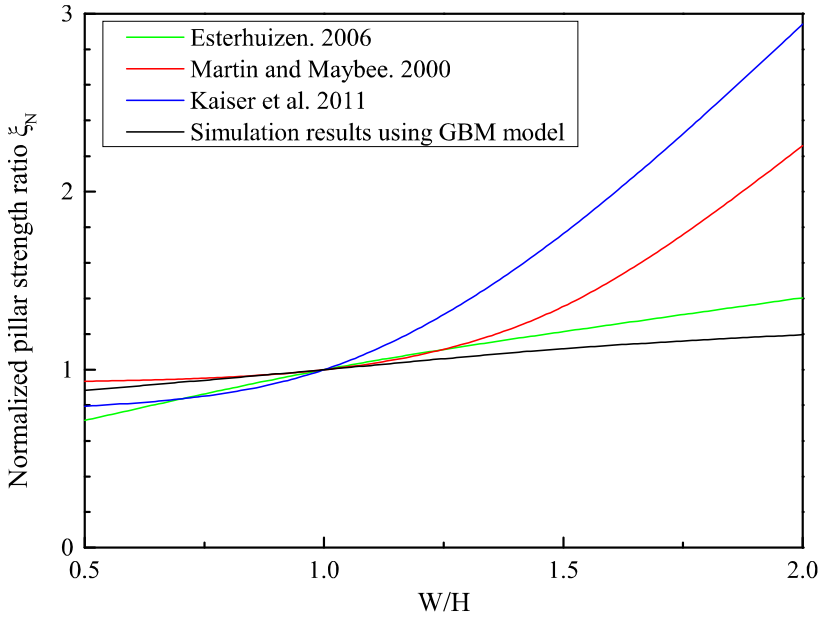

Figure 4-12. Relation between the normalized pillar strength ratio and the W/H ratio.

Figure 4-12 shows the relation between the normalized pillar strength and the W/H ratio. For the simulated curve of the GBM pillar models, the simulated long-term strength is used in Eq. (4.1) as the pillar strength to compare with other published results (Martin and Maybee, 2000, Kaiser et al., 2011, Esterhuizen, 2006). It can be seen that as the W/H ratio

increases, the increase rate of the simulated long-term strengths of the pillar models is small, which is similar to the trend presented by Esterhuizen (2006).

4.2.2 Time-dependent spalling and deformation

In this section, time-dependent spalling and deformation of the rock pillars are analyzed. As mentioned above, a rough boundary profile can result in higher stress concentrations on the pillar surface, which is helpful to simulate the spalling phenomenon observed in the field. The maximum principal stress distribution for the pillar model with W/H = 1.0 under σ_V = 125 MPa creep loading is presented in Figure 4-13(a)-(d). The contours of accumulated damage of grains are shown in Figure 4-13 (e)-(h), where the damage index is a user-defined parameter in the GBM-TtoF model, which is used to measure the accumulated damage of zones in grains. The damage index changes from 1.0 to 0 (1.0 represents intact, and 0 represents totally damaged). The initial value of the damage index is 1.0. It degrades with time and its value indicates the degree of damage of zones resulting from the stress corrosion during creep. It can be observed that the maximum principal stresses σ_{MAX} are concentrated on the irregular pillar surface at the beginning of the simulation (t = 1 s, 23 s); as a result, damages emerge at these positions due to the stress concentration (Figure 4-13 (f)). As pillar wall sub-parallel cracks are generated from the surface and they gradually propagate into the pillar core, time-dependent spalling of the pillar is captured (Figure 4-13 (c) and (d)).

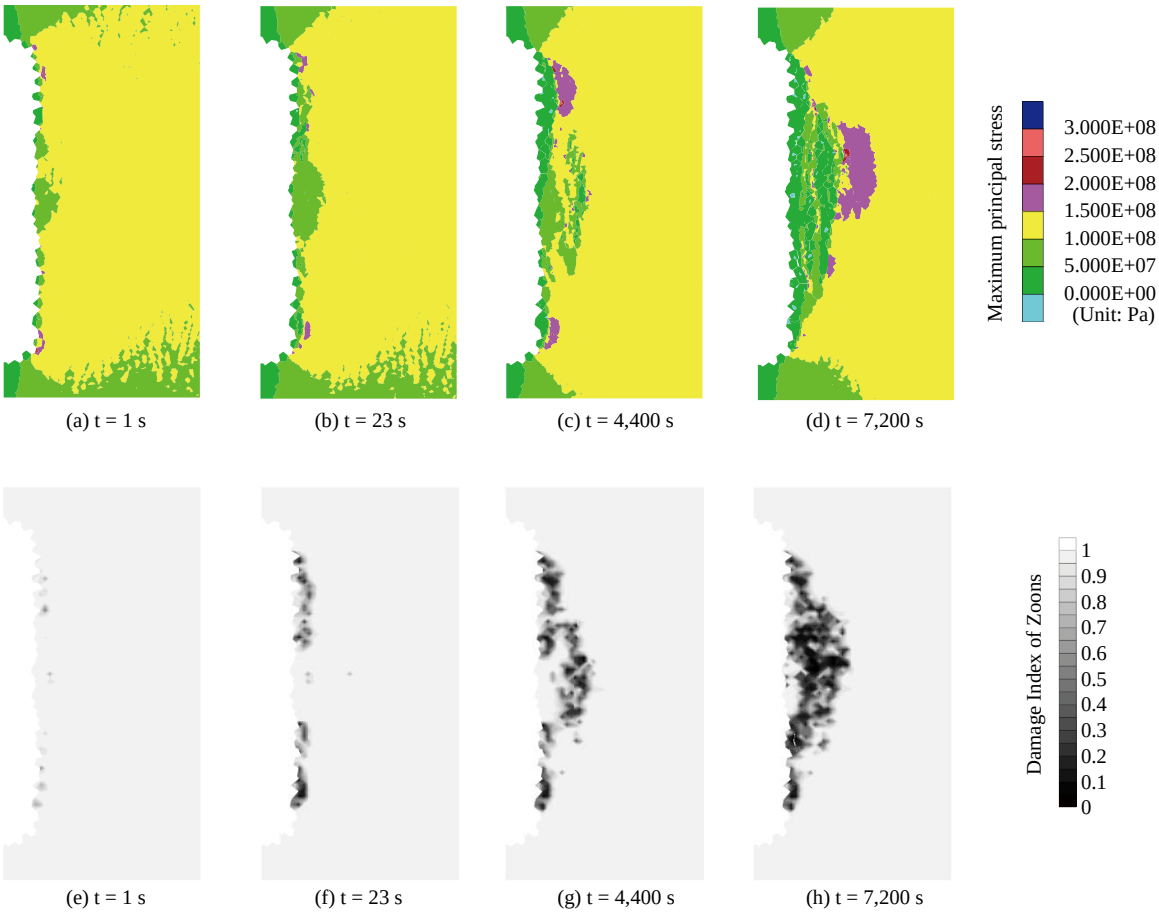

Figure 4-13. Time-dependent spalling of the pillar with W/H = 1.0 under σ_V = 125 MPa: (a) - (d) σ_{MAX} variation near the boundary; (e) - (h) accumulated damage near the boundary.

It is important to point out that time-dependent spalling can also occur in a pillar that is loaded below its long-term strength. In this case, the spalling will finally stop after some time without causing complete failure of the pillar structure. For all the cases that are loaded below their long-term strengths, the depths of spalling on the pillar walls are measured based on the spalling damages captured in the model, and the results are presented in Figure 4-14. It shows that for a squat pillar with W/H = 2.0 loaded with a load near 80% of the long-term strength, the normalized spalling depth is greater than 0.1. Squat pillars can tolerate deeper spalling on the walls without failure; for example, the normalized spalling

depth is about 0.27 for Case A when σ_V/σ_L = 0.95. However, for a slender pillar with W/H = 0.5, its normalized spalling depth is small even if it is loaded near its long-term strength (Case B, σ_V/σ_L = 0.975).

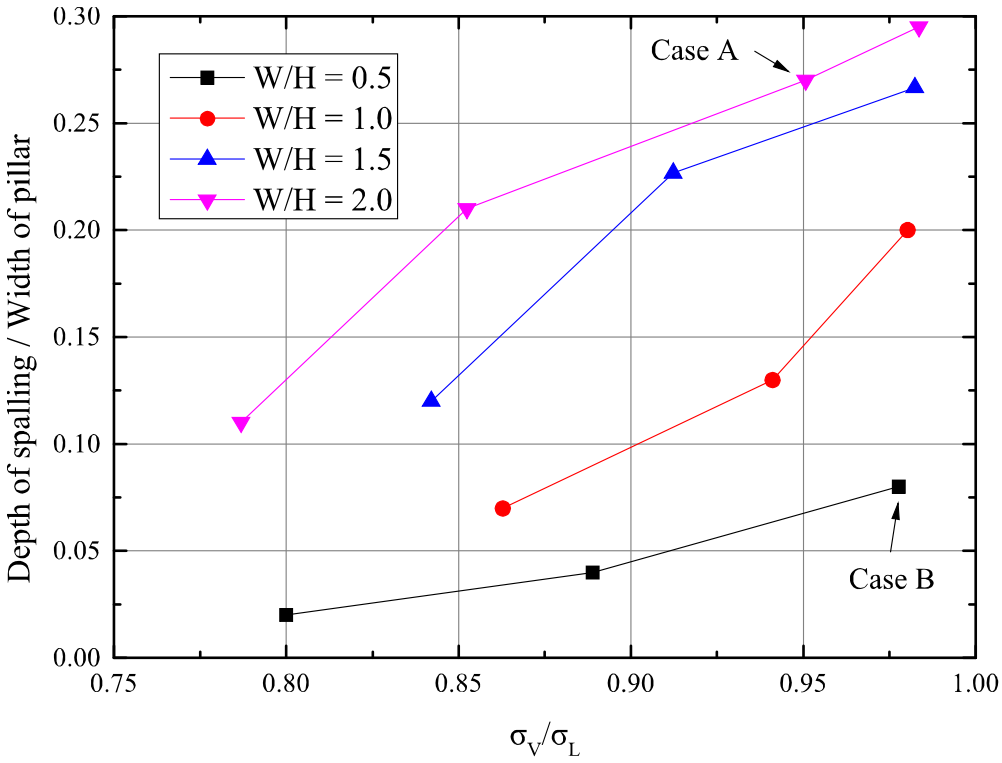

Figure 4-14. Relation between the loading ratio σ_V/σ_L and the depth of spalling for all the cases that are loaded below the long-term strength.

Two examples of depth of spalling are compared in Figure 4-15. Both pillars are loaded below but near their respective long-term strengths; as a result, they are stable in the long-term. It is seen that even though the squat pillar has a lower loading ratio, which is σ_V/σ_L = 0.95, the squat pillar has a deeper spalling depth on the walls compared with the slender pillar, whose σ_V/σ_L is 0.975. Due to the heterogeneities caused by the rough pillar walls and the geometry of the grains, the depths of spalling failure on both sides of the pillars are not symmetrical.

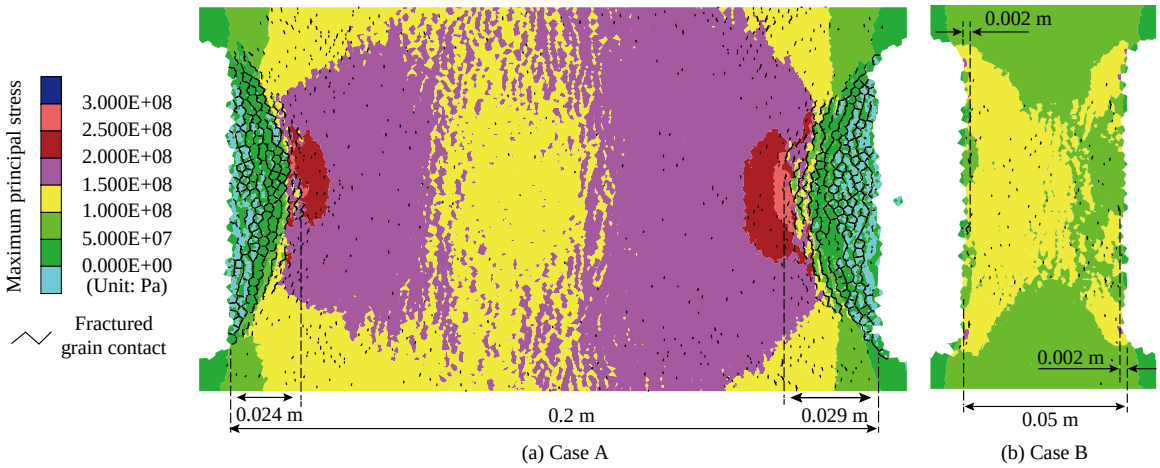

Figure 4-15. Depths of spalling for two pillars with different W/H ratios: (a) Case A with W/H = 2.0, σ_V =145 MPa, *t* = 3.0e5 s; (b) Case B with W/H = 0.5, σ_V = 105 MPa, *t* = 1.3e5 s.

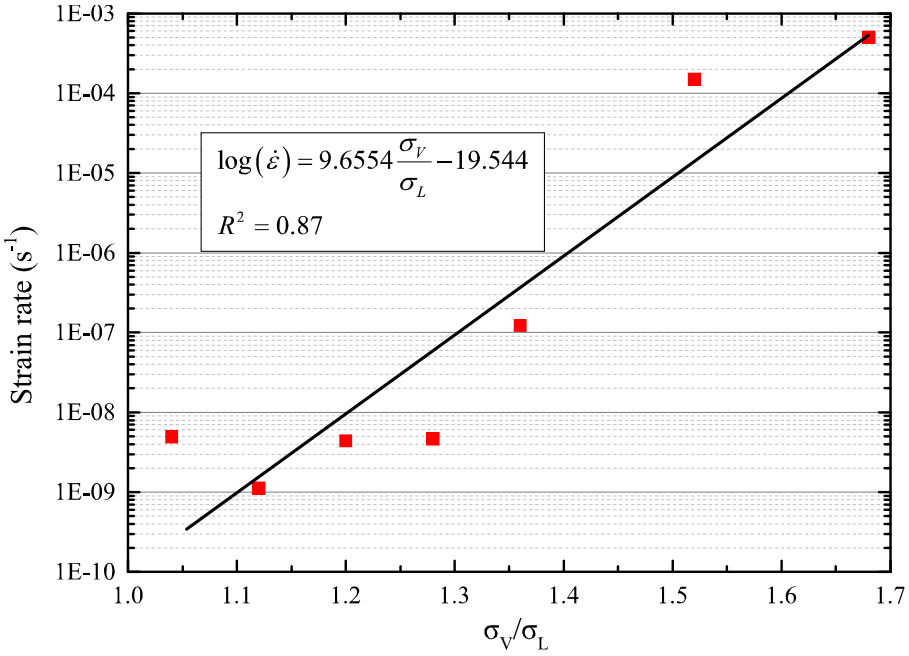

Figure 4-16. Exponential relation between creep strain rate and loading ratio σ_V/σ_L for the pillar model with W/H = 1.0.

When a pillar is loaded above its long-term strength, the vertical creep strain increases with time until the pillar fails. As can be seen in Figure 4-10, the higher the loading stress, the higher the creep strain rate is. The relation between the loading ratio σ_V/σ_L and the

average creep strain rate $\dot{\varepsilon}$ of the pillar model with W/H = 1.0 is presented in Figure 4-16. The loading ratios of these cases are larger than 1.0. It can be seen that the loading ratio σ_V/σ_L and the average creep strain rate $\dot{\varepsilon}$ fit an exponential function to within an order of magnitude.

4.3 Discussion

It is understood from the simulation results that the short-term strengths of the pillars increase with the increase of the W/H ratio, because a wider pillar provides more confinement to the pillar core (Kaiser et al., 2011). However, the increase of the long-term strength with the increase of the W/H ratio is small, even for squat pillars (Figure 4-11 and Figure 4-12). The reason is that the long-term strength, captured in the creep test simulations using the grain-based model, is controlled by gradual failure on the pillar walls. This time-dependent spalling depends on the geometry of a pillar. The results agree well with the result of Esterhuizen (2006), who stated that the pillar strength curve should be flat for squat pillars. Another reason why the pillar strength curve is flat for squat pillars is that the confinement enhancement due to the increase of the width of pillar is not unlimited. For example, Renani and Martin (2018) found that the confinement enhancement will not increase significantly with the increase of the W/H ratio for squat pillars when W/H is greater than 2.0 in their simulation. Hence, a rock pillar should be considered as a system as shown in Figure 4-17(a), in which the rocks on the pillar walls and in the pillar core have different failure patterns. The shear damage usually occurs in the pillar core, while the spalling damage occurs on the pillar wall. An example is given in Figure 4-17(b), in which the two types of damage are illustrated. According to the simulation results, the long-term

strength of a pillar is determined not only by the confinement to the core, but also by the development of the time-dependent spalling damage on the walls, which is influenced by the degree of stress concentration and the creep damage threshold of the rock on the pillar walls. In reality, spalling-failed rocks on the pillar walls will fall to the ground, exposing fresh pillar walls and reducing the effective W/H ratio. Compared with continuum modeling methods, this process can be better captured by DEM.

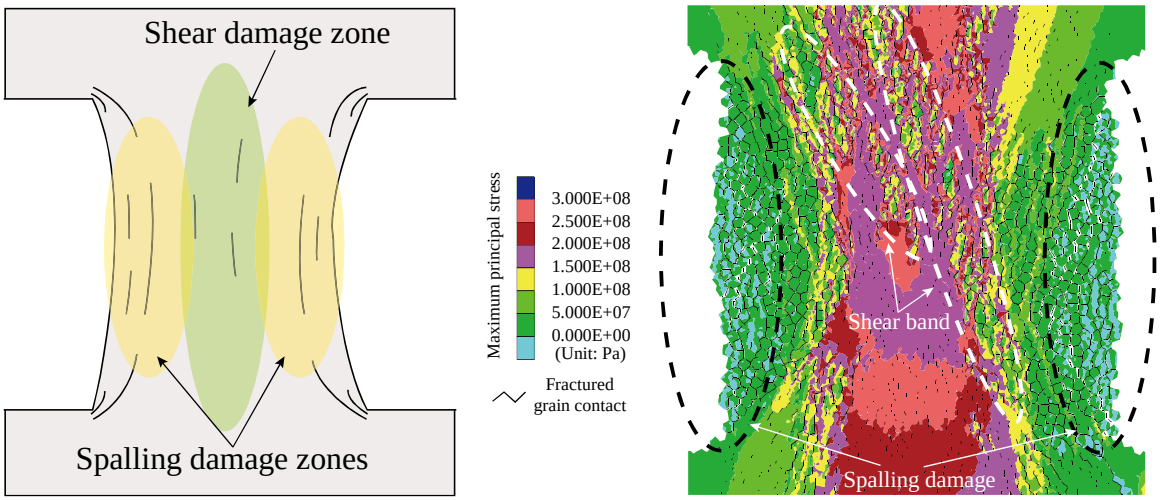

(a) (b)

Figure 4-17. Two types of damage that influence the long-term strength of a pillar: (a) schematic representation; (b) spalling and shear damages of pillar model R-1.0A with σ_V = 190 MPa and t = 29 s.

It is also observed that when the applied axial stress exceeds the long-term strength, the creep strain patterns for the slender and squat pillars are different. Even though those over-loaded pillars will ultimately collapse, the slender pillars experience a shorter stable creep deformation stage than the squat pillars (Figure 4-10). This agrees well with the result of King (1973), who used laboratory-scale pillar specimens of potash ore to conduct creep compression tests and found that pillars with a lower W/H ratio show abrupt brittle failure, while wider pillars show continuous deformation for a long time without failure. In other

words, an over-loaded slender pillar tends to fail abruptly and quickly, while the axial strain of an over-loaded squat pillar can be monitored continuously over a long period, which is helpful for pillar failure risk mitigation and ground control.

As shown in Figure 4-16, the creep strain rate of rock pillars is sensitive to the variation of loading stress. For example, even though the observed creep strain rate of a pillar is low when the applied loading slightly exceeds σ_L, due to stress increase caused by mining nearby the deformation of the pillar could increase rapidly if the applied stress is increased. As a result, the life time of slender pillars is largely influenced by the variation of loading stress. As shown in Figure 4-18, the life time of the pillar model with W/H = 0.5 has an exponential relation with the loading rate σ_V/σ_S, where σ_S is the short-term strength of the pillar. The trend of the data agrees with the static fatigue test results of Lajtai (1991), which were obtained using the rock specimens under uniaxial compression with W/H ratios around 0.5. It shows that a small variation of the vertical loading can influence the lifetime of the slender pillars significantly.

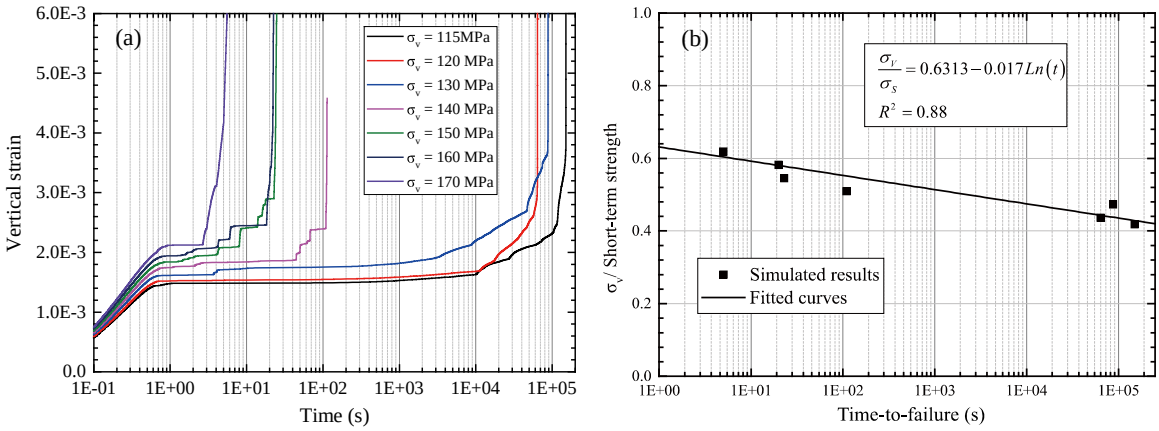

Figure 4-18. Time-to-failure of slender pillars with W/H = 0.5: (a) creep strain curves; (b) the relation between time-to-failure and loading ratio σ_V/σ_S.

In the short-term strength simulations, the failure process of the grain-based pillar models follows the five-stage failure patterns summarized by Roberts et al. (1998) (Figure 2-5). In the creep simulations, it is seen that time-dependent spalling starts by forming pillar wall sub-parallel cracks first and then the cracks gradually propagate from the surface to the pillar core. This again agrees well with field observations (Napier and Malan, 2012, Cording et al., 2015). In addition, the simulation results show that the normalized depth of spalling failure is larger for squat pillars (Figure 4-14).

The spalling limit (Kaiser et al., 2000) is commonly used to distinguish shear and spalling failures of rocks. For intact rock, the spalling limit is defined roughly by σ_1/σ_3 = 20 to 30 (Cai, 2010, Kaiser et al., 2000), and for jointed rock mass the limit is defined by σ_1/σ_3 = 5 to 10 (Cai et al., 2004a). The contour of σ_1/σ_3 for the pillar model with W/H = 2.0 at *t* = 0 s, which is the state of equilibrium before the creep calculation starts, is presented in Figure 4-19(b), and the spalling depth at *t* = 3.0e5 s is shown in Figure 4-19(a). It can be seen that the simulated depth of spalling agrees well with the estimate using the contour of the spalling limit of rock (σ_1/σ_3 = 30) at the start of creep loading.

This chapter presents a study of time-dependent spalling and deformation of pillars by simulating laboratory-scale rock samples with a pillar structure (King, 1973, Obert, 1965, Sun et al., 2020). The stress boundary conditions applied can be used to simulate an isolated pillar between two tunnels (Li et al., 2013, Chen et al., 2009). As to other types of pillars in underground mines, such as pillars in room and pillar mines, the implemented model and boundary conditions may not be suitable. However, this issue can be addressed by 3D modeling, which requires extremely long run times for the creep simulations. The time

span of the creep simulation is 1.5e5 s for pillar models with W/H = 0.5, 1.0 and 1.5. For the wider pillar model with W/H = 2.0, which has a lower creep strain rate, the time span is extended to 3.0e5 s to determine the long-term strength. Because the GBM pillar models are built with micro-scale structures shown in Figure 4-2, the creep simulations with longer time scales (e.g., several months and years) require extremely long run times. Creep simulations with a simplified modeling method need to be developed to address this issue.

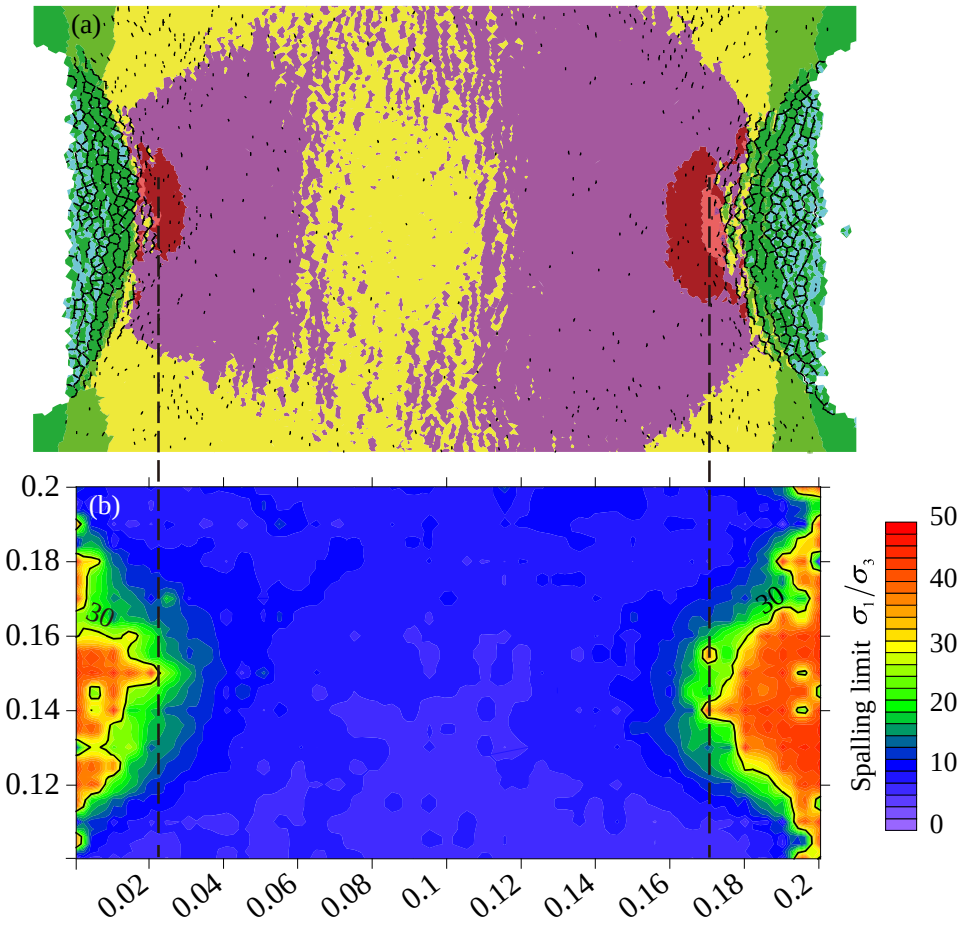

Figure 4-19. Spalling depth estimation using the spalling limit for the pillar model with W/H = 2.0, σ_V =145 MPa: (a) depth of spalling at *t* = 3.0e5 s; (b) contour of spalling limit σ_1/σ_3 at *t* = 0 s before creep calculation starts.

Size effect can also have a large impact on the results of the pillar models. Even though the strength of the grain-based material is calibrated using the test results of LdB granite, it is hard to up-scale the model parameters to a full-size pillar model if large grain sizes are used. In addition, no joints are considered in the pillar models. As a result, the strength of the laboratory-scale intact pillar model must be higher than the strength of the pillar in the field. Thus, only qualitative analysis is conducted in this study. Future research is needed to address these challenging issues.

Although the mechanical parameters of GBM-TtoF model are calibrated using uniaxial and triaxial compression tests of LdB granite, no creep test data of laboratory-scale pillar-shaped specimens could be found to validate the creep simulation results. When such experimental test data become available in the future, more work can be conducted to further validate the proposed creep model.

4.4 Summary and conclusion

Time-dependent spalling and deformation of rock pillars are investigated using laboratory-scale grain-based pillar models. Pillar models with different boundary profiles and W/H ratios are built, and time-dependent strengths and spalling of the pillars are simulated. The spalling mechanism and the deformation features of the rock pillars are discussed. The main conclusions can be drawn as follows:

The boundary profile has a small influence on the short-term strength, but a large influence on the long-term strength of the rock pillars. The time-dependent spalling phenomenon

observed in the field can be captured using the GBM-TtoF model with a rough boundary profile.

The long-term strengths of pillars are positively related to the W/H ratio. The simulation results indicate that the long-term strength will not increase significantly for squat pillars.

Gradual spalling damage is less likely to be observed in slender pillars even if they are loaded above the long-term strength. Squat pillars can tolerate more spalling damage on the walls without losing their stability. As a result, time-dependent spalling is often observed in squat pillars. For squat pillars, the depth of spalling can be estimated using the spalling limit.

An application of the GBM-TtoF model to simulate time-dependent deformation of rock pillars is presented in this chapter. The results show that the GBM-TtoF creep model is a useful tool for simulating creep deformation of intact rock. In the subsequent chapter, time-dependent deformations of rock joints will be investigated. Grain-based joint models will be established using the GBM-TtoF model. Shear creep simulations will be carried out using five lab-scale models with different joint roughness. A new creep model will be developed to describe the time-dependent responses of rock joints under different normal and shear loadings.

Chapter 5 A simplified model for time-dependent deformation of rock joints

5.1 Introduction

This Chapter presents a study of the creep mechanism of brittle rock joints under shear loading. Firstly, grain-scale joint models are established using the GBM-TtoF model to mimic the creep deformation of rock joints. Then, some major factors that influence the creep deformation of rock joints, such as normal stress, shear stress and joint roughness, are investigated numerically using the grain-scale joint models. Finally, a new strength degradation creep model for joints is introduced, which can be used to model time-dependent strength and deformation of flat joints in UDEC for engineering applications. Model is calibrated and validated using experimental data from the literature. A flowchart is presented in Figure 5-1 to illustrate the procedure of this study for the development of the joint creep-slipping model.

Main research findings presented in this chapter have been published in a paper entitled “A simplified model for time‐dependent deformation of rock joints” (Wang and Cai, 2021b).

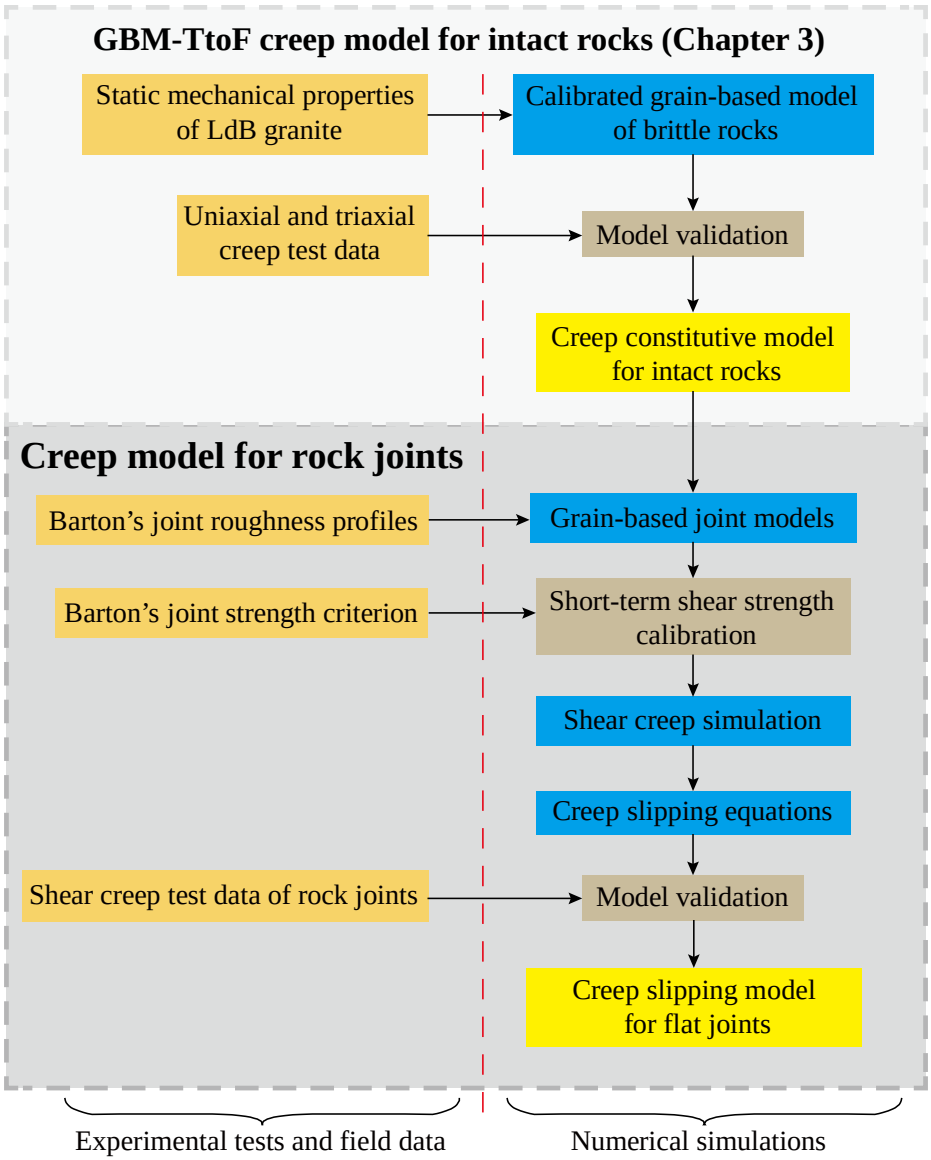

Figure 5-1. Flowchart of the joint creep-slipping model development.

5.2 Grain-scale model implementation

When investigating the mechanical responses of joints by numerical simulation, the meso-scale modeling method, which can establish the micro-structures of joint roughness, can be used to build joint models. Existing constitutive models of intact rock can be used to model the strength and time-dependent deformation of intact rock. In this way, the deformation

and damage that occur on the joint asperities can be captured (Bahaaddini et al., 2016). The resulting deformation behavior of the model represents the behavior of a rock joint.

According to the Barton's shear strength criterion of rock joints (Barton et al., 1985, Bandis et al., 1981), the joint roughness (measured using joint roughness coefficient (*JRC*)) and the joint wall compressive strength (*JCS*) are two important factors that influence the short-term shear strength of unweathered clean rock joints. For joints under creep loading, time-dependent deformations of asperities also influence the long-term strength and deformation of joints (Zhang et al., 2019, Wang et al., 2015). Thus, five joint models with realistic joint profiles are established in UDEC to represent the geometry of joint asperities, as shown in Figure 5-2(a) and (b).

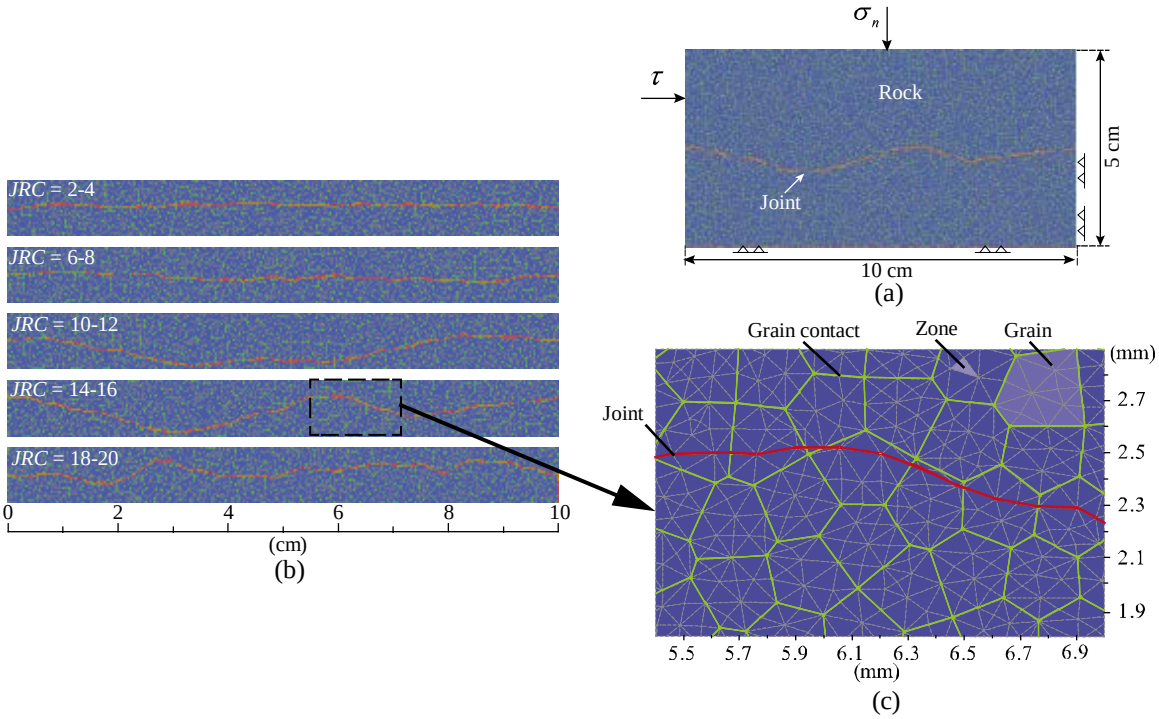

Figure 5-2. (a) Shear model of joint implemented in UDEC; (b) five grain-scale joint models based on Barton's standard joint profiles; (c) enlarged view of microstructure of asperities along the joint surface for *JRC* = 14 – 16.

The rock of the joint walls are modeled using the GBM-TtoF model developed in Chapter 3, and an enlarged view of the joint walls is shown in Figure 5-2(c). The degradation parameters which are calibrated using laboratory static fatigue test data are used in this Chapter to model the time-dependent deformation behavior of LdB granite joints.

The creep deformation and failure of joints with joint asperities are governed by the creep model of rock, i.e., the GBM-TtoF model. In this manner, the time-dependent deformation behavior of joints is controlled by the mechanical response of grains and the geometry of grains representing the joint asperities. Sliding and static fatigue of joint asperities can be presented at the grain-scale level in the simulation.

The micro-parameters of the GBM-TtoF models are calibrated using static fatigue experimental data of LdB granite which is introduced in Chapter 3. As mentioned above, Barton's standard joint roughness profiles (Barton and Choubey, 1977) are adopted to build surface waviness of the joints in the grain-scale joint models. The length of the contact elements of the joint is defined as small as possible. In this simulation, the contact length of 1.5e-3 m is adopted, which equals the average size of the zones in the grains of the GBM-TtoF model (Figure 5-2 (c)).

5.3 Short-term shear strength calibration

According to the Barton's non-liner shear strength model of rock joints, there is no cohesion between clean joint walls. The friction angle of an unweathered rock joint consists of two parts (Eq. (5.1)): one is the basic friction angle ϕ_b^j, which is determined by the friction angle of saw-cut smooth joint walls; the other is the dilation angle, which is

influenced by normal stress σ_n, *JCS* and *JRC*. For unweathered fresh joints of LdB granite, the basic friction angle ϕ_b^j is equal to 30° ± 2° (Barton et al., 1985, Alejano et al., 2012) and the *JCS* is equal to the *UCS* of 225 MPa (Schmidtke and Lajtai, 1985). The mechanical parameters of the grain-scale joint model are calibrated according to the Barton's strength criterion shown below:

$$\tau_S = \sigma_n \tan\left[JRC \log\left(\frac{JCS}{\sigma_n} \right) + \phi_b^j \right], \tag{5.1}$$

where the τ_S is the short-term shear strength of joint and *JCS* is the joint wall compressive strength.

As shown in Figure 5-2 (c), the macro-joint in the grain-scale joint model has many contact elements, the strength of which is assumed to follow the Mohr–Coulomb strength criterion. There are six mechanical parameters for the contact elements, which are cohesion c^{j-c}, friction angle ϕ^{j-c} (ϕ^{j-c} is a micro-parameter which is not the basic friction angle ϕ_b^j of the macro-joint), tensile strength σ_t^{j-c}, dilation angle i^{j-c}, shear stiffness Jks^{j-c}, and normal stiffness Jkn^{j-c}. Because a joint has no cohesion, c^{j-c} and σ_t^{j-c} are equal to zero. Because the grain-scale joint models are established using actual joint roughness profiles, dilation in the normal direction during shear deformation is driven by the waviness of the joint walls. Hence, the dilation angle of the joint element i^{j-c} is equal to zero. The initial values of Jks^{j-c} and Jkn^{j-c} are equal to those of the contacts of the grains. The initial value of the friction angle ϕ^{j-c} is equal to 30°.

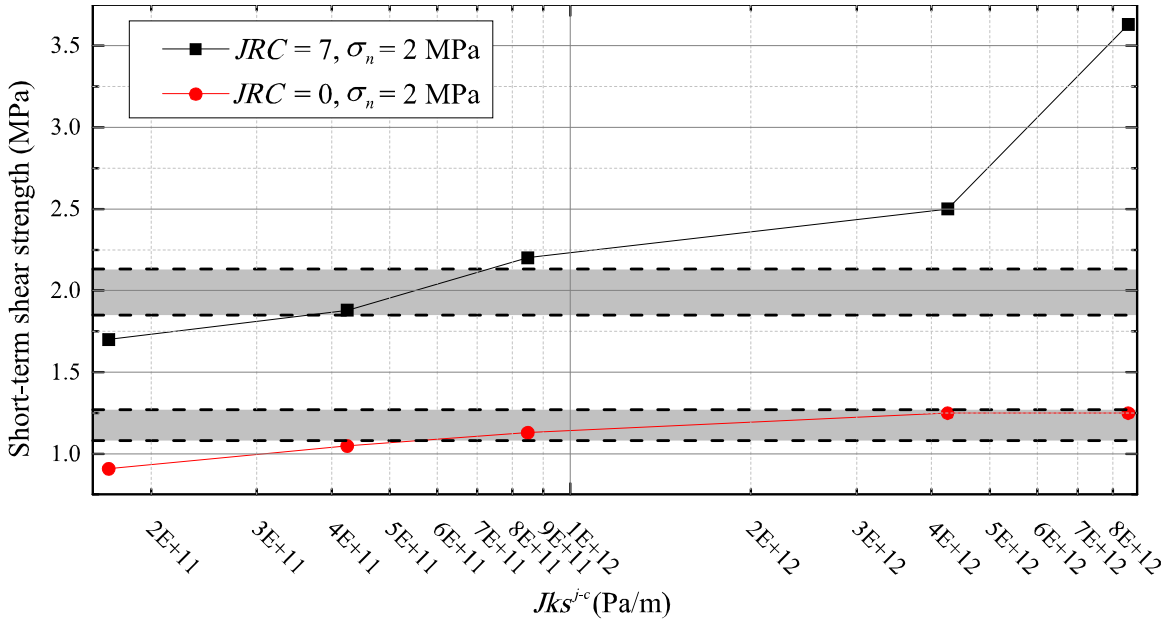

Figure 5-3. Influence of Jks^{j-c} on the short-term shear strength of joints with different roughness. The gray region indicates the shear strengths calculated from Eq. (5.1) with the basic friction angle ϕ_b^j = 30° ± 2°.

According to the results of a parameter study that was carried out, it is seen that both Jks^{j-c} and ϕ^{j-c} influence the short-term shear strength of a joint, the degree of which is governed by the joint roughness. Figure 5-3 presents the results for two joints with different roughness (*JRC* = 0 and 7) under a normal stress of 2 MPa. The short-term strength increases as Jks^{j-c} increases. For these two models, the friction angle of the joint contact elements ϕ^{j-c} is 30.5°. Figure 5-4 shows the influence of contact friction angle ϕ^{j-c} on the short-term shear strength of flat joints (*JRC* = 0) with Jks^{j-c} = 8.5e11 Pa/m. The gray region indicates the shear strengths calculated from Eq. (5.1) with the basic friction angle ϕ_b^j = 30° ± 2°. As illustrated in these two figures, the friction angle ϕ^{j-c} is the key parameter that controls the shear strength of a flat joint (*JRC* = 0). For a rough joint (*JRC* = 7), both ϕ^{j-c} and Jks^{j-c} influence the shear strength of the joint.

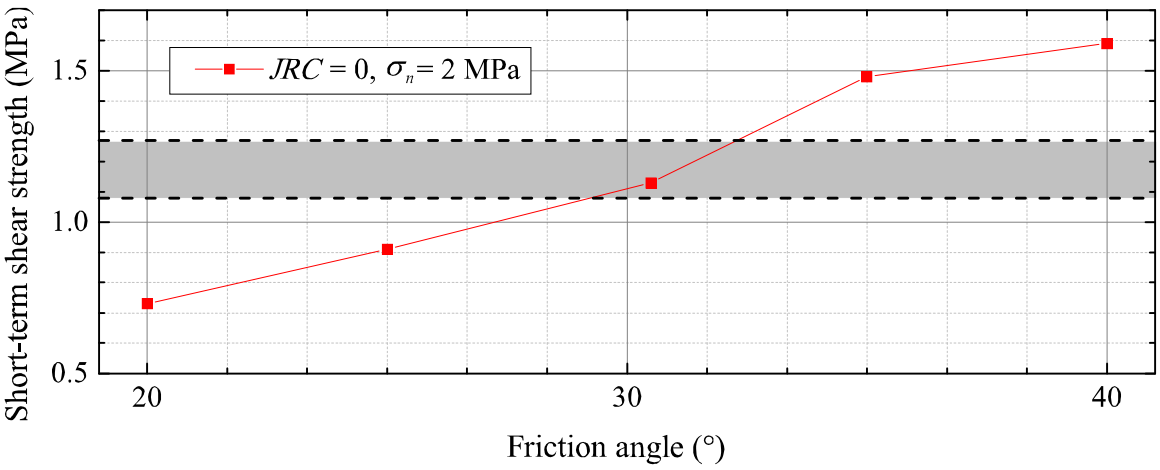

Figure 5-4. Influence of friction angle of contact elements on the short-term shear strength of flat joints. The gray region indicates the shear strengths calculated from Eq. (5.1) with the basic friction angle ϕ_b^j = 30° ± 2°.

The final values of Jks^{j-c}, Jkn^{j-c} and ϕ^{j-c} are determined following the process shown in Figure 5-5. First, the friction angle ϕ^{j-c} is determined by the shear test simulation using a flat joint model (*JRC* = 0). Then, the Jks^{j-c} values are determined by shear test simulations using the rough joint models (*JRC* = 3, 7, 11, …). A few iterations are necessary to obtain satisfactory results.

The calibrated shear strengths of the five joint models are presented in Figure 5-6, which agree well with the strengths defined by Barton's model. In the simulations, the fitted basic friction angle of LdB granite is 30.5°. The parameters of the contact elements of the joints are summarized in Table 5-1.

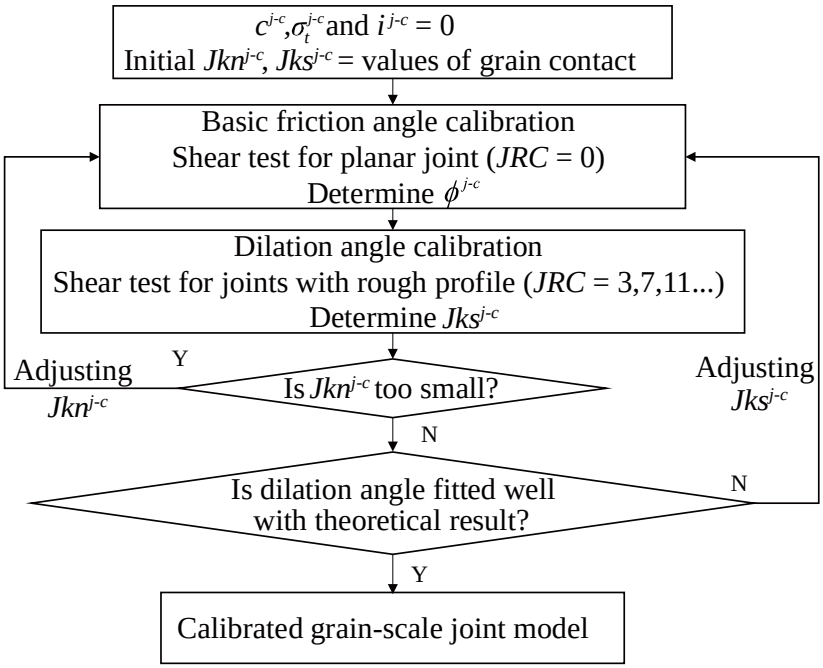

Figure 5-5. Flowchart showing the short-term shear strength calibration process.

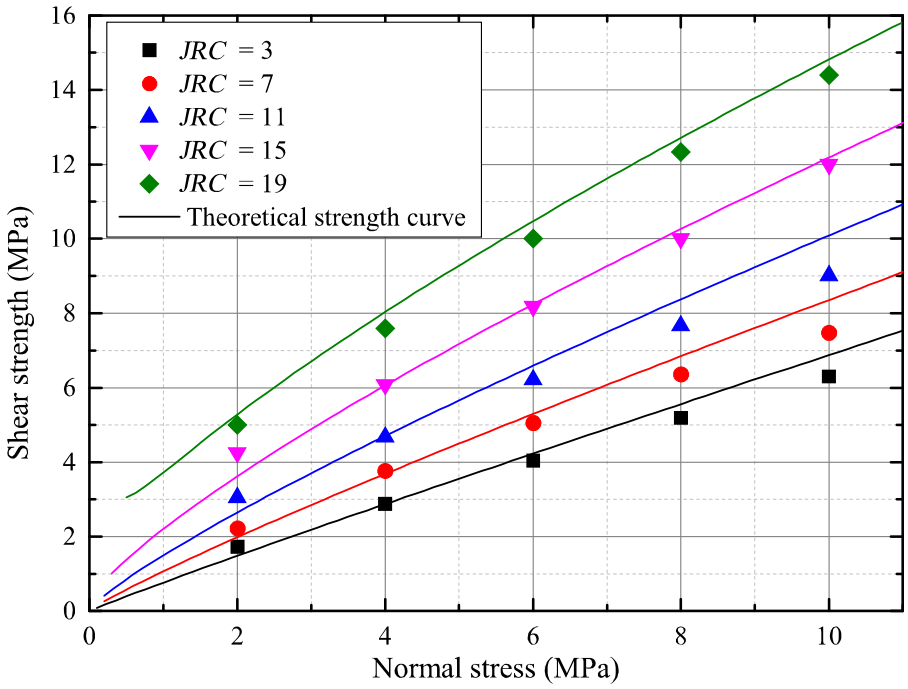

Figure 5-6. Calibrated results of short-term shear strength of five joint models with different roughness.

Table 5-1. Calibrated micro-parameters of contact elements of joint

Micro-parameters	Value
Shear stiffness of contact elements on joint surface, Jks^{j-c} (Pa/m)	8.5e11
Normal stiffness of contact elements on joint surface, Jkn^{j-c} (Pa/m)	8.8e14
Friction, ϕ^{j-c} (°)	30.5
Cohesion, c^{j-c} (MPa)	0
Tensile strength, σ_t^{j-c} (MPa)	0
Dilation angle, i^{j-c} (°)	0

5.4 Numerical simulation of joint creep under shear loading

5.4.1 Long-term shear strength

When loaded under constant normal and shear stresses, time-dependent deformation behaviors of joints are different under low and high shear loading ratios τ/τ_S, where τ is the shear stress and τ_S is the short-term shear strength of a joint. According to Bowden and Curran (1984)'s experimental results shown in Figure 2-9 (a) and (b), the creep deformation will stop eventually if the applied shear stress is below a threshold. If the applied shear stress is beyond the threshold, the joint will keep slipping at a relatively constant speed. If the ratio of the long-term (τ_L) to the short-term (τ_S) shear strengths is referred as the long-term shear strength ratio ξ, defined in Eq. (5.2), the ξ value is about 0.9 for Bowden and Curran (1984)'s experimental results (Figure 2-9 (a) and (b)).

$$\xi = \frac{\tau_L}{\tau_S}, \tag{5.2}$$

According to the test results of unfilled rock joints, the long-term shear strength ratio ξ is equal to 0.3 to 0.6 for joints of soft rock (Zhang et al., 2012), 0.7 to 0.9 for joints of brittle hard rock (He et al., 2019, Bowden and Curran, 1984). For the same rock type, the long-term shear strength of joints is largely influenced by two factors – joint roughness and normal stress. Currently, it is still not clear how the ξ values are influenced by these two factors. Thus, to improve the understanding of this issue, shear creep simulations are conducted using the five grain-scale joint models (*JRC* = 3, 7, 11, 15 and 19) under different normal stresses (σ_n = 2, 4 and 8 MPa).

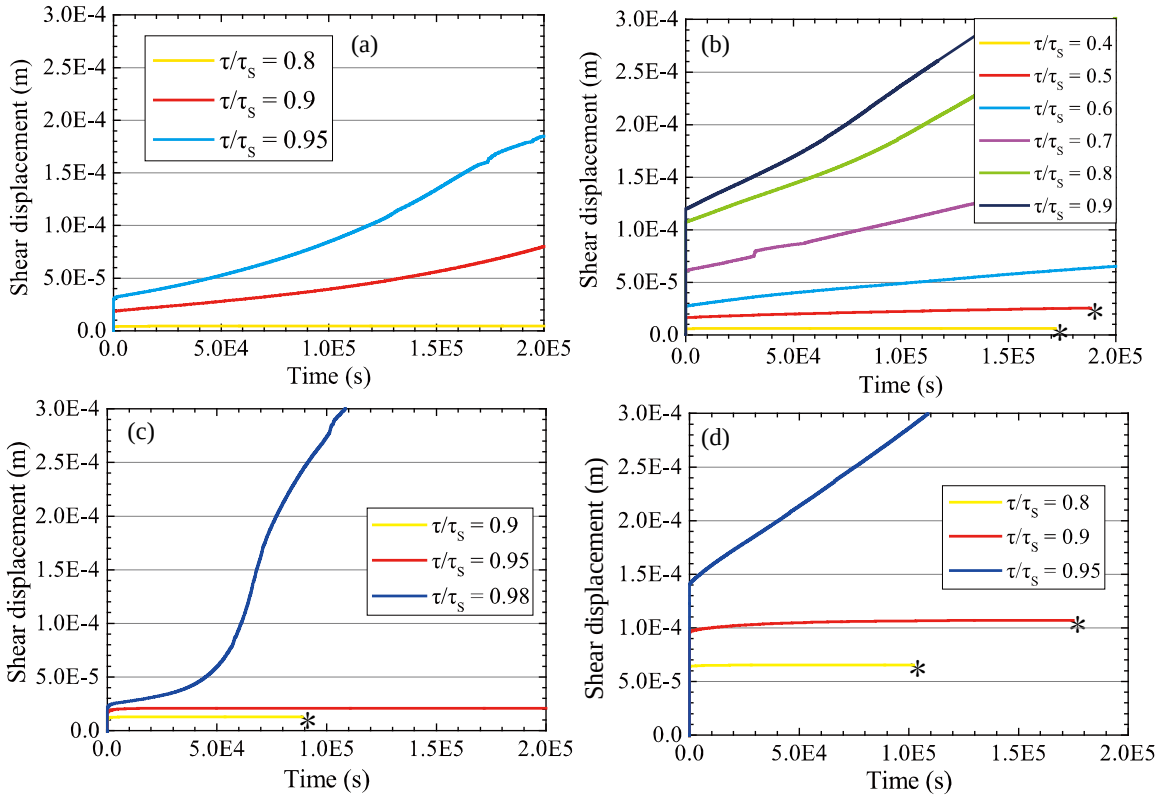

Figure 5-7. Simulated creep strain curves of joints under different τ/τ_S ratio: (a) joint with *JRC* = 3, σ_n = 2 MPa; (b) joint with *JRC* = 19, σ_n = 2 MPa; (c) joint with *JRC* = 3, σ_n = 8 MPa; (d) joint with *JRC* = 19, σ_n = 8 MPa. * means that the simulation is stopped by user.

Figure 5-7 presents the simulated creep strain curves of two joints (*JRC* = 3 and 19) under low (σ_n = 2 MPa) and high (σ_n = 8 MPa) normal stresses. It can be seen that the ξ values are equal to 0.850, 0.550, 0.975 and 0.925 for the cases shown in Figure 5-7(a), (b), (c) and (d), respectively. The trial and error method is used to determine ξ. When the shear loading ratio τ/τ_S exceeds ξ, the joint slips at a constant velocity. The slipping of a joint will stop if the shear loading ratio τ/τ_S is smaller than ξ. The average of the two shear loading ratios is determined as the long-term shear strength ratio ξ.

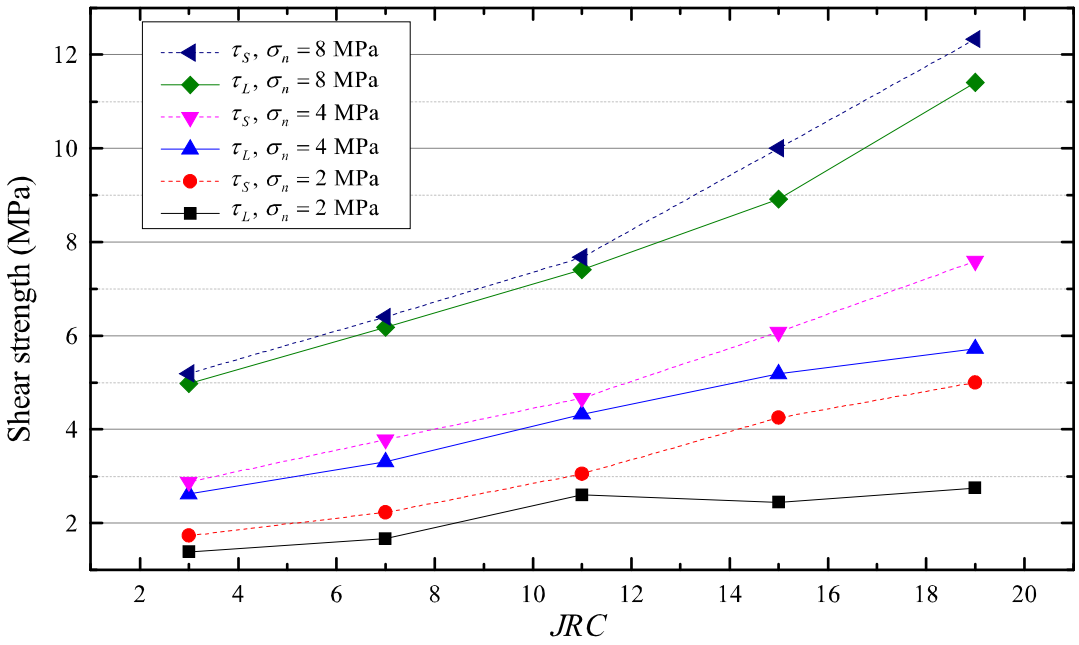

Figure 5-8. Influence of *JRC* and σ_n on the long-term shear strength of a joint.

The long-term shear strength ratio ξ depends on the normal stress and the *JRC* value. As shown in Figure 5-7 (a) and (c), for the joint with *JRC* = 3, the ξ value increases from 0.850 to 0.975 when the normal stress increases from 2 to 8 MPa. For the joint with *JRC* = 19, the ξ value increases from 0.550 to 0.925 when the normal stress increases from 2 to

8 MPa. The roughness also influence the ξ value. When the *JRC* values increase from 3 to 19 under the normal stress of 2 MPa, the ξ values decrease from 0.925 to 0.550 (Figure 5-7(a) and (b)).

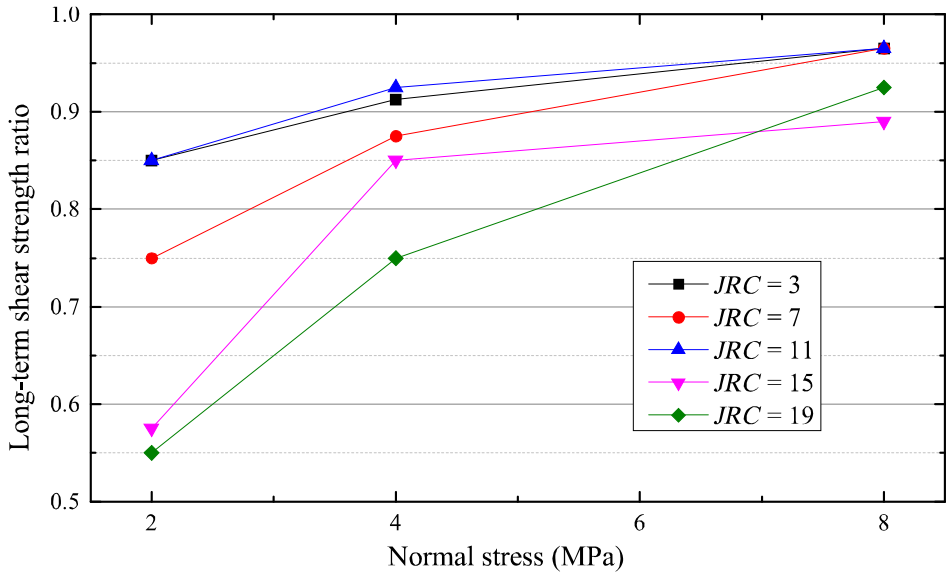

Figure 5-9. Influence of σ_n on the long-term shear strength ratio.

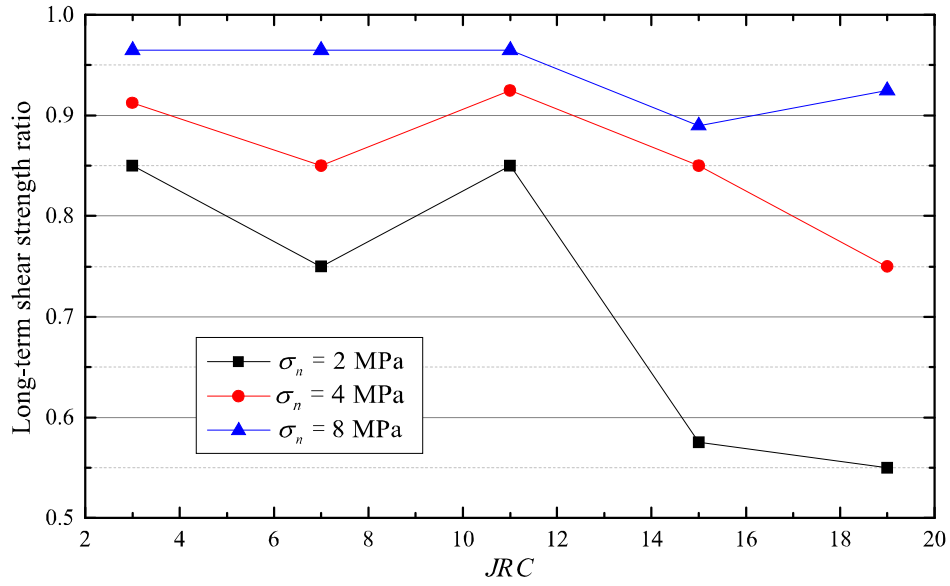

Figure 5-10. Influence of *JRC* on the long-term shear strength ratio.

It is easy to understand that both the σ_n and *JRC* have a positive correlation with the long-term (τ_L) and short-term (τ_S) shear strengths (Figure 5-8). However, the influence of σ_n and *JRC* on the long-term shear strength ratio ξ is complex. Figure 5-9 and Figure 5-10 present the simulated results of the five joint models. Figure 5-9 shows that the long-term shear-strength ratio ξ has a positive correlation with σ_n, especially for joints with rough profiles (*JRC* = 15 or 19). The ξ value is more sensitive to the normal stress. On the other hand, ξ tends to have a negative correlation with *JRC*, as illustrated in Figure 5-10. Although not very strong, the negative correlation can be observed. For example, ξ increases when *JRC* increase from 7 to 11 for σ_n = 4 MPa. The fluctuations result from the variation of the strength properties of joints due to the randomness of the Voronoi grain geometry. The negative correlation between *JRC* and ξ is also observed in the laboratory test results of Wang et al. (2017a) who used artificial concrete joints in their tests.

The influence of the *JRC* and normal stress on the long-term shear strength ratio ξ of rock joints can be explained using Barton's joint shear-strength model to consider what proportion of the shear strength from the joint asperity is used to resist creep slipping. According to Barton's model shown in Figure 5-11, after the peak strength is reached in static-shear tests, the roughness of joints is lost continuously with the increase of shear displacement. This part of the roughness is called JRC_{mob}, which is approximately 50% of the initial *JRC* when the post-peak shear displacement reaches 10 times of the displacement at the peak strength, i.e.,

$$\frac{JRC_{mob}}{JRC} \approx 0.5, \tag{5.3}$$

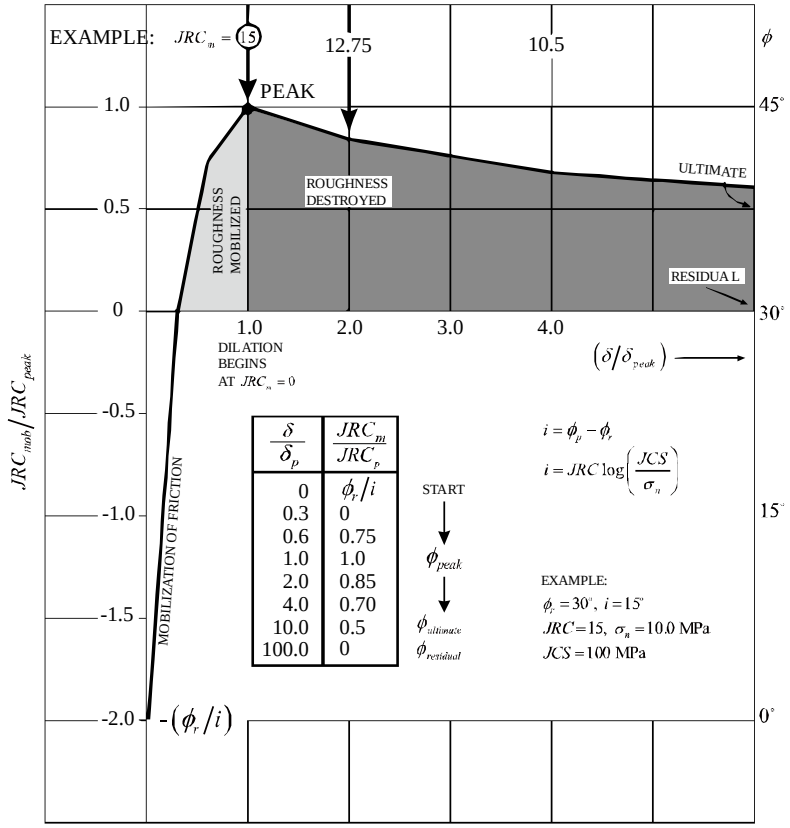

Figure 5-11. JRC_{mob} concept developed by Barton et al. (1985).

The decrease of the joint friction angle ϕ_{mob} due to the destruction of the roughness can be calculated using

$$\phi_{mob} = JRC_{mob} \log\left(\frac{JCS}{\sigma_n}\right), \tag{5.4}$$

Similar to that in the static shearing (Figure 5-12(a)), the degradation of joint asperities is also a major form of joint failure in creep deformation, as illustrated in Figure 5-12(b). The roughness degradation is quite obviously in the simulation using the grain-scale joint

models, as illustrated in Figure 5-12(c) and (d) using the damage-index contours to show the strength degradation of grains along the joint surfaces. Thus, it can be assumed that the maximum amount of roughness loss due to creep fatigue is also limited to a proportion of the initial roughness even after a long time, in a similar form as the roughness loss under static loading presented in Eq. (5.3). Hence, the maximum roughness loss that can occur in the creep fatigue process, JRC_{c-mob}, is assumed to be related to the initial *JRC* as

$$\frac{JRC_{c-mob}}{JRC} \approx cons, \tag{5.5}$$

where *cons* is a constant between 0 and 1.

For two joints (Joint I and Joint II) with different initial roughness with

$$JRC^{I} > JRC^{II}, \tag{5.6}$$

and if they are loaded under the same normal stress, according to Eqs. (5.1), (5.2) and (5.4), the long-term shear strength ratio ξ of Joint I can be calculated by

$$\xi^{I} = \frac{\left(JRC^{I} - JRC^{I}_{c-mob}\right)\log\left(\frac{JCS}{\sigma_n}\right) + \phi_b^j}{JRC^{I}\log\left(\frac{JCS}{\sigma_n}\right) + \phi_b^j}, \tag{5.7}$$

The long-term shear strength ratio ξ^{II} of Joint II can be calculated in the same way. Then, according to Eqs. (5.5), (5.6) and (5.7), we have

$$\xi^{I} < \xi^{II}, \tag{5.8}$$

which means that for a joint with a larger initial *JRC* value, it has a lower long-term shear strength ratio ξ.

The positive correlation between normal stress and ξ can also be explained. For example, if one joint is loaded under different normal stresses, which are denoted as σ_n^I and σ_n^{II} with

$$\sigma_n^I > \sigma_n^{II}, \tag{5.9}$$

then the long-term shear strength ratio of case I, which is referred as ξ^I, can be obtained from

$$\xi^I = \frac{\left(JRC - JRC_{c-mob}\right)\log\left(\frac{JCS}{\sigma_n^I}\right) + \phi_b^j}{JRC\log\left(\frac{JCS}{\sigma_n^I}\right) + \phi_b^j}, \tag{5.10}$$

For case II, the ξ^{II} value can be calculated similarly. Finally, according to Eqs. (5.5), (5.9) and (5.10), we have

$$\xi^I > \xi^{II}, \tag{5.11}$$

which means that the higher the normal stress is, the higher the long-term shear strength ratio ξ will be.

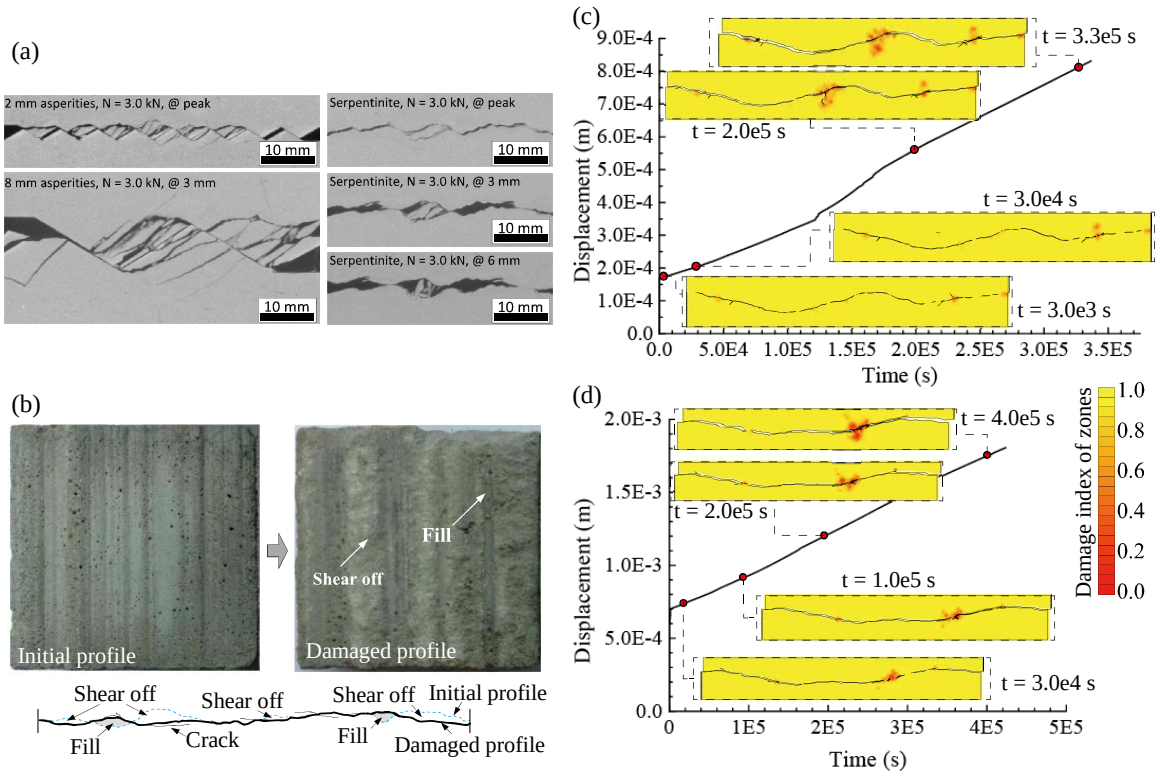

Figure 5-12. Asperity destruction observed in shear experiments: (a) asperity damage occurring in a static shear test (Tatone, 2014); (b) roughness damage due to static fatigue under shear, after Wang (2017b); (c) damage index contours in creep simulation for a joint with *JRC* = 15, σ_n = 4 MPa, and τ/τ_S = 0.95; (d) damage index contours in creep simulation for a joint with *JRC* = 11, σ_n = 4 MPa, and τ/τ_S = 0.95.

The analysis above presents a message that normal stress has more influence on the long-term stability of joints than roughness. For two joints with different roughness, they both may have lower long-term strengths if the rougher joint is loaded at a lower normal stress. For example, the long-term shear strengths are around 2.8 MPa for the joint models with *JRC* = 19, σ_n = 2 MPa, *JRC* = 3, σ_n = 4 MPa (Figure 5-8). A higher normal stress increases not only the long-term shear stress but also the long-term shear stress ratio (Figure 5-9 and Figure 5-10). Thus, a sufficiently high normal stress is needed to enable the asperities of rough joints to resist creep slipping under shear.

5.4.2 Creep deformation of joints

Three creep stages, i.e., initial, secondary and tertiary creeps, are commonly observed in creep experiments on rock. However, both experimental test and numerical simulation results (Figure 2-9 and Figure 5-7) reveal that the creep deformation of rock joints is very different from that of rock. A joint will slip at a relatively constant velocity if the applied shear stress is beyond its long-term shear strength. The higher the applied shear stress is, the larger the sliding velocity will be.

The sliding velocities obtained from the creep simulation are summarized in Table 5-2. For strain curves shown in Figure 5-7(a), (b) and (d), the sliding velocities, which are estimated using the average value from 0 to 1.5e5 s, are relatively stable. For the strain curves shown in Figure 5-7 (c), the sliding velocities are calculated using the part of the strain curves from 6.0e4 to 8.0e4 s.

It is seen that the shear loading ratio, the normal stress, and the *JRC* value all influence the sliding velocity. As shown in Figure 5-13, for joint models that are loaded with the same shear loading ratio, the creep sliding velocity is negatively correlated with the applied normal stress (Figure 5-13(c) and (d)) and positively correlated with the *JRC* value (Figure 5-13(a) and (b)).

The variation of the sliding velocity tends to be related to the long-term shear strength ratio ξ. On the one hand, as mentioned in Section 5.4.1, a larger *JRC* will decrease the long-term shear strength ratio of the joint. A rougher joint tends to slide faster under the same stress loading ratio. On the other hand, a higher normal stress will increase the long-term

shear strength ratio ξ significantly. The negative correlation between σ_n and the sliding velocity is observed under the same stress loading ratio.

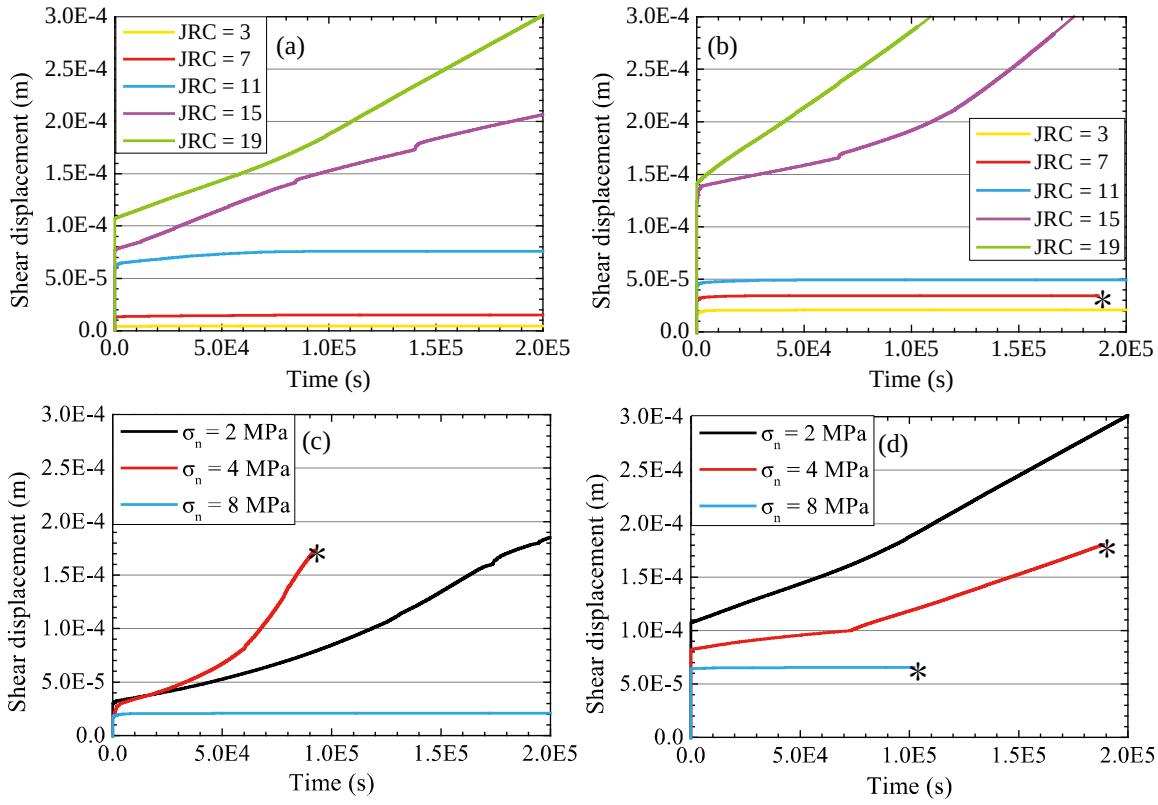

Figure 5-13. Creep strain curves of joints under the same loading stress ratio: (a) joints with different roughness for σ_n = 2 MPa, τ/τ_S = 0.8; (b) joints with different roughness for σ_n = 8 MPa, τ/τ_S = 0.95; (c) joint with *JRC* = 3, τ/τ_S = 0.95; (d) joint with *JRC* = 19, τ/τ_S = 0.8. * means that the simulation is stopped by the user.

Table 5-2. Loading condition and simulated deformation features of grain-scale models

JRC	σ_n (MPa)	τ_S (MPa)	ϕ^j (°)	τ/τ_S	τ (MPa)	Simulated ξ	Simulated $\dot{\varepsilon}$ (h^{-1})	*Predicted ξ	*Predicted $\dot{\varepsilon}$ (h^{-1})
3	2.00	1.63	39.15	0.80	1.30	0.85	–	0.89	–
			39.15	0.90	1.47		9.00e-6		1.37e-5
			39.15	0.95	1.55		2.50e-5		3.87e-5
	4.00	2.88	35.75	0.90	2.59	0.91	–	0.97	–
			35.75	0.93	2.66		3.60e-6		9.13e-6
			35.75	0.95	2.74		2.74e-5		2.37e-5
	8.00	5.16	32.85	0.95	4.91	0.97	–	0.99	–
			32.85	0.98	5.06		1.98e-4		3.75e-5
7	2.00	2.23	48.06	0.70	1.56	0.75	–	0.71	–
			48.06	0.80	1.78		1.80e-5		7.57e-6
			48.06	0.90	2.00		4.44e-5		2.62e-5
			48.06	0.95	2.11		5.22e-5		6.05e-5
	4.00	3.78	43.35	0.80	3.02	0.85	–	0.89	–
			43.35	0.90	3.40		7.92e-5		1.51e-5
			43.35	0.95	3.59		5.63e-5		4.28e-5
	8.00	6.40	38.64	0.95	6.08	0.97	–	0.97	–
			38.64	0.98	6.27		6.66e-5		4.14e-5
11	2.00	3.06	56.86	0.80	2.45	0.85	–	0.62	–

JRC	σ_n (MPa)	τ_S (MPa)	ϕ^j (°)	τ/τ_S	τ (MPa)	Simulated ξ	Simulated $\dot{\varepsilon}$ (h^{-1})	*Predicted ξ	*Predicted $\dot{\varepsilon}$ (h^{-1})
11	4.00	4.69	56.86	0.90	2.76	0.93	5.40e-5	0.80	1.63e-5
			56.86	0.95	2.91		6.99e-5		4.60e-5
			49.55	0.90	4.22		–		–
			49.55	0.95	4.46		7.20e-5		2.30e-5
	8.00	7.71	43.94	0.95	7.32	0.97	–	0.94	–
			43.94	0.98	7.56		3.24e-5		4.45e-5
15	2.00	4.28	64.97	0.55	2.36	0.58	–	0.58	–
			64.97	0.60	2.57		6.30e-6		3.04e-6
			64.97	0.70	3.00		1.53e-5		9.06e-6
			64.97	0.80	3.43		2.34e-5		1.82e-5
			64.97	0.90	3.85		2.64e-5		4.38e-5
	4.00	6.12	56.85	0.80	4.90	0.85	–	0.73	–
			56.85	0.90	5.51		2.88e-5		1.72e-5
			56.85	0.95	5.82		8.28e-5		4.86e-5
	8.00	10.07	51.54	0.88	8.86	0.89	–	0.90	–
			51.54	0.90	9.06		9.60e-6		7.69e-6
			51.54	0.95	9.57		2.83e-5		3.77e-5
			51.54	0.98	9.87		4.32e-5		1.15e-4
19	2.00	5.07	68.47	0.50	2.54	0.55	–	0.55	–

JRC	σ_n (MPa)	τ_S (MPa)	ϕ^j (°)	τ/τ_S	τ (MPa)	Simulated ξ	Simulated $\dot{\varepsilon}$ (h^{-1})	*Predicted ξ	*Predicted $\dot{\varepsilon}$ (h^{-1})
19	4.00	7.65	68.47	0.60	3.04	0.75	7.20e-6	0.68	4.50e-6
			68.47	0.70	3.55		1.68e-5		1.04e-5
			68.47	0.80	4.06		3.26e-5		2.01e-5
			68.47	0.90	4.56		4.44e-5		4.76e-5
			62.40	0.70	5.36		–		–
			62.40	0.80	6.12		1.78e-5		8.99e-6
			62.40	0.90	6.89		4.68e-5		3.12e-5
	8.00	12.43	57.23	0.90	11.19	0.93	–	0.87	–
			57.23	0.95	11.81		5.18e-5		2.54e-5

*Predicted values are calculated using Eqs. (5.12) and (5.13).

It is concluded that compared with joint roughness, confinement (normal stress) is a more important factor that influences joint-creep deformation. For a given rock mass structure, adding and preserving confinement can slow down creep deformations of discontinuities, thereby prolonging the lifetime of the structure.

In engineering design analysis, it is impractical to conduct grain-scale numerical analysis considering the details of joint surface profiles. In the next section, a macroscopic creep-slipping model for rock joints, which can be used to simulate joint-creep deformation in conventional numerical models that consider joints a planar feature explicitly, is proposed.

5.5 A creep-slipping model of rock joints

5.5.1 Creep deformation formulas

Based on the simulation results presented above, it is seen that joint roughness (*JRC*), shear loading ratio (τ/τ_S) and long-term shear strength ratio (ξ) are the three major factors that influence the sliding velocity of a joint. Thus, a creep-slipping model is proposed to estimate the sliding velocity, which is expressed as

$$\dot{\varepsilon} = C_j \cdot \log\left(10 + JRC\right) \cdot \frac{\tau/\tau_S - \xi}{1 - \tau/\tau_S}, \tag{5.12}$$

where the $\dot{\varepsilon}$ is the shear strain rate (unit: h^{-1}) of joint (the shear strain is equal to shear displacement divided by the length of the joint), C_j is a dimensionless parameter which is used to balance the influence of loading rate (for both normal and shear stresses) (Tang and Wong, 2016), rheological properties of rock, and filling materials (Malan, 1998) on the

shear strain rate. C_j can be expressed as $C_j = C_1 10^{C_2}$, and it ranges from 1 to 10 and can be determined by fitting experimental data; C_2 is the order of the tested creep strain rate of rock joints.

Figure 5-14 and Table 5-2 present the simulation results and the predicted value of $\dot{\varepsilon}$ using Eq. (5.12). In Figure 5-14, each point represents different simulation cases with different input parameters (i.e., *JRC*, normal stress and shear loading ratio), in which the x-axis represents the predicted results using Eq. (5.12) (where C_j is equal to 5.5e-6) and the y-axis represents the simulated results using the grain-scale joint model. A line $y = x$ is drawn as a reference. If the data points are closer to the reference line, it means that the predicted $\dot{\varepsilon}$ agrees well with the simulated result.

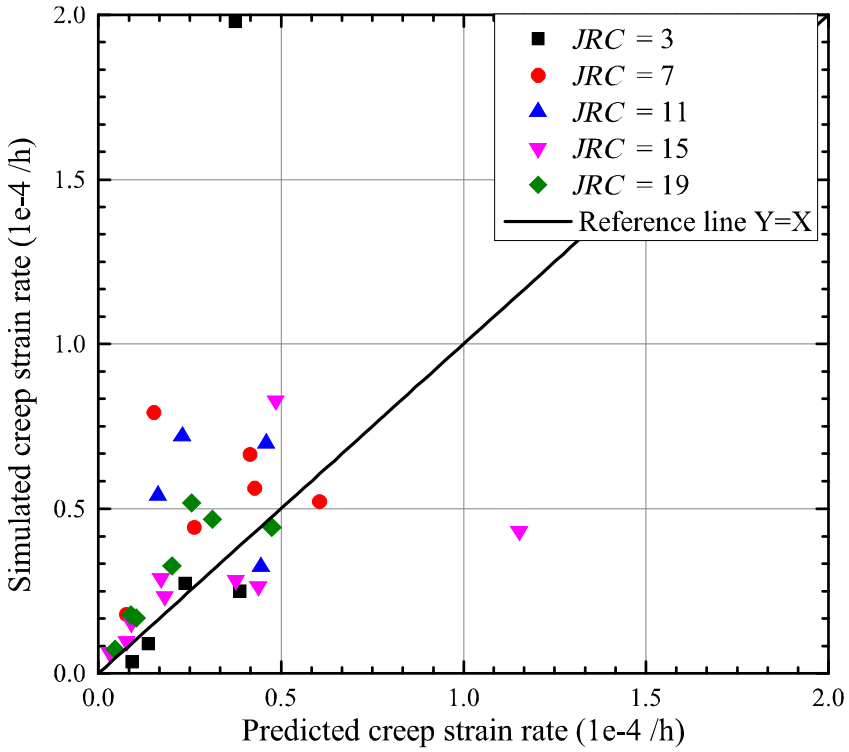

Figure 5-14. Simulated vs. predicted results of creep strain rates.

In addition to the validation using the simulation results of the grain-scale joint models, published data is also adopted to validate the proposed model (Eq. (5.12)). All available shear creep test data of rock joint from published literatures is collected. Key information including short-term shear strength, *JRC* value, normal stress, shear loading ratio, sliding velocity and long-term shear strength ratio are listed in Table 5-3. These data are used to validate Eq. (5.12). As shown in Figure 5-15, the x-axis presents the predicted results using Eq. (5.12), while the y-axis presents the experimental data. Data from the six datasets distribute near the reference line $y = x$, indicating that the proposed equation is able to predict the creep sliding velocity of joints fairly well.

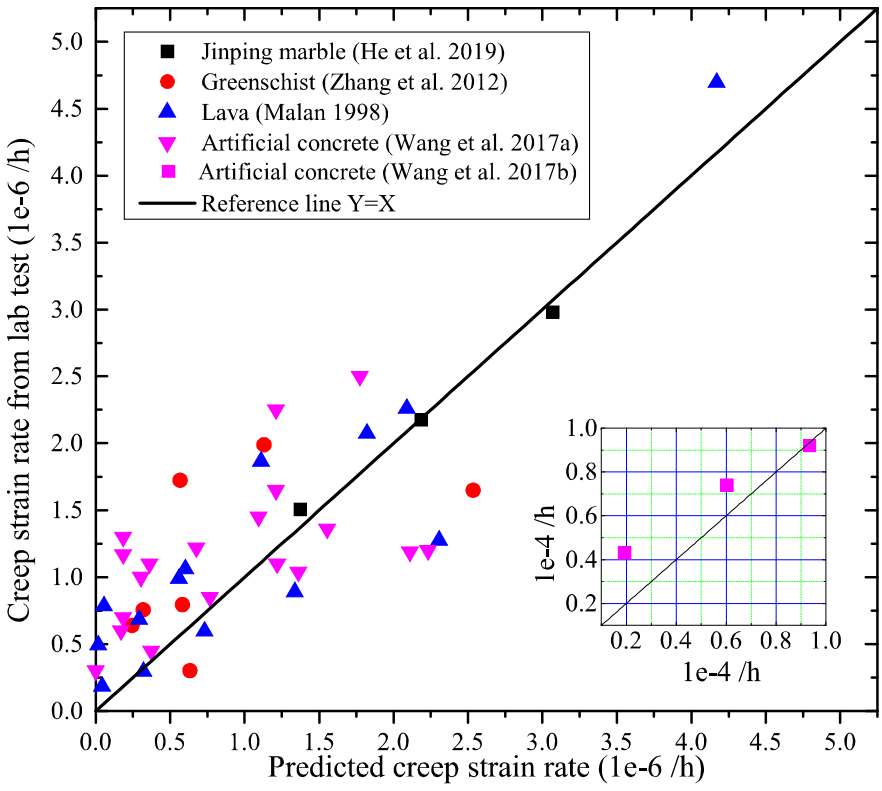

Figure 5-15. Experimental tested vs. predicted creep strain rates. One set of data from Wang (2017b) is located at 1e-5 h^{-1}, which is shown in the insert.

Table 5-3. Test conditions and experimental creep test results

UCS (MPa)	*JRC*	σ_n (MPa)	τ_S (MPa)	τ/τ_S	τ (MPa)	ξ	Tested $\dot{\varepsilon}$ (h^{-1})	*Predicted $\dot{\varepsilon}$ (h^{-1})	**Fitted C_j	Reference
21.7	1	2.17	1.76	0.80	1.41	0.79	7.00e-7	1.82e-7	3.5e-7	(Wang et al., 2017b)
				0.90	1.58		2.25e-6	1.21e-6		
		4.34	3.89	0.80	3.11	0.81	1.30e-6	1.82e-7		
				0.90	3.50		1.45e-6	1.09e-6		
		6.51	4.73	0.80	3.78	0.79	1.17e-6	1.82e-7		
				0.90	4.26		1.65e-6	1.21e-6		
	7	2.17	2.20	0.80	1.76	0.82	1.00e-6	3.05e-7		
				0.90	1.98		1.10e-6	1.22e-6		
		4.34	4.54	0.80	3.63	0.77	4.50e-7	3.73e-7		
				0.90	4.09		1.36e-6	1.55e-6		
		6.51	5.31	0.80	4.25	0.80	3.00e-7	0.00e0		
				0.90	4.78		1.04e-6	1.36e-6		
	19	2.17	3.58	0.80	2.86	0.78	1.10e-6	3.62e-7		
				0.90	3.22		2.50e-6	1.77e-6		
		4.34	6.26	0.80	5.01	0.73	1.22e-6	6.77e-7		
				0.90	5.63		1.19e-6	2.11e-6		
		6.51	7.90	0.70	5.53	0.71	6.00e-7	1.71e-7		
				0.80	6.32		8.50e-7	7.68e-7		

UCS (MPa)	*JRC*	σ_n (MPa)	τ_S (MPa)	τ/τ_S	τ (MPa)	ξ	Tested $\dot{\varepsilon}$ (h^{-1})	*Predicted $\dot{\varepsilon}$ (h^{-1})	**Fitted C_j	Reference
21.7	19			0.90	7.11		1.20e-6	2.23e-6		
190.0	4.8	0.20	0.11	0.99	0.10	0.85	1.51e-6	1.37e-6	3.5e-8	(He et al., 2019)
		0.40	0.20	0.99	0.20	0.85	2.17e-6	2.19e-6		
		0.60	0.30	1.00	0.30	0.86	2.98e-6	3.07e-6		
100.0	18	5.00	12.84	0.70	8.98	0.56	3.03e-7	5.95e-7	3.3e-7	(Zhang et al., 2012)
				0.89	11.37		1.65e-6	2.39e-6		
		12.50	22.33	0.56	12.58	0.52	6.40e-7	2.28e-7		
				0.67	14.88		7.96e-7	5.48e-7		
				0.77	17.28		1.99e-6	1.07e-6		
		15.00	25.50	0.59	14.97	0.52	7.58e-7	3.00e-7		
				0.66	16.88		1.73e-6	5.33e-7		
436.0	2	0.50	0.28	0.53	0.15	0.53	1.85e-7	4.55e-8	3.6e-7	(Malan, 1998)
				0.63	0.17		2.97e-7	3.30e-7		
				0.76	0.21		5.96e-7	7.53e-7		
				0.84	0.23		8.92e-7	1.38e-6		
				0.90	0.25		1.28e-6	2.37e-6		
		1.00	0.53	0.58	0.31	0.58	7.87e-7	5.56e-8		
				0.73	0.39		9.91e-7	5.75e-7		
				0.89	0.47		2.07e-6	1.87e-6		

UCS (MPa)	*JRC*	σ_n (MPa)	τ_S (MPa)	τ/τ_S	τ (MPa)	ξ	Tested $\dot{\varepsilon}$ (h^{-1})	*Predicted $\dot{\varepsilon}$ (h^{-1})	**Fitted C_j	Reference
436.0	2	1.50	0.82	0.37	0.30	0.37	4.93e-7	1.79e-8		
				0.51	0.42		6.83e-7	2.99e-7		
				0.66	0.54		1.06e-6	6.20e-7		
				0.78	0.64		1.86e-6	1.14e-6		
				0.87	0.72		2.26e-6	2.15e-6		
				0.93	0.77		4.70e-6	4.29e-6		
21.7	19	4.35	6.26	0.80	5.01	0.73	4.30e-5	1.93e-5	1.0e-5	(Wang et al., 2017b)
				0.90	5.63		7.40e-5	6.03e-5		
				0.93	5.82		9.20e-5	9.34e-5		

*Predicted values are calculated using Eq. (5.12).
**Model parameter of Eq. (5.12) used in each cases.

The long-term shear strength ratio ξ is one of the input parameters for calculating the creep strain rate using Eq. (5.12). As mentioned above, ξ is not a material constant, and it changes with joint roughness and normal stress. Thus, Eq. (5.13), which is an empirical equation fitted using the numerical simulation results, is presented to estimate the long-term shear strength ratio ξ of joints.

$$\xi = 1 - \frac{1-\xi_0}{\left(10^4 \cdot \left(\frac{\sigma_n}{JCS}\right)^{1.5} \Big/ JRC^{1.2}\right) + 1}, \tag{5.13}$$

where the basic long-term shear strength ratio ξ_0 is a constant, which is influenced by the rheological properties of rock. The ξ_0 value is equal to 0.5 for the grain-scale joint models.

The numerically-simulated and the equation-predicted (using Eq. (5.13)) ξ values are presented in Figure 5-16, showing a relatively good agreement between the two. Because the published data of long-term shear strength ratios are limited, there are not enough experiment data available to further verify Eq. (5.13). Hence, if Eq. (5.13) is used to estimate the long-term shear strength ratio ξ of joints of other rock types, it is suggested that some laboratory tests be conducted to determine the ξ_0 value and further verify Eq. (5.13).

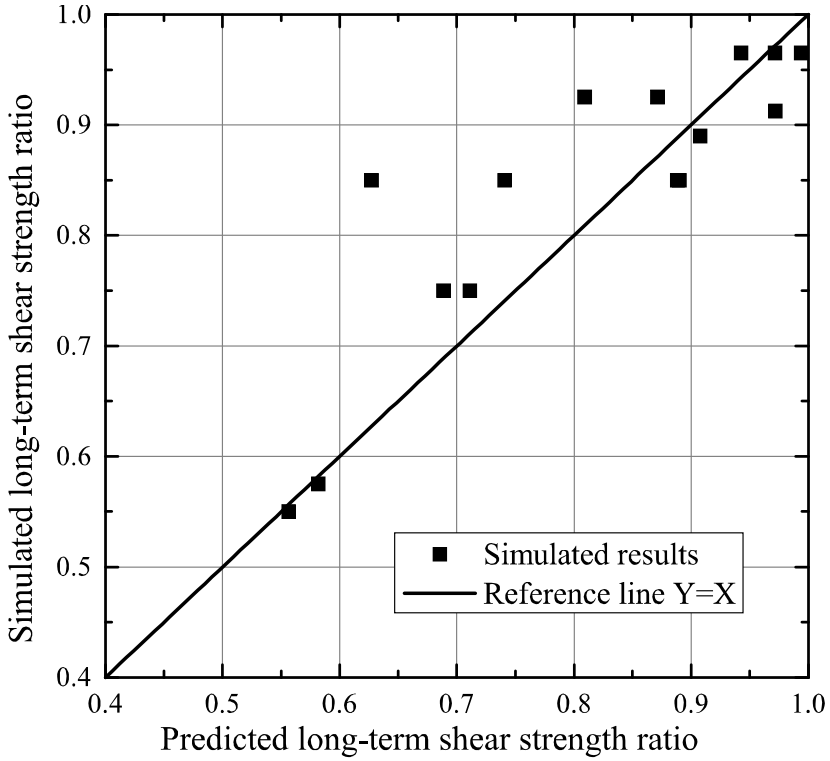

Figure 5-16. Simulated vs. predicted long-term shear strength ratios.

5.5.2 Model implementation for simplified flat joints

The grain-scale models perform well in simulating the creep behavior of rock joints. However, in numerical simulation it is unrealistic to build grain-scale models for all joints in large-scale rock structures. Thus, a creep constitutive model for simplified flat joints is needed. According to the literature, the creep strain curves of rock joints are usually fitted using Burgers model (Yang et al., 2013, Zhang et al., 2015, Zhang et al., 2016b, Xu and Yang, 2005, Yang et al., 2007); however, the four model parameters of Burgers model not only are affected by normal stress and joint roughness, but are also shear stress dependent. This is different from the Burgers creep model of intact rock, in which all four model parameters are stress independent. This means that when the shear stress is changed, the

model parameters will not be valid anymore. Therefore, Burgers model cannot be directly used as a creep constitutive model for rock joints.

On the other hand, Eqs. (5.12) and (5.13), in which the model parameter C_j and the constant ξ_0 are stress independent, can be adopted in a creep constitutive model to describe time-dependent deformation behaviors of rock joints.

In the creep fatigue process, damages that occur on the asperities of grain-scale joint models are observed (Figure 5-12(c) and (d)), which result in the reduction of joint roughness. For a simplified flat joint, the strength degradation method is adopted to mimic the roughness destruction under creep-loading conditions. A roughness degradation model is proposed and shown in Figure 5-17, which can be used to model short- and long-term strengths and time-dependent deformations of flat joints. The short-term shear strength is determined by the Barton's non-linear strength criterion, and the long-term shear strength is calculated using the short-term shear strength and Eq. (5.13). When the shear stress is beyond the long-term shear strength, the joint roughness (*JRC*) will be degraded which will result in slip deformation between joint walls. The sliding velocity is controlled by Eq. (5.12). When the shear stress or the normal stress is changed, the long-term strength and the sliding velocity will be adjusted accordingly.

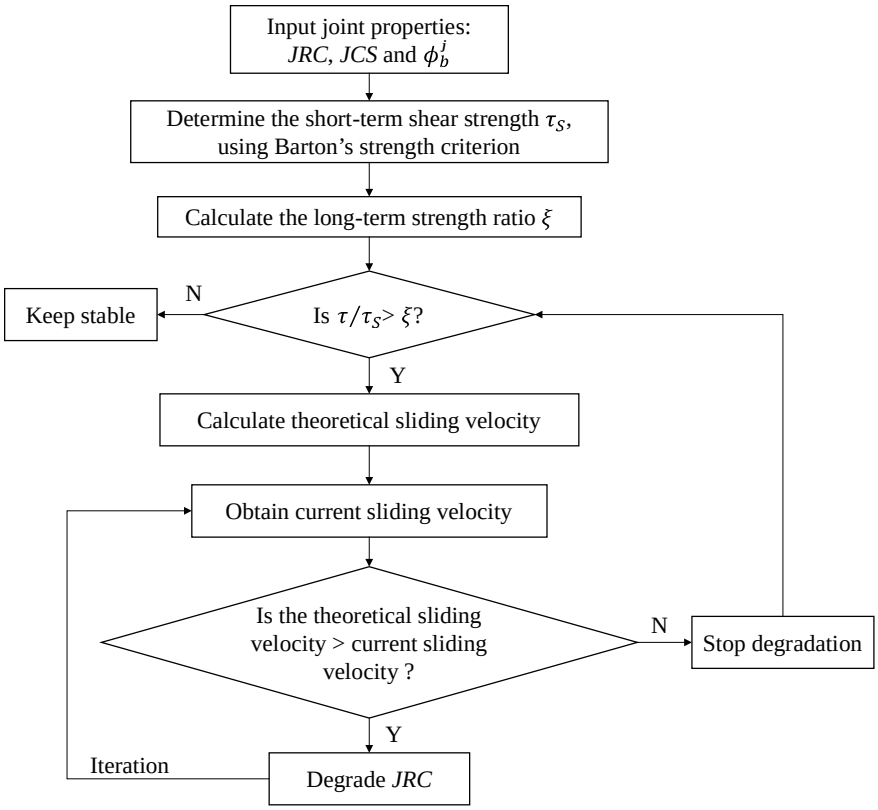

Figure 5-17. Flowchart of creep-slipping model for flat joint in UDEC.

The creep-slipping model performs well in controlling the creep behavior of simplified flat joints. As shown in Figure 5-18, the creep deformation of a flat joint is simulated using a shear model with a length of 10 cm and a height of 5 cm in UDEC. The short- and long-term shear strengths and creep deformation of the flat joint are controlled by the creep-slipping model of rock joints, without being affected by the mechanical properties of the rock of the joint walls. For the flat joint with input parameters of *JRC* = 7, σ_n = 4 MPa, the long-term strength ratio ξ is 0.89 according to Eq. (5.13), and creep slipping occurs when $\tau/\tau_S > \xi$. As shown in Figure 5-18(a), when τ/τ_S = 0.85, which is smaller than 0.89, there is no sliding velocity captured after 100 s. For the rest of the three cases with τ/τ_S > 0.89, creep sliping is observed. The sliding velocity is controlled by Eq. (5.12). The creep

strain curves of the grain-scale models are presented in Figure 5-18(a). The creep deformations of the grain-scale joint model after 100 s of each case are presented and compared with those of the flat-joint models. The initial shear displacement of the grain-scale joint model is influenced by the roughness profile of the joint. Even though joint roughness profile is not explicitly considered in the simplified creep-slipping model, the model captures the shear displacement well.

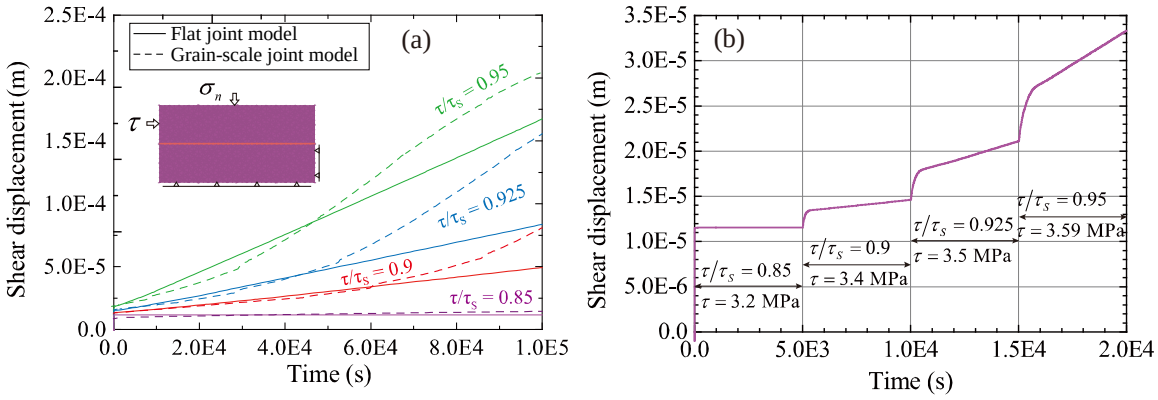

Figure 5-18. Creep deformation of a macroscopically flat joint under different shear loading ratios (for *JRC* = 7, σ_n = 4 MPa): (a) creep curves of joint under constant shear stress; (b) creep curves of joint under variable shear loadings.

Because the model parameters of Eq. (5.12) are all stress-independent, the creep deformation of flat joints can be controlled under variable shear loading conditions (Figure 5-18 (b)). When the shear loading ratio is increased from 0.85 to 0.95, the sliding velocity of the joint increases in a manner that follows the theoretical value determined from Eq. (5.12).

5.6 Discussion

The creep strain rate of joints obtained from the simulation results is in the order of 1e-5 h^{-1} (Figure 5-14). Most of the published experiment data show creep strain rates about 1e-6 h^{-1}, but one set of data from Wang (2017b) is located at 1e-5 h^{-1} (Figure 5-15). The large difference among the datasets is probably attributed to the variation of the rheological properties of rock types, the different loading rates (both normal and shear loadings) (Tang and Wong, 2016), and the difference among the creep-testing machines. This is why model parameter C_j in Eq. (5.12) is needed to balance the influence of these factors through parameter calibration. However, for the same dataset using the same rock type and under the same test condition, the influence of σ_n, τ/τ_S and *JRC* on the creep deformation (i.e., long-term shear strength and sliding velocity) can be described properly using Eqs. (5.12) and (5.13), as shown in Figure 5-14 and Figure 5-15.

One thing that needs to be mentioned is the independence between the parameters in the fitting formulas of Eqs. (5.12) and (5.13). The three input parameters, σ_n, τ/τ_S and *JRC*, are independent of each other. σ_n is independent of *JRC*. Both σ_n and *JRC* affect the short-term shear strength τ_S, but the loading ratio τ/τ_S is independent of both σ_n and *JRC*.

The simulated creep deformations of joints using the grain-scale models agree well with the experimental data. Firstly, the long-term shear strength and the relatively constant creep sliding velocity, which are important creep deformation characteristics, are captured in the simulation and they agree well with the experimental data (Bowden and Curran, 1984, Wang et al., 2017a, Yang et al., 2007). Secondly, the asperity destruction is captured in the

simulation, as illustrated in Figure 5-12(c) and (d). The roughness degradation method used in the creep model for the simplified flat joint performs well in mimicking the time-dependent strength and creep deformation of joints, which verifies the finding of Liu et al. (2019) who state that the asperity degradation governs the time-dependent deformation behavior of a joint under shear. Thirdly, the importance of normal stress is confirmed. The modeling results agree with the experimental results of granite discontinuities (Gadi, 1986), which state the creep deformations of joints are very different under different normal stress conditions. It explains that a higher confinement is beneficial to improving the long-term stability of jointed rock mass.

The grain-based joint model is demonstrated to be a good model to simulate time-dependent deformation of joints. Because the creep deformation governed by the joint asperities is simulated at the grain scale, it provides a novel approach to study the creep mechanism of rock joints. For simplified flat joints, the proposed creep-slipping model can simulate the long-term strength and creep-slipping velocity well. This makes it possible to consider creep deformation of rock joints when simulating time-dependent deformation of jointed rock mass, in which the creep deformation of joint plays an important role.

However, the limitation of this creep-slipping model should also be mentioned. The creep-slipping model considers only the strength degradation due to stress erosion of the joint asperities. Water seepage and weathering of rock joints during creep deformation are not considered. The empirical Eqs. (5.12) and (5.13) are fitted from the experimental data and the simulation results using the grain-scale joint models. Uncertainties associated with these two formulas may be due to the limited amount of usable published experimental

data and the uncertainty coming from the grain shape and size because the Voronoi tessellation generator in UDEC is used to model the geometry of mineral grains in the GBM-TtoF models.

5.7 Summary and conclusion

This chapter investigates the creep deformation of unweathered clean rock joints. Firstly, five grain-scale joint models are established using the GBM-TtoF creep model to simulate the creep deformation of rock joints with realistic surface roughness. Then, creep-slipping equations, which are fitted by the simulation results and verified using experimental data, are presented. Finally, a creep-slipping model for simplified flat joints is developed using the creep-slipping equations.

The grain-scale joint models perform well in simulating the creep deformation of rock joints. Using the calibrated GBM-TtoF creep models, time-dependent joint deformations governed by stress erosion of joint asperities can be simulated. In this manner, the long-term shear strength and the creep slipping of rock joint can be simulated.

Normal stress is more important than roughness to improve long-term stability of rock joints. For a rough joint under creep-shear loading, a high normal stress is beneficial to improving the long-term strength of the joint. This means that providing confinement to jointed rock masses through rock support is important to ensure longer stability of the rock masses.

It is impractical to conduct grain-scale numerical analysis considering detailed joint surface profiles in engineering design analyses. The proposed creep-slipping model captures well

the long-term strength and creep-slipping velocities of flat joints under both constant and variable shear loading conditions. It can be used to simulate time-dependent deformation of jointed rock mass using DEM by considering flat joints in the models.

Next, the creep sliding model is used to control the time-dependent deformation of flat joint structures in UDEC. A new creep model that can consider the creep deformation of both rock and joints will be developed in the subsequent chapter.

Chapter 6 Modeling of time‐dependent deformation of jointed rock mass

This chapter focuses on the simulation of time-dependent deformation of jointed rock mass using UDEC. In previous chapters, the time-to-failure phenomenon of rock (Chapter 3) and the creep slipping of rock joints (Chapter 5) were studied. In this chapter, a hybrid creep model for jointed rock masses, which can consider both the creep deformations of rock and joints, is proposed . The implementation of the model is described in Section 6.1. To study the mechanical response of the proposed model, creep simulations using square models with a single joint and a pillar model with multiple joints are carried out in Section 6.3. A case study is presented in Section 6.4 with the creep deformation of the Oppstadhornet rock slope in Norway simulated using the proposed creep model of jointed rock mass.

Main research findings presented in this chapter have been published in a paper entitled “Modeling of time−dependent deformation of jointed rock mass” (Wang and Cai, 2022a).

6.1 A creep model of jointed rock mass

Large-scale rock mass models are the focus of this chapter. A creep model of jointed rock mass is developed using UDEC. The concept of the creep model of jointed rock mass is shown in Figure 6-1. The model implementation is introduced in this section.

6.1.1 Implementation of the TtoF model for rock using the continuum method

In UDEC, rocks are modeled by deformable blocks and meshed as finite difference triangular zones instead of using the grain-based modeling approach, which is no longer practical considering the capacity of current PCs. In the proposed creep model of jointed rock mass, time-dependent deformations of rock are governed by a time-to-failure (TtoF) creep model implemented using the continuum method (FDM), which is based on the model of creep deformation of rock presented in Chapter 3. The implementation of the TtoF creep model of intact rock and the calibration process is presented in this section.

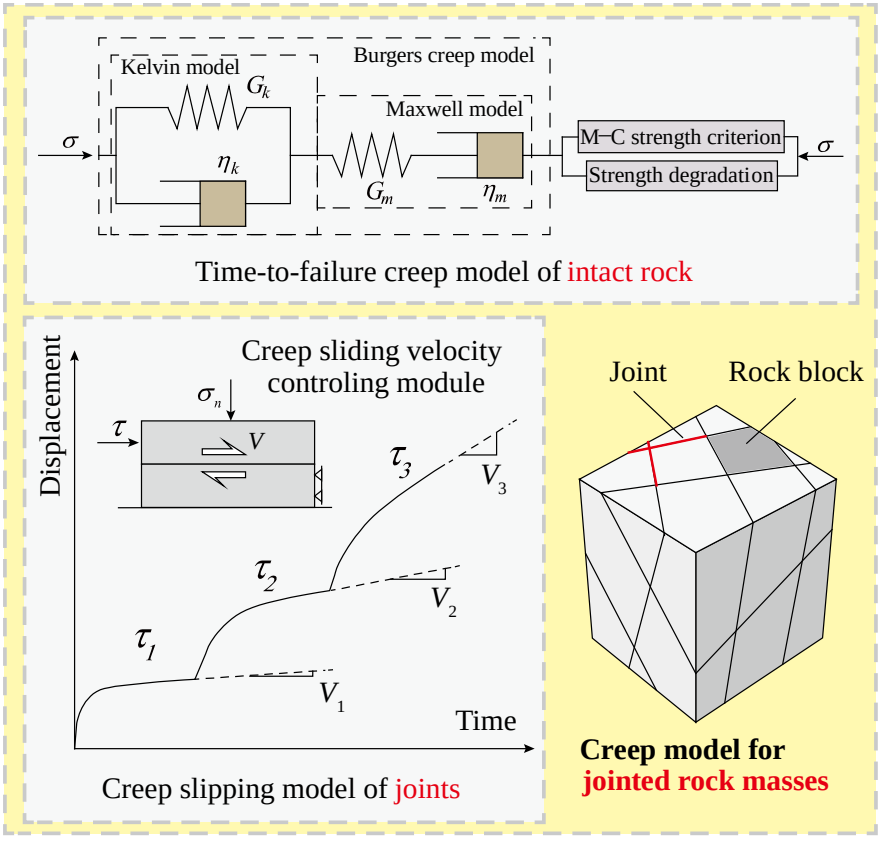

Figure 6-1. A creep model for jointed rock masses.

The creep deformation of a rock can be described in three stages, as shown in Figure 2-2. In the TtoF creep model, the Burgers model (Eqs. (3.1) and (3.2)) is used to describe the first two deformation stages.

The time to enter the tertiary creep stage (Figure 2-2) is controlled by a strength degradation method. According to the uniaxial and triaxial creep test data of LdB granite (Schmidtke and Lajtai, 1985, Lau et al., 2000), the relation between the lifetime of rock and the applied stress is given in Eq. (6.1).

$$r_{sc}^{\ 2} = 1 - 0.0124 \ln\left(\frac{T_F}{t_0}\right), \tag{6.1}$$

where T_F is the lifetime of rock specimen, t_0 is the time for determining the short-term strength (t_0 = 1 s in this study), $r_{sc} = (\sigma_1 - \sigma_3)/2\sigma_E$ is the driven stress ratio, where σ_1 and σ_3 are the maximum and minimum principal stresses, respectively, and $\sigma_E = \left[c\cot\phi + \frac{1}{2}(\sigma_1 + \sigma_3)\right]\sin\phi$ is the distance from the center of the stress circle to the strength envelope, where c and ϕ are the cohesion and friction angle, respectively.

In the TtoF model, the strength parameters of each block zone degrade with time. When the stress in a block zone is higher than the crack damage stress σ_{cd} of the rock, the cohesion of the block zone degrade with time. A damage index is defined to track the accumulated damage in each zone, which is the same as the method of degrading zones in the grains introduced in Chapter 3. Two degradation parameters, t_0' and q', are used to

control the strength degradation speed of the zones. These two parameters need to be calibrated to fit the time-to-failure of LdB granite (Eq.(6.1)).

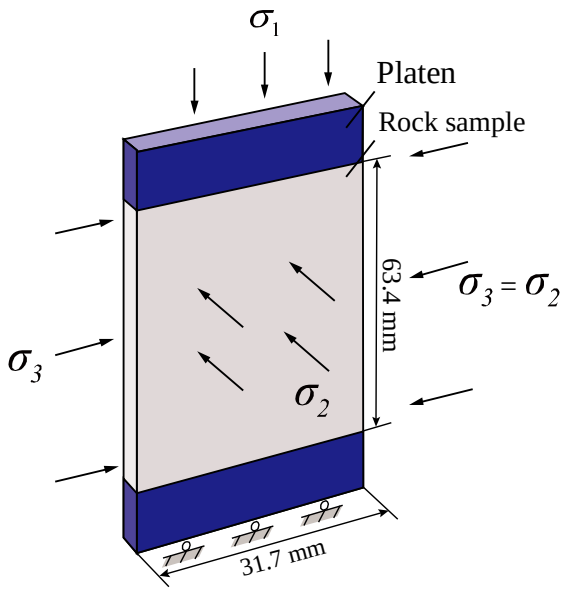

Figure 6-2. Loading conditions used in creep parameter calibration.

A series of creep simulations are conducted under triaxial compressive loading to calibrate the strength degradation parameters including t_0' and q'. The loading condition is presented in Figure 6-2. The joints of the specimen-platen interfaces have no shear strength, and the shear stiffness of the joints is assigned a very small value (*Jks* = 3.0e-3 Pa/m), which can reduce the end effect during compression tests. The axial stress σ_1 is set at three levels, which are 225, 275 and 325 MPa. The confinement σ_3 ($\sigma_2 = \sigma_3$) is set at five levels for each axial stress. The simulated axial strain curves are presented in Figure 6-3. As shown in Figure 6-4, the calibrated time-to-failure of the rock fits well with the experimental data. The calibrated t_0' and q' values along with other model parameters are presented in Table 6-1. The static strength and deformation properties are calibrated using the laboratory test data of LdB granite, which are also listed in Table 6-1.

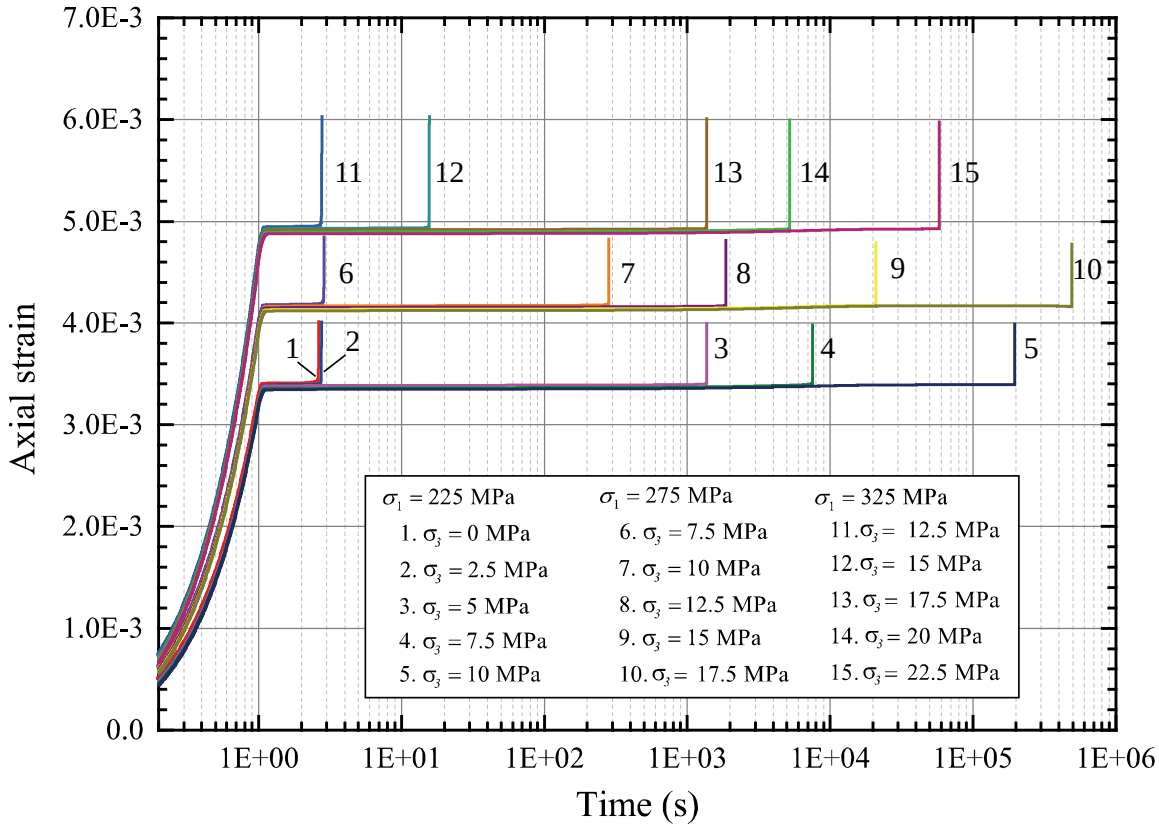

Figure 6-3. Simulated creep strain curves of the LdB granite specimen.

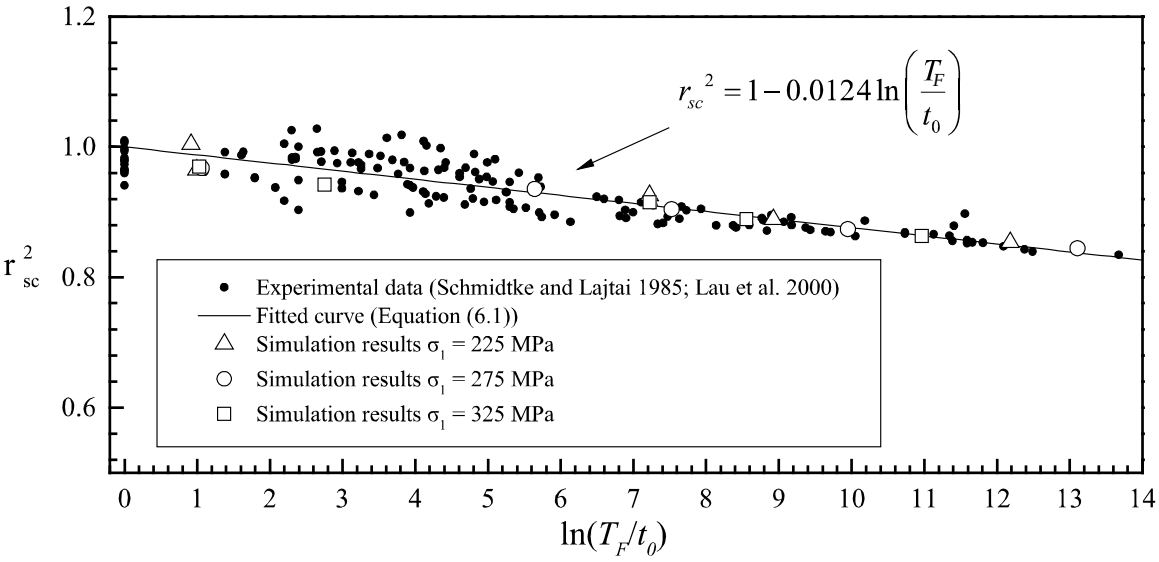

Figure 6-4. Calibrated lifetime of specimens under different confinements.

Table 6-1. Calibrated parameters of LdB granite for the TtoF model

Parameter		Value
	Static strength and deformation properties	
E	Young's modulus (GPa)	69
ν	Poisson's ratio	0.26
ρ	Density (g/cm^3)	2.6
c	Cohesion (MPa)	35
ϕ	Friction	55.6°
UCS	Uniaxial compressive strength (MPa)	225
σ_t	Tensile strength (MPa)	9.0
	Creep deformation and strength degradation parameters	
G_k	Shear modulus for Kelvin component (GPa)	100
η_k	Viscosity coefficient for Kelvin component (GPa^{-1})	1.5
G_m	Shear modulus for Maxwell component (GPa)	26.5
γ	Material constant for Maxwell component	1.8e35
β	Material constant for Maxwell component	3.0
t_0'	Model constant for the TtoF model	3.1e-3
q'	Model constant for the TtoF model	8.5e-3

6.1.2 Creep-slipping model for joints

In the developed creep model of a jointed rock mass, the time-dependent response of rock joints is governed by the creep-slipping model that proposed in Chapter 5, which has been proven effective in controlling time-dependent deformation of rock joints. The implementation of the creep-slipping model is briefly introduced in this section.

First, the short-term shear strength τ_S of rock joint is assumed to obey the Barton's shear strength criterion (Barton et al., 1985, Bandis et al., 1981), as presented in Eq. (5.1).

The strength of joint is scale dependent. According to Barton's theory (Barton and Bandis, 1980), when a large-scale joint is analyzed, the values of *JRC* and *JCS* in Eq. (5.1) need to be modified using the following equations.

$$JRC_n = JRC_0 \left(\frac{L_n}{L_0} \right)^{-0.02\,JRC_0}, \tag{6.2}$$

$$JCS_n = JCS_0 \left(\frac{L_n}{L_0} \right)^{-0.03\,JRC_0}, \tag{6.3}$$

where JRC_0 and JCS_0 are the joint roughness coefficient and joint wall compressive strength measured using lab-scale joint at length L_0, respectively, and JRC_n and JCS_n are the joint roughness coefficient and joint wall compressive strength at in-situ scale L_n, respectively.

Second, the rock joint is assumed to slide at a constant speed when the applied shear stress τ exceeds the long-term shear strength τ_L. Based on experimental data, it is found that the shear strain rate of joint $\dot{\varepsilon}$ can be obtained from the following Eqs. (5.12) and (5.13)

The slipping deformation of joint in UDEC can be captured by the degradation of the strength parameters. The steps of the implementation of the slipping model are shown in Figure 5-17. It has been shown that the slipping model performs well in simulating creep-slipping behaviors of joints under both constant and variable shear loading conditions. The calibrated parameters of LdB granite joints listed in Table 6-2 are used in this study.

Table 6-2. Calibrated parameters of joints of LdB granite

Parameter		Value
	Static strength and deformation properties	
Jkn^j	Normal stiffness (Pa/m)	6.85e12
Jks^j	Shear stiffness (Pa/m)	2.74e12
c^j	Cohesion of joint (MPa)	0
ϕ_b^j	Basic friction angle (°)	30.5°
σ_t^j	Tensile strength of joint (MPa)	0
JCS_0	Joint wall compressive strength measured in lab (MPa)	225
L_0	Length of joint used in lab tests (m)	0.1
	Creep deformation parameters	
ξ_0	Basic long-term shear strength ratio	0.5
C_j	Material constant of the sliding model of joint	5.5e-6

6.2 Parameter calibration

The parameter calibration procedure is summarized in this section. There are four kinds of model parameters in the proposed creep model of jointed rock mass, which are static mechanical parameters and time-dependent mechanical parameters of intact rock and rock joints, respectively, as shown in Figure 6-5.

The static mechanical parameters need to be determined first for both the rock and the joints. The static mechanical properties of intact rock, i.e., Young's modulus E, Poisson's ratio v and crack damage stress σ_{cd}, can be determined using uniaxial compression tests of rock. Cohesion c and friction angle ϕ can be determined by triaxial compression tests. Tension test is required to determine the tensile strength σ_t. In terms of the static properties of rock joints, Barton's joint model is adopted and the joint roughness coefficient JRC_0,

the joint wall compressive strength JCS_0, the basic friction angle ϕ_b^j and the in-situ scale L_n can be measured by field joint mapping and testing. Joint set parameters, such as orientation (inclination and inclination direction), spacing and gap, can also be collected from field joint mapping.

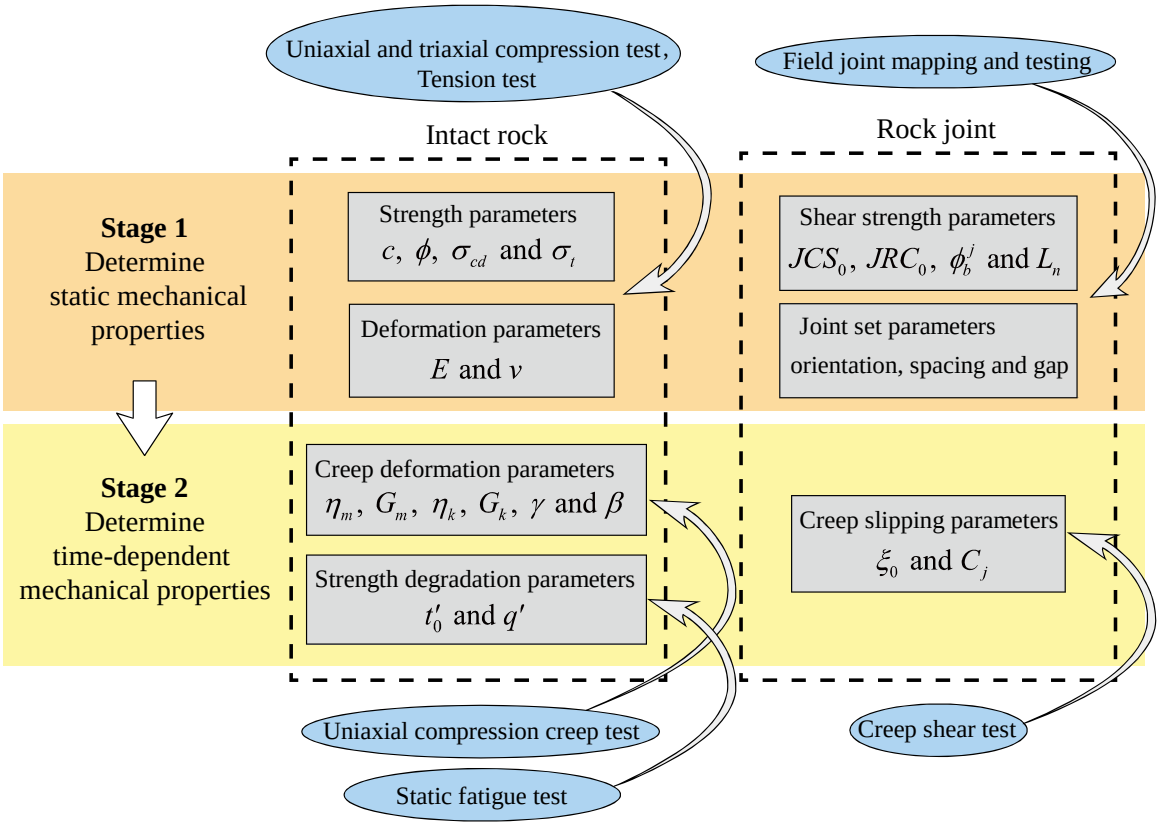

Figure 6-5. Parameter calibration procedure for the creep model of jointed rock mass.

Next, time-dependent mechanical parameters need to be calibrated using creep-test data. Firstly, for intact rock uniaxial compression creep tests are required to obtain the creep-strain curves of rock specimens, which can be used to calibrate the parameters of Burgers model, i.e., G_m, η_m, G_k, η_k, γ and β. Then, static fatigue test data can be used to calibrate the two strength degradation parameters, t_0' and q', which can ensure that the

simulated lifetime of the rock specimens is consistent with the experimental results. For rock joints, creep-shear test data are used to calibrate the long-term shear strength and the creep-slipping velocity of joints, which are controlled by the basic long-term shear strength ratio ξ_0 and a dimensionless model constant C_j, respectively. When laboratory test data are limited, field monitoring data can be used to determine these two parameters by back analysis.

In the next steps, the TtoF model of rock and the creep-slipping model of joint, both of which have been implemented in UDEC, are used together to study time-dependent deformation of jointed rock mass.

6.3 Time-dependent deformations of jointed rock masses

6.3.1 Model with a single joint

To investigate the influence of joint on the time-dependent response of jointed rock mass, numerical simulations are carried out using block models with a single joint. The two-dimensional plane strain model is shown in the insert in Figure 6-6. The dimension of the square model is 1.0 m × 1.0 m. The model is discretized into deformable triangular finite-difference zones with an average length of 5.0 cm. Stress boundary condition is adopted, and the maximum and minimum principal stresses, σ_1 and σ_3, are applied in the vertical and horizontal directions, respectively, and the out-of-plane stress σ_2 is kept at 5.0 MPa. The applied stresses are loaded at t = 0 and kept constant during creep calculation. The TtoF creep model and the creep-slipping model introduced in Section 6.1.2 are used to control the deformation of block and joint, respectively.

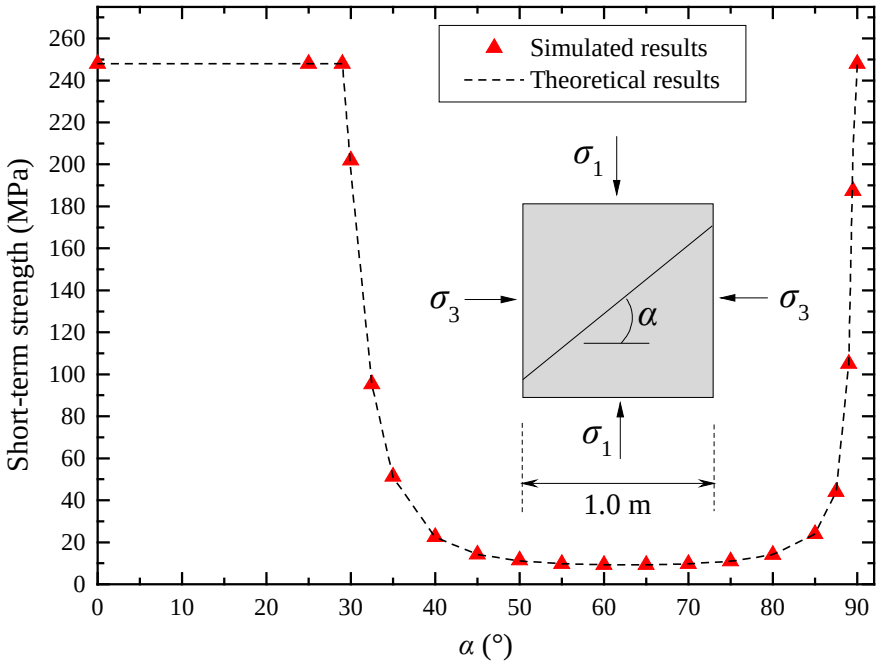

Figure 6-6. Short-term strength of the jointed rock model with a single joint.

First, the short-term strength σ_S of the jointed rock mass is simulated by turning the creep function off. σ_S is the value of the maximum principal stress σ_1 at failure for a given σ_3. It is influenced by the inclination angle α, and the simulated results are presented in Figure 6-6. The theoretical strength is obtained using Eqs. (5.1) to (6.4).

$$\left.\begin{aligned}\sigma_n &= \frac{1}{2}(\sigma_1+\sigma_3)+\frac{1}{2}(\sigma_1-\sigma_3)\cos 2\alpha \\ \tau &= \frac{1}{2}(\sigma_1-\sigma_3)\sin 2\alpha\end{aligned}\right\}, \tag{6.4}$$

In this simulation, σ_3 = 2.0 MPa, JRC_0 = 10.0, L_0 = 0.1 m, JCS_0 = 225 MPa, and L_n is determined by model geometry. The short-term strength of the model presents a 'U-shaped' curve. The minimum strength of the model is around $\alpha = 65^\circ$ (the theoretical value is 64.5°), and the maximum strength is at $\alpha = 90^\circ$ and $\alpha < 30.5^\circ$. It should to be mentioned

that the shape of the short-term strength curve shown in Figure 6-6 does not present the typical U-shaped strength curve from the literature, e.g. Halakatevakis and Sofianos (2010), where the Mohr–Coulomb failure criterion was used. In the model, Bardon's non-linear shear strength criterion (Eq. (5.1)) is adopted. The friction angle of joint, represented by $JRC\log\left(JCS/\sigma_n\right)+\phi_b^j$, is not a constant, but a function of normal stress σ_n.

Next, creep simulations are conducted using the conditions similar to that shown in Figure 6-6, but with σ_1 kept constant. The vertical displacement is monitored over time. The long-term strength σ_L can be determined using the trial-and-error method. To find the long-term strength of a model, several creep simulations need to be carried out using different σ_1 with a given σ_3. The time-dependent responses are significantly different when the model is loaded below and above its long-term strength; thus, it is easy to determine the long-term strength. For example, for the model with $\alpha = 70^\circ$, JRC_0 = 10, σ_3 = 2 MPa, the simulated short-term strength σ_S is 9.8 MPa. As shown in Figure 6-7, when the applied σ_1 is 9.4 MPa, the joint in the block keeps slipping continuously, which can be seen from the plot of the axial displacement in the figure. When the applied σ_1 is 9.0 MPa, the joint in the block does not present any creep sliding behavior, and the axial displacement does not increase with time. Hence, it can be judged that there is a stress threshold between 9.4 and 9.0 MPa, which can be defined as the long-term strength σ_L of the model with $\alpha = 70^\circ$. For this case, when the model is loaded beyond the long-term strength, a large deformation is resulted from the creep sliding of joints, and there is no creep damage captured in the

rock. Therefore, it can be judged that the long-term strength σ_L of the model is governed by the joints.

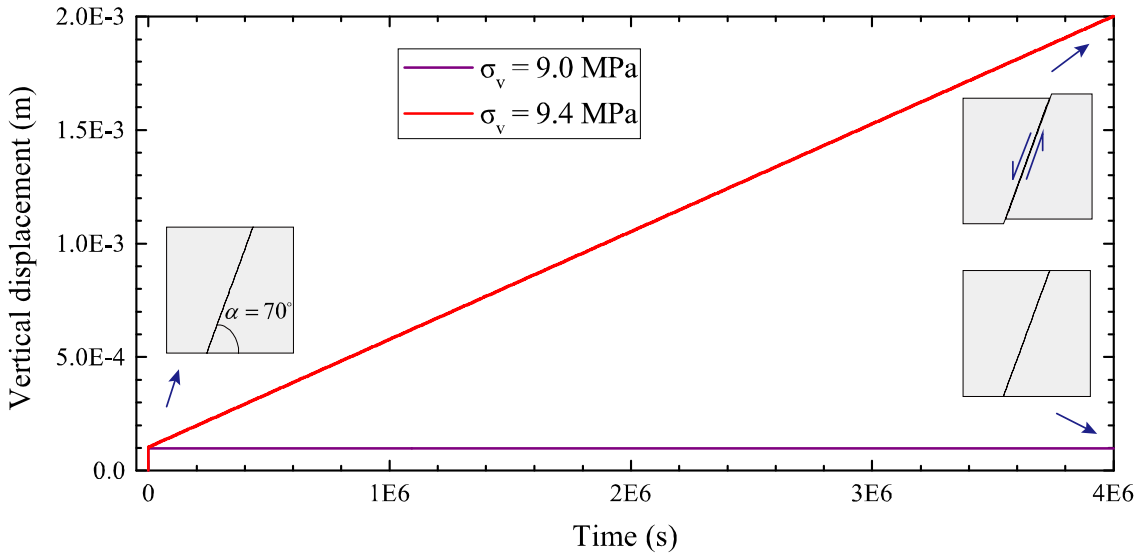

Figure 6-7. Time-dependent response of the jointed rock model under different loading stresses with α = 70°.

The long-term strengths of models for other joint inclinations are simulated and the results are presented in Figure 6-8. The σ_L/σ_S ratio, which is referred as the long-term strength ratio, is presented in the right ordinate of the figure. It can be observed that when the inclination is smaller than 25° or equal to 90°, the long-term strength of the jointed rock is controlled by the rock. When the inclination is between 25° and 90°, the joint has an influence on the strength of the jointed rock. The minimum value of σ_L is around $\alpha = 65^\circ$, which is the same as that of the minimum σ_S. The long-term strength ratio σ_L/σ_S varies with the inclination. For models with small inclinations (e.g., $30^\circ < \alpha < 50^\circ$), the σ_L/σ_S ratio is near 1.0. When the joint is steep, such as $70^\circ < \alpha < 85^\circ$, the σ_L/σ_S ratio decreases to about 0.92 – 0.94.

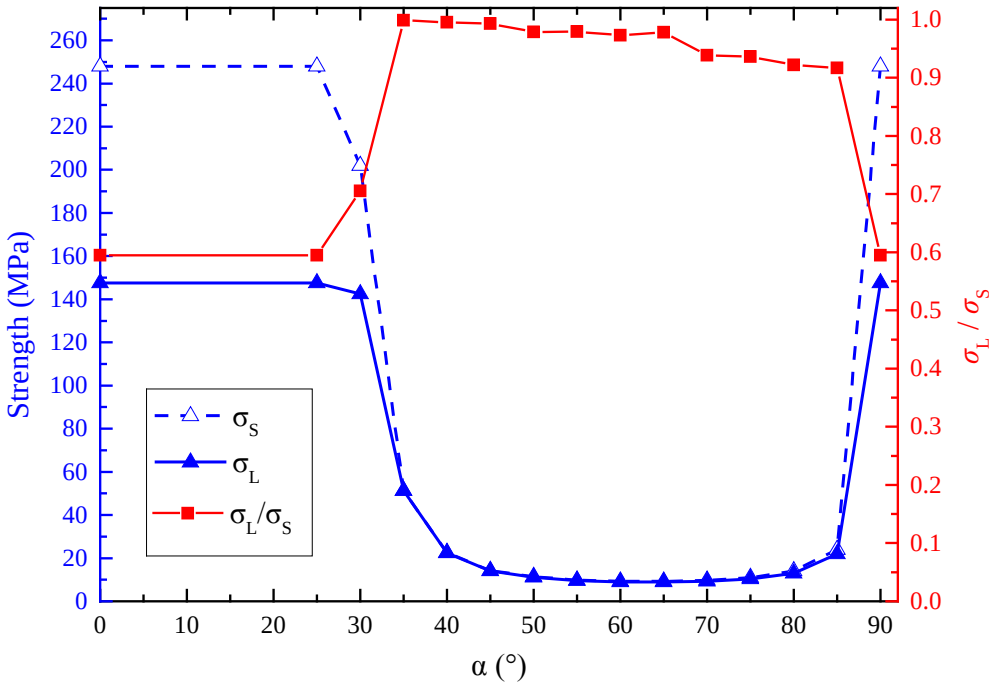

Figure 6-8. Simulated short-term and long-term strengths of the jointed rock model with different inclinations for σ_3 = 2 MPa.

To investigate the influence of confinement on the time-dependent response of the model, a series of creep simulations are carried out under confinements of σ_3 = 1.0, 2.0 and 4.0 MPa, and the simulated results are presented in Figure 6-9. The variation of the short-term strength σ_S and the long-term strength σ_L with inclination is presented in Figure 6-9 (a)-(c). The variation of the long-term strength ratio σ_L/σ_S with inclination (between 35° and 85°) is summarized in Figure 6-9 (d). It can be observed that both σ_S and σ_L are relatively low at low confinement ($\sigma_3 = 1.0$ MPa, Figure 6-9 (a)). The σ_L/σ_S ratio is also low for the case with $\sigma_3 = 1.0$ MPa (Figure 6-9 (d)). Both σ_S and σ_L increase with the increase of σ_3. When σ_3 = 4.0 MPa, the σ_L/σ_S ratio is higher than 0.95, even when the inclination is near 85° (Figure 6-9 (d)). The results indicate that joint creep slipping is less likely to

occur when the confinement is high. Hence, a high confining stress is beneficial to maintain long-term stability of jointed rock masses.

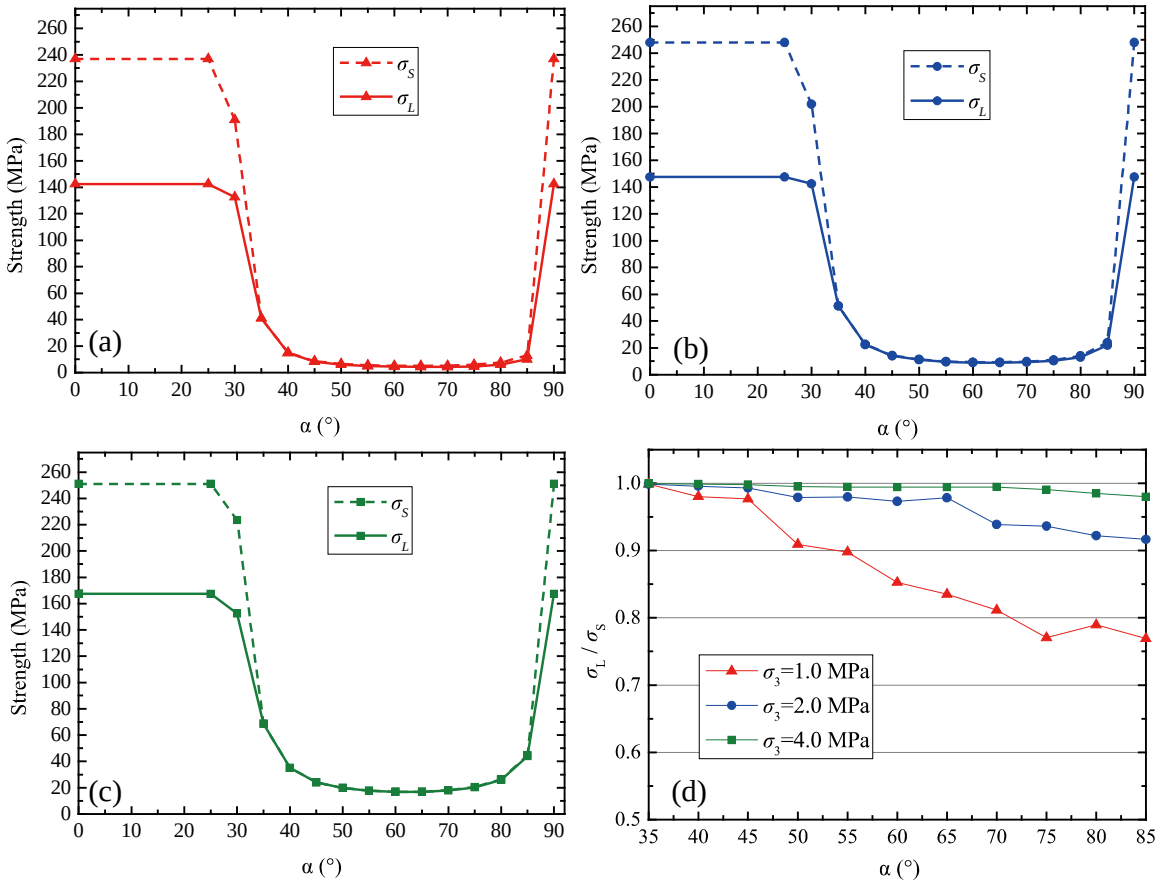

Figure 6-9. Influence of confinement on the long-term strength of the jointed rock model: (a) σ_3 = 1.0 MPa; (b) σ_3 = 2.0 MPa; (c) σ_3 = 4.0 MPa; (d) variation of the long-term strength ratio σ_L/σ_S with inclination.

6.3.2 Jointed pillar model

In this section, time-dependent deformation behaviors of moderately jointed rock mass are simulated using the proposed creep model. A jointed pillar model as shown in Figure 6-10 is built. The width of the pillar is 3.0 m, the height is 5.0 m, and roller boundaries are applied at both sides and the bottom of the model. Axial loading is applied at the top of the

model. Three non-persistent joint sets are considered, and the geometric and roughness parameters of the joint sets are presented in Table 6-3.

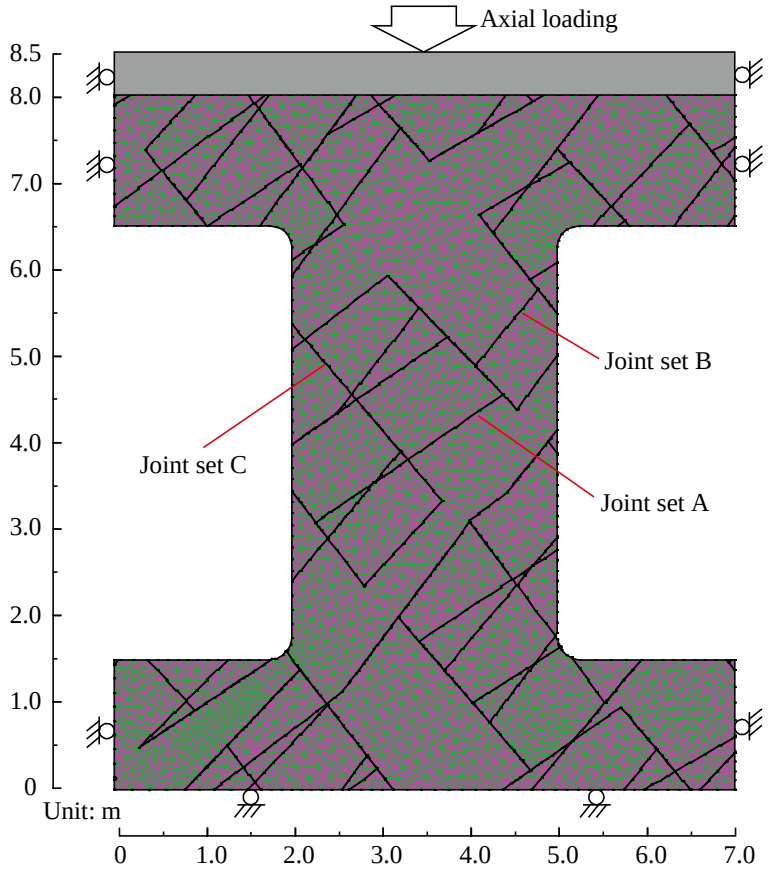

Figure 6-10. Jointed pillar model.

Table 6-3. Joint set properties in the pillar model

Joint set	Inclination (°)	Spacing (m)	Trace length (m)	Gap length (m)	JRC_0
A	35 ± 5	0.9 ± 0.1	2.8 ± 0.2	0.02 ± 0.01	10
B	50 ± 5	0.7 ± 0.2	2.5 ± 0.3	0.03 ± 0.02	12
C	130 ± 5	1.2 ± 0.1	2.8 ± 0.2	0.05 ± 0.01	10

First, the short-term compressive strength σ_S of the pillar is simulated with the creep option turned off. The simulated axial stress–displacement curve is presented in Figure

6-11. It is seen that the short-term strength of the pillar is 64 MPa. The pillar maintains some of the strength in the post-peak deformation stage.

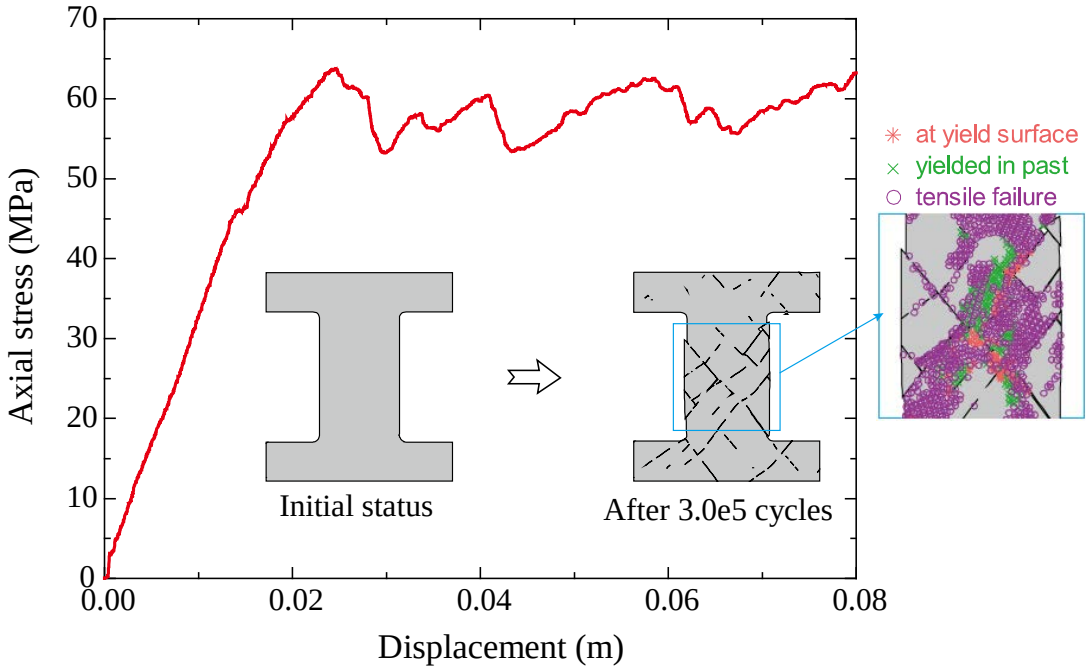

Figure 6-11. Axial strain curve of the pillar model in static loading test.

Next, creep simulations are conducted. According to the observations in the field (Sainoki and Mitri, 2017, Esterhuizen et al., 2011a, Korzeniowski, 1991) and in laboratories (Schmidtke and Lajtai, 1985, Zhao et al., 2018b), time-dependent responses of rock are largely influenced by the applied loads. In this section, creep tests of the pillar models are carried out under axial stresses of 36, 40, 44 and 48 MPa. The variations of the axial displacement with time are presented in Figure 6-12, showing two types of time-dependent responses. When the applied vertical stress is low, e.g. at σ_v = 36 MPa, the creep deformation stops after some time (i.e., 1e6 s), and neither observable creep damage of rock nor slipping of joint is captured after 1e6 s. In this case, it can be judged that the pillar

will be stable for a long time. When the loading is σ_v = 44 MPa, the pillar presents a deformation pattern similar to the three-stage creep curve shown in Figure 6-12. The primary deformation stage is from t = 0 to 5.0e5 s. The acceleration of displacement at around 4.0e5 s is resulted from the failure of some block zones due to stress concentration and the sudden sliding of joints. Because the damage occurs only locally, the pillar returns to stable deformation thereafter. The secondary stage is from 5.0e5 to 3.0e6 s, in which the creep strain rate is relatively stable. The deformation accelerates after 3.0e6 s, which means that the pillar enters into the tertiary deformation stage, and the lifetime of the pillar decreases as the applied stress increases. When the applied stress is equal to 48 MPa, the pillar cannot remain stable for a long time and it fails in 2.4 days. Based on the simulation results, it can be estimated that the long-term strength of the jointed pillar model is around 42 MPa.

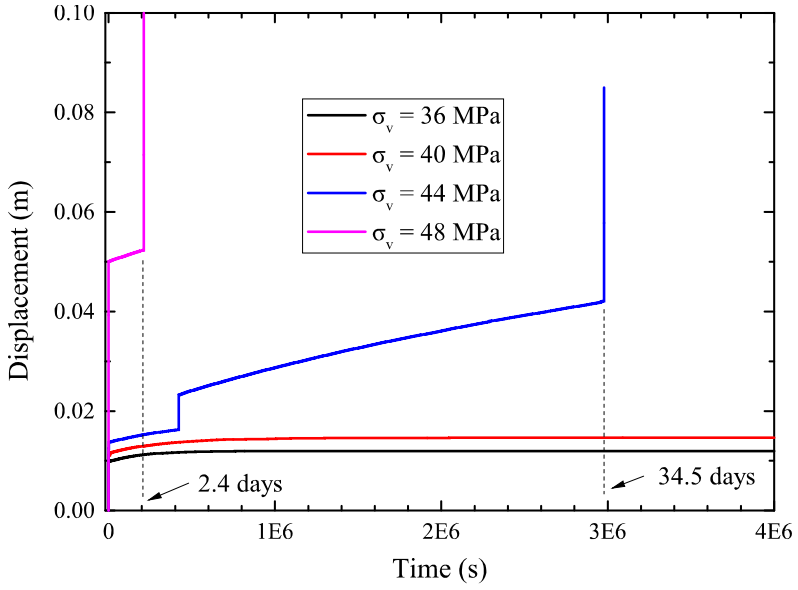

Figure 6-12. Creep displacement curves of the pillar model under different axial stresses.

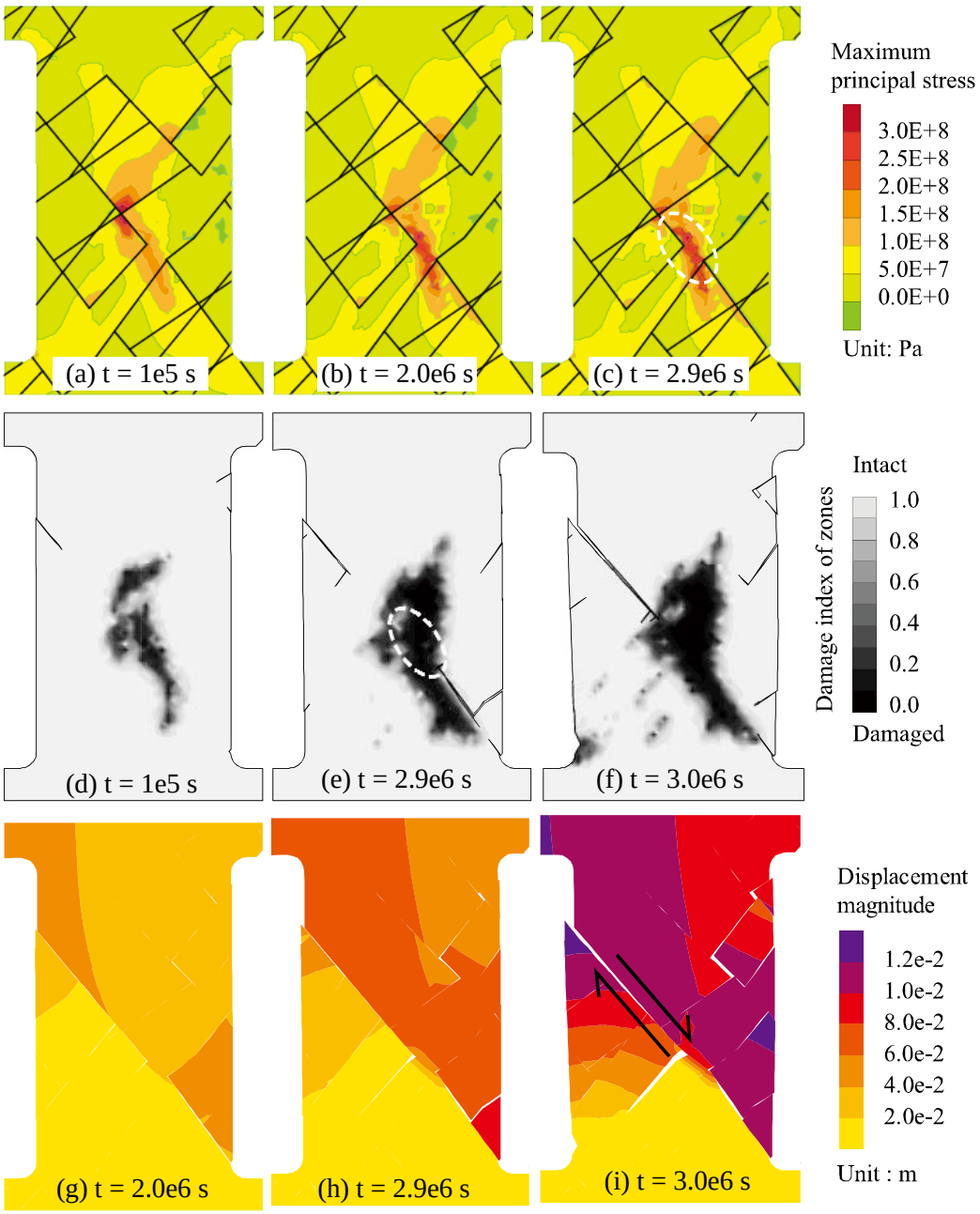

Figure 6-13. Structural failure evolution of the pillar model with σ_v = 44 MPa: (a)−(c) maximum principal stress distribution; (d)−(f) accumulated damage of rock; (g)−(i) displacement magnitude in the pillar model.

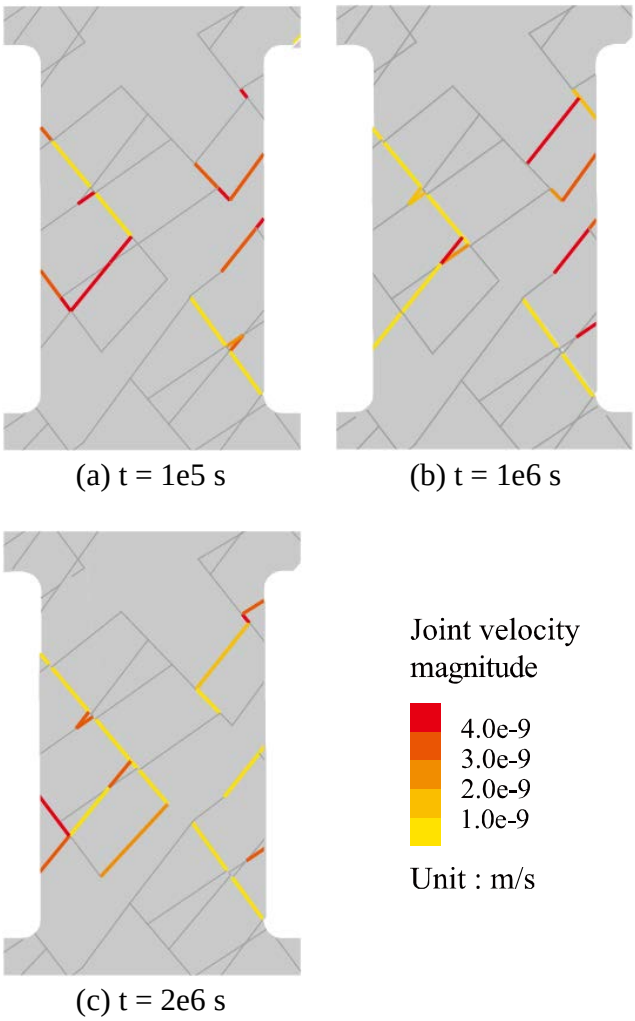

Figure 6-14. Creep slipping of joints in the pillar model with σ_v = 44 MPa.

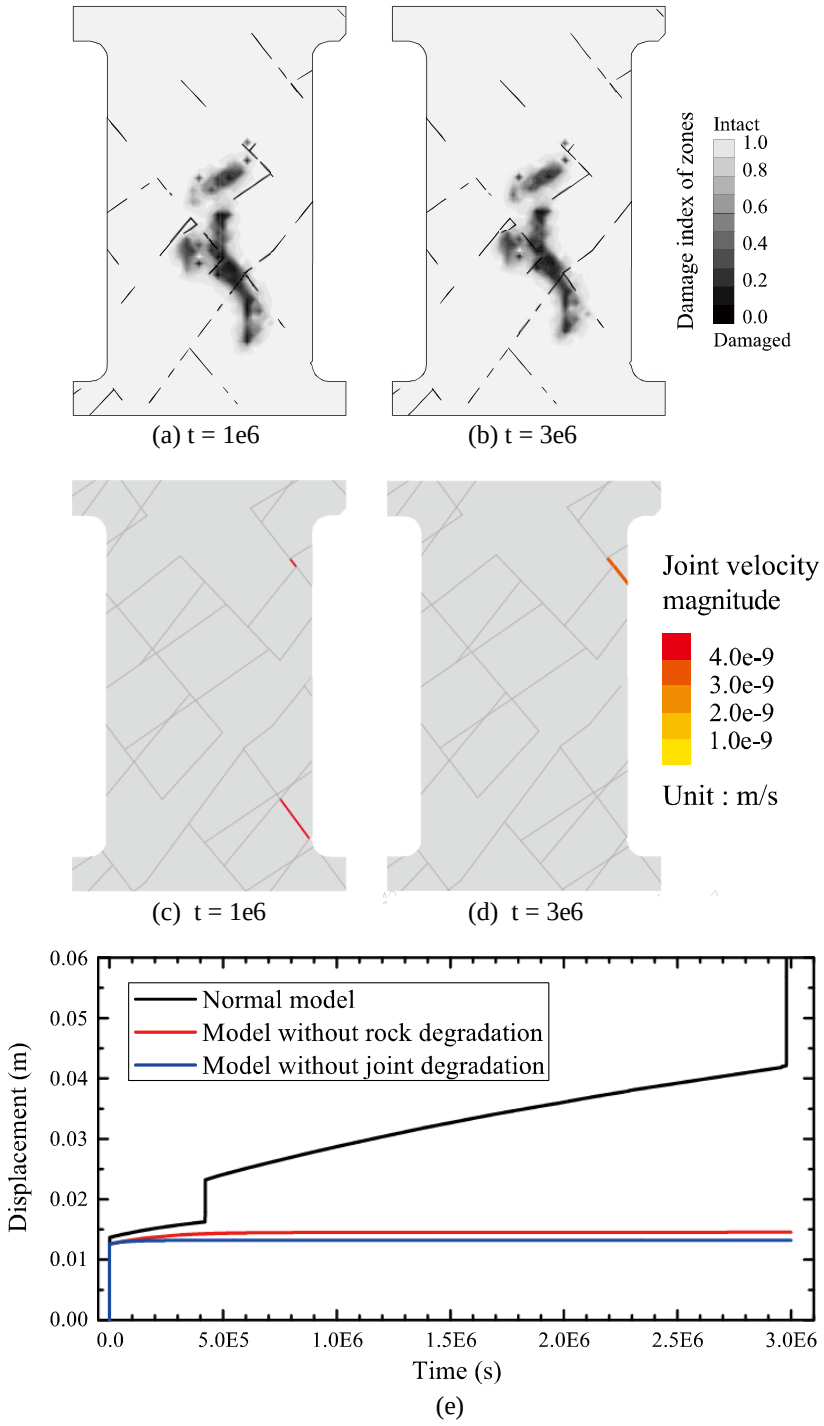

Figure 6-15. Model performance with different strength degradation configurations. Rock degradation is activated for the model without joint degradation; joint degradation is activated for the model without rock degradation; both rock and joint degradations are applied for the normal model: (a)–(b) accumulated damage of rock for the model without joint degradation; (c)–(d) joints in slipping status for the model without rock degradation; (e) creep strain of three models with different degradation configurations.

The failure process of the pillar for σ_v = 44 MPa is presented in Figure 6-13. It can be observed that the stresses concentrate near a rock bridge of two steep joints marked in Figure 6-13 (c), which results in creep damages occurring at the location, as marked in Figure 6-13 (e). As introduced in Section 2, the damage accumulated in a block is controlled by the time-to-failure model of rock, in which the strength of zones degrades if the stress is higher than the crack damage stress σ_{cd} of the rock. The accumulated damage of the zones in the blocks is monitored in the simulation process. The damage index of the zones ranges from 1.0 to 0, with 1.0 and 0 representing intact and failed zones, respectively. At *t* = 3.0e6 s, the collapse of the pillar is shown in a form of sliding along the steep joint in the pillar after the failure of the key rock bridge (Figure 6-13 (i)).

The creep deformation of the joints plays an important role in the failure process of the pillar. The slipping velocities of the joints at different times are monitored and the result are shown in Figure 6-14. It shows that there are many joints in sliding status during creep calculation that contribute to the creep deformation of the pillar model.

As mentioned in Section 1.2, both the deformations of rock and joints are important to the time-dependent deformation of a rock mass. This is also true for the creep deformation of the pillar model. Figure 6-15 (e) shows the results of three creep tests using different strength degradation configurations, i.e., model without rock degradation, model without joint degradation, and model with both rock and joint degradations (normal configuration). For the model without joint degradation, although there is still some damage accumulated in the model before 1.0e6 s, no obvious new creep damage accumulation is captured from 1.0e6 to 3.0e6 s (Figure 6-15 (a)-(b)), and no large deformation occurs as can be seen in

the creep strain curve in Figure 6-15 (e). For the model without rock strength degradation, the model can still present some creep deformation resulted from the creep slipping of the joints at primary creep stage, i.e., t = 0 to 1.0e6 s. However, there are just a few joints that are in sliding status from 1.0e6 to 3.0e6 s, as shown in Figure 6-15 (c)-(d), and no obvious creep strain is captured after 1.0e6 s (Figure 6-15 (e)).Therefore, the strength degradations of rock and joints are both important. If either one of them is neglected, the time-dependent deformation of jointed rock masses cannot be accurately simulated.

6.4 Case study: A high rock slope in Norway

The Oppstadhornet high rock slope, which is 734 m high and several kilometers wide, is located in western Norway. The geological information is shown in Figure 6-16 (a)-(b). In 1997, the Oppstadhornet rock slope was reported as unstable that could potentially collapse (Robinson et al., 1997). Thereafter, field monitoring was carried out from 2003 to 2011 using the Global Navigation Satellite System (GNSS) (Hermanns et al., 2013) to monitor the slope stability. Displacement was captured on the slope surface; however, the monitored displacement rate was very low, which was about 4.0 mm/yr (Hermanns et al., 2013). Some scholars suggested that such a slow deformation rate of the Oppstadhornet slope is governed by the gravitational creep deformation of the rock mass, rather than by earthquake and rainfall events, which usually result in violent avalanches or rockslide with higher displacement rates (Bhasin and Kaynia, 2004, Blikra et al., 2002). However, due to the difficulty to determine the geology in the rock mass and a lack of effective analysis method to study this issue, the creep deformation mechanism of the Oppstadhornet slope

is still unclear. In this section, creep simulations are carried out to investigate the time-dependent deformation of the Oppstadhornet slope.

The UDEC model of the Oppstadhornet slope is presented in Figure 6-16 (c), which is modified after Bhasin and Kaynia (2004). Possible shear surfaces and steep foliation planes are built in the jointed rock slope model. Such a simplified and idealized model has been proven to be effective to analyze the stability of the Oppstadhornet slope (Bhasin and Kaynia, 2004, Duzgun and Bhasin, 2009).

In the UDEC model, the rock in the blocks is simplified as an isotropic and homogeneous material. The strength and the rheological parameters of the gneiss and schists in the Oppstad area (Grøneng et al., 2009) are listed in Table 6-4. Because there are no static fatigue test data (Schmidtke and Lajtai, 1985) of the rocks, the normalized strength degradation parameters of LdB granite are used for the gneiss and schists. The suggested mechanical properties of the joints (Bhasin and Kaynia, 2004) are also listed in Table 6-4.

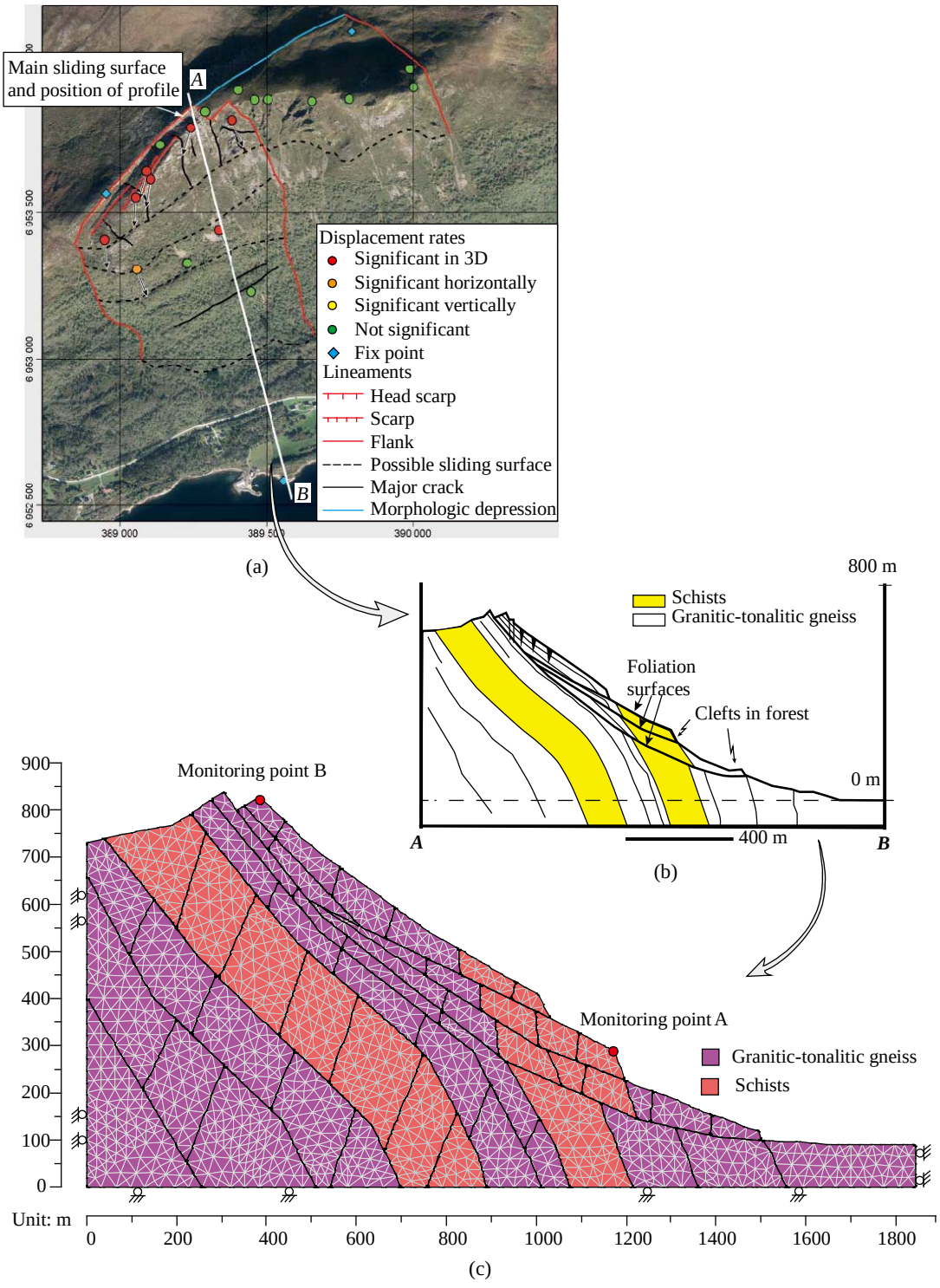

Figure 6-16. Geological information and numerical model of the Oppstadhornet rock slope in Norway: (a) field monitoring of slope deformation (Hermanns et al., 2013); (b) cross section of the main sliding surface (Blikra et al., 2002); (c) UDEC model of the Oppstadhornet slope, constructed after Bhasin and Kaynia (2004).

Table 6-4. Rock mass parameters used in the slope model

Parameter		Value	Reference
Rock properties of Granitic-tonalitic gneiss			Grøneng et al. (2009)
ϕ	Friction angle (°)	45.1	
c	Cohesion (MPa)	9.2	
σ_t	Tensile strength (MPa)	5.0	
E	Young's modulus (GPa)	42.1	
ν	Poisson ratio	0.25	
ρ	Density (g/cm^3)	2.75	
Rock properties of Schists			
ϕ	Friction angle (°)	41	
c	Cohesion (MPa)	7.3	
σ_t	Tensile strength (MPa)	5.0	
E	Young's modulus (GPa)	42.1	
ν	Poisson ratio	0.25	
ρ	Density (g/cm^3)	2.75	
Creep deformation properties of rocks			
G_k	Shear modulus for Kelvin component (Pa)	4.3e12	Grøneng et al. (2010)
η_k	Viscosity coefficient for Kelvin component (Pa^{-1})	4.3e12	
G_m	Shear modulus for Maxwell component (Pa)	1.7e10	
γ	Material constant for Maxwell component	2.75e33	Malan (1998)
β	Material constant for Maxwell component	3.0	
t_0'	Model constant for TtoF model	3.1e-3	Chapter 3
k'	Model constant for TtoF model	8.5e-3	
Joint properties			
Jkn^j	Normal stiffness (Pa/m)	4.25e12	Kulatilake et al. (1992)
Jks^j	Shear stiffness (Pa/m)	1.7e12	
JRC_0	Joint roughness measured in the lab (MPa)	12	

Parameter		Value	Reference
JCS_0	Joint wall compressive strength measured in lab (MPa)	100	Bhasin and Kaynia (2004)
L_0	Length of joint used in lab tests (m)	0.1	
ϕ_b^j	Basic friction angle (°)	30.5	

To investigate the time-dependent response of the jointed rock slope, two types of slope models with different rock joint properties are built. In Model I, the length of joint L_n in the field, which is used to adjust the strength parameters based on the Barton's model (Barton and Bandis, 1980), is determined by the model geometry. The average joint length is about 100 m, and the calculated strength properties of joints using Eqs. (6.2) and (6.3) are listed in Table 6-5. In Model II, L_n is fixed to 1.0 m, as suggested by Bhasin and Kaynia (2004). The calculated strength properties of the joints are listed in Table 6-5. It is seen that Model II has a higher joint strength.

Table 6-5. Joint parameters for two types of slope model

Parameter	Model I	Model II
L_n	around 100 m	1.0 m
Estimated JRC_n	2.29	6.9
Estimated JCS_n (MPa)	8.31	43.6

First, the deformation of the two slope models is calibrated. There are two monitoring points in the slope model (points A and B in Figure 6-16 (c)). The strength degradation parameters of joint are adjusted to calibrate the simulated displacement rate of monitoring point A using the field data. The calibrated displacement rate at monitoring point A and the degradation parameters of joint are listed in Table 6-6 and Table 6-7, respectively.

Next, the simulated displacement rates at monitoring point B of the two calibrated models are compared. The simulated displacement rates at monitoring point B are also presented in Table 6-6. The simulated displacement rate of Model II is 3.8 mm/year, which is closer to the field data. The simulated displacement rate of Model I is 45.6 mm/year, which is much higher than the field data. The simulated displacement curves are presented in Figure 6-17. The results of the two types of models show a large difference, but Model II seems more reasonable because the simulated displacements at the two monitoring points are closer to the field data.

Table 6-6. Calibrated strain rates of the two monitoring points

Strain rate	Model I	Model II	Field data (Hermanns et al., 2013)
Calibrated results at monitoring point A (mm/yr)	4.2	4.2	4.2 ± 0.8
Predicted results at monitoring point B (mm/yr)	45.6	3.8	2.3 ± 0.8

Table 6-7. Calibrated joint degradation parameters of the slope models

Calibrated parameters	Model I	Model II
ξ_0	0.550	0.255
C_j	5.5e-10	1.0e-10

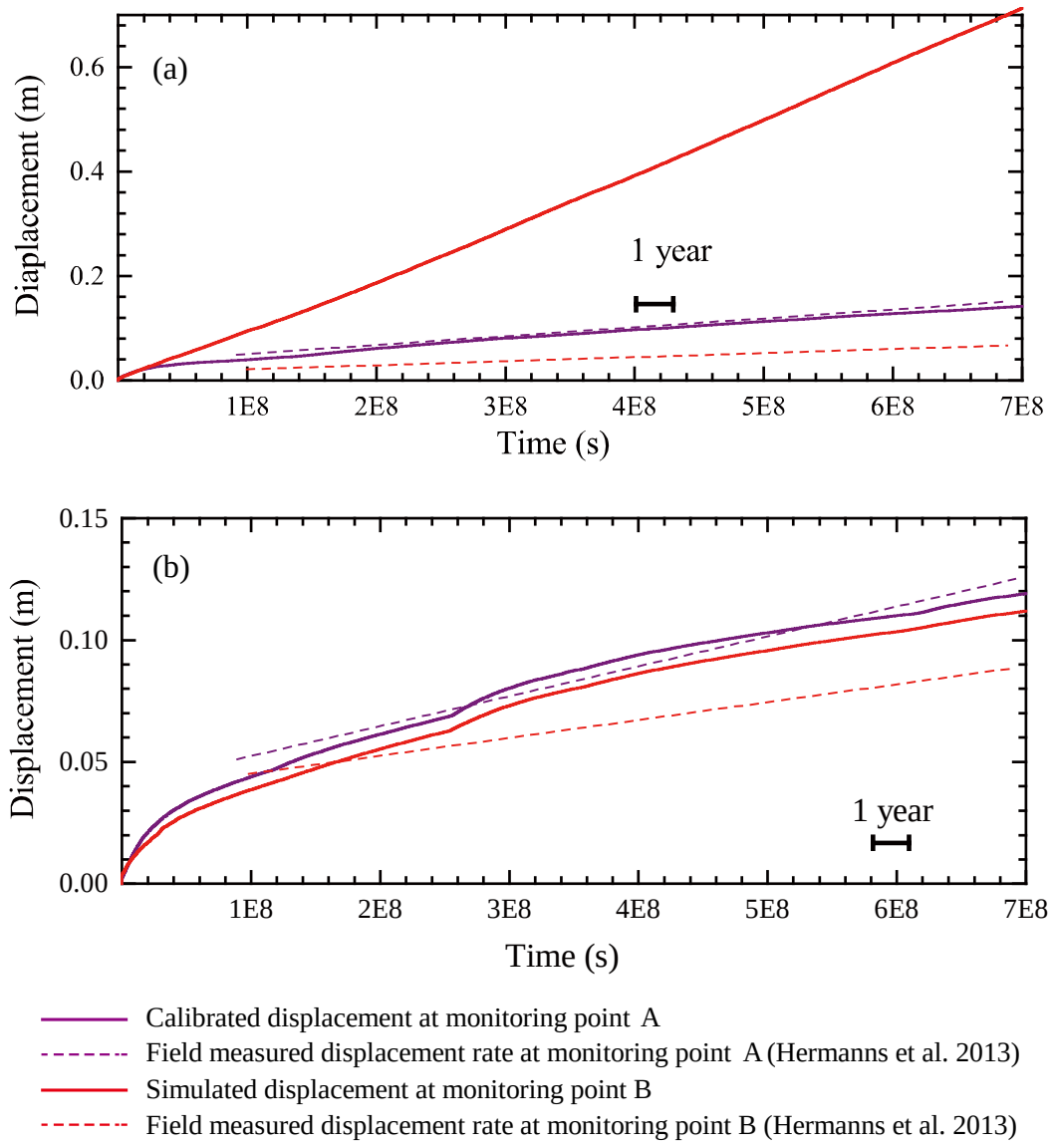

Figure 6-17. Displacement curves of the two monitoring points in the slope models: (a) Model I; (b) Model II.

Finally, the creep deformation mechanism of the Oppstadhornet slope is analyzed using the calibrated slope models. According to the simulation results, the time-dependent deformations of the two models are very different. The deformation mechanisms of the two models are illustrated in Figure 6-18, Figure 6-19 and Figure 6-20. The distribution of the displacement magnitude of Model I is presented in Figure 6-18. It is observed that the movements at the two monitoring points are caused by the sliding of pre-existing joints.

The displacement magnitude of Model II is shown in Figure 6-19. In this model, the creep deformation is caused by the sliding of the steep foliation planes of the rock mass (as marked by the black dashed line in the figure) and the creep deformation of the rocks. There is no significant creep deformation on the potential sliding surfaces, as seen in Figure 6-20 (b), where joints with large sliding velocities are marked. There are many joints with large sliding velocities located on the potential sliding surfaces in Model I. In Model II, the sliding velocities are small, which means that the slope is stable.

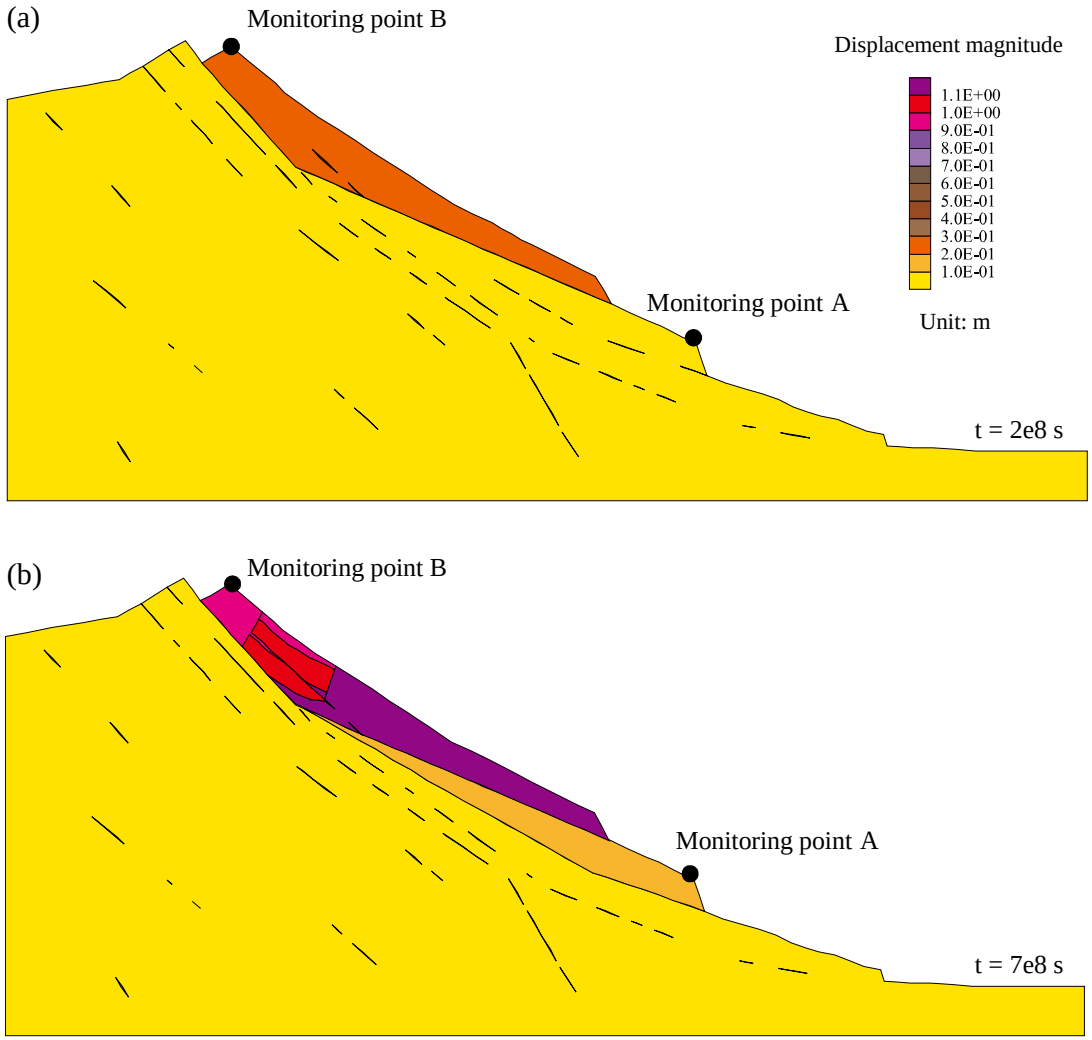

Figure 6-18. Displacement magnitude distributions of slope Model I: (a) *t* = 2e8 s; (b) *t* = 7e8 s.

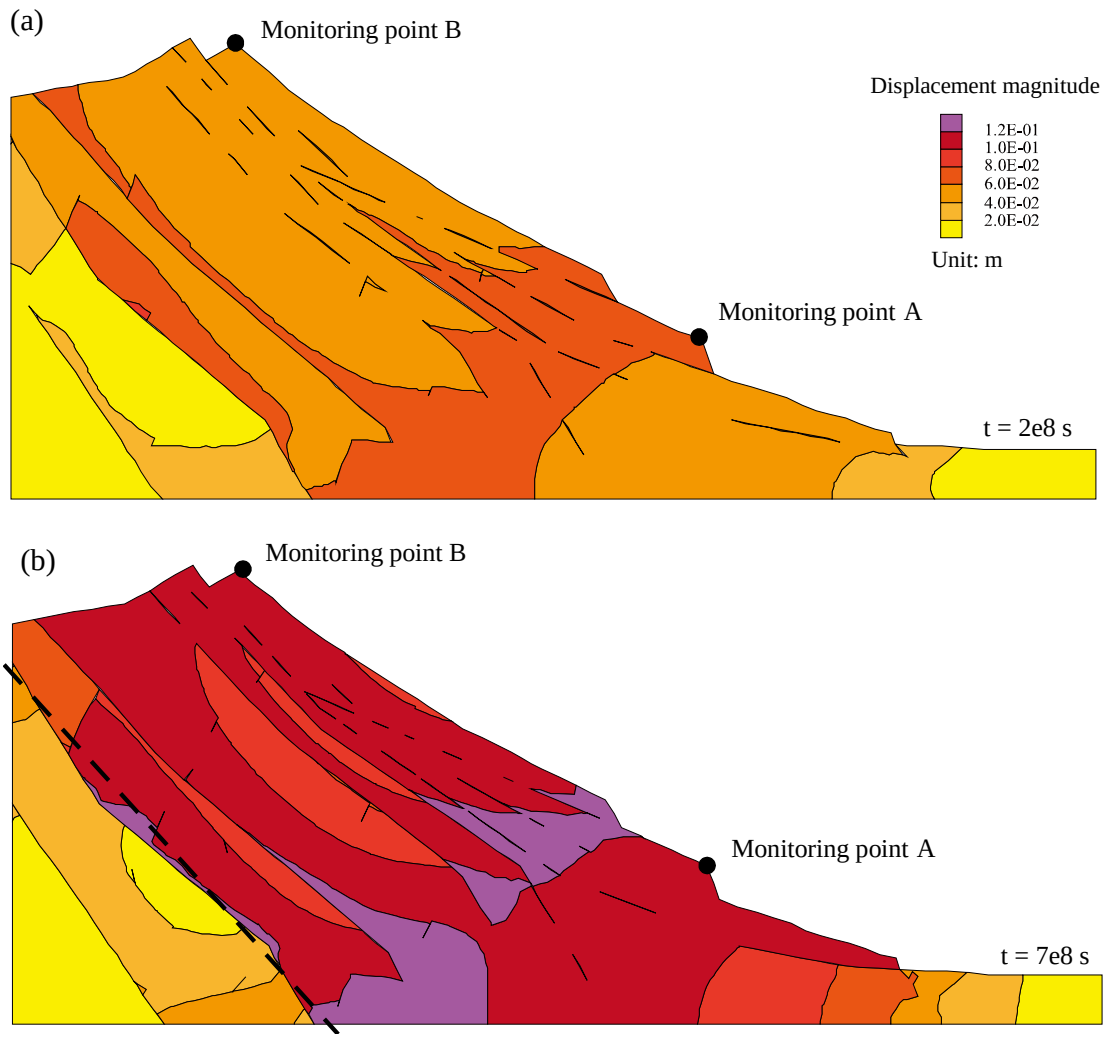

Figure 6-19. Displacement magnitude distributions of slope Model II: (a) *t* = 2e8 s; (b) *t* = 7e8 s.

In summary, the field monitored displacements from 2003 to 2011 of the Oppstadhornet slope (Hermanns et al., 2013) do not indicate any unstable deformation at the potential sliding surfaces. The low displacement rates at the monitoring points are resulted from the slipping deformation of the steep foliation planes and the creep deformation of the rocks as demonstrated in Model II. If the slope were unstable, the monitored displacement rates should have been higher, similar to the simulated displacement rate at monitoring point A in Model I (Figure 6-17 (a)). Hence, the slope was stable in the evaluation period.

Unfortunately, there are no field monitoring data of the Oppstadhornet slope published after 2011 and further comparison of the modeling results with the field condition is not possible.

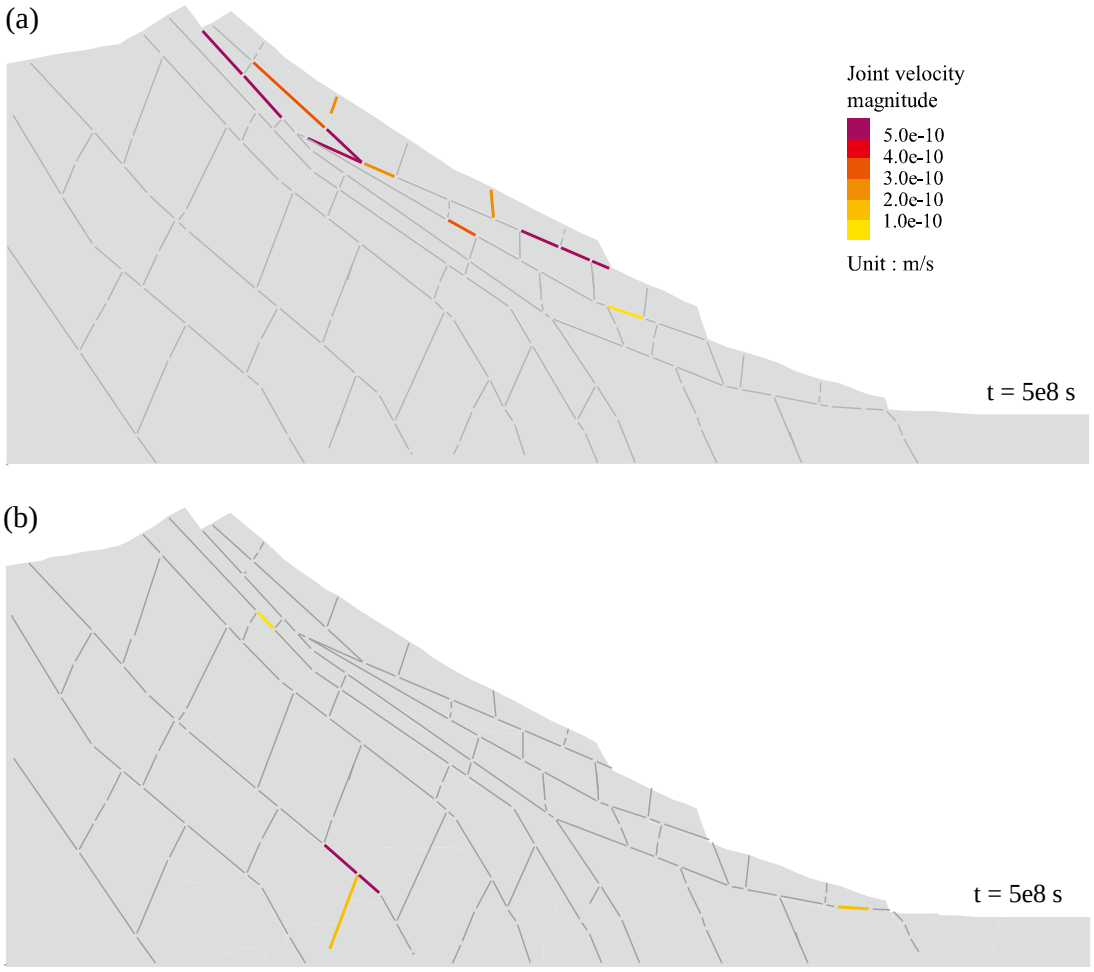

Figure 6-20. Joint velocity magnitude distributions of the two slope models: (a) Mode I, *t* = 5e8 s; (b) Mode II, *t* = 5e8 s.

6.5 Discussion

According to the simulation results of the square models with a single joint, the long-term strength ratio σ_L/σ_S is an important parameter to control the long-term stability of jointed rocks. As shown in Figure 6-9 (d), the σ_L/σ_S ratio is negatively correlated with the

inclination of the joint, but positively correlated with the confining stress. On one hand, it explains why fractures that are sub-parallel to the direction of the maximum principal stress can occur and cause large creep deformations, which can significantly decrease the long-term stability of rock masses. On the other hand, in terms of time-dependent spalling that are usually observed on the walls of rock pillars (Esterhuizen et al., 2011a, Roberts et al., 1998) and tunnels (Martin and Christiansson, 2009), the spalling failures near the surfaces may be attributed to the fact that the rock mass in that region usually has a low long-term strength due to the low confinement near the surface. Therefore, providing confinement can be an effective method to improve the long-term stability of jointed rock masses.

As to moderately jointed rock mass, only one jointed pillar model with non-persistent joints is simulated in this study. However, some characteristics of spatial distribution of joints such as joint density, inclination angle and persistency are not investigated in this study. More modeling and experiments will be carried out in the future to study this issue.

According to the simulation results of the jointed slope model, the maximum vertical stress at the bottom of the model due to gravity is around 16 MPa, which is very low compared with the strength of the rock (Bhasin and Kaynia, 2004). As a result, there should not be significant deformation resulting from the failure of the rock. The simulation results using the normalized strength degradation parameters of LdB granite agree well with this deduction. There is no continual creep damage of rock observed in the slope models. For example, the accumulated damage of Model II at t = 7e8 s is presented in Figure 6-21, in which only some local creep damages due to stress concentration are present. According

to the simulation results, the deformation of the slope models is governed by the sliding of rock joints and the creep deformation of rock.

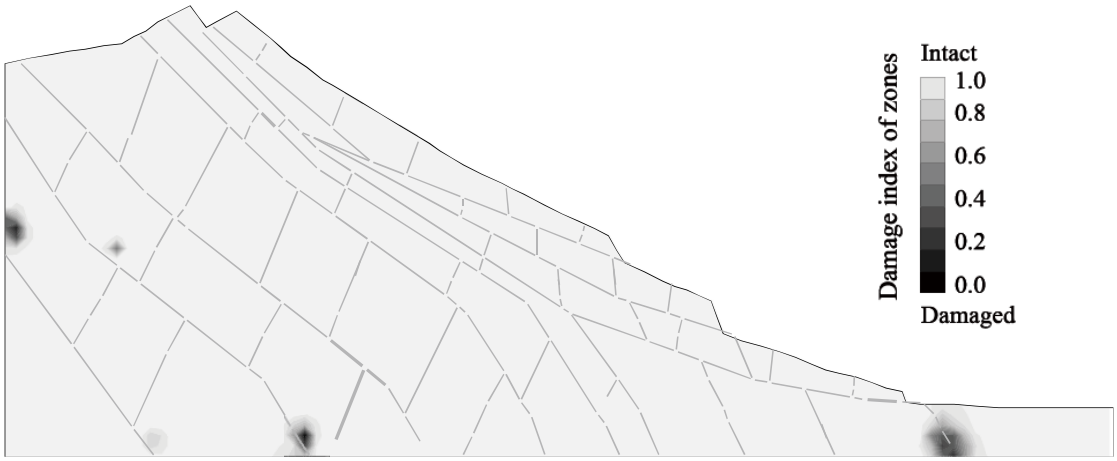

Figure 6-21. Accumulated damage of rock in Model II at t = 7e8 s.

6.6 Summary and conclusion

Creep deformations of jointed rock masses are simulated using a new creep model implemented in UDEC which considers time-dependent deformations of both rock and joints. Large deformations resulting from the creep slipping of joints are captured, and the model provides a novel approach to simulating structural failures of jointed rock masses under creep loading conditions.

The simulation results show that confinement and the angle between the joint sets and the direction of the maximum principal stress influence the time-dependent deformation of jointed rock mass significantly. In particular, providing confinement is an effective method to improve the long-term stability of jointed rock masses.

According to the simulation results of the jointed pillar model, time-dependent responses such as strain rate and the lifetime of rock mass is governed largely by the applied stress. Both the creep deformations of rock and joints contribute to the deformation of jointed rock masses.

The creep deformation of the Oppstadhornet rock slope is simulated using the creep model of jointed rock mass. The simulation results show that there are no significant sliding deformations on the potential sliding surfaces. The monitored creep deformations are resulted from the creep slipping of the steep foliation planes in the rock mass and the creep deformation of the rocks.

In Chapter 7, the creep model for jointed rock mass is used to analyze the time-dependent response of tunnels excavated in jointed rock masses. The weakening process of face-effect due to time-dependent deformation of rock mass will be analyzed and the stand-up time of tunnels simulated.

Chapter 7 Numerical modeling of stand-up time of tunnels considering time-dependent deformation of jointed rock masses

The creep model of jointed rock masses developed in Chapter 6 is used in this chapter to investigate time-dependent deformations of tunnels excavated in jointed rock masses. Displacements on tunnel walls due to time-dependent deformation of rock mass are simulated. The influence of unsupported roof span and rock mass quality on the stand-up time of tunnels are studied numerically. The simulation results are compared with Bieniawski's stand-up time chart to verify the analysis method adopted in this study.

The main research findings presented in this chapter have been published in a paper entitled "Numerical modeling of stand-up time of tunnels considering time-dependent deformation of jointed rock masses" (Wang and Cai, 2022b).

7.1 Convergence-confinement method considering time-dependent deformation of rock mass

7.1.1 Method of obtaining GRC and LDP of tunnels

As mentioned in Section 2.6.1, in two-dimensional analysis using the convergence-confinement method, a hypothetical pressure P_i is applied on the tunnel wall to mimic the face-effect on a tunnel cross-section behind the tunnel face. The hypothetical pressure decreases with the increase of radial displacement on the tunnel wall, which is linked by the ground reaction curve (GRC) shown in Figure 7-1. The longitudinal displacement

profile (LDP) is used to describe the variation of radial displacement along the tunnel due to tunnel face advance. As shown in Figure 7-1, at the tunnel face (normalized distance = 0), the displacement on the tunnel wall is about 30% of the final displacement (for a cross-section far away from the tunnel face, i.e., normalized distance > five). The convergence on a cross-section increases when the cross-section moves away from the face, which can be determined using the LDP. If the LDP and the GRC of a tunnel are known, the pressure and displacement on the tunnel wall can be estimated for any cross-section along the tunnel. For example, at cross-section A-A that is 1.2 *D* from the face, the tunnel convergence is about 59% of the maximum convergence and the pressure is about 10% of the maximum pressure.

Using a two-dimensional tunnel model, several gradual excavation approaches (Cai, 2008) can be used to obtain the GRC of the tunnel. In this study, two approaches, i.e., internal pressure reduction (Figure 7-2(a)) and tunnel core de-stressing with material softening (Figure 7-2 (b)) are used. Both methods can simulate the gradual reduction of the face-effect resulting from the tunnel face advance (Carranza-Torres and Fairhurst, 2000). A circular tunnel excavated in a Hoek–Brown material (with material properties shown in Figure 7-2 (c)) is simulated using UDEC and the simulated GRCs are assembled in Figure 7-2 (d). The simulated GRCs from the two methods are the same as the theoretical curve obtained using the equations from Carranza-Torres and Fairhurst (2000), which proves that these two face-effect simulation methods are equivalent.

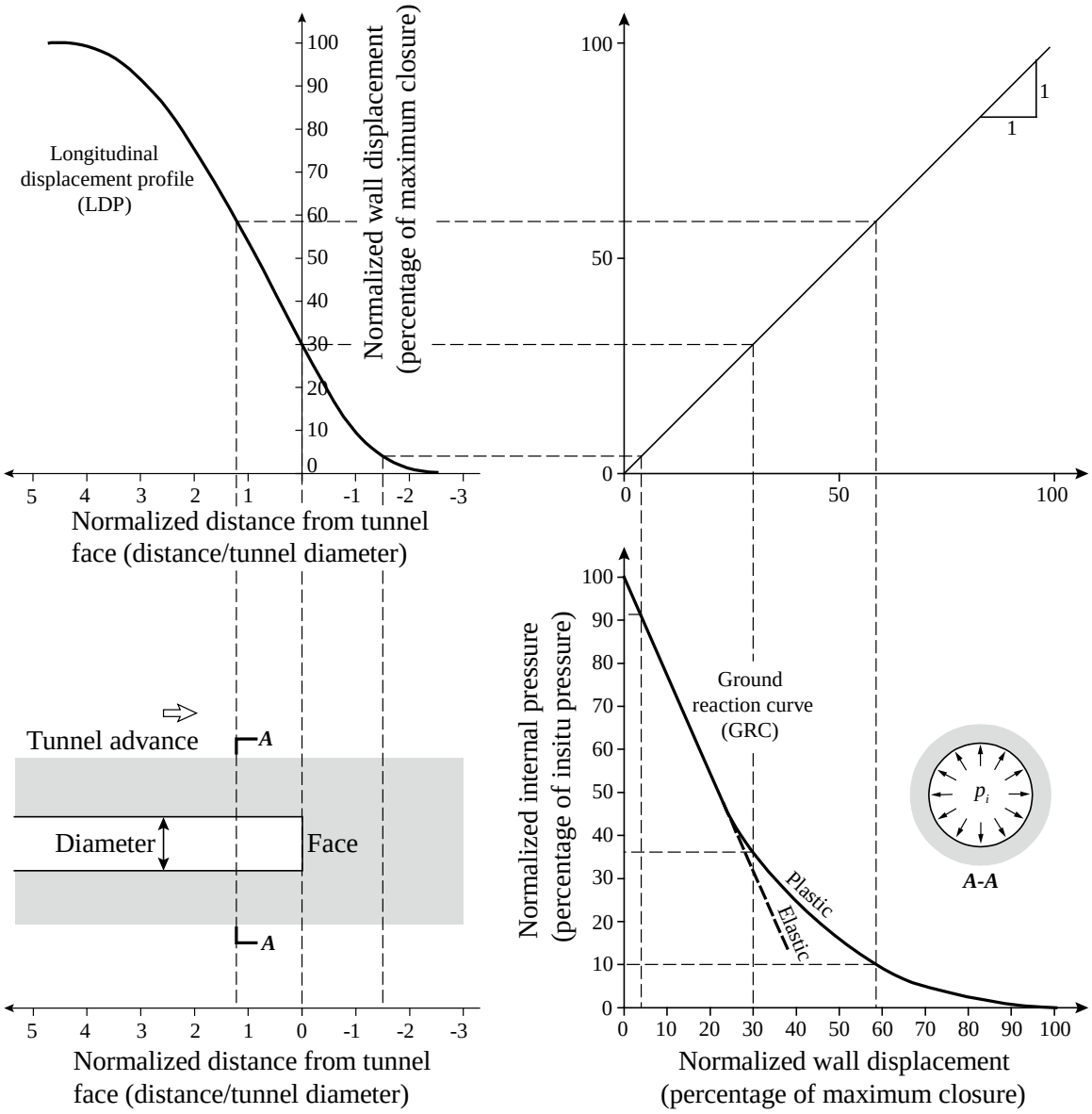

Figure 7-1. The convergence-confinement analysis method, after Carranza-Torres and Fairhurst (2000).

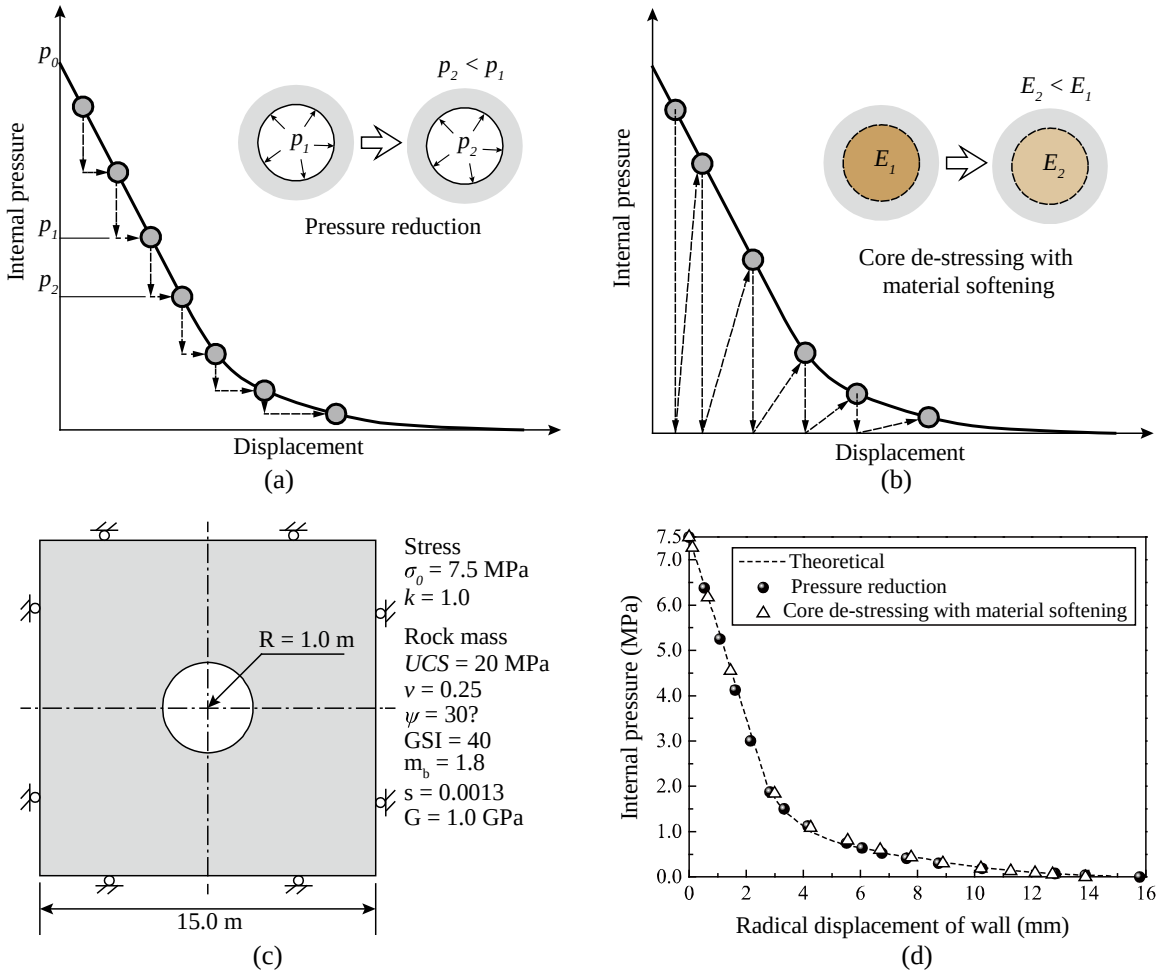

Figure 7-2. Approaches to obtain GRC of tunnel using the two-dimensional analysis method: (a) internal pressure reduction method; (b) tunnel core de-stressing with material softening method ((a) and (b) are modified after Vlachopoulos and Diederichs (2014)); (c) model geometry of a circular tunnel and material properties; (d) theoretical and numerical results of GRCs of the circular tunnel.

The LDP describes the variation of the radial displacement on tunnel walls along the tunnel axis. To determine the LDP curve of a tunnel excavated in an elastic-plastic material, Eq.(7.1), which is proposed by Vlachopoulos and Diederichs (2009), is used in this study.

$$u^* = \begin{cases} \frac{1}{3} e^{2X^* - 0.15R^*} & \text{, for } X^* \le 0 \text{ (ahead of tunnel face)} \\ 1 - (1 - \frac{1}{3} e^{-0.15R^*}) \cdot e^{-\frac{3X^*}{R^*}} & \text{, for } X^* > 0 \text{ (behind tunnel face)} \end{cases} , \qquad (7.1)$$

where u^* is the normalized wall displacement (displacement/maximum displacement), R^* is the normalized plastic zone radius (maximum plastic zone radius/tunnel radius R), and X^* is the normalized distance (distance to the tunnel face/tunnel diameter D (= $2R$)).

The LDP curve of a circular tunnel with R^* = 1.7 is presented in Figure 7-3. Using the LDP curve, the radial displacement on any cross-section along the tunnel axis can be estimated. For example, for a cross-section that is 0.6D away from the face, the displacement on the wall is 72.5% of the maximum value.

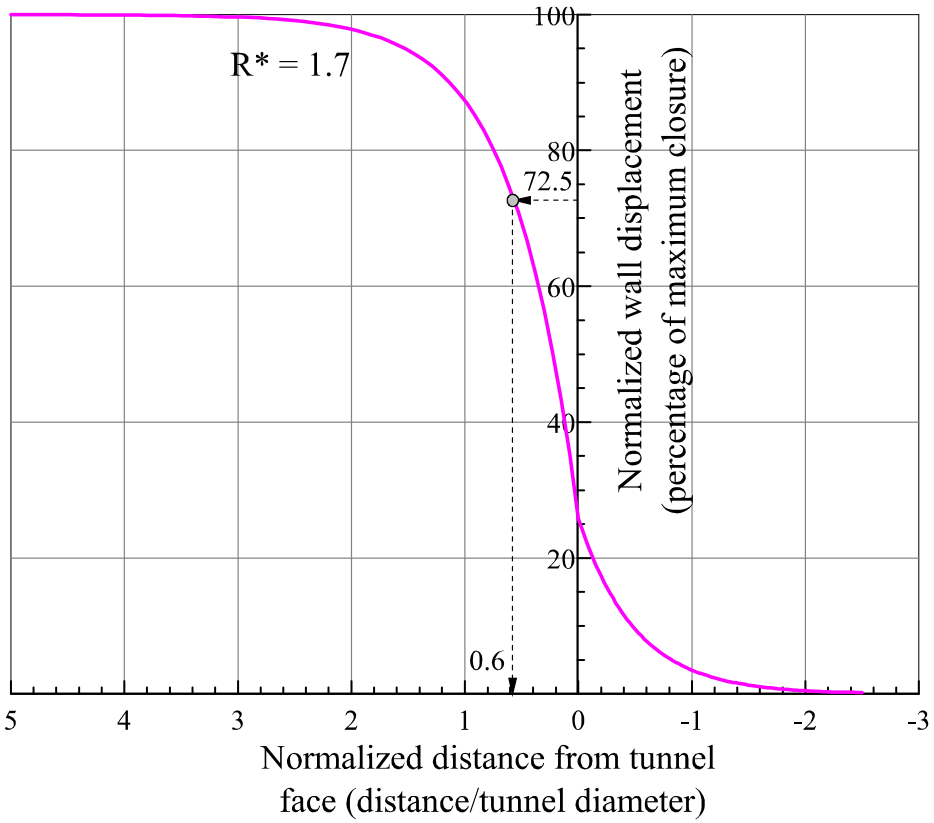

Figure 7-3. LDP curve of a circular tunnel with R^* = 1.7.

7.1.2 Influence of time on the GRC and LDP profiles

Tunnel wall deformations are caused not only by face advance but also by time-dependent deformation of rock mass (Kontogianni et al., 2006). In an excavated tunnel, even if the face stops advancing, the radial displacements keep increasing due to creep deformation of rock mass, which can be observed in the field (Barla et al., 2010).

When time-dependent deformation of rock mass is considered, both the GRC and the LDP become time-dependent. The influence of time-dependent deformation of rock mass on the GRC and LDP profiles is demonstrated in Figure 7-4. For the same level of internal pressure, more displacements will occur in an elastic-visco-plastic rock mass than in an elastic-plastic rock mass. As a result, the shapes of GRC are different for these two types of materials (Kabwe et al., 2020b, Panet et al., 2001). The plastic radius around the tunnel expands due to strength degradation of rock mass near the elastic-plastic interface (Sakurai, 1978). According to Eq.(7.1), the shape of the LDP is changed due to the increase of the maximum plastic radius R^* (e.g., when R^* increases from 1.0 to 1.5, the LDP changes from the blue curve to the pink curve, as shown in Figure 7-4).

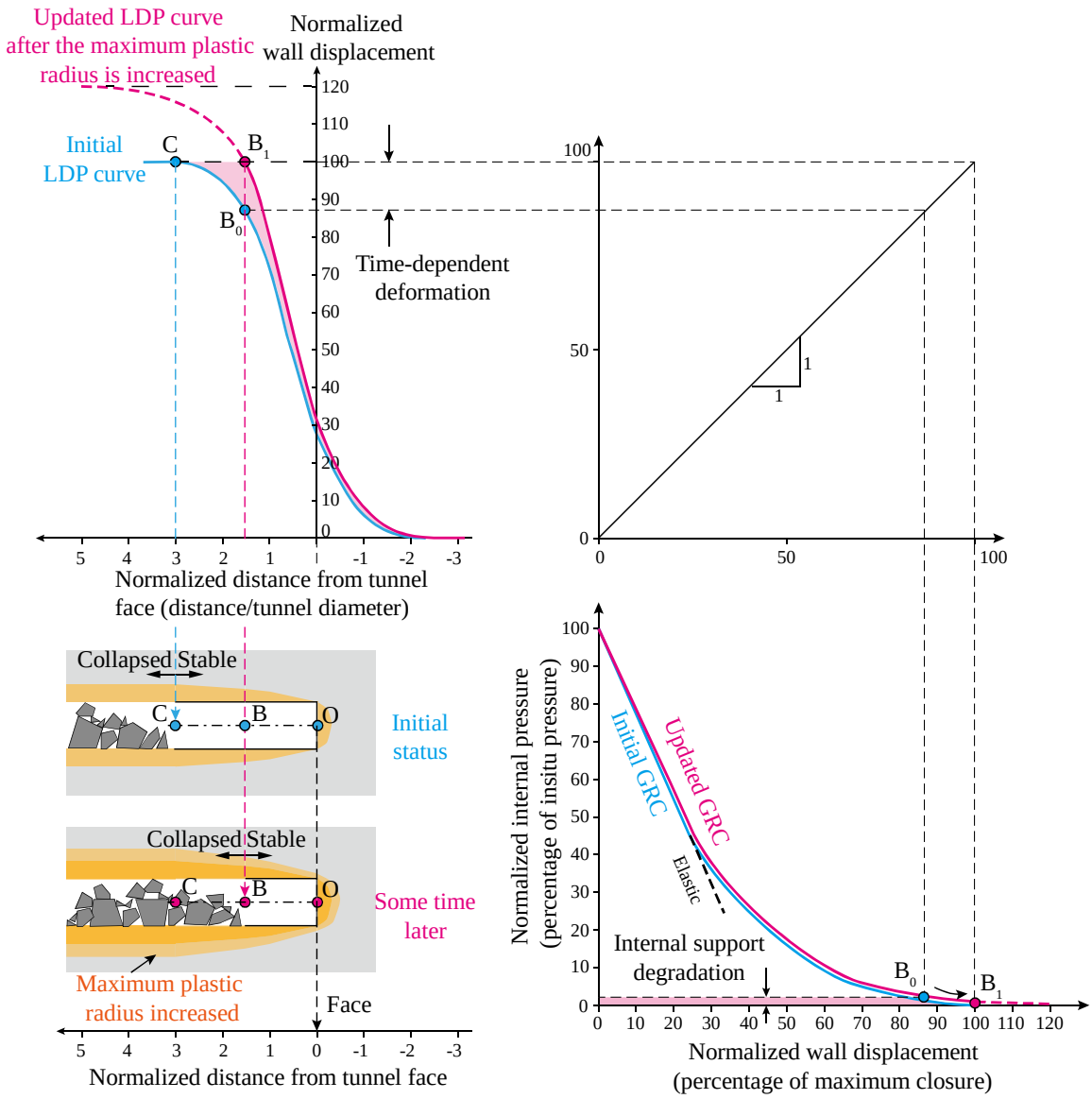

Figure 7-4. Influence of time-dependent deformation of rock mass on GRC and LDP profiles of tunnels.

Figure 7-4 illustrates how the face-effect (internal support pressure) decreases due to time-dependent deformation of rock mass. For the tunnel cross-section at point B (B_0 represents the initial status and B_1 represents the status after some time), which is 1.5D behind the tunnel face, the convergence is around 87% of the maximum displacement at the initial status according to the LDP curve. The internal pressure is about 3% of the maximum value.

After some time, the displacement increases at point B due to time-dependent deformation of the rock mass. According to the updated LDP curve, the displacement increases from 87% to 100% of the initial maximum value. The internal pressure reduces to zero, as shown in the GRC graph (from point B_0 to B_1).

For a tunnel excavated in a jointed rock mass, if the displacements on the wall are too large, the tunnel will collapse and lose the support from the face, rather than keep deforming excessively (Sakurai, 1997, Kuesel et al., 2012, Abdollahi et al., 2019). By assuming a deformation limit on tunnel walls, Nguyen and Nguyen (2015) obtained an analytical solution of stand-up time of tunnels, which shows the longitudinal relation between the stand-up time and the unsupported roof span of tunnels presented on Bieniawski's stand-up time chart. Therefore, it can be assumed that a tunnel cross-section has a radial deformation threshold. When the deformation exceeds the threshold, the tunnel will collapse and lose all the internal support. For the case illustrated in Figure 7-4, it is assumed that the displacement threshold is the maximum displacement value of the initial status. The tunnel within the section OC is at the initial status, and the tunnel is stable. The tunnel on the left of point C is unstable. After some time, the displacement at point B increases from 87% to 100% of the previous maximum value due to time-dependent rock mass deformation. As a result, the tunnel within section BC will be unstable.

In this section, a preliminary understanding about the time-dependent deformation behavior of tunnels is achieved using the convergence-confinement analysis. The continuous deformation of tunnel walls and the reduction of support from the face due to time-dependent deformations of rock mass are explained theoretically. Next, time-

dependent deformation behaviors of tunnels are simulated numerically using UDEC. Two-dimensional plane strain models are built, and creep deformations of both rock and joints are considered using a creep model for jointed rock masses. The creep model used, numerical model setup, simulation approaches and results are introduced respectively in the subsequent parts of the thesis.

7.2 Simulation of time-dependent deformation of a tunnel cross-section

In this study, both the deformations of rock and joints are modeled as time-dependent, using the creep model of jointed rock masses developed in Chapter 6. Model parameters of the TtoF creep model for intact rock and joints presented in Table 6-1 and Table 6-2, which are calibrated using laboratory data of rock and joints, are directly used in this chapter to model time-dependent behavior to tunnels excavated in jointed rock mass.

7.2.1 Model setup

Several tunnel models in jointed rock masses are built using UDEC. The model geometry and boundary condition are shown in Figure 7-5. The width of the back-arched tunnels is 5.0 m (the equivalent diameter D is 5.4 m) and the whole model size is 35 m × 35 m. To reduce computing time, only a zone of 15 m × 15 m around the tunnel is modeled as jointed rock mass and the rest of the model is modeled using an elastic material. It has been checked that there are no failed rock zones and joint elements near the jointed rock mass–continuum rock mass interfaces in all simulation cases for the in-situ stress and material properties used in this study. This ensures that the accuracy of the simulation results is not influenced significantly due to the model simplification. Roller boundaries are applied at

the bottom and the two sides of the model, and a stress boundary is applied on the top of the model. For the in-situ stress field, the vertical stress σ_v is 35 MPa, the horizontal stress σ_H is 60 MPa and the out-of-plane stress σ_h is 50 MPa, which is equivalent to the field stress at a depth of about 1300 m with k = 1.7 in the Canadian Shield (Herget, 1987). Gravity is applied to the models.

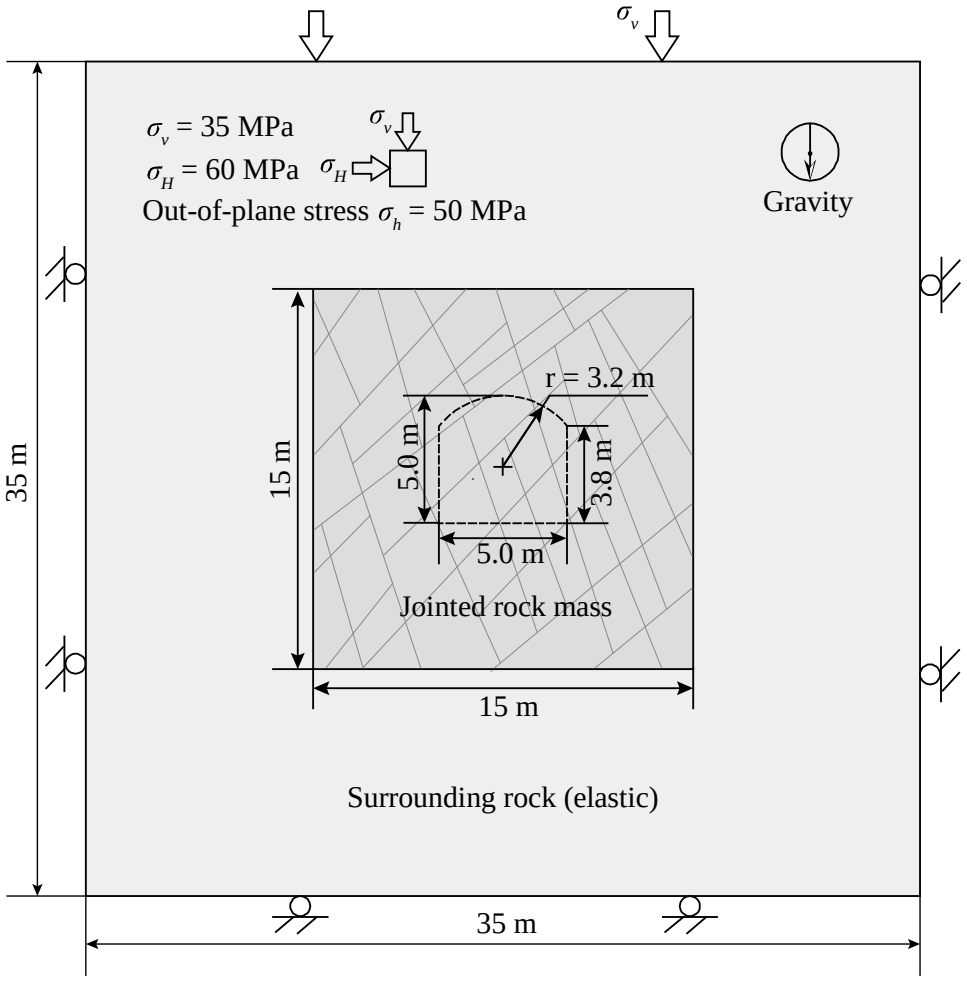

Figure 7-5. Model geometry and boundary condition.

The model responses depend on the degree of jointing. Three types of jointed rock masses are considered in this study, and Model I with the joint parameters shown in Table 7-1 is presented in Figure 7-6. There are four non-persistent joint sets whose inclination angles

range from 30° to 140°. The roughness parameter (JRC_0) of the joints ranges from 2 to 4. Rocks in the blocks are meshed into triangular finite difference zones with an average edge length of 0.1 m.

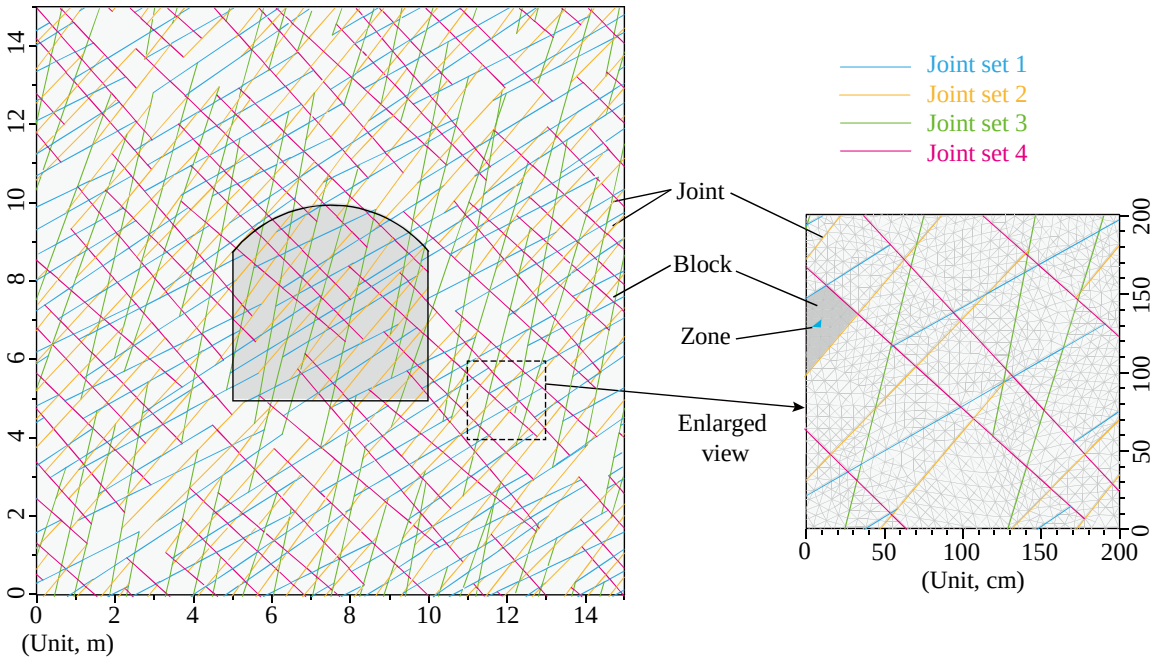

Figure 7-6. Joint set distributions and zone meshing of tunnel Model I.

Table 7-1. Joint set properties of tunnel Model I

Joint set	Inclination angle (°)	Spacing (m)	Trace length (m)	Gap length (m)	JRC_0
1	35 ± 5	0.5 ± 0.2	5.0 ± 1.0	0.4 ± 0.1	4
2	50 ± 5	0.5 ± 0.1	5.0 ± 5.0	0.3 ± 0.15	4
3	75 ± 5	0.7 ± 0.2	8.0 ± 1.3	1.3	2
4	135± 5	0.7 ± 0.2	6.0 ± 1.2	1.0	2

7.2.2 Construction of GRC and LDP

The GRC of tunnels introduced in Section 7.1.1 is needed using the convergence-confinement analysis method. For tunnel Model I, the tunnel shape is arch-backed and the material around the tunnel is jointed rock mass, which leads to complex stress distribution on the tunnel walls. As a result, it is extremely difficult to obtain the GRC curve directly using the internal pressure reduction method, and the tunnel core de-stressing and material softening approach is used. The Young's modulus of the tunnel core is softened gradually, and the displacement and resistant force on each grid point are traced. In this manner, the GRC on each grid point on the tunnel walls can be obtained.

This approach is achieved by writing a FISH script in UDEC and the flowchart is presented in Figure 7-7. Firstly, in-situ stress, boundary conditions and gravity are applied and cycling steps are taken to bring the model to an initial equilibrium; then, the displacements on the tunnel walls are reset to zero. Next, the Young's modulus of the tunnel core is softened step by step and the stress in the core is reset to zero in each step. According to Vlachopoulos and Diederichs (2014), the softening step size should not be too large; otherwise, it would influence the shape of GRC. To address this issue, the Young's modulus is softened 5% to 10% at the elastic stage, and as small as 1% at the plastic stage. After each modulus softening, the stress in the core is reset to zero at the same time, and then cycling steps are taken for the model to reach equilibrium and the stresses and displacements of each grid point on the walls are recorded. The modulus softening process is repeated until the Young's modulus of the tunnel core reaches zero. Finally, a GRC for each grid point is obtained, forming a GRC series for the tunnel walls. The average GRC

of the model can then be calculated, which will be used for the subsequent analysis. The average GRC defined in this way shows the relation between the average displacement and the Young's modulus of the tunnel core (or average internal support pressure). It represents the average deformation status of the tunnel cross-section during the tunnel core softening process. GRCs of three grid points and the average GRC of Model I are shown in Figure 7-8.

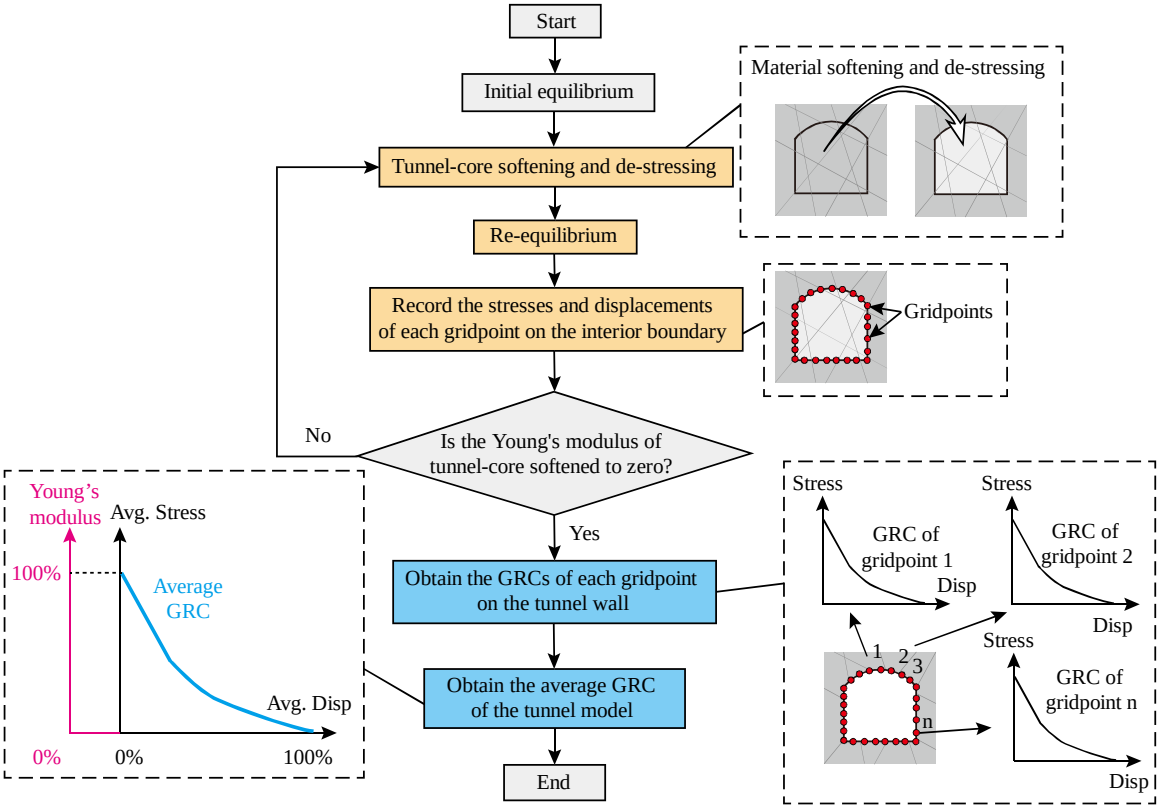

Figure 7-7. Flowchart showing the process of obtaining GRCs of a back-arched tunnel using the tunnel core softening and de-stressing method.

Because the tunnel shape is not circular, the in-situ status is not hydrostatic, and the rock mass is discontinuum, there are no analytical solutions that can be used to obtain the LDP curve. Moreover, it is not possible to obtain the LDP curve of a tunnel using a two-

dimensional cross-section model. Therefore, Eq. (7.1) from Vlachopoulos and Diederichs (2009) is used to approximate the LDP curve of tunnel Model I.

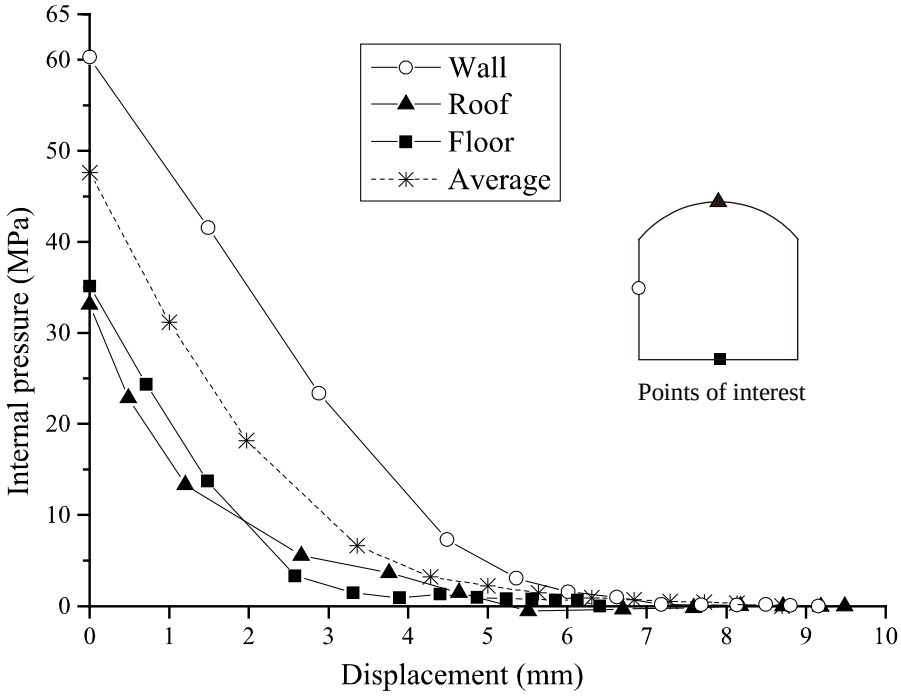

Figure 7-8. GRC curves of selected points of Model I.

7.2.3 Internal pressure reduction

Combining the GRC and LDP curves obtained, the convergence-confinement method is used to simulate time-dependent deformation in a cross-section along the tunnel. The procedure is presented in the flowchart shown in Figure 7-9 and explained below.

First, the initial deformation status of the cross-section under consideration is assigned and the corresponding model parameters are obtained. For example, for a cross section 8.0 m away from the face, it has a 60% deformation of the maximum value, which will be referred to as the start point on the average GRC. As introduced in Section 7.2.2, a point on the average GRC can be referred to the deformation status of a cross section during the tunnel

core softening process. Then, the numerical model corresponding to the deformation status referred to by the start point on the average GRC needs to be obtained. It starts with the unexcavated model, and then soften the tunnel core gradually. After the equilibrium is reached, the tunnel model has a 60% average convergence. This mimics the tunnel excavation and face advancing process (the face advanced 8.0 m in this case). At this step, the numerical model with the assigned deformation status is ready. Thereafter, the face advancing is stopped and only time-dependent deformation is considered in the simulation. It should be noted that the average GRC is just used at this step (i.e., at the start of creep calculation) to determine the stress and displacement on the walls. In the subsequent steps, GRC curves of each grid point that have been obtained in Section 7.2.2 are used to analyze the stress and displacement on each grid point.

Second, the displacements on each grid point on the walls are measured. As mentioned in Section 7.1.1, the GRC curves recorded represent the relations between the internal pressure and displacement of each grid point on the tunnel walls. Using the GRC curves of each grid point, the normal pressures to be applied on each grid point based on the current displacements can be determined. Then, the tunnel core is deleted while applying the internal pressure on each grid point simultaneously. By this step, the internal support from the tunnel core media is replaced by equivalent pressures applied on the grid points.

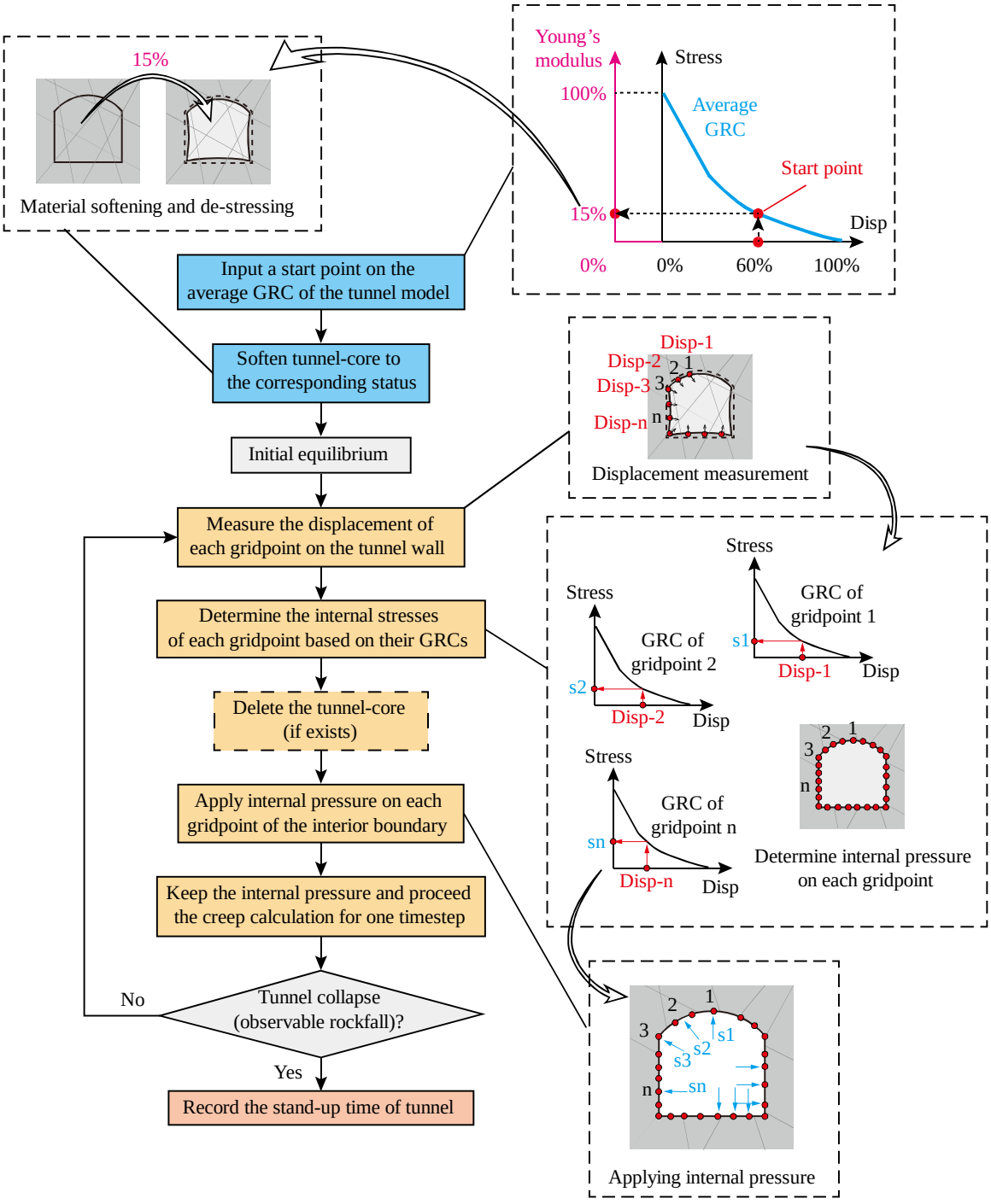

Figure 7-9. Flowchart illustrating the internal pressure reduction process using the convergence-confinement analysis approach. Coupled with the creep deformation simulation, this allows modeling the stand-up time of unsupported tunnels.

Third, the creep calculation is carried out. The internal pressure is kept constant during the creep calculation in one time step. In this study, the time step is set to 72 hours, which is

long enough to ensure that the creep deformations on the walls can grow sufficiently at each time step so that the internal pressure adjustment at the subsequent step is accurate. During the time step, the convergence on the walls will increase due to time-dependent deformation of the jointed rock mass, which is resulted from visco deformation of rock blocks, plastic flow of yield zones due to strength degradation, and creep sliding of joints.

After the creep calculation is finished, the displacements on the walls are measured again, then the internal pressure on each grid point is adjusted based on the respective GRC curve obtained in Section 7.2.2.Then, another round of creep calculation is executed for one time step. The procedure is repeated until there are observable rockfalls on the walls or in the roof, which can be used to judge tunnel instability. In this manner, the time-dependent deformation of a tunnel cross-section can be simulated.

It should be noted that the creep calculation starts when the tunnel face stops advancing. As a result, time-dependent deformation during the tunnel face advancement is not considered.

7.2.4 Simulation example

Time-dependent deformation of a tunnel cross-section (Model I) is simulated using the method introduced in Section 7.2.3. It is assumed that the tunnel cross-section has a 72.5% of the maximum average displacement when the face stops advancing, and time-dependent deformation on the tunnel cross-section is simulated.

The displacement magnitudes of the rock blocks at different times are presented in Figure 7-10, which shows that the convergence increases over time. When t = 0 s, the displacement

due to face advance is small. Then, creep calculation is started and creep deformations occur in the jointed rock mass. At t = 1.5e6 s (17 days), rocks on the roof start to fall down continuously. Therefore, it can be judged that the cross-section collapses at t = 1.5e6 s. After about 3.3 months (t = 8.5e6 s), rockfall from the roof stops and the tunnel is stable afterwards. The notch depth is about 1.3 m, as shown in Figure 7-10 (e).

In this study, the maximum plastic radius R^* in Eq. (7.1) is an important parameter for determining the LDP curve of a tunnel. Using two-dimensional cross-section models, the R^* of a tunnel model can be estimated by measuring the equivalent radius of plastic zones when the tunnel collapses. For the simulation example, the plastic zone distributions around the tunnel at different time are presented in Figure 7-11. It shows that at t = 0 s some yielded zones and joints occur within 1.3 times of the equivalent tunnel diameter D. At t = 1.5e6 s (17 days), with more yielded zones and joints occurring in the model, the tunnel collapses and the plastic zones expand to about 1.7 times of the tunnel diameter D. It can be judged from Vlachopoulos and Diederichs (2009) that R^* = 1.7, which will be used in subsequent analysis.

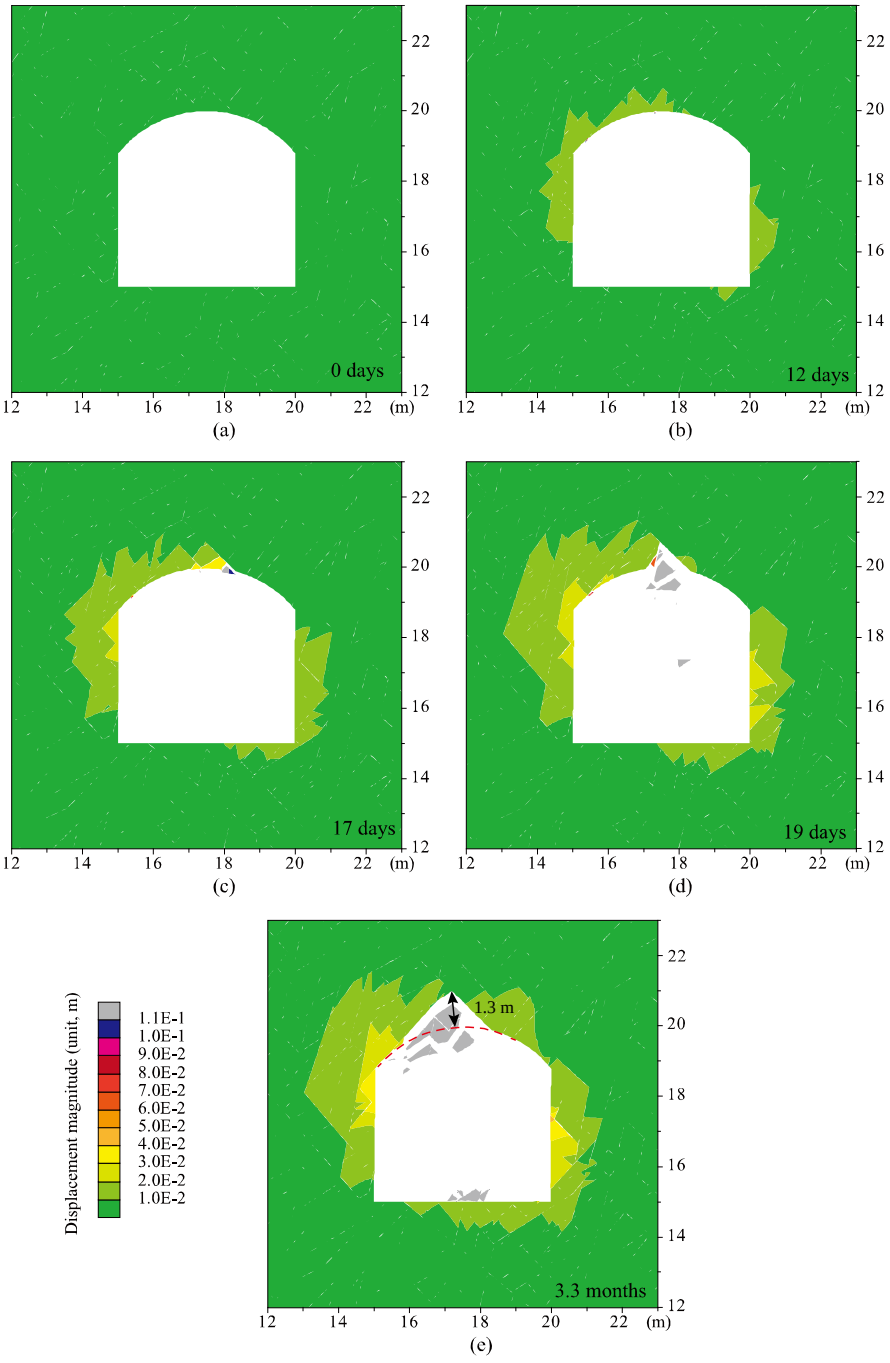

Figure 7-10. Displacement magnitude contours of analysis Case B: (a) t = 0 s; (b) t = 1e6 s (12 days); (c) t = 1.5e6 s (17 days), rocks start falling from the roof; (d) t = 1.7e6 s (19 days), rockfalls from the roof occur continuously; (e) t = 8.5e6 s (98 days or 3.3 months), the notch on the tunnel roof stabilizes.

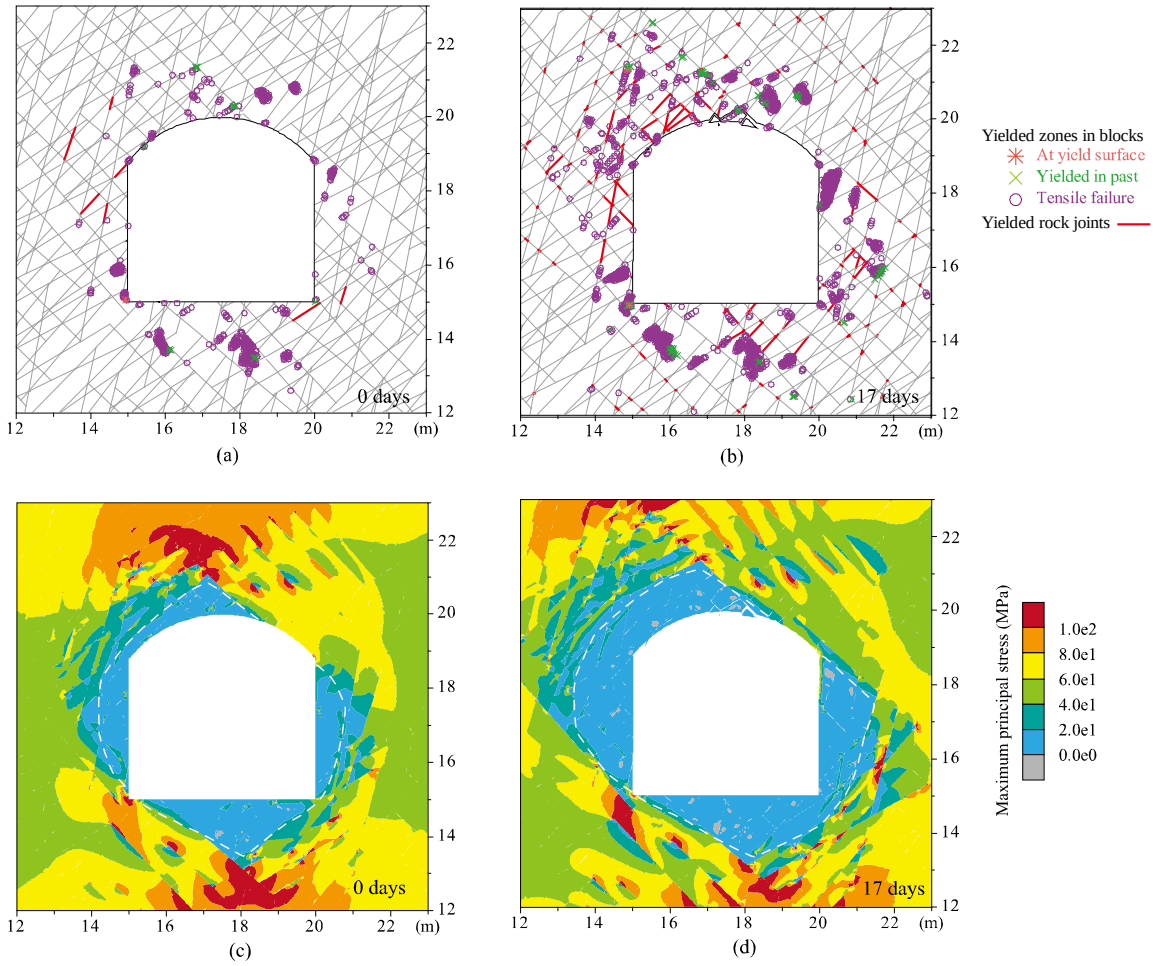

Figure 7-11. Plastic zone and stress distributions of analysis Case B. Yielded zones and joints around the tunnel: (a) t = 0 s; (b) t = 1.5e6 s (17 days). Maximum principal stress distributions: (c) t = 0 s; (d) t = 1.5e6 s (17 days).

Because the mechanical response of rock joints is time-dependent, the status of each rock joint is monitored during the creep calculation. The distribution of the sliding velocity of rock joints at t = 1.0e6 s (12 days) is presented in Figure 7-12. It can be seen that many joint elements near the tunnel wall are in creep sliding status, contributing to the time-dependent deformation of the jointed rock mass.

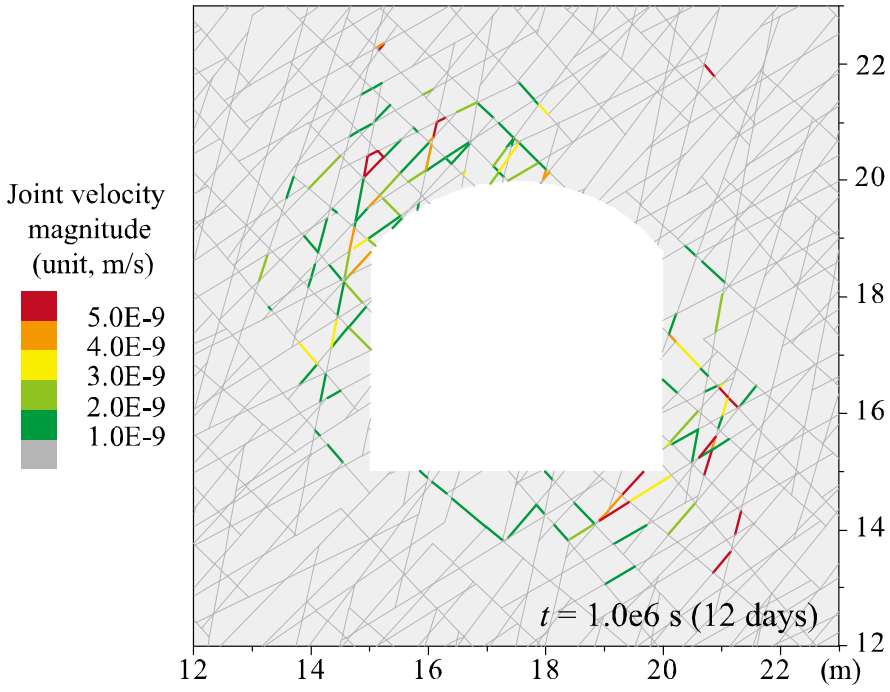

Figure 7-12. Rock joints in creep sliding status of analysis Case B at t = 1.0e6 s (12 days).

The time-dependent deformation of rock blocks also plays an important role in affecting the time-dependent deformation of the jointed rock mass. The visco deformation of intact rock is governed by the Burgers model, and the strength of the zones in rock blocks degrades with time when the stress is higher than the long-term strength. Newly yielded zones can generate more plastic deformation. The accumulated damage in each zone is monitored in the creep calculation step and represented by the damage index, which is a dimensionless parameter used to measure the degree of damage of a zone (1.0 represents intact and 0 represents totally damaged). The distributions of the accumulated damages in rock blocks at three times are presented in Figure 7-13. It can be seen that damage around the tunnel accumulates over time due to strength degradation of intact rock, which contributes to the time-dependent deformation of the jointed rock mass.

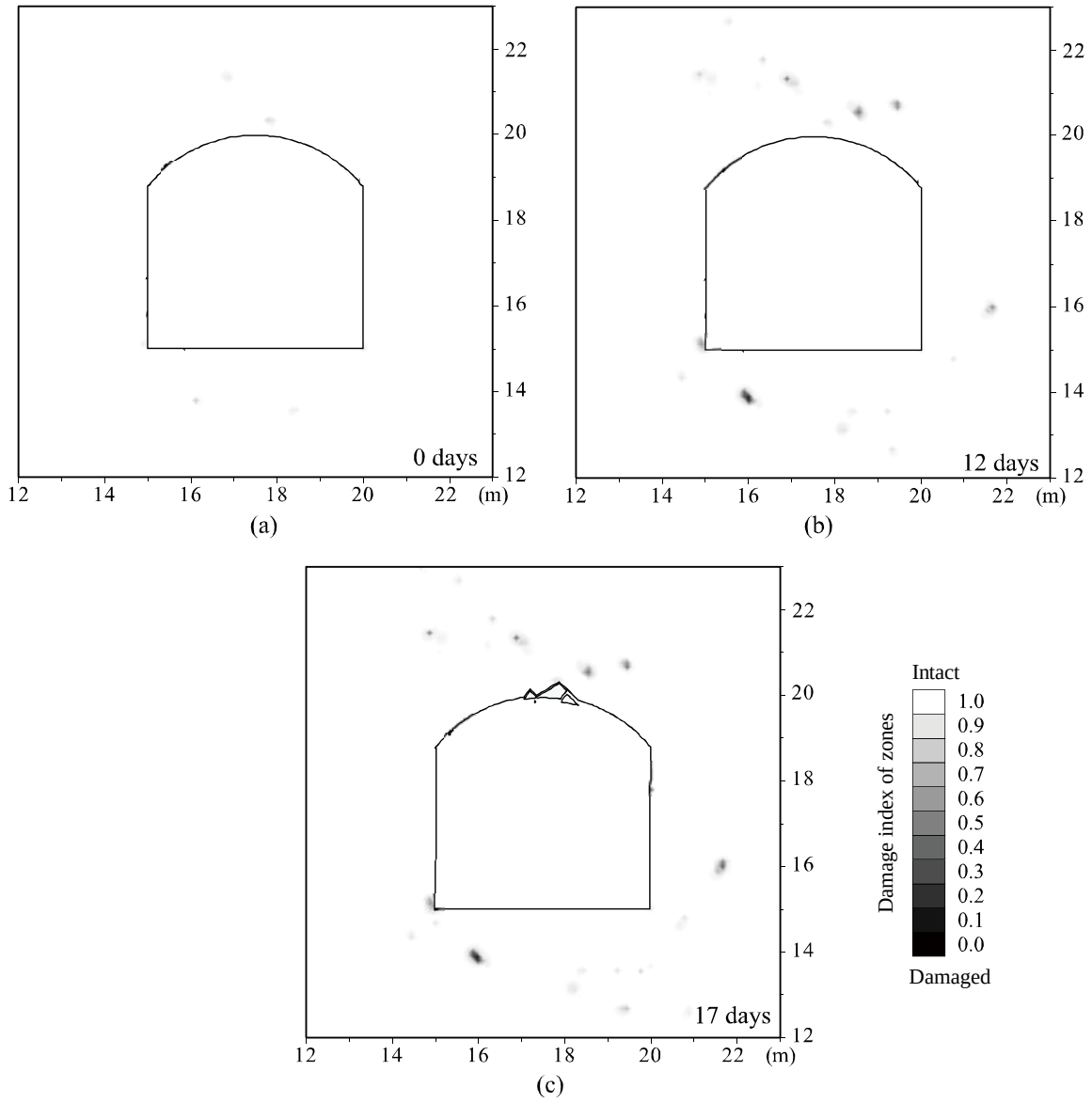

Figure 7-13. Contours of accumulated damage of zones of analysis Case B: (a) t = 0 s; (b) t = 1e6 s (12 days); (c) t = 1.5e6 s (17 days).

The lifetime evolution of the tunnel cross-section traced on the average GRC can be demonstrated in Figure 7-14. At the initial status (when face advancement is stopped), around 4% of internal pressures are applied on the interior boundary of the tunnel model. Then, creep calculation is started. Deformations on the tunnel wall increase, which results in the reduction of the internal pressure. As the creep deformation cycle is repeated, the

support from the face to the cross-section is gradually weakened. At t = 1.5e6 s (17 days), even though there are still some internal pressures on several grid points on the wall, these supports are not strong enough to prevent the rock blocks from falling down, and the collapse of the tunnel is inevitable. In this manner, the weakening of the support from the face due to time-dependent deformation of rock mass is simulated.

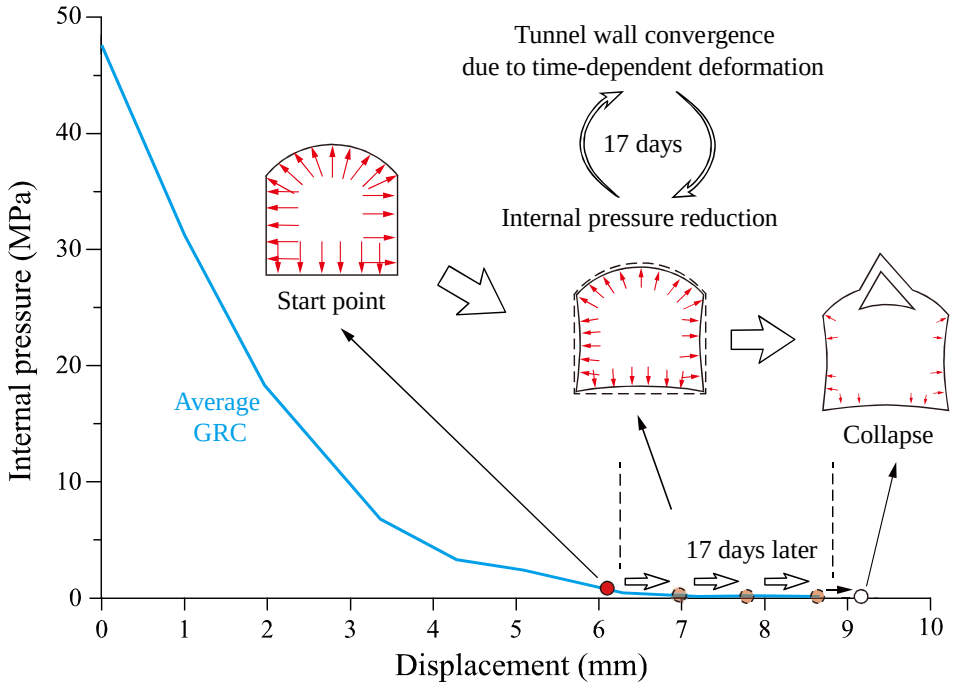

Figure 7-14. Lifetime evolution traced on the average GRC of analysis Case B of tunnel Model I.

7.3 Simulation of stand-up time of unsupported tunnels

7.3.1 Simulation of stand-up time of tunnels with different unsupported roof spans

In Section 7.2, the time-dependent deformation of a tunnel cross-section is simulated. The methodology provides an approach to investigate the stand-up time of tunnels with different unsupported roof spans. For an analysis case of a given initial status, the wall displacement can be obtained at the location along the tunnel axis using the LDP curve. If

it is assumed that the tunnel cross-section is located at the supported/unsupported interface, the long-term stability of the tunnel can be analyzed.

As an example, Case B represents a cross-section location with a 72.5% of the maximum convergence, which is about 0.6 *D* (or 3.3 m) from the face (Figure 7-3). As mentioned in Section 7.2.4, the maximum plastic radius is estimated to be 1.7 *R* for this LDP curve. It is assumed that this cross-section is located at the interface of the supported and the unsupported sections of the tunnel, as shown in Figure 7-15. Because it is the farthest cross-section away from the tunnel without rock support, it determines the stand-up time of the tunnel with a 3.3 m unsupported roof span. It should be noted that the influence of installed rock support behind the cross-section cannot be considered using this method.

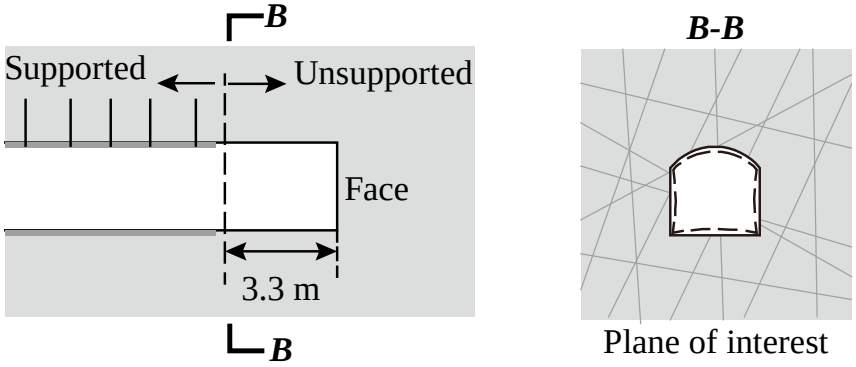

Figure 7-15. Location of the plane of analysis (Case B).

In a similar fashion, tunnels with four different unsupported roof spans of Model I are analyzed. As shown in Figure 7-16, the unsupported roof spans of the four cases are 2.4, 3.3, 5.1 and 7.0 m. The average displacement and initial internal pressure of each case are assembled in a table shown in Figure 7-16.

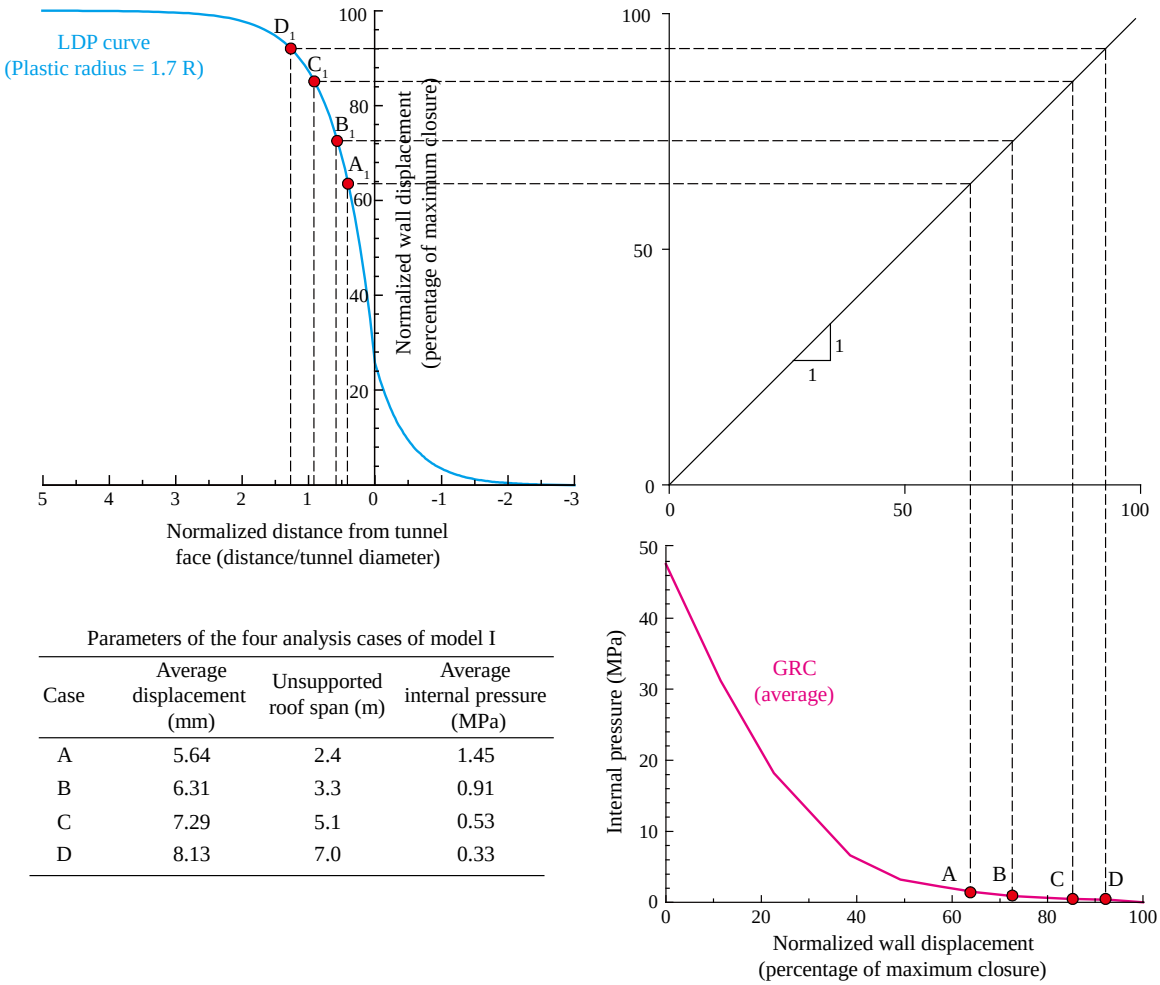

Parameters of the four analysis cases of model I

Case	Average displacement (mm)	Unsupported roof span (m)	Average internal pressure (MPa)
A	5.64	2.4	1.45
B	6.31	3.3	0.91
C	7.29	5.1	0.53
D	8.13	7.0	0.33

Figure 7-16. Parameters of the four analysis cases of tunnel Model I.

Next, the stand-up times of the four cases are simulated. The displacements on the roof of the tunnel are monitored during creep simulation and the results are presented in Figure 7-17. The initial convergences of the four cases are different because they have different initial internal pressures due the face-effect for cross-sections at different locations. The convergences on the roof increase with time due to the creep deformation of the rock mass. The simulated stand-up time of Case B (for an unsupported roof span of 3.3 m) is 1.5e6 s (17 days). For Case A, whose unsupported roof span is 2.4 m, the simulated stand-up time is 1.6e6 s, which is about 19 days. For Cases C and D, whose unsupported roof spans are

5.1 and 7.0 m, respectively, the simulated stand-up times are 13 and 8 days, respectively. It shows that a tunnel with a larger unsupported roof span usually has a shorter stand-up time.

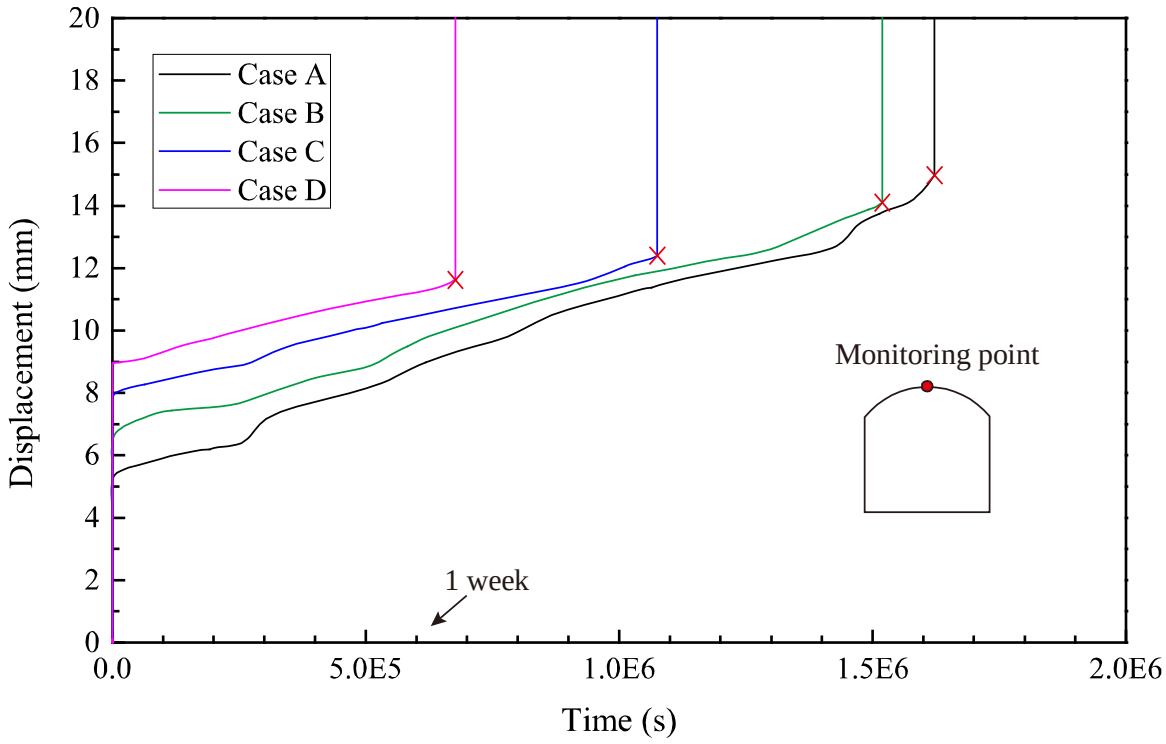

Figure 7-17. Creep strain curves of the monitoring point on the top of the roof of tunnel Model I.

7.3.2 Influence of rock mass quality on stand-up time

Rock mass quality is an important factor that influences long-term stability of tunnels (Bieniawski, 1989). In this section, another two tunnel models with different joint set parameters are built to investigate the influence of rock mass quality on the stand-up time of tunnels. As shown in Figure 7-18, there are three and two sets of joints in tunnel Models II and III, respectively. The joint set geometrical and strength parameters of the two models

are assembled in Table 6-3 and Table 6-4. The width of the tunnels and the in-situ stresses are the same as those of Model I.

The GRCs of Models II and III are obtained using the approach introduced in Section 7.1.1 and the results are presented in Figure 7-19.

Table 7-2. Joint set properties of tunnel Model II

Joint set	Inclination angle (°)	Spacing (m)	Trace length (m)	Gap length (m)	JRC_0
1	50 ± 5	1.8 ± 0.2	8.0 ± 0.2	0.2 ± 0.1	10
2	75 ± 5	3.3 ± 0.3	9.0 ± 0.3	0.2	8
3	130 ± 5	2.4 ± 0.2	9.0 ± 0.2	0.2	10

Table 7-3. Joint set properties of tunnel Model III

Joint set	Inclination angle (°)	Spacing (m)	JRC_0
1	50 ± 5	4.4 ± 0.5	15
2	130 ± 5	3.5 ± 0.5	15

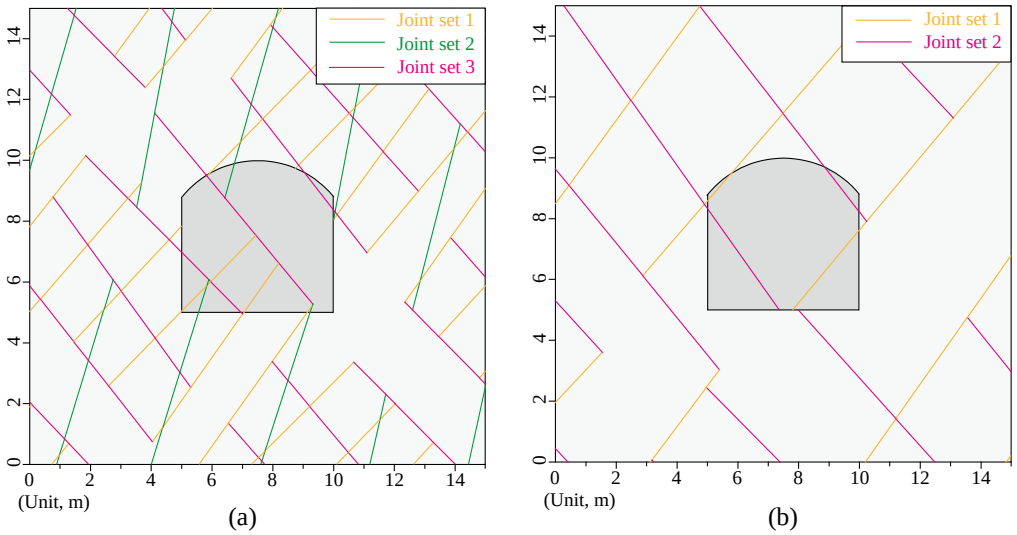

Figure 7-18. Two tunnel models with different joint set properties: (a) tunnel Model II; (b) tunnel Model III.

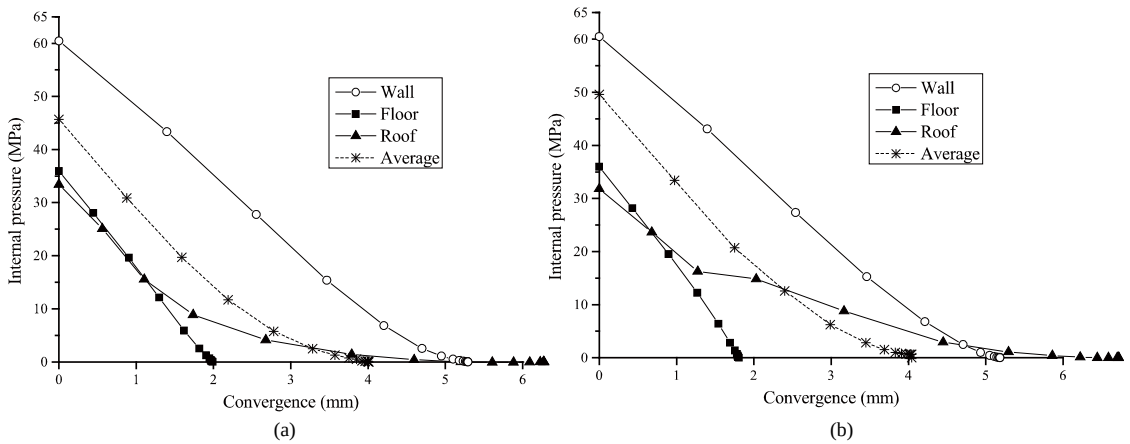

Figure 7-19. GRC curves of tunnel Model II (a) and tunnel Model III (b).

Using tunnel Model II, three analysis cases with different unsupported roof spans (Cases E, F and G, shown in Figure 7-20) are simulated. For the initial statuses of Cases E, F and G, the average convergences on the wall are 3.28, 3.82 and 4.00 mm, which are 81.8%, 96.0% and 99.8% of the maximum value, respectively. Based on simulation results, the plastic radius after the tunnel is fully excavated is about 1.3 *R*; therefore, the maximum plastic radius is estimated to be 1.3 *R* for this case. According to the LDP curve, the unsupported roof spans of the Cases E, F and G are 3.5, 6.5 and 10.3 m, respectively. The simulation results of plastic zones and creep damage of Case F are presented in Figure 7-21. At t = 0 s, there is no observable damage in the cross-section. At t = 1.4e6 s (16 days), there are some accumulated damage in the model, and rock blocks start to fall down from the roof. Thus, the simulated stand-up time of Case F of tunnel Model II is 1.4e6 s.

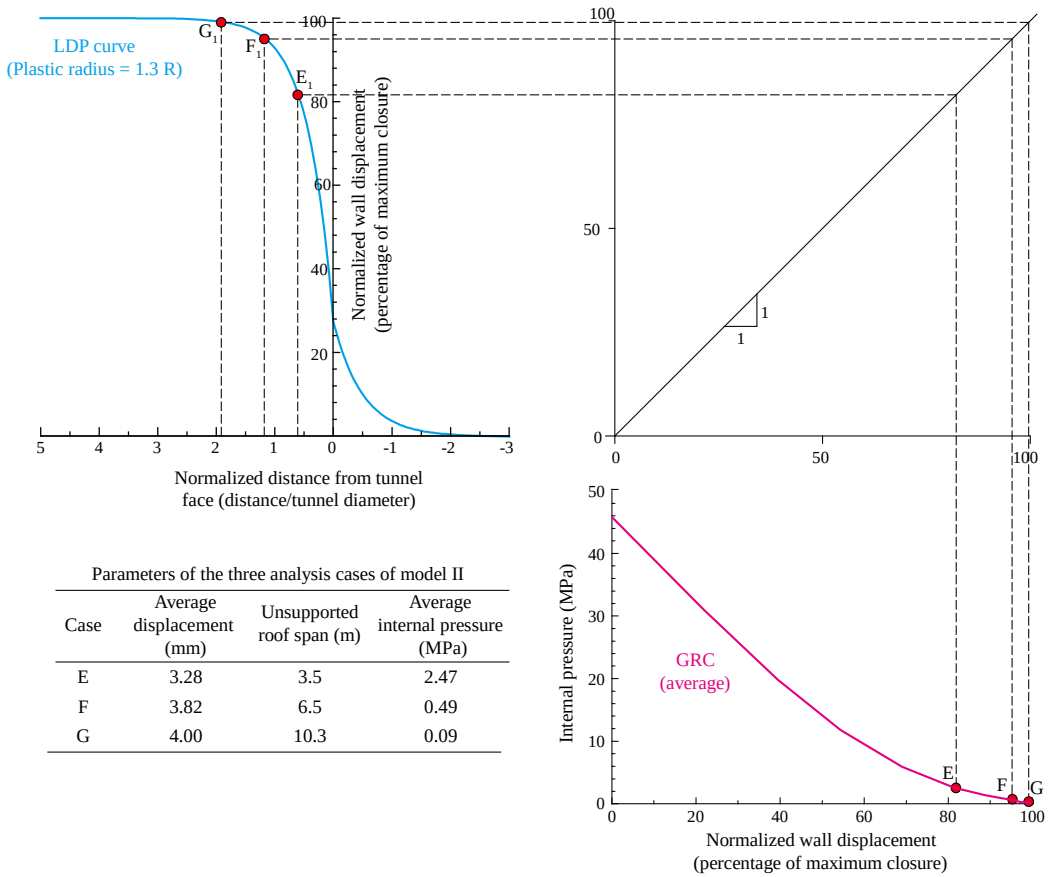

Parameters of the three analysis cases of model II

Case	Average displacement (mm)	Unsupported roof span (m)	Average internal pressure (MPa)
E	3.28	3.5	2.47
F	3.82	6.5	0.49
G	4.00	10.3	0.09

Figure 7-20. GRC and LDP curves and modeling parameters of the three analysis cases of tunnel Model II.

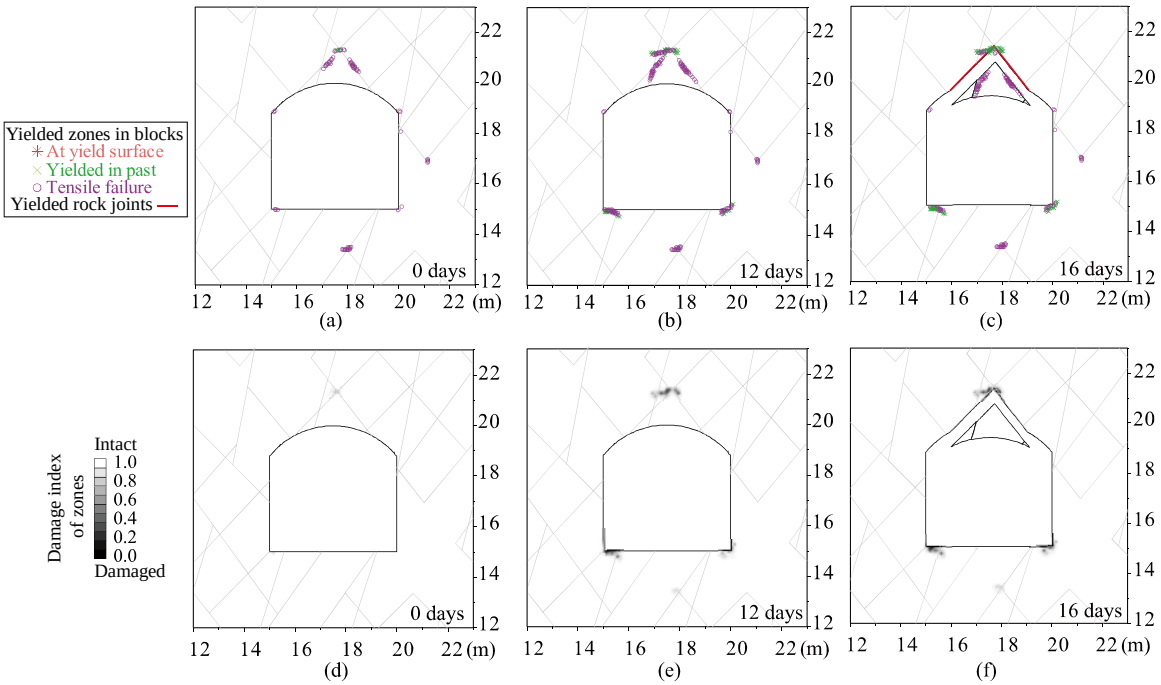

Figure 7-21. Plastic zones and creep damages of analysis Case F. Yielded zones and joints: (a) t = 0 s; (b) t = 1.0e6 s (12 days); (c) t = 1.4e6 s (16 days), rocks fall from the roof. Accumulated creep damage of zones: (d) t = 0 s; (e) t = 1.0e6 s (12 days); (f) t = 1.4e6 s (16 days).

Using tunnel Model III, Cases H, I, J and K (Figure 7-22) are analyzed. The initial average convergences of Cases H, I, J and K are 2.99, 3.45, 3.91 and 4.04 mm, which are 74.0%, 85.4%, 9,68% and 99.9% of the maximum convergence, respectively. According to the LDP curve (the maximum plastic radius is 1.2 R for the case), the unsupported roof spans of the four cases are 2.4, 3.5, 6.8 and 18.1 m, respectively. The simulation results of Case I are presented in Figure 7-23. The tunnel is stable until t = 9.0e6 s (3.5 months) when a wedge falls down from the roof, and there are some accumulated damages in the cross-section (Figure 7-23 (d)). Hence, the stand-up time of this case with an unsupported span of 3.5 m is about 3.5 months.

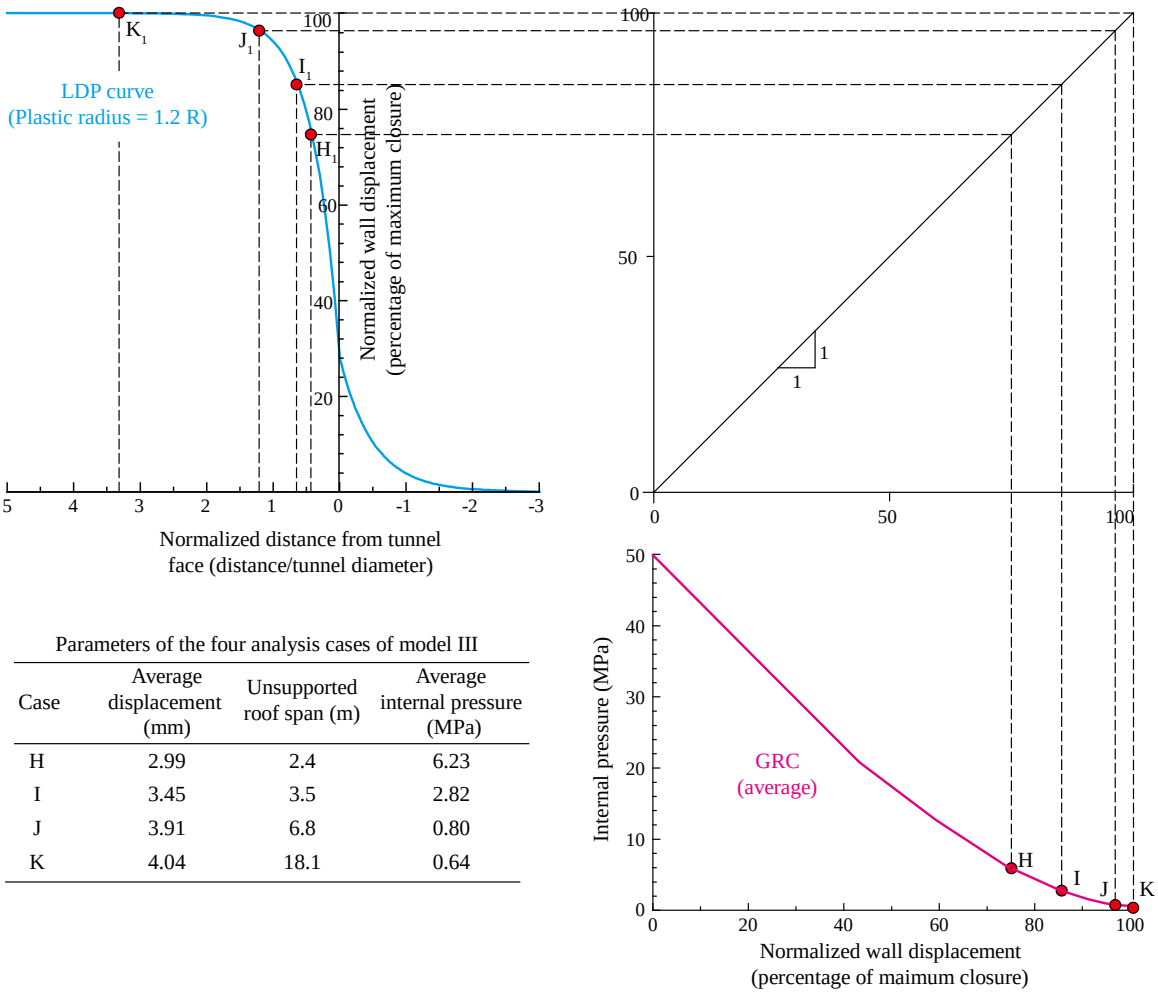

Parameters of the four analysis cases of model III

Case	Average displacement (mm)	Unsupported roof span (m)	Average internal pressure (MPa)
H	2.99	2.4	6.23
I	3.45	3.5	2.82
J	3.91	6.8	0.80
K	4.04	18.1	0.64

Figure 7-22. GRC and LDP curves and modeling parameters of the four analysis cases of tunnel Model III.

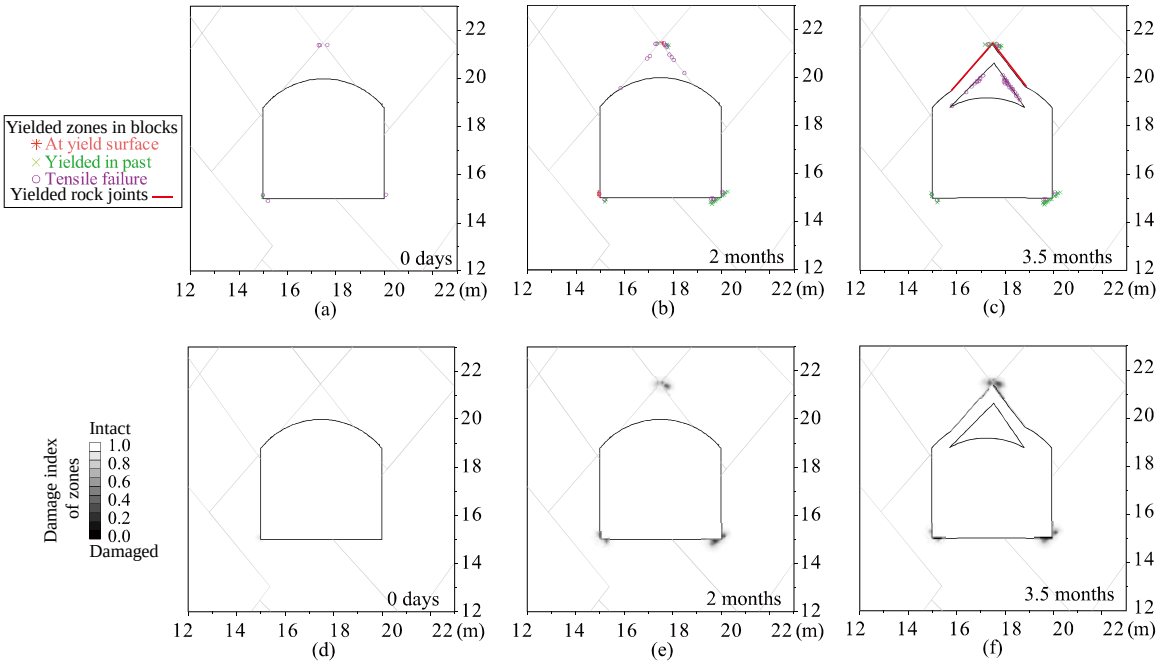

Figure 7-23. Plastic zones and creep damages of analysis Case I. Yielded zones and joints: (a) t = 0 s; (b) t = 5.0e6 s (2 months); (c) t = 9.0e6 s (3.5 months), rocks fall from the roof. Accumulated creep damage of zones: (d) t = 0 s; (e) t = 5.0e6 s (2 months); (f) t = 9.0e6 s (3.5 months).

The rock mass qualities of the three tunnel models (Models I, II and III) are evaluated using the Q system, which is suitable for deep tunnels because the stress condition can be considered. The Q value is calculated using the following equation,

$$Q = \frac{RQD}{J_n} \cdot \frac{J_r}{J_a} \cdot \frac{J_w}{SRF}, \tag{7.2}$$

where RQD is rock quality designation, J_n is joint set number, J_r is joint roughness number, J_a is joint alteration number, J_w is joint water reduction factor and SRF is stress reduction factor.

Based on the in-situ stress, joint set parameters and the mechanical properties of joints, Q values of the three tunnel models are calculated and the results are presented in Table 7-4,

Table 7-5 and Table 7-6. In all cases, J_a = 1 and J_w = 1 are assumed. Based on the Q values, RMR values are obtained using Eq. (7.3) (Barton, 1995).

$$RMR = 15\log(Q) + 50. \tag{7.3}$$

Table 7-4. Rock mass rating of tunnel Model I using the Q system

Parameter	Value	Description
RQD	85%	Average value using four different scanlines in the rock mass model
J_n	15	Four sets of joints
J_r	2	Smooth joint (JCS_0 = 2 to 4)
J_a	1.0	Fresh joint walls
J_w	1.0	No water
SRF	15	UCS / σ_1 = 3.7 (3 to 5)
Q	0.8	*RMR* = 49

Table 7-5. Rock mass rating of tunnel Model II using the Q system

Parameter	Value	Description
RQD	99.7%	Average value using four different scanlines in the rock mass model
J_n	9	Three sets of joints
J_r	3	Rough or irregular, undulating (JCS_0 = 8 to 10)
J_a	1.0	Fresh joint walls
J_w	1.0	No water
SRF	15	UCS / σ_1 = 3.7 (3 to 5)
Q	2.2	*RMR* = 55

Table 7-6. Rock mass rating of tunnel Model III using the Q system

Parameter	Value	Description
RQD	100%	Average value using four different scanlines in the rock mass model
J_n	4	Two sets of joints
J_r	4	Rough joint (JCS_0 = 13 to 15), and spacing greater than 3 m
J_a	1.0	Fresh joint walls
J_w	1.0	No water
SRF	15	UCS / σ_1 = 3.7 (3 to 5)
Q	6.7	*RMR* = 62

Based on the RMR values and the unsupported tunnel spans, the simulated stand-up times of the 11 cases are plotted in Bieniawski's stand-up time chart, as shown in Figure 7-24. It shows that the simulated stand-up times of tunnels with different unsupported roof spans, excavated in rock masses of different qualities agree well with the trend reckoned from the field data. It validates the effectiveness of the proposed method in simulating the time-dependent behavior of tunnels excavated in jointed rock masses.

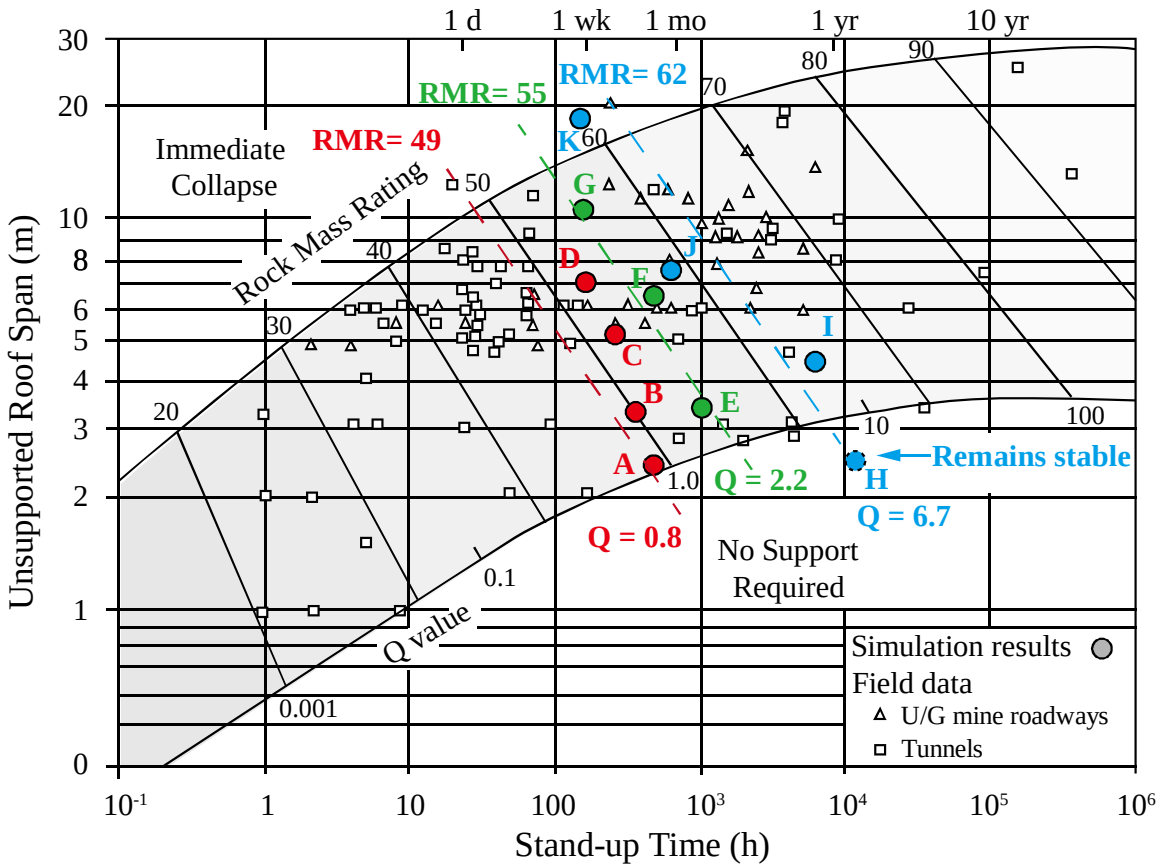

Figure 7-24. Simulated stand-up times of tunnels with different rock mass qualities and unsupported roof spans, plotted with the field data of Bieniawski (1989)

7.4 Discussions

As seen in Figure 7-24, 11 analysis cases (Cases A to K) are presented in the stand-up time chart. Nine cases (Cases A to G, I and J) are within the boundary defined by Bieniawski (1989). For Case H, the creep deformations on the walls stop after some time, and the tunnel remains stable afterwards. Because it is located in the 'No support required' zone, it conforms to the expectation of Bieniawski's stand-up time chart. For Case K, the simulated stand-up time is 7 days; however, it is located in the 'Immediate collapse' zone. This disagreement with Bieniawski's stand-up time chart may be attributed to the two assumptions used in the simulations, which may overestimate the stand-up time of tunnels.

The first assumption is that the time-dependent deformations during face advancement is not considered. In fact, creep deformations occur on the wall once the tunnel core is excavated (i.e., at the beginning of creep calculation, $t \leq 0$). In this case, The underestimation of the initial deformation on the walls can lead to an overestimation of the simulated stand-up time. The second assumption is that the simulations are carried out under pure creep deformation condition, and no dynamic disturbance (e.g., blast waves and seismic events) is considered during the creep calculation. Even though the key wedge on the roof is certain to fall down, it can keep stable for 7 days in the analysis. In reality, a small dynamic disturbance nearby can trigger the key wedge to fall.

In this study, the material is built as jointed rock mass and rock falls on the walls can be simulated, which makes it possible to evaluate the 'collapse' of a tunnel and determine the stand-up time. It shows that the distinct-element method is advantageous compared with the continuum method for simulating the stand-up time of tunnels. In analytical or numerical modeling using continuum method, the convergence on tunnel walls is 'unlimited' before the total closure of the tunnel. Because the yielded rock mass in plastic zones can generate continuous plastic flow, the simulated displacement on the wall can be 1 to 2 m for a tunnel with a width of 5 m (Vlachopoulos and Diederichs, 2009), which is unlikely to happen in the field, especially for tunnels excavated in jointed rock masses. Nguyen and Nguyen (2015) addressed this issue by assuming a displacement limit on tunnel walls. However, the value of the limit can be arbitrary in the analysis using the continuum method. For the distinct-element method, convergence on the tunnel wall is not unlimited. When the convergence on a tunnel cross-section is too large, the face-effect is reduced and rocks can fail from the roof or walls, leading to collapse of the tunnel, which

is closer to reality. This phenomenon is simulated in this study. For example, for the four simulation cases of tunnel Model I (Cases A, B, C and D, Figure 7-17), the rock blocks on the roof fall when the displacements on the roof exceed 12 to 15 mm. Such a 'displacement limit' is determined by the mechanical properties of the model material rather than given as a presumed value, which is more rational compared with the continuum method.

Analysis of tunneling-induced stress change and deformations near the tunnel face is a three-dimensional problem (Eberhardt, 2001). As a result, some limitations resulting from the two-dimensional analysis need to be mentioned. First, without the real connection between the cross-section and the tunnel face, a hypothetical internal pressure is used to mimic the face-support effect, which is different from the actual situation. In addition, the influence of installed rock support behind the cross-section under analysis cannot be considered. Other limitations of the two-dimensional and LDP-based analysis method, such as the influence of non-circular tunnel shape and the anisotropy stress field ($k \neq 1$), are mentioned in Vlachopoulos and Diederichs (2014). In addition, the time-dependent deformation in the face-advancement period and the influence of advance rate can hardly be simulated using a 2D model. Therefore, a 3D creep model, which can be used to consider more influencing factors in the actual tunneling engineering, will be developed in the future.

The randomness of joint distribution may affect the simulation results. For example, the location, persistence and orientation of joints can influence the shape and the location of key blocks. Three tunnel models (Models I, II and III) are built with wedges near the excavation boundary to observe time-dependent collapse of the tunnels. The actual situation in the field is more complex; for example, tunnels without key blocks can have a

longer stand-up time, which is controlled by new crack initiation and propagation leading to the formation of key blocks. Numerical modeling of this failure mechanism requests very fine zones of the blocks, which is computationally not possible given the time-dependent modeling nature of the problem.

7.5 Summary and conclusion

This study investigates the time-dependent deformations of tunnels excavated in jointed rock masses. A creep model for jointed rock masses, which considers the time-dependent deformations of both intact rock and joints, is adopted. The convergence-confinement method is used to model tunnels with different unsupported roof spans. Tunnels excavated in rock masses with different rock mass qualities are simulated.

Time-dependent deformation of jointed rock mass near the tunnel face can be simulated using the convergence-confinement analysis approach. The internal pressure reduction method can mimic the degradation of face-effect due to creep deformation of jointed rock mass effectively.

The stand-up time of an unsupported tunnel can be evaluated by simulating the time-to-collapse of the cross-section located at the supported/unsupported interface. The stand-up time of unsupported tunnels is influenced by unsupported roof span and rock mass quality. The simulated stand-up times agree well with Bieniawski's field data, which validates the simulation results. The simulation approach used in this study provides a novel tool to improve the understanding of the time-dependent deformation behavior of tunnels excavated in jointed rock mass.

In future studies, multiple factor analysis will be conducted to investigate the key factors that influence the stand-up time of tunnels. More analysis cases will be simulated and factors such as in-situ stress, joint roughness and joint inclination will be considered. In addition, considering the limitations of the two-dimensional analysis method, as discussed in the thesis, a three-dimensional creep model of jointed rock masses will be developed and used to simulate time-dependent deformation behaviors of jointed rock mass.

Chapter 8 Conclusions and future research

8.1 Thesis summary

This thesis presents a numerical study of time-dependent deformations of rock, joints, and jointed rock masses. The grain-based modeling approach is used to investigate the time-dependent failure mechanism of intact rock and joints at laboratory scale. A creep model for jointed rock mass is developed to simulate field-scale jointed rock mass models and time-dependent deformation of tunnels. A summary of the research presented in this thesis is presented below.

Firstly, understanding of the time-dependent deformation behavior of intact rock is enhanced. The GBM-TtoF creep model is proposed in Chapter 3 for the simulation of the lifetime of intact brittle rock under uniaxial and triaxial loading conditions. In the GBM-TtoF model, the grain-based modeling approach using UDEC is adopted to describe the heterogeneity and micro-fractures of rock. The time-dependent deformation of a grain cell is assumed to obey the Burgers creep model. The viscosity coefficient of the Maxwell component is modified to relate it to stress. The time to enter the acceleration creep deformation stage is considered as a function of the stresses and the strength parameters of the grain cell. A damage index is defined as a function of the strength parameters and the center driving stress ratio at a given time. Degradation of grain boundaries is considered to measure the roughness corrosion of a contact. The validity of the TtoF model is verified using laboratory uniaxial and triaxial compression test data of brittle rocks.

In Chapter 4, a model application of the GBM-TtoF model is simulating the time-dependent deformation of brittle rock pillars using laboratory-scale pillar models. First, time-dependent deformations of rock pillars are analyzed and the results are compared qualitatively with field observations. Second, the influence of the boundary profile of pillar walls on time-dependent strength and deformation of rock pillars is investigated. Two factors, pillar shape and loading ratio, which influence the time-dependent strength and deformation of rock pillars, are studied by conducting a series of creep simulations using four pillar models with width to height ratios of W/H = 0.5, 1.0, 1.5 and 2.0. Finally, long-term strengths and deformation features of slender and squat pillars are analyzed. It is found that time-dependent strengths and deformation of rock pillars can be simulated using the GBM-TtoF creep model properly. Gradual spalling on the pillar walls can be simulated using pillar models with rough boundary profiles. Creep deformations of slender and squat pillars could be quite different. Slender pillars are more likely to fail as time passes but squat pillars can tolerate more spalling on the walls without losing their stability. It is demonstrated that the GBM-TtoF creep model is successful in simulate time-dependent strength and deformation of hard rock pillars under creep-loading conditions.

In Chapter 5, a new creep model for time-dependent deformation of unweathered clean rock joints is developed. Firstly, five grain-scale joint models are established based on Barton's standard joint profiles using the GBM-TtoF creep material model. Barton's non-linear shear strength criterion is adopted to determine the short-term shear strength of the joints. Secondly, a series of creep simulations are conducted to investigate major factors (normal stress, shear loading ratio, and joint roughness) that influence the long-term shear strength and the sliding velocity of the joints. The results reveal that normal stress has more

influence than joint roughness on resisting creep slipping of the joints. Thirdly, an equation for the prediction of creep sliding velocity is developed by fitting the simulation results and the equation is verified by experimental data. Finally, a creep-slipping model for simplified flat joints is proposed, which can be used to model the long-term shear strength and sliding velocity of joints under creep deformation conditions. The creep-slipping model, which can be used in both stationary and variable stress conditions, is useful for simulating time-dependent behaviors of jointed rock mass using the DEM.

Based on the results of Chapter 3 and Chapter 5, a new creep model for jointed rock masses is developed in Chapter 6, which considers time-dependent deformations of both rock and joints. First, the implementation of the TtoF model for rock and the creep-slipping model for joints using UDEC is introduced. Then, creep simulations are conducted to study the influence of joint inclination and confining stress on the long-term stability of rock masses using square models with a single joint. Time-dependent deformation of a moderately jointed rock mass is simulated using a pillar model with multiple joints. Finally, a case study of a high-rock slope in western Norway is conducted and the creep deformation mechanisms of the rock mass are analyzed by comparing two slope models with different joint strength properties. It is found that there is no unstable movement on the potential sliding surfaces of the slope. The creep model of jointed rock mass provides a novel approach to analyze structural failures of jointed rock mass under creep loading conditions.

Finally, time-dependent deformation of tunnels excavated in jointed rock masses is investigated in Chapter 7. The creep deformations of both rock and joints are considered using the creep model for jointed rock masses developed in Chapter 6. Simulations of the

time-dependent deformation of tunnels are conducted using two-dimensional plane strain models based on the convergence-confinement analysis method. The weakening of the rock mass in a cross-section in an excavated tunnel due to time-dependent deformation of rock mass is simulated using the internal pressure reduction method. Stand-up times of tunnels excavated in jointed rock masses with different rock mass qualities and unsupported roof spans are simulated. The simulation results agree with field data, which validates the effectiveness of the analysis approach used. The analysis approach provides a useful tool for improving the understanding of time-dependent deformation behavior of tunnels.

8.2 Main conclusions

The main conclusions of this thesis are summarized below.

The GBM-TtoF creep model can model the viscous deformation and the time-to-failure phenomenon of intact brittle rock under uniaxial and triaxial compressive loading conditions. The time-dependent failure of rock is triggered by the sudden expansion of failed grains and contacts, which is resulting from stress re-distributions near the yield zones that are generated in the first two creep deformation stages. A higher confinement can effectively reduce stress concentrations in rock and prolong its lifetime.

The boundary profile is an important factor that can influence the long-term strength and time-dependent deformation patterns of rock pillars. Both the short-term and the long-term strengths of rock pillars increase with the increasing W/H ratio, but the long-term strength of squat pillars do not increase significantly due to the impact of spalling damage on the pillar walls. A slender pillar cannot tolerate severe spalling damage, and it is more likely

to collapse quickly and abruptly when it is loaded beyond its long-term strength. When a squat pillar is loaded beyond its long-term strength, the pillar presents continuous axial straining for a long time, and gradual spalling damage occurs on the pillar walls.

The grain-scale joint models perform well in simulating time-dependent deformations of rock joints. The simulated long-term shear strength and creep-slipping velocities agree well with laboratory results. The long-term shear strength has a positive correlation with normal stress and *JRC*. Under a constant shear-loading ratio, the long-term shear-strength ratio has a positive correlation with normal stress, a negative correlation with *JRC*. The creep sliding velocity has a negative correlation with normal stress, but it has a positive correlation with *JRC*. A higher normal stress is important for a rock joint to improve its long-term stability. The creep-slipping model for rock joints can be used to control the time-dependent deformation behavior of a flat-joint structure in DEM under both constant and variable shear-loading conditions.

The creep model of rock mass can be used to model time-dependent deformation of jointed rock masses effectively. The time-dependent deformation of a jointed rock mass is largely influenced by confinement and the angles between joint sets and the maximum principal stress. The axial strain rate and the lifetime of moderately jointed pillars are governed largely by the applied stress. The deformations of both intact rock and joints play important parts in the time-dependent deformation of jointed rock masses. As can be seen in the results of the case study, there are no significant sliding deformations on the potential sliding surfaces of the Oppstadhornet rock slope from 2003 to 2011. The creep slipping of

the steep foliation planes in the rock mass and the creep deformation of the rocks contributes to the time-dependent deformations of the slope.

Time-dependent deformation of rock mass near the tunnel face can be modeled effectively using the creep model of a jointed rock mass. The weakening of the face-effect due to time-dependent deformation of rock mass can be analyzed using the convergence-confinement method and the internal pressure reduction approach. Stand-up times of unsupported tunnels in jointed rock masses are evaluated by simulating the time-to-collapse of the cross-section at the support/unsupported interface. The stand-up time of tunnels is largely influenced by unsupported roof span and rock mass quality. The simulated stand-up times agree well with Bieniawski's field data.

8.3 Answers to research questions

Question (a). How do we describe the time-dependent deformation behavior of rocks properly? How do we understand the long-term strength of intact rocks?

Answer:

According to experimental tests, rocks present three deformation stages under creep loading conditions as shown in Figure 2-2. Existing creep models can model the deformations on the first two creep stages. However, time-dependent failure of rock cannot be modeled properly. To address this issue, the GBM-TtoF model for intact brittle rocks is developed in Chapter 3, which can effectively model the time-to-failure phenomenon under uniaxial and triaxial loading conditions. The model is calibrated and validated using experimental data of LdB granite. It can be useful for analyzing time-dependent

deformation behaviors of rocks; for example, the time-dependent spalling on pillar walls is simulated in Chapter 4.

The long-term strength of rock is an important parameter in engineering designs. In this study, the long-term strength of intact rock is assumed as the crack damage stress σ_{cd} of rock, which can be measured using laboratory tests. When a rock is loaded below the long-term strength, the creep deformations occur for some time, but the rock will not fail because damages in the rock cannot grow. When a rock is loaded above the long-term strength, the rock undergoes the three creep deformation stages, and the rock will eventually fail when it reaches the time to failure.

Question (b). If the time-dependent deformation of discontinuities is considered, how can it influence the time-dependent response of a jointed rock mass?

Answer:

For highly jointed rock masses, continuum methods can be used by adopting the isotropic material assumption. However, for moderately jointed rock masses, the deformations of joints make the mechanical response of a rock mass nonlinear and anisotropic. In addition, discontinuities usually contribute more than the intact rock to the time-dependent deformations of a jointed rock mass. For example, in a non-interlocked jointed rock-mass system, the deformations of joints dominate the deformation of the structure. Hence, the creep model developed specifically for describing time-dependent deformation of rock joints is necessary. Therefore, the creep deformation of rock joints is investigated and a

new creep model of joints is proposed in Chapter 5, allowing the time-dependent deformation behavior of jointed rock mass to be properly modeled.

Question (c). How do we develop an effective analysis approach for the creep deformation of rock mass that can consider time-dependent deformations of both rock and joints?

Answer:

In DEM, intact rocks are modeled as blocks (continuum zones meshed by finite-difference zones) and joints are modeled using flat joints. The mechanical responses of rock and joints are controlled separately by two different constitutive models. To properly model the time-dependent deformations of a jointed rock mass that can consider the deformations of both rock and joints, two effective creep constitutive models for rock and joints are required.

In this study, the time-to-failure creep model for rock is implemented for continuum finite-difference zones to model the creep deformation of blocks. Model parameters are calibrated using experimental data of LdB granite. The creep-slipping model of joints that was developed in Chapter 5 can be used to control the flat joints in DEM. These two models are combined to model time-dependent deformations of jointed rock masses. Details of the implementation of the creep model of jointed rock mass are documented in Section 6.1.

Question (d). How the time-dependent deformations of jointed rock mass influence the stand-up time of tunnels? How can we predict the stand-up time of a tunnel accurately?

Answer:

Time-dependent failure of tunnels results from the time-dependent deformation of the rock mass. In an unsupported tunnel, the tunnel face can provide a support effect to the adjacent rock mass along the tunnel, which is called the face-effect. When the time-dependent deformation of a rock mass is considered, the deformation on tunnel walls increases with time, which weakens the face-effect gradually. When the support from the face-effect is not sufficient to bear the loading from the surrounding rock mass, the tunnel will collapse and the stand-up time is reached.

To predict the stand-up time of a tunnel accurately, the time-dependent deformation of rock mass needs to be properly modeled. In Chapter 7, the stand-up time of tunnels is simulated using the creep model of a jointed rock mass in which the creep deformations of both rock and joints are considered. The convergence-confinement method is used to analyze the relation between displacement and internal pressure on tunnel walls. The internal pressure reduction method is used to mimic the weakening of face-effect as the tunnel face advances. Two factors, i.e., rock mass quality and unsupported roof span, that influence the stand-up time of tunnels are considered. The simulated stand-up time of tunnels agree well with Bieniawski's data. It shows that the simulation approach used in Chapter 7 can model the stand-up time of tunnels effectively.

8.4 Original contributions

Achievement 1

A new creep model for intact brittle rock is proposed. The GBM-TtoF creep model that uses the grain-based modeling method can capture time-dependent deformations of brittle

rocks, including the deformation in the first two creep stages and the crack coalescence in the tertiary creep stage. The model is useful for investigating creep mechanism of brittle rocks, e.g., time-dependent failure of rock pillars.

Achievement 2

A new simulation method for investigating time-dependent deformation of laboratory scale joints is proposed. The grain-based joint models perform well in simulating creep deformation of rock joints. Using the calibrated GBM-TtoF creep models, time-dependent joint deformations governed by stress corrosion of joint asperities can be simulated. In this manner, the long-term shear strength and the creep slipping of rock joint can be captured.

Achievement 3

A new creep constitutive model for rock joints is proposed and implemented in UDEC that can be used to control the time-dependent deformation of flat joints. The long-term strength and theoretical sliding velocity can be updated in each time step. The creep-slipping model is suitable for both constant and variable shear-loading conditions. This creep model of joint is computationally very efficient compared with the grain-based joint model.

Achievement 4

A new creep constitutive model for jointed rock masses is proposed. The TtoF model is implemented in the continuum numerical method (FDM) to control the time-dependent deformation of rocks. The creep-slipping model is used to govern the creep slipping of flat joints in DEM. The proposed creep constitutive model for jointed rock masses is

computationally efficient and it can be used for investigating time-dependent deformations of jointed rock masses using DEM.

Achievement 5

Using the developed creep model of a jointed rock mass and the convergence and confinement analysis method, stand-up times of tunnels excavated in jointed rock masses are simulated. The simulation results agree well with Bieniawski (1973)'s stand-up chart of unsupported tunnels. The proposed analysis method for time-dependent deformation of tunnels provides a useful tool for making important decisions related to rock support in drift development.

8.5 Recommendations for future research

Based on the findings achieved and attempts made from this thesis, additional research is still recommended to further improve the knowledge of the time-dependent deformation of rock, joints and rock mass and enhance creep modeling of jointed rock masses using DEM. Some recommendations for future research are made below.

Firstly, the influence of heterogeneity of mineral grains on time-dependent responses of brittle rock needs to be investigated in the future. The time-dependent deformation of brittle rocks is simulated in Chapter 3 using the grain-based modeling approach coupled with a strength degradation method. For simplicity, only one type of mineral grains is built for the micro-structure of LdB granite. However, there are various types of mineral grains in a rock. The properties of each grain, i.e., strength, size and shape, can influence the heterogeneity, and consequently affect the mechanical response of rock (Liu et al., 2018).

Based on the numerical study carried out in Chapter 3, it is understood that the lifetime of rock specimens is largely influenced by the occurrence and the expansion of creep damages accumulated during the creep loading process. It is expected that the heterogeneity of mineral grains can affect the stress concentrations in mineral grains and on grain boundaries, which in turn can influence the speed of creep damage accumulation at those locations. According to the literature, the heterogeneity of mineral grains can be an important factor that can explain why different types of rocks present different time-to-failure curves from static fatigue tests (Innocente, 2021). This assumption could be verified numerically in the future using an enhanced GBM-TtoF model that considers the grain heterogeneity of rock. This can be helpful for improving the understanding of time-dependent deformation of intact rock.

Secondly, the influence of filling materials (clay, silt or sand) and water in rock joints needs to be focused in the future. A creep model for unweathered clean rock joints is developed in Chapter 5 and is adopted to model the time-dependent response of flat joints in jointed rock mass models in UDEC. In creep-shear simulations using grain-based joint models (Chapter 5), joint roughness degradation due to creep damage occuring on joint asperities is simulated. Actually, many joint networks in the field are neither clean nor unweathered. Filling materials (sand, silt or clay) and seepage can influence the short-term shear strength and time-dependent deformations of rock joints. Therefore, further research is recommended to investigate the influence of filling materials and seepage on time-dependent response of rock joints.

Thirdly, an improved stand-up chart of tunnels can be developed. Stand-up time of tunnels excavated in jointed rock masses is simulated in Chapter 7. Based on Bieniawski (1973)'s stand-up chart, two main factors that influence the stand-up time of tunnels, which are rock mass quality and unsupported roof span, are considered, and a novel creep model for jointed rock mass proposed in Chapter 6 is used to simulate the creep deformation of jointed rock mass. However, additional factors such as in-situ stress, tunnel shape, excavation method and rock support are not considered. In the future, additional research can be conducted to address these issues. With more data of failed tunnel cases collected, the time-to-failure mechanism of tunnels can be back analyzed using the novel creep model of jointed rock masses proposed in this research. It can be expected that the stand-up time chart can be improved with more factors taken into consideration, which can be a useful tool for making important decisions related to rock support in drift development.

Then, a three-dimensional creep model needs to be developed. The creep model for jointed rock mass is implemented in a two-dimensional numerical program (UDEC). Jointed rock mass models are established and analyzed in two-dimensions based on plane-strain assumptions. In the future, to address the limitation of the two-dimensional model, a three-dimensional creep model for jointed rock mass needs to be developed and implemented in a three-dimensional numerical platform such as 3DEC (Itasca, 2018).

Finally, more experimental creep tests and field observations are recommended. The creep test data are relatively limited compared with the data of static mechanical properties of rock and joints, which makes it difficult to fully understand the deformation characteristics and failure mechanism of jointed rock masses under creep loading conditions. The problem

has drawn the attention of many scholars in the rock mechanics community, and ISRM released a suggested methods for determining the creep characteristics of rock in 2013 (Aydan et al., 2013). However, the creep-shear experimental data of rock joints is still quite limited. In addition, field data of time-dependent deformation of jointed rock masses is also limited; for example, failed case data of tunnels on Bieniawski (1973) stand-up chart have not been updated since 1973. Therefore, it is recommended that more experimental tests for creep deformation behaviors of rock and joints and case studies focusing on the creep deformation of rock masses could be carried out in the future. This data would be helpful for improving the understanding of creep deformation behavior of a rock mass and providing fundamental data and constants for the development of new numerical approaches that focus on this urgent topic, just as the author suggested in the background section (Section 1.1) of this thesis.

References

Lau et al., 2000Abdollahi, M. S., Najafi, M., Bafghi, A. Y. & Marji, M. F. 2019. A 3D numerical model to determine suitable reinforcement strategies for passing TBM through a fault zone, a case study: Safaroud water transmission tunnel, Iran. *Tunnelling and Underground Space Technology,* 88**,** 186-199.

Aftes 1976. Recommandations relatives à la méthode convergence-confinement. *Tunnels et Ouvrages souterrains,* 14**,** 139-164.

Ahmadi, S. & Eskandari, M. 2013. Vibration analysis of a rigid circular disk embedded in a transversely isotropic solid. *Journal of Engineering Mechanics,* 140**,** 04014048.

Alejano, L., Alonso, E., Rodriguez-Dono, A. & Fernandez-Manin, G. 2010. Application of the convergence-confinement method to tunnels in rock masses exhibiting Hoek-Brown strain-softening behaviour. *International journal of rock mechanics and mining sciences (1997),* 47**,** 150-160.

Alejano, L. R., González, J. & Muralha, J. 2012. Comparison of different techniques of tilt testing and basic friction angle variability assessment. *Rock mechanics and rock engineering,* 45**,** 1023-1035.

Alshkane, Y., Marshall, A. M. & Stace, L. 2017. Prediction of strength and deformability of an interlocked blocky rock mass using UDEC. *Journal of Rock Mechanics and Geotechnical Engineering,* 9**,** 531-542.

Aydan, Ö., Ito, T., Özbay, U., Kwasniewski, M., Shariar, K., Okuno, T., Özgenoğlu, A., Malan, D. F. & Okada, T. 2013. ISRM suggested methods for determining the creep characteristics of rock. *The ISRM Suggested Methods for Rock Characterization, Testing and Monitoring: 2007-2014.* Springer.

Aydan, O. & Nawrocki, P. Rate-dependent deformability and strength characteristics of rocks. The geotechnics of hard soils-soft rocks, 1998. 403-411.

Aydan, Ö., Sakamoto, A., Yamada, N., Sugiura, K. & Kawamoto, T. 2005. The characteristics of soft rocks and their effects on the long term stability of abandoned room and pillar lignite mines. *Post Mining.* Nancy, France.

Bahaaddini, M., Hagan, P., Mitra, R. & Khosravi, M. 2016. Experimental and numerical study of asperity degradation in the direct shear test. *Engineering geology,* 204**,** 41-52.

Bandis, S., Lumsden, A. & Barton, N. 1981. Experimental studies of scale effects on the shear behaviour of rock joints. *International journal of rock mechanics and mining sciences & geomechanics abstracts,* 18**,** 1-21.

Barla, G., Bonini, M. & Debernardi, D. 2010. Time dependent deformations in squeezing tunnels. *ISSMGE International Journal of Geoengineering Case Histories,* 2**,** 40-65.

Barla, G., Debernardi, D. & Sterpi, D. 2012. Time-dependent modeling of tunnels in squeezing conditions. *International Journal of Geomechanics,* 12**,** 697-710.

Barton, N. 1973. Review of a new shear-strength criterion for rock joints. *Engineering geology,* 7**,** 287-332.

Barton, N. Recent experiences with the Q-system of tunnel support design. Proceedings of the Symposium on Exploration for Rock Engineering, November 1978 Johannesburg. 107-117.

Barton, N. The influence of joint properties in modelling jointed rock masses. 8th ISRM Congress, 1995. International Society for Rock Mechanics and Rock Engineering.

Barton, N. & Bandis, S. 1980. Technical Note: Some Effects of Scale on the Shear Strength of Joints. *International Journal of Rock Mechanics and Mining Sciences,* 17**,** 69-73.

Barton, N., Bandis, S. & Bakhtar, K. 1985. Strength, deformation and conductivity coupling of rock joints. *International journal of rock mechanics and mining sciences & geomechanics abstracts,* 22**,** 121-140.

Barton, N. & Choubey, V. 1977. The shear strength of rock joints in theory and practice. *Rock mechanics,* 10**,** 1-54.

Bhasin, R. & Høeg, K. 1998. Parametric study for a large cavern in jointed rock using a distinct element model (UDEC-BB). *International Journal of Rock Mechanics and Mining Sciences,* 35**,** 17-29.

Bhasin, R. & Kaynia, A. M. 2004. Static and dynamic simulation of a 700-m high rock slope in western Norway. *Engineering Geology,* 71**,** 213-226.

Bieniawski, Z. 1973. Engineering classification of jointed rock masses. *Civil Engineer in South Africa,* 15.

Bieniawski, Z. 1990. Tunnel design by rock mass classifications. Technical report, Pennsylvania State Univ University Park Dept of Mineral Engineering.

Bieniawski, Z. 1993. Classification of rock masses for engineering: the RMR system and future trends. *Rock Testing and Site Characterization.* Elsevier.

Bieniawski, Z. T. 1989. *Engineering rock mass classifications: a complete manual for engineers and geologists in mining, civil, and petroleum engineering,* John Wiley & Sons.

Blikra, L. H., Skurtveit, E. & Braathern, A. 2002. Hazard evaluation of rock avalanches; the Baraldsnes-Oterøya area. *NGU-Report (Geological Survey of Norway) Report No. 2001.108.*

Boon, C. W. 2013. *Distinct element modelling of jointed rock masses: algorithms and their verification.*, Ph. D. thesis, Oxford University, UK.

Bowden, R. K. & Curran, J. Time-dependent behaviour of joints in Shale. The 25th US Symposium on Rock Mechanics (USRMS), 1984. American Rock Mechanics Association.

Brady, B. H. & Brown, E. T. 1993. *Rock mechanics: for underground mining,* Springer science & business media.

Brown, E. T., Bray, J. W., Ladanyi, B. & Hoek, E. 1983. Ground response curves for rock tunnels. *Journal of geotechnical Engineering,* 109**,** 15-39.

Cai, M. 2008. Influence of stress path on tunnel excavation response–Numerical tool selection and modeling strategy. *Tunnelling and Underground Space Technology,* 23**,** 618-628.

Cai, M. 2010. Practical estimates of tensile strength and Hoek–Brown strength parameter mi of brittle rocks. *Rock Mechanics and Rock Engineering,* 43**,** 167-184.

Cai, M. 2011. Rock mass characterization and rock property variability considerations for tunnel and cavern design. *Rock mechanics and rock engineering,* 44**,** 379-399.

Cai, M. & Kaiser, P. 2014. In-situ rock spalling strength near excavation boundaries. *Rock mechanics and rock engineering,* 47**,** 659-675.

Cai, M., Kaiser, P., Tasaka, Y., Maejima, T., Morioka, H. & Minami, M. 2004a. Generalized crack initiation and crack damage stress thresholds of brittle rock masses near underground excavations. *International Journal of Rock Mechanics and Mining Sciences,* 41**,** 833-847.

Cai, M., Kaiser, P., Tasaka, Y. & Minami, M. 2007. Determination of residual strength parameters of jointed rock masses using the GSI system. *International Journal of Rock Mechanics and Mining Sciences,* 44**,** 247-265.

Cai, M., Kaiser, P., Uno, H., Tasaka, Y. & Minami, M. 2004b. Estimation of rock mass deformation modulus and strength of jointed hard rock masses using the GSI system. *International Journal of Rock Mechanics and Mining Sciences,* 41**,** 3-19.

Carranza-Torres, C. 2009. Analytical and numerical study of the mechanics of rockbolt reinforcement around tunnels in rock masses. *Rock Mechanics and Rock Engineering,* 42**,** 175-228.

Carranza-Torres, C. & Fairhurst, C. 2000. Application of the convergence-confinement method of tunnel design to rock masses that satisfy the Hoek-Brown failure criterion. *Tunnelling and underground space technology,* 15**,** 187-213.

Chan, K. S., Brodsky, N. S., Fossum, A. F., Munson, D. E. & Bodner, S. R. 1997. Creep-induced cleavage fracture in WIPP salt under indirect tension. *Journal of Engineering Materials and Technology, Transactions of the ASME,* 119**,** 393-394.

Charles, R. 1958. Static fatigue of glass. I. *Journal of Applied Physics,* 29**,** 1549-1553.

Chen, L., Wang, C., Liu, J., Li, Y., Liu, J. & Wang, J. 2017. Effects of temperature and stress on the time-dependent behavior of Beishan granite. *International Journal of Rock Mechanics and Mining Sciences***,** 316-323.

Chen, S., Lee, S. & Gui, M. 2009. Effects of rock pillar width on the excavation behavior of parallel tunnels. *Tunnelling and underground space technology,* 24**,** 148-154.

Chen, W. & Konietzky, H. 2014. Simulation of heterogeneity, creep, damage and lifetime for loaded brittle rocks. *Tectonophysics,* 633**,** 164-175.

Chen, W., Wang, Z., Wu, G., Yang, J. & Zhang, B. 2007. Nonlinear creep damage constitutive model of rock salt and its application to engineering. *Yanshilixue Yu Gongcheng Xuebao/Chinese Journal of Rock Mechanics and Engineering,* 26**,** 467-472.

Chen, W. Z., Zhu, W. S. & Shao, J.-F. 2004. Damage coupled time-dependent model of a jointed rock mass and application to large underground cavern excavation. *International journal of rock mechanics and mining sciences,* 4**,** 669-677.

Chin, H.-P. & Rogers, J. D. 1987. Creep parameters of rocks on an engineering scale. *Rock mechanics and rock engineering,* 20**,** 137-146.

Christianson, M., Board, M. & Rigby, D. UDEC simulation of triaxial testing of lithophysal tuff. Golden Rocks 2006, The 41st US Symposium on Rock Mechanics (USRMS), 2006. American Rock Mechanics Association.

Cording, E., Hashash, Y. M. & Oh, J. 2015. Analysis of pillar stability of mined gas storage caverns in shale formations. *Engineering geology,* 184**,** 71-80.

Costin, L. 1983. A microcrack model for the deformation and failure of brittle rock. *Journal of Geophysical Research: Solid Earth,* 88**,** 9485-9492.

Cruden, D. M. 1971. Single- increment creep experiments on rock under uniaxial compression. *International Journal of Rock Mechanics and Mining Sciences,* 8**,** 127-142.

Damjanac, B. & Fairhurst, C. 2010. Evidence for a long-term strength threshold in crystalline rock. *Rock Mechanics and Rock Engineering,* 43**,** 513-531.

Duzgun, H. & Bhasin, R. 2009. Probabilistic stability evaluation of Oppstadhornet rock slope, Norway. *Rock mechanics and rock engineering,* 42**,** 729.

Eberhardt, E. 2001. Numerical modelling of three-dimension stress rotation ahead of an advancing tunnel face. *International Journal of Rock Mechanics and Mining Sciences,* 38**,** 499-518.

Estébanez, E. & Lage, A. Analytical Formulation of Stand-Up Time Based on 1989 Beniawski's Chart. ISRM European Rock Mechanics Symposium-EUROCK 2018, 2018. OnePetro.

Esterhuizen, G. 2006. An evaluation of the strength of slender pillars. *SME annual meeting and exhibit.* St. Louis, Missouri, preprint 06-003: Society for Mining, Metallurgy, and Exploration, Inc., Littleton.

Esterhuizen, G., Dolinar, D. & Ellenberger, J. 2011a. Pillar strength in underground stone mines in the United States. *International Journal of Rock Mechanics and Mining Sciences,* 48**,** 42-50.

Esterhuizen, G. S., Dolinar, D. R., Ellenberger, J. L. & Prosser, L. J. 2011b. Pillar and roof span design guidelines for underground stone mines. *Pittsburgh, PA: National Institute for Occupational Safety and Health***,** 1–64.

Fahimifar, A. & Soroush, H. 2005. Effect of time on the stress–strain behaviour of a single rock joint. *Bulletin of Engineering Geology and the Environment,* 64**,** 383-396.

Fahimifar, A., Tehrani, F. M., Hedayat, A. & Vakilzadeh, A. 2010. Analytical solution for the excavation of circular tunnels in a visco-elastic Burger's material under hydrostatic stress field. *Tunnelling and Underground Space Technology,* 25**,** 297-304.

Feng, J., Chuhan, Z., Gang, W. & Guanglun, W. 2003. Creep modeling in excavation analysis of a high rock slope. *Journal of Geotechnical and Geoenvironmental Engineering,* 129**,** 849-857.

Gadi, A. M. 1986. *Creep along a discontinuity in granite.* Master thesis, University of Manitoba.

Gao, F. 2013. *Simulation of failure mechanisms around underground coal mine openings using discrete element modelling.* Ph.D. thesis, Simon Fraser University.

Gao, F. & Stead, D. 2014. The application of a modified Voronoi logic to brittle fracture modelling at the laboratory and field scale. *International Journal of Rock Mechanics and Mining Sciences,* 68**,** 1-14.

Gao, W., Liu, Z. & Zhang, Z. 2015. Numerical simulation study on compression creep experiment of siltstone based on FLAC3D. *Tumu Gongcheng Xuebao/China Civil Engineering Journal,* 48**,** 96-102.

Gao, Y., Zhou, H., Zhang, C., Chen, J., He, S. & Liu, N. 2018. Research on the time-dependent strength criterion of brittle hard rock. *Yanshilixue Yu Gongcheng Xuebao/Chinese Journal of Rock Mechanics and Engineering,* 37**,** 671-678.

Glamheden, R. & Hoekmark, H. 2010. Creep in jointed rock masses. State of knowledge.: Tecnical report, Report No. R-0-49, Swedish Nuclear Fuel and Waste Management Co.

Goodman, R. E. 1989. *Introduction to rock mechanics.*, Wiley New York.

Grøneng, G., Lu, M., Nilsen, B. & Jenssen, A. K. 2010. Modelling of time-dependent behavior of the basal sliding surface of the Åknes rockslide area in western Norway. *Engineering Geology,* 114**,** 414-422.

Grøneng, G., Nilsen, B. & Sandven, R. 2009. Shear strength estimation for Åknes sliding area in western Norway. *International Journal of Rock Mechanics and Mining Sciences,* 46**,** 479-488.

Guan, Z., Jiang, Y., Tanabashi, Y. & Huang, H. 2008. A new rheological model and its application in mountain tunnelling. *Tunnelling and Underground Space Technology,* 23**,** 292-299.

Habib, P. & Berest, P. 1993. Rock mechanics for underground nuclear waste disposal in France. *Surface and Underground Project Case Histories.* Elsevier.

Haifei, J., Yuanguang, X., Baoyun, Z. & Kaixi, X. 2015. The creep properties of fine sandstone under uniaxial tensile stress. *Journal of Engineering Science and Technology Review,* 8**,** 136-142.

Halakatevakis, N. & Sofianos, A. 2010. Strength of a blocky rock mass based on an extended plane of weakness theory. *International Journal of Rock Mechanics and Mining Sciences,* 47**,** 568-582.

Han, B., Wang, Z. & Hao, Q. 2007. Study on damage and bifurcation properties of some granites based on triaxial creep experiment. *Yanshilixue Yu Gongcheng Xuebao/Chinese Journal of Rock Mechanics and Engineering,* 26**,** 4123-4129.

He, Z. L., Zhu, Z. D., Ni, X. H. & Li, Z. J. 2019. Shear creep tests and creep constitutive model of marble with structural plane. *European Journal of Environmental and Civil Engineering,* 23**,** 1275-1293.

Heap, M., Baud, P., Meredith, P., Bell, A. & Main, I. 2009. Time‐dependent brittle creep in Darley Dale sandstone. *Journal of Geophysical Research: Solid Earth,* 114, B07203.

Hedley, D. & Grant, F. 1972. Stope-and-pillar design for the Elliot Lake Uranium Mines. *Canadian Institute of Mining Metallurgy and Petroleum Bulletin (CIM Bulletin),* 65**,** 37-44.

Herget, G. 1987. Stress assumptions for underground excavations in the Canadian Shield. *International Journal of Rock Mechanics and Mining Sciences & Geomechanics Abstracts,* 24**,** 95-97.

Hermanns, R. L., Oppikofer, T., Dahle, H., Eiken, T., Ivy-Ochs, S. & Blikra, L. H. Understanding long-term slope deformation for stability assessment of rock slopes: the case of the Oppstadhornet rockslide, Norway. International Conference on Vajont–1963–2013, edited by: Genevois, R. and Prestininzi, A., Italian J. Eng. Geol. Environ., Book Ser, 2013. 255-264.

Hoek, E., Carranza-Torres, C. & Corkum, B. 2002. Hoek-Brown failure criterion-2002 edition. *Proceedings of NARMS-Tac,* 1**,** 267-273.

Hoek, E., Kaiser, P. K. & Bawden, W. F. 2000. *Support of underground excavations in hard rock*, CRC Press.

Hu, K., Feng, Q., Li, H. & Hu, Q. 2018. Study on creep characteristics and constitutive model for thalam rock mass with fracture in tunnel. *Geotechnical and Geological Engineering,* 36**,** 827-834.

Huang, S.-L., Feng, X.-T., Zhou, H. & Zhang, C.-Q. 2010. Study of aging failure mechanics and triaxial compression creep experiments with water pressure coupled stress of brittle rock. *Yantu Lixue/Rock and Soil Mechanics,* 31**,** 3441-3446+3451.

Innocente, J. C. 2021. *Time-Dependency and Long-Term Strength of Rocks-Limitations, Interpretation, and Application in Finite Difference Continuum Models.* Master thesis, Queen's University (Canada).

Itasca 2015. UDEC-Universal distinct element code. 6.0 ed. Minneapolis: Itasca Consulting Group. Inc.

Itasca 2018. 3DEC–Three dimensional distinct element code. 5.2 ed. Minneapolis: Itasca Consulting Group. Inc.

Jaeger, J. C., Cook, N. G. & Zimmerman, R. 2009. *Fundamentals of rock mechanics*, John Wiley & Sons.

Jing, L. & Hudson, J. 2002. Numerical methods in rock mechanics. *International Journal of Rock Mechanics and Mining Sciences,* 39**,** 409-427.

Kabwe, E., Karakus, M. & Chanda, E. K. 2020a. Isotropic damage constitutive model for time-dependent behaviour of tunnels in squeezing ground. *Computers and Geotechnics,* 127**,** 103738.

Kabwe, E., Karakus, M. & Chanda, E. K. 2020b. Time-dependent solution for non-circular tunnels considering the elasto-viscoplastic rockmass. *International Journal of Rock Mechanics and Mining Sciences,* 133**,** 104395.

Kachanov, M. 1980. *Microcrack Modelfor Rock Inelasticity.* Ph.D. thesis, Brown University, Providence, RI.

Kaiser, P., Diederichs, M., Martin, C., Sharp, J. & Steiner, W. Underground works in hard rock tunnelling and mining. ISRM international symposium, 2000. International Society for Rock Mechanics and Rock Engineering.

Kaiser, P. & Kim, B. Rock mechanics challenges in underground construction and mining. Proceedings of the First Southern Hemisphere International Rock Mechanics Symposium, 2008. Australian Centre for Geomechanics, 23-38.

Kaiser, P. K., Kim, B., Bewick, R. P. & Valley, B. 2011. Rock mass strength at depth and implications for pillar design. *Mining Technology,* 120**,** 170-179.

Kaiser, P. K. & Morgenstern, N. R. 1981. Phenomenological model for rock with time-dependent strength. *International Journal of Rock Mechanics and Mining Sciences,* 18**,** 153-165.

Kemeny, J. 2003. The time-dependent reduction of sliding cohesion due to rock bridges along discontinuities: A fracture mechanics approach. *Rock Mechanics and Rock Engineering,* 36**,** 27-38.

King, M. Creep in model pillars of Saskatchewan potash. International Journal of Rock Mechanics and Mining Sciences & Geomechanics Abstracts, 1973. Elsevier, 363-371.

Kontogianni, V., Psimoulis, P. & Stiros, S. 2006. What is the contribution of time-dependent deformation in tunnel convergence? *Engineering Geology,* 82**,** 264-267.

Korzeniowski, W. 1991. Rheological model of hard rock pillar. *Rock mechanics and rock engineering,* 24**,** 155-166.

Krauland, N. & Soder, P. 1987. Determining pillar strength-from pillar failure observation. *E&MJ-Engineering and Mining Journal,* 188**,** 34-40.

Kuesel, T. R., King, E. H. & Bickel, J. O. 2012. *Tunnel engineering handbook*, Springer Science & Business Media.

Kulatilake, P., Ucpirti, H., Wang, S., Radberg, G. & Stephansson, O. 1992. Use of the distinct element method to perform stress analysis in rock with non-persistent joints and to study the effect of joint geometry parameters on the strength and deformability of rock masses. *Rock Mechanics and Rock Engineering,* 25**,** 253-274.

Lajtai, E. & Gadi, A. 1989. Friction on a granite to granite interface. *Rock mechanics and rock engineering,* 22**,** 25-49.

Lajtai, E. Z. 1991. Time-dependent behaviour of the rock mass. *Geotechnical and Geological Engineering,* 9**,** 109-124.

Lajtai, E. Z. & Bielus, L. P. 1986. Stress corrosion cracking of lac du bonnet granite in tension and compression. *Rock mechanics and rock engineering,* 19**,** 71-87.

Lan, H., Martin, C. D. & Hu, B. 2010. Effect of heterogeneity of brittle rock on micromechanical extensile behavior during compression loading. *Journal of Geophysical Research,* 115.

Lau, J., Gorski, B., Conlon, B. & Anderson, T. 2000. Long-term loading tests on saturated granite and granodiorite. *Ontario Power Generation, Nuclear Waste Management Division Report,* Report No: 06819-REP-01300-10016 ROO.

Lauffer, H. 1958. Gebirgsklassifizierung für den Stollenbau: Geology Bauwesen. 24**,** 46-51.

Lavasani, M., Namin, M. L. & Fartash, H. 2015. Experimental investigation on mineral and organic fibers effect on resilient modulus and dynamic creep of stone matrix asphalt and continuous graded mixtures in three temperature levels. *Construction and Building Materials,* 95**,** 232-242.

Li, J. & Yao, Y. 2001. A study on creep and drying shrinkage of high performance concrete. *Cement and Concrete Research,* 31**,** 1203-1206.

Li, L., Tang, C., Wang, S. & Yu, J. 2013. A coupled thermo-hydrologic-mechanical damage model and associated application in a stability analysis on a rock pillar. *Tunnelling and underground space technology,* 34**,** 38-53.

Li, X., Kim, E. & Walton, G. 2019. A study of rock pillar behaviors in laboratory and in-situ scales using combined finite-discrete element method models. *International Journal of Rock Mechanics and Mining Sciences,* 118**,** 21-32.

Li, X. & Konietzky, H. 2015. Numerical simulation schemes for time-dependent crack growth in hard brittle rock. *Acta Geotechnica,* 10**,** 513-531.

Lim, S. S., Martin, C. D. & Åkesson, U. 2012. In-situ stress and microcracking in granite cores with depth. *Engineering geology,* 147**,** 1-13.

Liu, A., Lin, W. L. & Jiang, J. C. 2019. Investigation of the Long-Term Strength Properties of a Discontinuity by Shear Relaxation Tests. *Rock Mechanics and Rock Engineering***,** 1-10.

Liu, G. & Cai, M. Modeling time-dependent failure of brittle rock using PFC grain-based model. 52nd U.S. Rock Mechanics/Geomechanics Symposium, June 17, 2018 - June 20, 2018, 2018 Seattle, WA, United states. American Rock Mechanics Association (ARMA).

Liu, G. & Cai, M. 2020. Modeling time-dependent deformation behavior of brittle rock using grain-based stress corrosion method. *Computers and Geotechnics,* 118**,** 103323.

Liu, G., Cai, M. & Huang, M. 2018. Mechanical properties of brittle rock governed by micro-geometric heterogeneity. *Computers and Geotechnics,* 104**,** 358-372.

Liu, J., Feng, X. T., Ding, X. L. & Zhou, H. M. In situ tests on creep behavior of rock mass with joint or shearing zone in foundation of large-scale hydroelectric projects. Key Engineering Materials, 2004. Trans Tech Publ, 1097-1102.

Lunder, P. & Pakalnis, R. 1997. Determination of the strength of hard-rock mine pillars. *Canadian Institute of Mining Metallurgy and Petroleum Bulletin (CIM Bulletin),* 90**,** 51-55.

Malan, D. 1998. *An investigation into the identification and modeling of time-dependent behaviour of deep level excavations in hard rock.* Ph.D. thesis, South Africa: University of Witwatersrand.

Malan, D. 1999. Time-dependent behaviour of deep level tabular excavations in hard rock. *Rock Mechanics and Rock Engineering,* 32**,** 123-155.

Manh, H. T., Sulem, J., Subrin, D. & Billaux, D. 2015. Anisotropic time-dependent modeling of tunnel excavation in squeezing ground. *Rock Mechanics and Rock Engineering,* 48**,** 2301-2317.

Martin, C. & Christiansson, R. 2009. Estimating the potential for spalling around a deep nuclear waste repository in crystalline rock. *International Journal of Rock Mechanics and Mining Sciences,* 46**,** 219-228.

Martin, C., Kaiser, P. & Mccreath, D. 1999. Hoek-Brown parameters for predicting the depth of brittle failure around tunnels. *Canadian Geotechnical Journal,* 36**,** 136-151.

Martin, C. & Maybee, W. 2000. The strength of hard-rock pillars. *International Journal of Rock Mechanics and Mining Sciences,* 37**,** 1239-1246.

Martin, C. D. 1993. *The strength of massive Lac du Bonnet Granite around underground openings.* Ph.D. thesis, University of Manitoba.

Martin, C. D. & Chandler, N. A. 1994. The progressive fracture of Lac du Bonnet granite. *International Journal of Rock Mechanics and Mining Sciences & Geomechanics Abstracts,* 31**,** 643-659.

Mayer, J. & Stead, D. 2017. Exploration into the causes of uncertainty in UDEC grain boundary models. *Computers and Geotechnics,* 82**,** 110-123.

Mcclain, W. The effect of nonelastic behavior of rocks. The 8th US Symposium on Rock Mechanics (USRMS), 1966. American Rock Mechanics Association.

Mercer, K. 2007. Time dependent deformational behaviour of unsupported rock slopes. *Newsletter - Australian Centre for Geomechanics,* 29**,** 9-11.

Misra, A. K. 1973. Time-dependent strain or "creep" in rocks. *Journal of Mines, Metals and Fuels,* 21**,** 71-78.

Napier, J. & Malan, D. F. 2012. Simulation of time-dependent crush pillar behaviour in tabular platinum mines. *Journal of the Southern African Institute of Mining and Metallurgy,* 112**,** 711-719.

Nemat-Nasser, S. & Obata, M. 1988. A microcrack model of dilatancy in brittle materials. *Journal of Applied Mechanics,* 55**,** 24-35.

Ng, C. W., Lee, K. M. & Tang, D. K. 2004. Three-dimensional numerical investigations of new Austrian tunnelling method (NATM) twin tunnel interactions. *Canadian Geotechnical Journal,* 41**,** 523-539.

Nguyen, V.-M. & Nguyen, Q.-P. 2015. Analytical solution for estimating the stand-up time of the rock mass surrounding tunnel. *Tunnelling and Underground Space Technology,* 47**,** 10-15.

Nomikos, P., Rahmannejad, R. & Sofianos, A. 2011. Supported axisymmetric tunnels within linear viscoelastic Burgers rocks. *Rock Mechanics and Rock Engineering,* 44**,** 553-564.

Nopola, J. R. & Roberts, L. A. Time-dependent deformation of Pierre Shale as determined by long-duration creep tests. 50th US Rock Mechanics / Geomechanics Symposium 2016, June 26, 2016 - June 29, 2016, 2016 Houston, TX, United states. American Rock Mechanics Association (ARMA), 584-591.

Obert, L. 1965. *Creep in model pillars*, Tecnical report, report No. 6703, US Department of the Interior, Bureau of Mines.

Ortlepp, W. D. 2001. The behaviour of tunnels at great depth under large static and dynamic pressures. *Tunnelling and Underground Space Technology,* 16**,** 41-48.

Pan, Y.-W. & Dong, J.-J. Time-dependent tunnel convergence—I. Formulation of the model. International journal of rock mechanics and mining sciences & geomechanics abstracts, 1991. Elsevier, 469-475.

Pane, I. & Hansen, W. 2002. Early age creep and stress relaxation of concrete containing blended cements. *Materials and structures,* 35**,** 92.

Panet, M., Givet, P., Guilloux, A., Duc, J., Piraud, J. & Wong, H. 2001. The convergence–confinement method. *Press ENPC*.

Panet, M. & Guellec, P. Contribution à l'étude du soutènement d'un tunnel à l'arrière du front de taille. proceedings of the 3rd congress of the International Society for Rock Mechanics, September 1-7 1974 Denver, Colo., 1130-1134.

Panet, M. & Sulem, J. 2022. *Convergence-Confinement Method for Tunnel Design*, Springer.

Paraskevopoulou, C. & Diederichs, M. 2018. Analysis of time-dependent deformation in tunnels using the Convergence-Confinement Method. *Tunnelling and Underground Space Technology,* 71**,** 62-80.

Paraskevopoulou, C., Perras, M., Diederichs, M., Amann, F., Löw, S., Lam, T. & Jensen, M. 2017. The three stages of stress relaxation-Observations for the time-dependent behaviour of brittle rocks based on laboratory testing. *Engineering geology,* 216**,** 56-75.

Potvin, Y. 2017. Design guidelines for open stope support. *Rock Mechanics and Engineering.* CRC Press.

Potyondy, D. O. 2007. Simulating stress corrosion with a bonded-particle model for rock. *International Journal of Rock Mechanics and Mining Sciences,* 44**,** 677-691.

Qi, C. & Fourie, A. 2019. Numerical investigation of the stress distribution in backfilled stopes considering creep behaviour of rock mass. *Rock Mechanics and Rock Engineering,* 52**,** 3353-3371.

Ramamurthy, T. A realistic approach to estimate stand-up time. 11th ISRM Congress, 2007. OnePetro.

Read, R., Chandler, N. & Dzik, E. 1998. In situ strength criteria for tunnel design in highly-stressed rock masses. *International Journal of Rock Mechanics and Mining Sciences,* 35**,** 261-278.

Renani, H. R. & Martin, C. 2018. Modeling the progressive failure of hard rock pillars. *Tunnelling and Underground Space Technology,* 74**,** 71-81.

Riva, F., Agliardi, F., Amitrano, D. & Crosta, G. B. 2018. Damage-based time-dependent modeling of paraglacial to postglacial progressive failure of large rock slopes. *Journal of Geophysical Research: Earth Surface,* 123**,** 124-141.

Roberts, D., Lane, W. & Yanske, T. Pillar extraction at the Doe run Company, 1991–1998. Proceedings of the Conference 'The Mining Cycle', Australia, 1998. 227-233.

Robinson, P., Tveten, E. & Blikra, L. 1997. A post-glacial bedrock failure at Oppstadhornet, Oteroeya, More og Romsdal: a potential major rock avalanche. *NGU Bull,* 433**,** 46-47.

Sainoki, A. & Mitri, H. S. 2017. Numerical investigation into pillar failure induced by time-dependent skin degradation. *International Journal of Mining Science and Technology,* 27**,** 591-597.

Sainoki, A., Tabata, S., Mitri, H. S., Fukuda, D. & Kodama, J.-I. 2017. Time-dependent tunnel deformations in homogeneous and heterogeneous weak rock formations. *Computers and Geotechnics,* 92**,** 186-200.

Sakurai, S. 1978. Approximate time‐dependent analysis of tunnel support structure considering progress of tunnel face. *International Journal for Numerical and Analytical Methods in Geomechanics,* 2**,** 159-175.

Sakurai, S. Strength parameters of rocks determined from back analysis of measured displacements. First Asian Rock Mechanics Symposium. ISRM, Seoul, 1997. 95-99.

Salmi, E. F., Nazem, M. & Karakus, M. 2017. The effect of rock mass gradual deterioration on the mechanism of post-mining subsidence over shallow abandoned coal mines. *International Journal of Rock Mechanics and Mining Sciences,* 91**,** 59-71.

Schmidtke, R. H. & Lajtai, E. Z. 1985. The long-term strength of Lac du Bonnet granite. *International Journal of Rock Mechanics and Mining Sciences & Geomechanics Abstracts,* 22**,** 461-465.

Scholz, C. 1968. Experimental study of the fracturing process in brittle rock. *Journal of Geophysical Research,* 73**,** 1447-1454.

Sharifzadeh, M., Tarifard, A. & Moridi, M. A. 2013. Time-dependent behavior of tunnel lining in weak rock mass based on displacement back analysis method. *Tunnelling and Underground Space Technology,* 38**,** 348-356.

Shen, B. & Barton, N. 1997. The disturbed zone around tunnels in jointed rock masses. *International Journal of Rock Mechanics and Mining Sciences,* 34**,** 117-126.

Shen, M. & Zhang, Q. 2010. Study of shear creep characteristics of greenschist discontinuities. *Chin J Rock Mech Eng,* 29**,** 1149-55.

Shi, G. H. & Goodman, R. E. 1989. The key blocks of unrolled joint traces in developed maps of tunnel walls. *International Journal for Numerical and Analytical Methods in Geomechanics,* 13**,** 131-158.

Sinha, S. & Walton, G. 2018. A progressive S-shaped yield criterion and its application to rock pillar behavior. *International Journal of Rock Mechanics and Mining Sciences,* 105**,** 98-109.

Sjoberg, J. Failure modes and pillar behaviour in the Zinkgruvan mine. The 33th US Symposium on Rock Mechanics (USRMS), June 3rd 1992 Santa Fe, New Mexico. American Rock Mechanics Association.

Smith, G. & Rosenbaum, M. 1993. Recent underground investigations of abandoned chalk mine workings beneath Norwich City, Norfolk. *Engineering geology,* 36**,** 67-78.

Song, F., Rodriguez-Dono, A., Olivella, S. & Zhong, Z. 2020. Analysis and modelling of longitudinal deformation profiles of tunnels excavated in strain-softening time-dependent rock masses. *Computers and Geotechnics,* 125**,** 103643.

Sulem, J., Panet, M. & Guenot, A. 1987. An analytical solution for time-dependent displacements in a circular tunnel. *International journal of rock mechanics and mining sciences & geomechanics abstracts,* 24**,** 155-164.

Sun, H., Liu, X., Zhang, S. & Nawnit, K. 2020. Experimental investigation of acoustic emission and infrared radiation thermography of dynamic fracturing process of hard-rock pillar in extremely steep and thick coal seams. *Engineering Fracture Mechanics,* 226**,** 106845.

Tang, Z. C. & Wong, L. N. Y. 2016. Influences of normal loading rate and shear velocity on the shear behavior of artificial rock joints. *Rock Mechanics and Rock Engineering,* 49**,** 2165-2172.

Tatone, B. S. A. 2014. *Investigating the evolution of rock discontinuity asperity degradation and void space morphology under direct shear*, Ph.D. thesis, University of Toronto (Canada).

Unlu, T. & Gercek, H. 2003. Effect of Poisson's ratio on the normalized radial displacements occurring around the face of a circular tunnel. *Tunnelling and Underground Space Technology,* 18**,** 547-553.

Vlachopoulos, N. & Diederichs, M. 2009. Improved longitudinal displacement profiles for convergence confinement analysis of deep tunnels. *Rock mechanics and rock engineering,* 42**,** 131-146.

Vlachopoulos, N. & Diederichs, M. S. 2014. Appropriate uses and practical limitations of 2D numerical analysis of tunnels and tunnel support response. *Geotechnical and Geological Engineering,* 32**,** 469-488.

Von Kimmelmann, M., Hyde, B. & Madgwick, R. The use of computer applications at BCL Limited in planning pillar extraction and the design of mining layouts. Design and Performance of Underground Excavations: ISRM Symposium—Cambridge, UK, 3–6 September 1984, 1984. Thomas Telford Publishing, 53-63.

Wang, J., Li, D. & Shang, X. 2012. Creep failure of roof stratum above mined-out area. *Rock mechanics and rock engineering,* 45**,** 533-546.

Wang, J. A., Wang, Y. X., Cao, Q. J., Ju, Y. & Mao, L. T. 2015. Behavior of microcontacts in rock joints under direct shear creep loading. *International journal of rock mechanics and mining sciences,* 78**,** 217-229.

Wang, M. & Cai, M. 2020. A grain-based time-to-failure creep model for brittle rocks. *Computers and Geotechnics,* 119**,** 103344.

Wang, M. & Cai, M. 2021a. Numerical modeling of time-dependent spalling of rock pillars. *International Journal of Rock Mechanics and Mining Sciences,* 141**,** 104725.

Wang, M. & Cai, M. 2021b. A Simplified Model for Time-Dependent Deformation of Rock Joints. *Rock Mechanics and Rock Engineering,* 54**,** 1779-1797.

Wang, M. & Cai, M. 2022a. Modeling of time-dependent deformation of jointed rock mass. *Rock Mechanics and Rock Engineering,* 55**,** 2049–2070.

Wang, M. & Cai, M. 2022b. Numerical modeling of stand-up time of tunnels considering time-dependent deformation of jointed rock masses. *Rock Mechanics and Rock Engineering,* 55**,** 4305–4328.

Wang, M., Shi, X. & Zhou, J. 2018a. Charge design scheme optimization for ring blasting based on the developed Scaled Heelan model. *International Journal of Rock Mechanics and Mining Sciences,* 110**,** 199-209.

Wang, M., Shi, X., Zhou, J. & Qiu, X. 2018b. Multi-planar detection optimization algorithm for the interval charging structure of large-diameter longhole blasting design based on rock fragmentation aspects. *Engineering Optimization,* 50**,** 2177-2191.

Wang, X. & Cai, M. 2019. A comprehensive parametric study of grain-based models for rock failure process simulation. *International Journal of Rock Mechanics and Mining Sciences,* 115**,** 60-76.

Wang, Z., Gu, L., Shen, M., Zhang, F., Zhang, G. & Wang, X. 2019. Shear stress relaxation behavior of rock discontinuities with different joint roughness coefficient and stress histories. *Journal of Structural Geology,* 126**,** 272-285.

Wang, Z., Shen, M., Tian, G. & Zhang, Q. 2017a. Time-dependent strength of rock mass discontinuity with different values of JRC. *Chinese Journal of Rock Mechanics and Engineering,* 31**,** 3287-3296.

Wang, Z., Shen, M. R., Ding, W. Q., Jang, B. & Zhang, Q. Z. 2017b. Time-dependent behavior of rough discontinuities under shearing conditions. *Journal of Geophysics and Engineering,* 15**,** 51-61.

Wasantha, P., Ranjith, P., Zhang, Q. & Xu, T. 2015. Do joint geometrical properties influence the fracturing behaviour of jointed rock? An investigation through joint orientation. *Geomechanics and Geophysics for Geo-energy and Geo-resources,* 1**,** 3-14.

Wu, Z., Jiang, Y., Liu, Q. & Ma, H. 2018. Investigation of the excavation damaged zone around deep TBM tunnel using a Voronoi-element based explicit numerical manifold method. *International Journal of Rock Mechanics and Mining Sciences,* 112**,** 158-170.

Xu, G., He, C., Yang, Q. & Wang, B. 2019. Progressive failure process of secondary lining of a tunnel under creep effect of surrounding rock. *Tunnelling and Underground Space Technology,* 90**,** 76-98.

Xu, T., Xu, Q., Deng, M., Ma, T., Yang, T. & Tang, C. 2014. A numerical analysis of rock creep-induced slide; a case study from Jiweishan Mountain, China. *Environmental Earth Sciences,* 72**,** 2111-2128.

Xu, T., Xu, Q., Tang, C. A. & Ranjith, P. 2013. The evolution of rock failure with discontinuities due to shear creep. *Acta Geotechnica,* 8**,** 567-581.

Xu, T., Zhou, G., Heap, M. J., Yang, S., Konietzky, H. & Baud, P. 2018. The modeling of time-dependent deformation and fracturing of brittle rocks under varying confining and pore pressures. *Rock Mechanics and Rock Engineering,* 51**,** 3241-3263.

Xu, W. & Yang, S. 2005. Experiment and modeling investigation on shear rheological property of joint rock. *Chinese Journal of Rock Mechanics and Engineering,* 24**,** 5536-5542.

Xue, Y. T. & Mishra, B. Numerical Study on the Time-Dependent Behavior of Rock Joints. 53rd US Rock Mechanics/Geomechanics Symposium, 2019. American Rock Mechanics Association.

Yang, B., Mo, S., Wu, P. & He, C. 2013. An Empirical Constitutive Correlation for Regular Jugged Discontinuity of Rock Surfaces. *Advances in Applied Mathematics and Mechanics,* 5**,** 258-268.

Yang, H., Liu, J. & Zhou, X. 2017. Effects of the loading and unloading conditions on the stress relaxation behavior of pre-cracked granite. *Rock Mechanics and Rock Engineering,* 50**,** 1157-1169.

Yang, S.-Q., Xu, W.-Y. & Yang, S.-L. 2007. Investigation on shear rheological mechanical properties of shale in Longtan Hydropower Project. *Yantu Lixue(Rock and Soil Mechanics),* 28**,** 895-902.

Yang, S. & Jiang, Y. 2010. Triaxial mechanical creep behavior of sandstone. *Mining Science and Technology,* 20**,** 339-349.

Zhang, L., Liu, Y. & Yang, Q. 2016a. Study on time-dependent behavior and stability assessment of deep-buried tunnels based on internal state variable theory. *Tunnelling and Underground Space Technology,* 51**,** 164-174.

Zhang, Q., Shen, M. & Ding, W. 2012. Study of shear creep constitutive model of greenschist structural plane. *Rock and Soil Mechanics,* 33**,** 3632-3638.

Zhang, Q., Shen, M. & Ding, W. 2015. The shear creep characteristics of a green schist weak structural marble surface. *Mechanics of Advanced Materials and Structures,* 22**,** 697-704.

Zhang, Q., Wu, C., Fei, X., Jang, B. A. & Liu, D. 2019. Time-dependent behavior of rock joints considering asperity degradation. *Journal of Structural Geology,* 121**,** 1-9.

Zhang, Q. Z., Shen, M. R., Jang, B. A. & Ding, W. Q. 2016b. Creep behavior of rocks with rough surfaces. *Journal of Materials in Civil Engineering,* 28**,** 04016063.

Zhang, X.-P. & Wong, L. N. Y. 2013. Crack initiation, propagation and coalescence in rock-like material containing two flaws: a numerical study based on bonded-particle model approach. *Rock mechanics and rock engineering,* 46**,** 1001-1021.

Zhang, X., Gu, X., Lu, J. & Zhu, Z. 2016c. Experiment and simulation of creep performance of basalt fibre asphalt mortar under uniaxial compressive loadings. *Journal of Southeast University (English Edition),* 32**,** 472-478.

Zhang, Z. & Pan, E. 2019. Vertical and torsional vibrations of an embedded rigid circular disc in a transversely isotropic multilayered half-space. *Engineering Analysis with Boundary Elements,* 99**,** 157-168.

Zhang, Z., Wu, S., Tang, H., Liu, G. & Li, G. 2014. Time dependent deformation of antithetic dip rock slope. 33**,** 181-187.

Zhao, B., Liu, D., Huang, W., Liu, W., Huang, T. & Chen, C. 2018a. Creep behavior of red sandstone under uniaxial cyclic compression and tension loading. *Zhongnan Daxue Xuebao (Ziran Kexue Ban)/Journal of Central South University (Science and Technology),* 49**,** 2058-2066.

Zhao, J., Feng, X., Zhang, X., Yang, C. & Zhou, Y. 2018b. Time-dependent behaviour and modeling of Jinping Marble under true triaxial compression. *International Journal of Rock Mechanics and Mining Sciences,* 110**,** 218-230.

Appendix A: Verification of central driving stress ratio

As shown in the Figure A-1, there are four stress circles in the Mohr's diagram, and the centers of these circles are indicated as Points A, B, G and H. Circle B is generated from circle A by increasing σ_1 by $\Delta\sigma_1$, as presented in Eq. (A.1), while keeping σ_3 unchanged.

$$\sigma_1^B = \sigma_1^A + \Delta\sigma_1 . \tag{A.1}$$

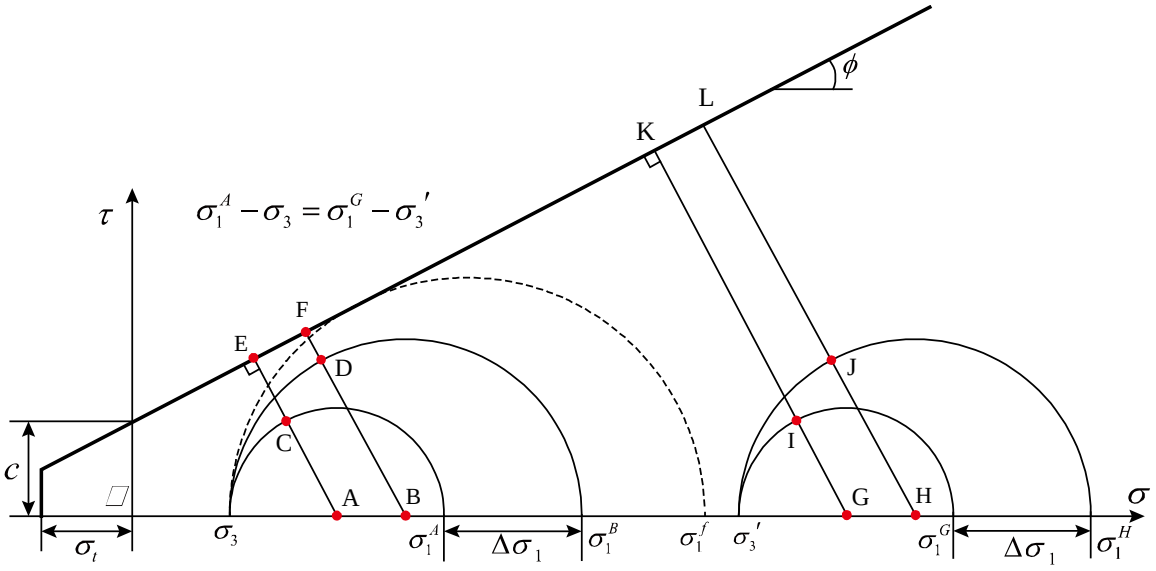

Figure A-1. Comparison of two different driving-stress ratios.

Circle H is generated from circle G by increasing σ_1 by $\Delta\sigma_1$, while keeping σ_3 unchanged. The differential stresses of status A and status G are equal to each other, as shown in Eq. (A.2).

$$\sigma_1^A - \sigma_3 = \sigma_1^G - \sigma_3' . \tag{A.2}$$

For the two stress variation processes, circles A to B and circles G to H, it is seen that the first stress increase is riskier than the second because the Mohr's circle is closer to the strength envelope. In the following discussion, two driving stress ratios are adopted to evaluate these two stress changes.

For the stress change from circles A to B, the right-driving-stress-ratio r_{sr} can be calculated as follow:

For circle A,

$$r_{sr}^{A} = \frac{\sigma_1^A - \sigma_3}{\sigma_1^f - \sigma_3}. \tag{A.3}$$

For circle B,

$$r_{sr}^{B} = \frac{\sigma_1^B - \sigma_3}{\sigma_1^f - \sigma_3}. \tag{A.4}$$

From Eqs. (A.3), (A.4) and (A.1), we have

$$\frac{r_{sr}^{B}}{r_{sr}^{A}} = 1 + \frac{\Delta\sigma_1}{\sigma_1^A - \sigma_3}. \tag{A.5}$$

Similarly, for the stress change from circles G to H, we have

$$\frac{r_{sr}^{H}}{r_{sr}^{G}} = 1 + \frac{\Delta\sigma_1}{\sigma_1^G - \sigma_3'}. \tag{A.6}$$

From Eqs. (A.5), (A.6) and (A.2), we can get

$$\frac{r_{sr}^{B}}{r_{sr}^{A}}=\frac{r_{sr}^{H}}{r_{sr}^{G}}. \tag{A.7}$$

Eq. (A.7) means that for these two cases, increasing σ_1 by $\Delta\sigma_1$ under different have the same effect compared with the initial stress status. It is obviously incorrect because the influence of the difference for σ_3 is ignored.

Next, the center-driving-stress-ratio r_{sc} is adopted to evaluate these two stress changes. For the stress change from circles A to B, the center driving stress ratio of circle A is

$$r_{sc}^{A}=\frac{AC}{AE}=\frac{\sigma_1^{A}-\sigma_3}{2AE}. \tag{A.8}$$

The center driving stress ratio of circle B is

$$r_{sc}^{B}=\frac{BD}{BF}=\frac{\sigma_1^{B}-\sigma_3}{2BF}. \tag{A.9}$$

From Eqs. (A.8) and (A.9), we have

$$\frac{r_{sc}^{B}}{r_{sc}^{A}}=\frac{AE}{BF}\frac{\sigma_1^{B}-\sigma_3}{\sigma_1^{A}-\sigma_3}. \tag{A.10}$$

Using Eq. (A.1), Eq. (A.10) can be written as

$$\frac{r_{sc}^{B}}{r_{sc}^{A}}=\frac{AE}{BF}\left(1+\frac{\Delta\sigma_1}{\sigma_1^{A}-\sigma_3}\right). \tag{A.11}$$

Similarly, for the stress change from circles G to H, we can get

$$\frac{r_{sc}^{H}}{r_{sc}^{G}} = \frac{GK}{HL}\left(1+\frac{\Delta\sigma_1}{\sigma_1^{G}-\sigma_3'}\right). \tag{A.12}$$

From Eqs. (A.11), (A.12) and (A.2), we can get

$$\frac{r_{sc}^{B}/r_{sc}^{A}}{r_{sc}^{H}/r_{sc}^{G}} = \frac{AE/BF}{GK/HL} < 1. \tag{A.13}$$

Eq. (A.13) means that a stress increment $\Delta\sigma_1$ has different impacts for these two stress changes. Because the average stress is considered in the center driving stress ratio r_{sc}, it is suitable for triaxial loading conditions as well. Hence, the center driving stress ratio r_{sc} is adopted in the model to evaluate the stress status of each zone.

Curriculum Vitae

Name:	Mingzheng Wang
Post-secondary Education and Degrees:	Northeastern University Shenyang, Liaoning, China 2011-2015 B.Eng. Central South University Changsha, Hunan, China 2015-2018 M.A.Sc. Laurentian University Sudbury, Ontario, Canada 2018-2022 Ph.D.
Honours and Awards:	Province of Ontario Graduate Scholarship 2020-2021
Related Work Experience:	Teaching Assistant Laurentian University 2018-2022 Research Assistant MIRARCO-Mining Innovation Laurentian University 2018-2022

Publications Related to PhD Thesis:

Journals

Wang, M., & Cai, M. (2020). A grain-based time-to-failure creep model for brittle rocks. *Computers and Geotechnics*, 119, 103344.

Wang, M., & Cai, M. (2021). Numerical modeling of time-dependent spalling of rock pillars. *International Journal of Rock Mechanics and Mining Sciences*, 141, 104725.

Wang, M., & Cai, M. (2021). A simplified model for time-dependent deformation of rock joints. *Rock Mechanics and Rock Engineering*, 54(4), 1779-1797.

Wang, M., & Cai, M. (2022). Modeling of Time-Dependent Deformation of Jointed Rock Mass. *Rock Mechanics and Rock Engineering*, 55 (4), 2049–2070. https://doi.org/10.1007/s00603-021-02750-2

Wang, M., & Cai, M. (2022). Numerical modeling of stand-up time of tunnels considering time-dependent deformation of jointed rock masses. *Rock Mechanics and Rock Engineering*, 55 (7), 4305–4328. https://doi.org/10.1007/s00603-022-02871-2

Conferences

Wang, M., & Cai, M. (2020). Modeling time-dependent deformation of rock joint. In *54th US Rock Mechanics/Geomechanics Symposium*. American Rock Mechanics Association.

Wang, M., & Cai, M. (2021). Simulation of time-dependent deformation of brittle rock pillars using a grain-based time-to-failure model. In *55th US Rock Mechanics/Geomechanics Symposium*. American Rock Mechanics Association.